SISSA **ISAS**

SCUOLA INTERNAZIONALE SUPERIORE DI STUDI AVANZATI
INTERNATIONAL SCHOOL FOR ADVANCED STUDIES

Numerical relativity simulations of non-vacuum spacetimes in three dimensions

Thesis submitted for the degree of
"Doctor Philosophiæ"

Candidate: Supervisor:

Luca Baiotti Prof. Luciano Rezzolla

October 2004

Contents

Chapter 1

Overview

The discovery of radio waves from extraterrestrial sources in the 1930's and their detailed study in the following decades started a revolution in our view of the Universe [241]. Earlier, only the slow orbital motion and the evolution of luminous stars and planets could be observed, while after the birth of radioastronomy much more rapid and/or violent phenomena became observable, such as collisions among galaxies, matter emission from active galactic nuclei, very luminous and very variable quasars and millisecond pulsars. The revolution brought about by radioastronomy has been so spectacular because the information carried by radio waves is very different from the one carried by visible light, which only allows to observe thermal photons produced by atomic excitation in the atmosphere of the stars. The radio wavelengths, instead, being about seven orders of magnitude larger than the ones of visible light, allow the observation of non thermal photons.

The difference between radio waves and visible light, though, is not nearly as dramatic as the difference between electromagnetic waves and gravitational waves. The former are oscillations of the electromagnetic field, propagating through spacetime; the latter are oscillations of the spacetime itself. The electromagnetic waves we can detect from outside the Earth are incoherent superpositions of single emissions by atoms, molecules or other charged particles and originate essentially in low-gravity regions, since strong-gravity regions tend to be surrounded by dense matter, which absorbs most of the electromagnetic radiation. On the contrary, the most intense gravitational radiation is produced in regions of strong gravitational fields by coherent movements of large compact masses and is not considerably absorbed by matter; thus it carries out information from such dense regions, which would not be possible to study otherwise, not even through neutrinos (which are not absorbed, but scatter many times before escaping the region). All these differences indicate that, if and when gravitational waves are directly detected, they would trigger an astronomical revolution much larger than the one originated by the discovery of radio waves. We know very little about the sources that are considered to be the greatest producers of gravitational waves. It is also likely that copious amounts of gravitational radiation reach the Earth from unexpected or unknown sources.

In addition to starting a new epoch in our observation of the Universe, the detection of gravitational waves will allow key tests on the fundamental laws of physics; tests that nowadays cannot be performed in any other way. First of all, the very detection of gravitational waves would confirm directly [1] a fundamental prediction of general relativity (and of metric gravitational theories in general), one of the last

[1] There are, however, important indirect observations that strongly suggest the existence of gravitational waves and their conformity to the waves predicted by general relativity; the first of these observations was the one on the Hulse Taylor binary pulsar PSR$1913+16$ [120]; others then followed, allowing even more precise measurements [249, 227, 131] (as, *e.g.*, in PSR B$1534+12$ [228]). New discoveries of binary pulsars systems have occurred recently [61].

that remain to be proven observationally or experimentally. Other tests on gravitational theories would come from the measurement of the gravitational-wave speed (predicted to be equal to the speed of light by general relativity and by tensor-multiscalar theories, but to be different from it by other theories [252]) and the polarization, indicating the spin content of the fields mediating the gravitational interaction. Furthermore, measurements of gravitational-wave signals will give direct proof of the existence of black holes [97, 98], will give insight on early-Universe physics (through the cosmic gravitational background radiation, whose time of last scattering dates back to much earlier than the one of the cosmic microwave background radiation) and will give information on the nuclear equations of state at the highest densities and on the birth and evolution of supernovæ and neutron stars (NSs, hereafter), also in connection with γ-ray bursts. For all these reasons, we strongly believe that the study and the detection of gravitational waves is a fundamental goal of contemporary scientific research.

The first detection of gravitational radiation has been imminent since several years... However, with the sensitivity of the detectors approaching the expected minimum sensitivity necessary for measuring gravitational radiation from the most intense sources, it is of growing urgency that we become able to accurately predict theoretically the gravitational waveforms emitted by those sources, especially the coalescence of two compact objects and non-spherical gravitational collapse leading to black-hole formation and/or to supernova explosion.

In order to improve our understanding of the above scenarios, it is important to solve the entire set of the Einstein and relativistic-hydrodynamics equations without approximations; these sources, in fact, are characterized by strong gravitational fields that cannot be even qualitatively (let alone a quantitatively) studied with perturbative theories. Given the high non-linearity and complexity of these equations, the only way to solve them is through large-scale numerical simulations, which must be performed in 3 dimensions, because of the absence of symmetries in the studied scenarios. The rapid increase in computing power through parallel supercomputers and the associated advance in software technologies is, at last, making such simulations technically possible also in the framework of general relativity.

Despite the recent efforts of several groups [102, 211, 100, 218, 88], though, such simulations are still plagued by many difficulties, among the biggest of which there are the choice of spacetime foliations and gauges that allow for stable and accurate numerical evolutions, the implementation of boundary conditions well suited to the treatment of the outgoing gravitational radiation and the presence of physical singularities on the numerical grids in the case of black holes.

However, progress on the overcoming of these obstacles is steady. We hope and believe that the work presented in this thesis is a step that will lead to important contributions to the numerical simulations of strong-field sources and thus to the theoretical needs of gravitational-wave astronomy. And not only.

With these goals in mind, we have written the `Whisky` [2] code, which solves on a 3-dimensional Cartesian numerical grid the general-relativistic hydrodynamics equations in a generic and time-varying curved spacetime, which is evolved with the Einstein equations. `Whisky` was not designed with a specific problem in mind, but, rather, it was conceived as a virtual laboratory, a tool to perform numerical experiments in the astrophysics of compact objects. Indeed, it has been, it is being and it will be used for the study of a variety of astrophysically-relevant issues, such as the ones mentioned above, also by people who originally did not participate in the writing of `Whisky`.

The `Whisky` code is the result of an ongoing and ever-growing collaboration among several European institutes. The original and main contributors to the writing of `Whisky` are, in addition to ourselves, Ian Hawke and Pedro Montero, while other developers joined later (in particular Frank Löffler).

[2] A note on the origin of the name of our code. It was finally decided on February 2$^{\text{nd}}$ 2002 in the Red Lion pub in Southampton, after the proposal by a Scottish friend. In Gaelic, *uisge*, or *whisky*, means *water of life*.

This thesis is composed of two parts. In the first one, comprising Chapters 2, 3 and 4, we will describe in detail the physical and mathematical framework upon which `Whisky` is built and we will give an outline of the internal workings of the code itself. In Chapter 2, among the many possible formulations of the Einstein equations, we will describe those which represent the state of the art in general-relativistic numerical simulations (*i.e.* the Nakamura Oohara Kojima formulation of the Einstein equations with "Gamma-driver" shift conditions) and which are implemented in the code that provides the evolution of the spacetime variables in our simulations. Chapter 3, then, will serve to illustrate the conservative formulation of the general-relativistic hydrodynamics equations which is implemented in our code and which permits the use of state-of-the-art numerical schemes for the evolution of hydrodynamical quantities, *i.e.* the *high-resolution shock-capturing* methods. In the first part of Chapter 4, the outline of `Whisky` will be given, while in the second part the validation of the code will be illustrated. The long series of convergence tests and the comparisons with analytical and perturbative solutions and with the results of other independent numerical codes are the necessary steps for gaining confidence in the results produced by the code.

In the second part of this thesis, on the other hand, we will concentrate on presenting physical results of the application of `Whisky` to specific problems. Chapter 5 is the first application of `Whisky` to a relevant astrophysical scenario: the collapse of a uniformly-rotating unstable NS to a Kerr black hole. We will show how accurately the code can follow the direct but modulated infall of matter up to the formation of black-hole horizons and farther. The dynamics of the horizons will be in turn analysed in detail, in order to produce quantitative upper limits to the energy emitted in gravitational radiation from the collapsing object. Through the use of fixed and progressive mesh refinement, we will show that we can now confidently extract the produced waveforms. This is the first such result in 3-dimensional general-relativistic numerical computations and it confirms, 20 years later, the seminal work of Stark and Piran [229] in axisymmetry.

In Chapter 6, as an intermediate step before simulating the merger of binary NS systems, but yet investigating an important physical scenario, we will show our evolutions of head-on and near-head-on collisions of two identical, non-spinning, cold NSs, which fall toward the centre of mass of the system. The systematic analysis of this problem has not yet ended, but we can already report some relevant results. We confirmed that the kinetic energy of the stars (transformed into internal energy through shock heating, if the equation of state allows for them) is not always – *i.e.* not for any initial rest masses of the stars – sufficient to avoid a prompt collapse, as was conjectured by Shapiro [207]. We find, instead, a critical mass (which is different and higher than the critical mass for the stability against collapse of a cold spherical star) above which, despite the presence of strong shocks, an apparent horizon forms promptly and engulfs all the stellar material in a dynamical timescale.

In Chapter 7, finally, we will turn to binary NS coalescences. This problem is both easier and more difficult than the binary black-hole problem. It is easier in that at early times there are no singularities and no horizons to contend with numerically. It is more difficult in that one cannot work with the vacuum Einstein equations, but must solve the equations of relativistic hydrodynamics in conjunction with the field equations. The results presented in this chapter are meant to be essentially preliminary investigations; in particular, despite having used resolutions comparable with those of other groups [149] who claim to have reached a convergent regime, we have found that with our code convergent numerical simulations of these systems require higher resolutions and farther numerical boundaries than the ones presently available for uniform grids with the computational resources at our disposal. These limitations were also experienced by [162]. As in the case of the gravitational-wave signal extraction in the collapse evolutions reported in Chapter 5, we believe that the present limitations will be to a great degree removed

by performing simulations on refined grids; such a possibility has recently become available.

Notation

Throughout this thesis we use the signature $(-,+,+,+)$ and units in which $c = G = M_{\odot} = 1$, unless explicitly specified. Greek indices are taken to run from 0 to 3; the Latin indices i, j, k, l, m run from 1 to 3 and indicate spatial components; Latin indices form the first part of the alphabet and different from the previous ones run from 1 to the dimension of the system of equations under study; Latin indices form the second part of the alphabet and different from the previous ones are reserved to label points on a numerical grid or for other miscellaneous purposes.

Computational resources

All the numerical computations discussed in this thesis were performed on the *Albert100* cluster at the University of Parma (Italy); some of the computations of Chapter 5 were also performed on the *Peyote* cluster at the Albert Einstein Institute (Golm, Germany).

Chapter 2

Numerical relativity in vacuum spacetimes

In this chapter we discuss the general principles of numerical relativity in the absence of matter. The treatment will be extended to non-vacuum spacetimes in the next chapter.

The Einstein equations describing the highly non-linear relation between the metric and the energy-matter fields are

$$G_{\mu\nu} \equiv R_{\mu\nu} - \frac{1}{2} g_{\mu\nu} R = 8\pi T_{\mu\nu} \,, \tag{2.0.1}$$

where $T_{\mu\nu}$ is the *stress-energy tensor*, $G_{\mu\nu}$ is the *Einstein tensor*, $R \equiv R^{\rho}{}_{\rho}$ is the *Ricci scalar*, $R_{\mu\nu} \equiv R^{\rho}{}_{\mu\rho\nu}$ is the *Ricci tensor*,

$$R^{\sigma}{}_{\mu\rho\nu} \equiv \partial_\rho \Gamma^{\sigma}_{\mu\nu} - \partial_\nu \Gamma^{\sigma}_{\mu\rho} + \Gamma^{\sigma}_{\tau\rho}\Gamma^{\tau}_{\mu\nu} - \Gamma^{\sigma}_{\tau_\nu}\Gamma^{\tau}_{\mu\rho} \tag{2.0.2}$$

is the *Riemann tensor* and

$$\Gamma^{\sigma}_{\mu\rho} \equiv \frac{1}{2} g^{\sigma\tau} \left(\partial_\mu g_{\rho\tau} + \partial_\rho g_{\mu\tau} - \partial_\tau g_{\mu\rho} \right) \tag{2.0.3}$$

are the *Christoffel symbols* expressed in terms of the metric $g_{\mu\nu}$. All these objects are 4-dimensional, that is they are defined on the 4-dimensional spacetime manifold $\mathcal{M}$.

Despite the covariant nature of the equations, the ability to perform long-term numerical simulations of self-gravitating systems in general relativity strongly depends on the formulation adopted for the Einstein equations (2.0.1) and forces the choice of appropriate coordinate charts that allow for stable accurate simulations. Over the years, the standard approach has been mainly based upon the "3+1" formulation of the field equations, which was first introduced by Arnowitt, Deser and Misner (ADM) [23]. In the following section we will give an outline of this formalism, while in Section 2.2 we will present a more recent formulation, which is numerically better behaved, thus permitting longer evolutions, and which is implemented in the code we use.

2.1 The Arnowitt Deser Misner "3+1" formalism

According to the ADM formalism, the spacetime manifold $\mathcal{M}$ is assumed to be globally hyperbolic and to admit a foliation by 3-dimensional spacelike hypersurfaces Σ_t parameterized by the parameter $t \in \mathcal{R}$: $\mathcal{M} = \mathcal{R} \times \Sigma_t$. The future-pointing 4-vector $\mathbf{n}$ orthonormal to Σ_t is then proportional to the gradient of t: $\mathbf{n} = -\alpha \boldsymbol{\nabla} t$, where α is chosen following the normalization $\mathbf{n} \cdot \mathbf{n} = -1$. Introducing a coordinate basis $\{\mathbf{e}_{(\mu)}\} = \{\mathbf{e}_{(0)}, \mathbf{e}_{(i)}\}$ of 4-vectors and choosing the normalization of the timelike

coordinate basis 4-vector $\mathbf{e}_{(0)}$ to be $\mathbf{e}_{(0)} \cdot \boldsymbol{\nabla} t = 1$, with the other three basis 4-vectors to be spacelike (*i.e.* tangent to the hypersurface: $\mathbf{n} \cdot \mathbf{e}_{(i)} = 0 \quad \forall i$), then the decomposition of $\mathbf{n}$ into the basis $\{\mathbf{e}_{(\mu)}\}$ is

$$\mathbf{n} = \frac{\mathbf{e}_{(0)}}{\alpha} + \frac{\boldsymbol{\beta}}{\alpha} , \tag{2.1.4}$$

where $\boldsymbol{\beta} = \beta^i \mathbf{e}_{(i)}$ is a purely spatial vector called the *shift* vector, since it describes how the spatial coordinates shift when moving from a slice Σ_t to another $\Sigma_{t'}$. The function α is instead called *lapse* and describes the rate of advance of time along the timelike unit-vector $\mathbf{n}$ normal to a spacelike hypersurface Σ_t. Defining $\gamma_{\mu\nu} \equiv g_{\mu\nu} + n_\mu n_\nu$ to be the spatial part of the 4-metric, so that $\boldsymbol{\gamma}$ is the projector orthogonal to $\mathbf{n}$ (*i.e.* $\boldsymbol{\gamma} \cdot \mathbf{n} = 0$) and γ_{ij} is the 3-metric of the hypersurfaces, the line element in the 3+1 splitting reads

$$\mathrm{d}s^2 = -(-\alpha^2 - \beta^i \beta_i)\mathrm{d}t^2 + 2\beta_i \mathrm{d}x^i \mathrm{d}t + \gamma_{ij} \mathrm{d}x^i \mathrm{d}x^j . \tag{2.1.5}$$

Eulerian observers at rest in the slice Σ_t, *i.e.* those having the 4-velocity $\mathbf{u}$ parallel to $\mathbf{n}$, measure the following 3-velocity of the fluid:

$$v^i = \frac{\boldsymbol{\gamma} \cdot \mathbf{u}}{-\mathbf{n} \cdot \mathbf{u}} = \frac{\gamma^i_\delta u^\delta}{\alpha u^0} = \frac{g^i_\delta u^\delta + n^i n_\delta u^\delta}{\alpha u^0} = \frac{u^i}{\alpha u^0} - n^i = \frac{u^i}{W} + \frac{\beta^i}{\alpha} , \tag{2.1.6}$$

where (2.1.4) has been used and where $-\mathbf{n}\cdot\mathbf{u} = \alpha u^0 = W$ is the Lorentz factor. Other useful expressions we will use in the next chapter are the covariant components of (2.1.6)

$$v_i = \frac{\gamma^\rho_i u_\rho}{-\mathbf{n} \cdot \mathbf{u}} = \frac{(\delta^\rho_i + n^\rho n_i) u_\rho}{W} = \frac{u_i}{W} \tag{2.1.7}$$

and

$$\begin{aligned} u_0 = u^\mu g_{\mu 0} &= u^0 g_{00} + u^i g_{i0} = u^0(-\alpha^2 + \beta_i \beta^i) + u^i \beta_i = \\ &= -W\left(\alpha - \frac{\beta^2}{\alpha}\right) + W\left(v^i - \frac{\beta^i}{\alpha}\beta_i\right) = W(v^i \beta_i - \alpha) . \end{aligned} \tag{2.1.8}$$

The original ADM formulation casts the Einstein equations into a first-order-in-time second-order-in-space quasi-linear system of equations [192] and a set of elliptic equations (the *constraint equations*). The dependent variables for which there is a time evolution are the 3-metric γ_{ij} and the extrinsic curvature

$$K_{ij} \equiv -\gamma^k_i \gamma^l_j \nabla_k n_l , \tag{2.1.9}$$

where ∇_i denotes the covariant derivative with respect to the 3-metric γ_{ij}. By construction, the extrinsic curvature is symmetric and purely spatial. The extrinsic curvature describes the embedding of the 3-dimensional spacelike hypersurfaces Σ_t in the 4-dimensional manifold $\mathcal{M}$. The first-order evolution equations are then given by

$$\mathcal{D}_t \gamma_{ij} = -2\alpha K_{ij} , \tag{2.1.10}$$

$$\mathcal{D}_t K_{ij} = -\nabla_i \nabla_j \alpha + \alpha \left[R_{ij} + K\, K_{ij} - 2K_{im}K^m_j - 8\pi\left(S_{ij} - \frac{1}{2}\gamma_{ij} S\right) - 4\pi\rho\gamma_{ij} \right] . \tag{2.1.11}$$

Here, $\mathcal{D}_t \equiv \partial_t - \mathcal{L}_{\boldsymbol{\beta}}$, $\mathcal{L}_{\boldsymbol{\beta}}$ is the Lie derivative[1] with respect to the vector $\boldsymbol{\beta}$, R_{ij} is the Ricci tensor of the 3-metric, $K \equiv \gamma^{ij}K_{ij}$ is the trace of the extrinsic curvature, $\rho \equiv n_\mu n_\nu T^{\mu\nu}$ is the total energy density as measured by a normal observer (*i.e.* the projection of the stress-energy tensor on the normal to the spatial hypersurface Σ_t), $S_{ij} \equiv \gamma_{i\mu}\gamma_{j\nu}T^{\mu\nu}$ is the projection of the stress-energy tensor onto the spacelike hypersurfaces and $S \equiv \gamma^{ij}S_{ij}$ (for a more detailed discussion, see [262]). Equation (2.1.10) illustrates the intuitive interpretation of the extrinsic curvature as the "time derivative" of the spatial metric γ_{ij}. The spatial metric on two different slices may still differ by a coordinate transformation, of course. In this intuitive framework, equation (2.1.11) represents the "acceleration", *i.e.* the variation of the variations of the spatial metric.

In addition to the evolution equations, the Einstein equations also provide four constraint equations to be satisfied on each spacelike hypersurface. The first of these is the Hamiltonian constraint equation

$$R + K^2 - K_{ij}K^{ij} - 16\pi\rho = 0 \,, \tag{2.1.12}$$

where R denotes the Ricci scalar of the 3-metric. The other three constraint equations are the momentum constraint equations

$$\nabla_j K^{ij} - \gamma^{ij}\nabla_j K - 8\pi S^i = 0 \,, \tag{2.1.13}$$

where $S^i \equiv -\gamma^{i\mu}n^\nu T_{\mu\nu}$ is the momentum density as measured by an observer moving orthogonally to the spacelike hypersurfaces.

The system of equations (2.1.10)–(2.1.13) is not closed; in fact, we are free to specify additional *gauge* conditions to determine the coordinate system. These are usually imposed as equations on the lapse and the shift. Different choices, though giving the same physical results, produce relevant differences in non-invariant quantities, which may determine the success or failure of numerical evolutions; thus a choice of good gauge conditions is fundamental for numerical relativity. There are numerous well tested gauge conditions and we will discuss some of them in Section 2.2.2.

Finally, we give here the expressions of the total mass and of the total angular momentum as measured at infinity in an asymptotically-flat spacetime

$$M_{\rm ADM} \equiv \frac{1}{16\pi}\int_{r=\infty}\sqrt{\gamma}\gamma^{im}\gamma^{jl}(\gamma_{ml,j} - \gamma_{jl,m})d^2\mathcal{S}_i \,, \tag{2.1.14}$$

$$(J_{\rm ADM})_i \equiv \frac{1}{8\pi}\varepsilon_{ij}{}^k\int_{r=\infty} x^j K^m_k d^2\mathcal{S}_m \,, \tag{2.1.15}$$

where $\mathcal{S}$ is a closed surface in an asymptotically-flat region and $\varepsilon_{ij}{}^k$ is the flat-space Levi-Civita tensor.

2.2 Conformal transverse traceless formulation

The first attempts to derive a stable and accurate formulation of the Einstein field equations in numerical relativity were based on the unconstrained solution (*i.e.* the solution of the time-evolution equations only, disregarding the constraint equations, except for checking the accuracy of the results) of the 3+1 ADM formulation of the field equations, which though, despite large-scale and dedicated collaborations [72, 2, 109], has gradually been shown to lack the stability properties necessary for

[1] For an arbitrary tensor $T^{s_1,\ldots,s_u}_{t_1,\ldots,t_w}$ and an arbitrary vector $\mathbf{v}$ the Lie derivative is defined as

$$\mathcal{L}_{\mathbf{v}}T^{s_1,\ldots,s_u}_{t_1,\ldots,t_w} \equiv v^r\nabla_r T^{s_1,\ldots,s_u}_{t_1,\ldots,t_w} - \sum_{n=1}^{u} T^{s_1,\ldots,r,\ldots,s_u}_{t_1,\ldots,t_w}\nabla_r v^{s_n} + \sum_{n=1}^{w} T^{s_1,\ldots,s_u}_{t_1,\ldots,r,\ldots,t_w}\nabla_{t_n} v^r \,.$$

long-term numerical simulations. In recent years, however, a considerable effort has been invested in extending the set of ADM equations solved, by including at some level the solution of the constraint equations on each spatial hypersurface [16, 202, 49] or by reformulating the ADM approach in order to achieve long-term stability (see, *e.g.*, [141] and references therein). Building on the experience developed with lower-dimensional formulations, Nakamura, Oohara and Kojima [173] presented in 1987 a conformal traceless reformulation of the ADM system, which subsequent authors (see, *e.g.*, [215, 41, 214, 212, 10, 100, 260, 125]) gradually showed to be robust enough to accomplish such a goal for different classes of spacetimes including black holes and NSs (both isolated and in coalescing binary systems). The most widespread version developed from this formalism, which we refer to here as the NOK formulation, was given by [215, 41] and is commonly referred to as the BSSN formulation.

2.2.1 Evolution of the field equations

In order to solve the system of equations for the evolution of the field equations (2.0.1), we adopt the above-mentioned NOK formulation [173], together with the important improvements introduced in [215, 41]. We will outline this formalism in what follows, but more details on how this formulation is actually implemented in `Cactus` can be found in [10, 9].

The conformal traceless reformulations of the ADM equations (2.1.10)–(2.1.13) make use of a conformal decomposition of the 3-metric and the trace-free part of the extrinsic curvature. Here we follow the presentation of [10]. The conformal 3-metric $\tilde{\gamma}_{ij}$ is defined as

$$\tilde{\gamma}_{ij} \equiv e^{-4\phi}\gamma_{ij} \ , \tag{2.2.16}$$

with the conformal factor chosen to be

$$e^{4\phi} = \gamma^{1/3} \equiv \det(\gamma_{ij})^{1/3} \ . \tag{2.2.17}$$

In this way the determinant of $\tilde{\gamma}_{ij}$ is unity. The trace-free part of the extrinsic curvature K_{ij}, defined by

$$A_{ij} \equiv K_{ij} - \frac{1}{3}\gamma_{ij}K \ , \tag{2.2.18}$$

is also conformally decomposed:

$$\tilde{A}_{ij} = e^{-4\phi}A_{ij} \ . \tag{2.2.19}$$

The evolution equations for the conformal 3-metric $\tilde{\gamma}_{ij}$ and the related conformal factor ϕ are then written as

$$\mathcal{D}_t\tilde{\gamma}_{ij} = -2\alpha\tilde{A}_{ij} \ , \tag{2.2.20}$$

$$\mathcal{D}_t\phi = -\frac{1}{6}\alpha K \ . \tag{2.2.21}$$

The evolution equation for the trace of the extrinsic curvature K can be found to be

$$\mathcal{D}_t K = -\gamma^{ij}\nabla_i\nabla_j\alpha + \alpha\left[\tilde{A}_{ij}\tilde{A}^{ij} + \frac{1}{3}K^2 + \frac{1}{2}\left(\rho + S\right)\right] \ , \tag{2.2.22}$$

where the Hamiltonian constraint was used to eliminate the Ricci scalar. For the evolution equation of the trace-free extrinsic curvature $\tilde{A}_{ij}$ there are many possibilities. A trivial manipulation of equation (2.1.11) yields:

$$\mathcal{D}_t\tilde{A}_{ij} = e^{-4\phi}\left[-\nabla_i\nabla_j\alpha + \alpha\left(R_{ij} - S_{ij}\right)\right]^{\mathrm{TF}} + \alpha\left(K\tilde{A}_{ij} - 2\tilde{A}_{il}\tilde{A}^l_j\right) \ , \tag{2.2.23}$$

where $[T_{ij}]^{\rm TF}$ refers to the trace-free part of a 3-dimensional second-rank tensor T_{ij}, *i.e.*, $[T_{ij}]^{\rm TF} \equiv T_{ij} - \gamma_{ij}T^k_k/3$. Note that, as shown in [215, 41], there are many ways to write several of the terms of (2.2.23), especially those involving the Ricci tensor; the expression which proved more convenient for numerical simulations consists in conformally decomposing the Ricci tensor as

$$R_{ij} = \tilde{R}_{ij} + R^{\phi}_{ij} \,, \tag{2.2.24}$$

where the "conformal-factor" part R^{ϕ}_{ij} is given directly by straightforward computation of the spatial derivatives of ϕ:

$$R^{\phi}_{ij} \;=\; -2\tilde{\nabla}_i\tilde{\nabla}_j\phi - 2\tilde{\gamma}_{ij}\tilde{\nabla}^l\tilde{\nabla}_l\phi + 4\tilde{\nabla}_i\phi\;\tilde{\nabla}_j\phi - 4\tilde{\gamma}_{ij}\tilde{\nabla}^l\phi\;\tilde{\nabla}_l\phi \,, \tag{2.2.25}$$

while the "conformal" part $\tilde{R}_{ij}$ can be computed in the standard way from the conformal 3-metric $\tilde{\gamma}_{ij}$. To simplify the notation, it is convenient to define what Baumgarte *et al.* [41] call the "conformal connection functions"

$$\tilde{\Gamma}^i \equiv \tilde{\gamma}^{jk}\tilde{\Gamma}^i_{jk} = -\partial_j\tilde{\gamma}^{ij} \,, \tag{2.2.26}$$

where the last equality holds if the determinant of the conformal 3-metric $\tilde{\gamma}$ is unity (note that this may well not be true in numerical simulations). Using the conformal connection function, the Ricci tensor can be written as[2]

$$\tilde{R}_{ij} \;=\; -\frac{1}{2}\tilde{\gamma}^{lm}\partial_l\partial_m\tilde{\gamma}_{ij} + \tilde{\gamma}_{k(i}\partial_{j)}\tilde{\Gamma}^k + \tilde{\Gamma}^k\tilde{\Gamma}_{(ij)k} + \tilde{\gamma}^{lm}\left(2\tilde{\Gamma}^k_{l(i}\tilde{\Gamma}_{j)km} + \tilde{\Gamma}^k_{im}\tilde{\Gamma}_{klj}\right) \,.$$

Also in this case there are several different choices of how the terms involving the conformal connection functions $\tilde{\Gamma}^i$ are computed. A straightforward computation based on the Christoffel symbols could be used (as in standard ADM formulations), but this approach leads to derivatives of the 3-metric in no particular elliptic form. Alcubierre *et al.* [10] found that if the $\tilde{\Gamma}^i$ are promoted to independent variables, then the expression for the Ricci tensor retains an elliptic character, which is positive in the direction of bringing the system a step closer to being hyperbolic. The price to pay is that in this case one must evolve three additional quantities. This has, however, net numerical advantages, which will be discussed below.

Following this argument of promoting the $\tilde{\Gamma}^i$ to independent variables, it is straightforward to derive their evolution equation

$$\partial_t\tilde{\Gamma}^i \;=\; -\partial_j\Big(2\alpha\tilde{A}^{ij} - 2\tilde{\gamma}^{m(j}\partial_m\beta^{i)} + \frac{2}{3}\tilde{\gamma}^{ij}\partial_l\beta^l + \beta^l\partial_l\tilde{\gamma}^{ij}\Big) \,. \tag{2.2.27}$$

Here too, there are different possibilities for writing these evolution equations; as pointed out in [41] it turns out that the above choice leads to an unstable system. Alcubierre *et al.* [10] found that a better choice can be obtained by eliminating the divergence of $\tilde{A}^{ij}$ with the help of the momentum constraint

$$\begin{aligned}\partial_t\tilde{\Gamma}^i \;=\;& -2\tilde{A}^{ij}\partial_j\alpha + 2\alpha\Big(\tilde{\Gamma}^i_{jk}\tilde{A}^{kj} - \frac{2}{3}\tilde{\gamma}^{ij}\partial_j K - \tilde{\gamma}^{ij}S_j + 6\tilde{A}^{ij}\partial_j\phi\Big) \\ & -\partial_j\Big(\beta^l\partial_l\tilde{\gamma}^{ij} - 2\tilde{\gamma}^{m(j}\partial_m\beta^{i)} + \frac{2}{3}\tilde{\gamma}^{ij}\partial_l\beta^l\Big) \,.\end{aligned} \tag{2.2.28}$$

With this reformulation, in addition to the evolution equations for the conformal 3-metric $\tilde{\gamma}_{ij}$ (2.2.20) and the conformal traceless extrinsic curvature variables $\tilde{A}_{ij}$ (2.2.23), there are evolution equations for the conformal factor ϕ (2.2.21) and the trace K of the extrinsic curvature (2.2.22). If the $\tilde{\Gamma}^i$ are promoted

[2] We define $T_{(ij)}$ as the symmetrized part of the tensor T_{ij}.

to the status of fundamental variables, they can be evolved with (2.2.28). We note that, although the final first-order-in-time and second-order-in-space system for the 17 evolved variables $\left\{\phi, K, \tilde{\gamma}_{ij}, \tilde{A}_{ij}, \tilde{\Gamma}^i\right\}$ is not in any immediate sense hyperbolic, there is evidence showing that the formulation is at least equivalent to a hyperbolic system [198, 47, 168].

In references [10, 6] the improved properties of this conformal traceless formulation of the Einstein equations were compared to the ADM system. In particular, in [10] a number of strongly gravitating systems were analysed numerically with convergent *high-resolution shock-capturing* (*cf.* Section 3.4) methods with *total-variation-diminishing* (*cf.* Section 3.6) schemes using the equations described in [103]. These included weak and strong gravitational waves, black holes, boson stars and relativistic stars. The results showed that this treatment leaded to a numerical evolution of the various strongly gravitating systems which did not show signs of numerical instabilities for sufficiently long times. However, it was also found that the conformal traceless formulation requires grid resolutions higher than the ones needed in the ADM formulation to achieve the same accuracy, when the foliation is made using the "K-driver" approach discussed in [35]. Because in long-term evolutions a small error growth-rate is the most desirable property, we have adopted the conformal traceless formulation as our standard form for the evolution of the field equations.

In conclusion of this section, we report the expressions (2.1.14) and (2.1.15) of the total mass and of the total angular momentum as measured in an asymptotically-flat spacetime, expressed in the variables introduced in this formulation and transformed, using the Gauss law, in volume integrals, which are better suited to Cartesian numerical computations [259]:

$$M = \int_V \left[e^{5\phi} \left(\rho + \frac{1}{16\pi} \tilde{A}_{ij} \tilde{A}^{ij} - \frac{1}{24\pi} K^2 \right) - \frac{1}{16\pi} \tilde{\Gamma}^{ijk} \tilde{\Gamma}_{jik} + \frac{1 - e^{\phi}}{16\pi} \tilde{R} \right] d^3x \,, \quad (2.2.29)$$

$$J_i = \varepsilon_{ij}{}^k \int_V \left(\frac{1}{8\pi} \tilde{A}^j_k + x^j S_k \quad + \frac{1}{12\pi} x^j K_{,k} - \frac{1}{16\pi} x^j \tilde{\gamma}^{lm}{}_{,k} \tilde{A}_{lm} \right) e^{6\phi} d^3x \,. \quad (2.2.30)$$

2.2.2 Gauge choices in `Cactus`

The code for the evolution of the Einstein equations implemented in `Cactus` is designed to handle arbitrary shift and lapse conditions, which can be chosen as the most appropriate for a given spacetime simulation. More information about the possible families of spacetime slicings which have been tested and used with the present code can be found in [10, 11]. Here, we limit ourselves to recall details about the specific gauges used in the evolutions reported in this thesis. In particular, we have used hyperbolic K-driver slicing conditions of the form

$$(\partial_t - \beta^i \partial_i) \alpha = -f(\alpha)\, \alpha^2 (K - K_0) \,, \quad (2.2.31)$$

with $f(\alpha) > 0$ and $K_0 \equiv K(t = 0)$. This is a generalization of many well-known slicing conditions. For example, setting $f = 1$ we recover the "harmonic" slicing condition, while, by setting $f = q/\alpha$, with q an integer, we recover the generalized "1+log" slicing condition [48]. In particular, all of the simulations discussed in this thesis are done using condition (2.2.31) with $f = 2/\alpha$. This choice has been made mostly because of its computational efficiency, but we are aware that "gauge pathologies" could develop with the "1+log" slicings [5, 12].

As for the spatial-gauge, we use one of the "Gamma-driver" shift conditions proposed in [11] (see also [9]), that essentially act so as to drive the $\tilde{\Gamma}^i$ to be constant. In this respect, the "Gamma-driver" shift conditions are similar to the "Gamma-freezing" condition $\partial_t \tilde{\Gamma}^k = 0$, which, in turn, is closely related to the well-known minimal distortion shift condition [222]. The differences between these two

conditions involve the Christoffel symbols and, while the minimal distortion condition is covariant, the Gamma-freezing condition is not.

All of the results reported here have been obtained using the hyperbolic Gamma-driver condition,

$$\partial_t^2 \beta^i = F\, \partial_t \tilde{\Gamma}^i - \eta\, \partial_t \beta^i \,, \tag{2.2.32}$$

where F and η are, in general, positive functions of space and time. For the hyperbolic Gamma-driver conditions it is crucial to add a dissipation term with coefficient η to avoid strong oscillations in the shift. Experience has shown that by tuning the value of this dissipation coefficient it is possible to almost freeze the evolution of the system at late times. We typically choose $F = 3/4$ and $\eta = 3$ and do not vary them in time.

2.3 Boundary conditions in Cactus

In standard 3+1 numerical simulations with spacelike hypersurfaces, the computational domain covers only a finite region of spacetime. One must therefore apply appropriate boundary conditions at the edges of the numerical grid. This issue equally applies to the field variables and to the hydrodynamics variables, even if the outer boundaries are usually placed in regions without matter (except for a tenuous *atmosphere*, as explained in Section 4.3.4) and so their evolution is often trivial. The same boundary condition are anyway applied to all variables.

Ideally, one would like to find a boundary condition that does not introduce numerical instabilities and allows gravitational waves to leave the grid cleanly, with no artificial reflections. This in itself is a very difficult problem. Firstly, there is no local boundary condition that allows waves coming from any arbitrary direction to leave the grid without reflections. Secondly, not all of the evolved quantities behave as waves and for those that do so this happens at spatial infinity only. Thirdly, presently available computational resources place the boundaries close to strong-field and highly-dynamical regions of spacetime, where the field variables do not have a mathematical behaviour that can be described by simple boundary conditions. In practice, what one looks for is a condition that remains stable and allows some "wave-like" solutions to leave the grid without introducing large reflections at the boundaries. The amount of artificial reflection that results typically depends on the specific form of the boundary condition and on the direction of motion of the wave fronts as they hit the boundary [113].

The boundary conditions actually implemented in the code are the following.

- *Static boundary condition.* The evolved variables are simply not updated at the boundary and maintain their initial values there. This condition is very bad at handling waves since it reflects everything back in, but it can be very useful when studying situations that are supposed to remain static (as are some of the systems studied below) and where a great part of the dynamics may come from numerical truncation errors.

- *Zero-order extrapolation or "flat" boundary condition.* After evolving the interior, the value of a given variable at the boundary is simply copied from the value of the inner neighbouring grid point (along the normal direction to the boundary). This condition allows for some dynamics at the boundaries and is better at letting waves leave the grid cleanly than the static boundaries, but it still introduces a considerable amount of reflections.

- *Sommerfeld or "radiative" boundary condition.* In this case we assume that the dynamical variables behave like a constant plus an outgoing radial wave at the boundaries, that is

$$f(x^i, t) = f_0 + u(r - t)/r, \tag{2.3.33}$$

where $r = \sqrt{x^2+y^2+z^2}$ and where the constant f_0 is taken to be one for diagonal metric components and zero for everything else. The radiative condition assumes that the boundaries are in the wave zone, where the gravitational waves behave as spherical wave fronts. This boundary condition has been used before in [215, 41], where it was found that in practice it is very good at letting waves leave the grid cleanly.

In practice, it is easier to implement a differential form of the radiative boundary condition than to use (2.3.33) directly. If we consider a boundary that corresponds to a coordinate plane $x_i =$ constant, the condition (2.3.33) implies

$$\frac{x_i}{r}\,\partial_t f + \partial_i f + \frac{x_i}{r^2}\,(f - f_0) = 0. \tag{2.3.34}$$

One can now use simple finite differences to implement this last condition. In our code we have implemented condition (2.3.34) consistently to second order in both time and space.

- *Robin boundary condition.* This is a different type of "extrapolating" boundary condition, where one assumes that for large r a given field behaves as

$$f(x^i) = f_0 + k/r, \tag{2.3.35}$$

with k constant. This condition is clearly related to the radiative condition described above, but it contains no information about the time evolution. Just as we did with the radiative condition, we implement the Robin condition in differential form:

$$\partial_i f + \frac{x_i}{r^3}\,(f - f_0) = 0. \tag{2.3.36}$$

The Robin boundary condition is usually better suited for solving elliptic problems than for a use on dynamical variables.

Most of the simulations discussed below have been performed applying the radiative boundary condition (2.3.34) to all field variables.

2.4 Field excision in `Cactus`

We here restrict our attention to excision algorithms in vacuum simulation; the extension of excision to hydrodynamics evolutions will be reported in Section 4.3.5. Traditional techniques using singularity avoiding slicings are not able to follow dynamical evolutions of black holes because of problems associated with the stretching of the slice which typically cause simulations to crash or to become extremely inaccurate on timescales far shorter than the ones needed for, *e.g.*, the evolution of binary-black-hole collisions. In these cases, removing the black hole interiors is crucial since those are the regions where the spacetime singularities reside, where the largest values of the curvature are present and where the main sources of the computational errors come from. In addition to the improvements achieved in the formulation of the field equations, successful long-term 3-dimensional evolutions of black holes in vacuum have been obtained in the last few years using excision techniques (see, *e.g.*, [206, 56, 8, 128, 127, 11, 259, 134, 68, 225]), although the original idea is much older [157].

Black-hole excision was first attempted successfully by Nadëzhin *et al* in spherical symmetry [167] and was later studied in more detail in [206, 22, 201, 151, 112, 199, 200, 128]. The idea is simple:

one places a boundary inside the black hole and excises its interior from the computational domain [3]. However, although conceptually simple, black-hole excision in 3 dimensions is a complicated problem numerically. Since no information can leave the interior of the black hole, excision cannot have any effect on the physics outside and no "excision boundary condition" should be needed. However, achieving this "boundary-without-a-boundary condition" [206, 112] in 3 dimensions is difficult, particularly if one uses a formulation of the evolution equations that is not hyperbolic. In fact, numerical calculations may violate this assumption, since disturbances, such as gauge waves, may travel at speeds larger than the speed of light, thus leaving the physically disconnected regions. What stated above, thus, is valid only if stable and causality-preserving boundary conditions are specified at the excision surface.

Another numerical problem in the implementation of excision is due to the fact that one has to cut a "hole" in the computational domain that has a spherical topology and is therefore not well adapted to the Cartesian coordinates typically used. Despite these difficulties, excision has now been implemented also with a 3+1 approach in 3 dimensions [8, 127, 11, 259, 134, 225], obtaining long-term stable, accurate evolutions of black hole spacetimes and overcoming the instabilities that typically plagued these evolutions [21, 80, 60, 248].

The algorithm implemented in `Cactus` is discussed in references [8, 11] and is as follows. Once an apparent horizon is found, either on the initial time slice or on any subsequent one, a *legosphere* (*i.e.* a region on the Cartesian grid approximating a sphere) is excised. The boundary condition at the first grid point inside the excision region simply consists in setting the value of each field at the excision boundary to the value of the field one grid point out along the normal direction to the legosphere (at edges and corners the normal direction is defined as the diagonal). This condition is perfectly consistent with evolving a static solution, where the time derivatives are supposed to be zero. Even in a dynamical situation, this condition is still consistent with the evolution equations since it is equivalent to calculating the source term one grid point away. This means that our boundary condition should introduce a first-order error, but as mentioned above, we do not expect this error to affect the solution outside the horizon. One could in principle argue that nothing prevents gauge modes and constraint violating modes from propagating outside the horizon, thus spoiling the second-order convergence of the exterior scheme. Alcubierre *et. al.* [8, 11] have looked carefully at the convergence of this set up and have found no evidence that error propagation outside the horizon happens in practice.

[3] Ideally, one would like to know the position of the event horizon which marks the true causal boundary, but the global character of its definition means that in principle one can only locate it once the whole evolution of the spacetime is known. The apparent horizon, on the other hand, can be located on every time slice and is guaranteed to be inside the event horizon. In practice one therefore needs to find the apparent horizon and excise a region contained inside it.

Chapter 3

Numerical relativity in non-vacuum spacetimes

The standard view on the dynamics of fluids includes only macroscopic phenomena. A fluid is thus considered as a set of *fluid elements*, *i.e.* of volumes of fluid that are much smaller than the typical size of the macroscopic system they are part of, so that they can be considered point-like for all physical and mathematical purposes. On the other hand, the linear dimensions of these fluid elements must be larger than the collision mean free path of the particles, in order to be representative of the mean quantities of the particles which are contained in it. The hydrodynamical quantities referring to the fluid in each point are defined as the averages over the fluid element at that point.

The hydrodynamics equations (the baryon-number conservation, the energy conservation and the Euler equations) form a non-linear system of hyperbolic equations that describes the motion of an ideal fluid, *i.e.* a fluid whose viscosity and heat conduction are assumed to be negligible. These equations allow for the formation of arbitrarily large and localized spatial variations of the hydrodynamical variables, which are mathematically treated as discontinuities in the hydrodynamical variables.

From a computational point of view, discontinuities are often a serious problem, especially for finite difference methods. However, the mathematical structure of hyperbolic equations can be exploited in order to develop numerical methods that are very efficient in resolving discontinuities. These techniques are known as High-Resolution Shock-Capturing (HRSC) methods and will be discussed in Section 3.4.

3.1 A summary of general-relativistic hydrodynamics

Before describing in detail the formulation and the numerical schemes upon which `Whisky` is based, we summarize here briefly some alternative formulations of general-relativistic hydrodynamics. The pioneering numerical work in general-relativistic hydrodynamics dates back to the 1-dimensional gravitational-collapse code of May and White [156, 157]. Building on theoretical work by Misner and Sharp [164], May and White developed a time-dependent numerical code to solve the evolution equations describing adiabatic spherical collapse in general relativity. This code was based on a Lagrangian finite-difference scheme, in which the coordinates are co-moving with the fluid. Artificial-viscosity terms were included in the equations to damp the spurious numerical oscillations caused by the presence of shock waves in the flow solution. The formulation of May and White became the starting point of a large number of numerical investigations in subsequent years. Hydrodynamics codes based on the original formulation of May and White and on later versions of it have been used in many non-linear simulations of supernova and NS collapse (see, *e.g.*, [235] and references therein), as well as in perturba-

tive computations of spherically-symmetric gravitational collapse within the framework of the linearized Einstein equations [204, 205]. An interesting analysis of the above formulation in the context of gravitational collapse is provided by Miller and Sciama [161]. By comparing the Newtonian and relativistic equations, these authors showed that the net acceleration of the infalling mass shells is larger in general relativity than in Newtonian gravity. The Lagrangian character of the formulation of May and White, together with other theoretical considerations concerning the particular coordinate gauge, has prevented its extension to multi-dimensional calculations. However, for 1-dimensional problems, the Lagrangian approach adopted by May and White has considerable advantages with respect to an Eulerian approach with spatially-fixed coordinates, most notably the lack of numerical diffusion.

The use of Eulerian coordinates in multi-dimensional numerical relativistic hydrodynamics started with the pioneering work by Wilson [254]. Instead of the rest-mass density ρ, of the 4-velocity u_{μ} and of the internal energy ϵ, he introduced the basic dynamical variables $D = \rho u^{0}$, $S_{\mu} = \rho h u_{\mu} u^{0}$ and $E = \rho\epsilon u^{0}$, representing the relativistic density, momenta and energy respectively, and rewrote the equations of motion as a coupled set of advection equations, in which the terms containing derivatives (in space or time) of the pressure were treated as source terms. This formulation was then referred to as the *Wilson formulation* [254, 255].

This approach, however, sidestepped an important guideline for the formulation of non-linear hyperbolic systems of equations, namely the preservation of their *conservation form*. This is a necessary condition to guarantee correct evolution in regions of sharp entropy generation (*i.e.*, shocks). Furthermore, some amount of numerical dissipation must be used to stabilize the solution across discontinuities. The first attempt to solve the equations of general-relativistic hydrodynamics in the original Wilson scheme [254] employed a combination of finite difference upwind techniques with artificial-viscosity terms.

The Wilson formulation has been widely used in hydrodynamical codes developed by a variety of research groups. Many different astrophysical scenarios were first investigated with these codes, including axisymmetric stellar core-collapse [169, 170, 38, 229, 93], accretion onto compact objects [118, 183], numerical cosmology [65, 20] and, more recently, the coalescence of NS binaries [256, 257, 154]. This formalism has also been employed, in the special-relativistic limit, in numerical studies of heavy-ion collisions [158].

The Wilson formulation showed some limitations in handling situations involving ultra-relativistic flows (*i.e.* flows with Lorentz factor $W \gg 2$), as first pointed out by Centrella and Wilson [65]. Norman and Winkler [176] performed a comprehensive numerical assessment of such formulation by means of special-relativistic hydrodynamical simulations. They concluded that those large errors were mainly due to the way in which the artificial-viscosity terms were included in the numerical scheme in the Wilson formulation. These terms, in fact, were originally only added to the pressure terms in some places, namely at the pressure gradient in the source of the momentum equation and at the divergence of the velocity in the source of the energy equation. However, Norman and Winkler [176] proposed to add the artificial-viscosity terms in a relativistically consistent way, in order to consider the artificial viscosity as a real viscosity. The consistent addition of the artificial-viscosity terms, made the relativistic equations much more coupled than their Newtonian counterparts. As a result Norman and Winkler proposed the use of implicit schemes as a way to describe more accurately such a coupling. Their code, which in addition incorporated an adaptive grid, reproduced very accurate results even for ultra relativistic flows with Lorentz factors of about 10 in 1-dimensional, flat-spacetime simulations.

Covariant (that is not restricted to spacelike foliations) conservative formulations of the general-relativistic hydrodynamics equations for ideal fluids were first reported in [92] and, more recently,

in [182, 180]. The *form invariance* of these approaches with respect to the nature of the spacetime foliation implies that existing work on highly specialized techniques for fluid dynamics (*i.e.* HRSC schemes, see Section 3.4) can be adopted straightforwardly.

Eulderink and Mellema [92] were the first to derive a covariant formulation of the general-relativistic hydrodynamics equations. As in the formulation implemented in `Whisky` and discussed in Section 3.3.1, these authors took special care of the conservative form of the system and so rewrote the system with no derivatives of the dependent fluid variables appearing in the source terms. Additionally, this formulation was strongly adapted to a particular numerical method based on a generalization of the Roe approximate Riemann solver. Such solver was first applied to the non-relativistic Euler equations in [193] and has been widely employed since in simulating compressible flows in computational fluid dynamics. It is also one of the approximate Riemann solvers we have implemented in `Whisky` (*cf.* Section 3.5.1). Eulderink and Mellema computed the exact "Roe matrix" (*cf.* Section3.5.1) and obtained the corresponding spectral decomposition. The performance of this general-relativistic Roe solver was tested in a number of 1-dimensional problems for which exact solutions are known, including non-relativistic shock tubes, special-relativistic shock tubes and spherical accretion of dust and a perfect fluid onto a (static) Schwarzschild black hole.

Another covariant formulation was derived by Papadopoulos and Font [182]. Instead of the rest-mass density ρ, of the spatial components of the 4-velocity u^i and of the internal energy ϵ, they introduced the basic dynamical variables $D = \rho u^0$, $S^i = \rho h u^0 u^i + p g^{0i}$ and $E = \rho h u^0 u^0 + p g^{00}$, representing the relativistic density, momenta and energy respectively. Note that these variables differ slightly from previous choices of the Wilson formulation. With these definitions the equations of general-relativistic hydrodynamics take a conservation law form, the local characteristic structure of which was presented in [182], where the formulation proved well suited for the numerical implementation of HRSC schemes.

Procedures for integrating various forms of the hydrodynamical equations on null (light-like) spacetime foliations have also been proposed, but they are much less common than those providing solutions on spacelike hypersurfaces. They were first presented by Isaacson *et al.* [122]. This approach was developed for the study of smooth isentropic flows. A Lagrangian method, limited to spherical symmetry, was developed by Miller and Motta [160]. More recently, a general lightcone-hydrodynamics formalism was laid out by Papadopoulos and Font [182, 180] and has been applied to complex astrophysical problems [181].

3.2 Hyperbolic partial differential equations

The homogeneous system of m partial differential equations (PDEs)

$$\partial_t u^c(x,t) + \sum_{b=1}^{m} a^{cb}(x,t)\partial_x u^b(x,t) = 0 \tag{3.2.1}$$

or, in matrix notation,

$$\partial_t \mathbf{U}(x,t) + \mathbf{A}(x,t)\partial_x \mathbf{U}(x,t) = 0 \tag{3.2.2}$$

is said to be *quasi-linear* if the matrix $\mathbf{A}$ of the coefficients is a function of $\mathbf{U}$ only and is said to be *hyperbolic* if $\mathbf{A}$ is diagonalizable with a set of real eigenvalues $\lambda_1, \ldots, \lambda_m$ and a corresponding set of m linearly-independent right eigenvectors $\mathbf{R}^{(1)}, \ldots, \mathbf{R}^{(m)}$ such that

$$\mathbf{A}\mathbf{R}^{(a)} = \lambda_a \mathbf{R}^{(a)} \ . \tag{3.2.3}$$

Furthermore, if all the eigenvalues λ_a are distinct, the system is said to be *strictly hyperbolic*. When a system of PDEs is written in the form

$$\partial_t \mathbf{U} + \partial_x [\mathbf{F}(\mathbf{U})] = 0 \,, \tag{3.2.4}$$

it is said to be in a *conservative form*. In this case it can also be written in form (3.2.2) with $\mathbf{A}(\mathbf{U}) \equiv \partial \mathbf{F}/\partial \mathbf{U}$ being the Jacobian of the flux vector $\mathbf{F}(\mathbf{U})$. In a conservative system, knowledge of the state vector $\mathbf{U}(x,t)$ at one point in spacetime allows to determine the flux for each state variable. As we will see, this is the case for the hydrodynamics equations. It was shown by Lax and Wendroff [138] in a theorem that, if shocks are present, converging conservative numerical methods, *i.e.* methods relying on a conservative form of the equations, converge to the *weak solution*[1] of the problem, while non conservative methods generally do not. Furthermore, Hou and LeFloch [119] demonstrated that, in general, a non-conservative scheme will converge to the wrong weak solution in the presence of a shock and hence they underlined the importance of flux-conservative formulations.

In order to appreciate the importance of a conservative formulation of the hydrodynamics equations, let us consider the prototype of a hyperbolic equation in conservation form, that is the scalar linear advection equation in one dimension

$$\partial_t u(x,t) + \lambda \partial_x u(x,t) = 0 \,, \tag{3.2.5}$$

with initial conditions at $t = 0$

$$u(x,0) = u_0(x) \,. \tag{3.2.6}$$

The solution of (3.2.5) is easily calculated and is given by

$$u(x,t) = u(x - \lambda t, 0) \tag{3.2.7}$$

for $t \geq 0$. As time evolves, the initial data simply propagates unchanged with speed $|\lambda|$ toward the right or the left according to the sign of λ, which is called *characteristic speed*. The *characteristic curves* of the equation are the curves in the $x - t$ plane satisfying the ordinary differential equation (ODE) $x'(t) = \lambda$, $x(0) = x_0$. The solution $u(x,t)$ is constant along a characteristic curve

$$\frac{\mathrm{d}u(x(t),t)}{\mathrm{d}t} = 0 \qquad \text{when} \qquad x = x_0 - \lambda t \,. \tag{3.2.8}$$

This notation can be extended to a system of m hyperbolic PDEs like (3.2.2). Since, by definition, hyperbolicity guarantees that a complete set of right eigenvectors $\mathbf{R}^{(a)}$ exists, if we indicate with $\mathbf{K}$ the matrix whose columns are the $\mathbf{R}^{(a)}$, then

$$\mathbf{\Lambda} = \mathbf{K}^{-1} \mathbf{A} \mathbf{K} \,, \tag{3.2.9}$$

where

$$\mathbf{\Lambda} = \mathrm{diag}(\lambda_1, \lambda_2, \ldots, \lambda_\mathrm{m}) \,. \tag{3.2.10}$$

Introducing now the *characteristic variables*

$$\mathbf{W} \equiv \mathbf{K}^{-1} \mathbf{U} \,, \tag{3.2.11}$$

[1] Weak solutions are solutions of the integral form of the conservative system; they are continuous and differentiable or have at most a finite number of discontinuities.

system (3.2.2) becomes

$$\partial_t \mathbf{W} + \mathbf{\Lambda}\partial_x \mathbf{W} = 0 \,. \tag{3.2.12}$$

This is called the *canonical form* of the system and consists of m decoupled independent linear advection equations, each of which has solution

$$w^a(x,t) = w^a(x - \lambda_a t, 0) \,. \tag{3.2.13}$$

The solution of the original system is found from the one of the canonical system through inversion of (3.2.11), that is $\mathbf{U} = \mathbf{K}\mathbf{W}$ or, in components,

$$\mathbf{U}(x,t) = \sum_{a=1}^{m} w^a(x,t)\mathbf{K}^{(a)} = \sum_{a=1}^{m} w^a(x - \lambda_a t, 0)\mathbf{K}^{(a)} \,. \tag{3.2.14}$$

From the last relation it is clear that the solution can be written as the superposition of m waves, each propagating undistorted with a speed given by the corresponding eigenvalue.

3.3 Formulation of the equations

We now discuss how the mathematical formalism described in the previous section can be used to derive a conservative form of the relativistic hydrodynamics equations in a curved spacetime.

3.3.1 Conservative form of the relativistic Euler equations

In a generic curved spacetime the local conservation of baryon number and of energy momentum are expressed as

$$\nabla \cdot \mathbf{J} = 0 \,, \tag{3.3.15}$$

$$\nabla \cdot \mathbf{T} = 0 \,, \tag{3.3.16}$$

where $\nabla\cdot$ stands for the covariant divergence with respect to the metric $g_{\mu\nu}$. In the coordinate basis $\{\mathbf{e}_{(0)}, \mathbf{e}_{(i)}\}$ (*cf.* Section 2.1), the rest-mass-current vector $\mathbf{J}$ and of the stress-energy tensor $\mathbf{T}$ have components

$$J^\mu = \rho u^\mu \,, \qquad T^{\mu\nu} = \rho h u^\mu u^\nu + p g^{\mu\nu} \,, \tag{3.3.17}$$

where ρ is the rest-mass density, u^μ is the 4-velocity of the fluid, p is the pressure, $h = 1 + \epsilon + p/\rho$ is the specific enthalpy and ϵ is the specific internal energy. An equation of state (EoS) $p = p(\rho, \epsilon)$ closes the system. After substituting (3.3.17) into (3.3.15)–(3.3.16), the obtained system is not in a conservative form. However, it was shown by Banyuls *et al* [36] that the system (3.3.15)–(3.3.16) can be put in a conservative form after the introduction of a suitable set of *conservative* variables. We start from the conservation of baryon number (3.3.15), which is already in conservative form, but does not make use of the conservative variables we will need in the following. To exploit this we write

$$\begin{aligned}
0 &= \nabla_\alpha\left(\rho u^\alpha\right) = \\
&= \partial_\alpha\left(\rho u^\alpha\right) + \rho\Gamma^\alpha_{\alpha\beta}u^\beta = \partial_\alpha\left(\rho u^\alpha\right) + \frac{1}{2}\rho u^\beta g^{\alpha\gamma}\left(\partial_\alpha g_{\gamma\beta} + \partial_\beta g_{\alpha\gamma} - \partial_\gamma g_{\alpha\beta}\right) = \\
&= \partial_\alpha\left(\rho u^\alpha\right) + \frac{1}{2}\rho u^\beta g^{\alpha\gamma}\partial_\beta g_{\alpha\gamma} = \partial_\alpha\left(\rho u^\alpha\right) + \frac{1}{2}\rho u^\beta \frac{1}{g}\partial_\beta g = \\
&= \partial_\alpha\left(\rho u^\alpha\right) + \rho u^\beta \frac{1}{\sqrt{-g}}\partial_\beta\sqrt{-g} = \frac{1}{\sqrt{-g}}\partial_\alpha\left(\sqrt{-g}\rho u_\alpha\right) = \\
&= \frac{1}{\sqrt{-g}}\left[\partial_t\left(\sqrt{-g}\rho u^0\right) + \partial_i\left(\sqrt{-g}\rho u^i\right)\right] \,,
\end{aligned} \tag{3.3.18}$$

where $g \equiv \det(g_{\alpha\beta})$. It is natural now to define the *conserved* variable $D = \rho W = \rho\alpha u^0$ and to write, using also (2.1.6) and $\sqrt{-g} = \alpha\sqrt{\gamma}$,

$$\frac{1}{\sqrt{-g}}\{\partial_t\big(\sqrt{\gamma}D\big) + \partial_i\big[\sqrt{\gamma}D\big(\alpha v^i - \beta^i\big)\big]\} = 0\ . \tag{3.3.19}$$

Equations (3.3.16), instead, are not in conservative form and a more extended algebraic manipulation is necessary. While it this straightforward, it is not easy to find it in the literature and for this reason we sketch it here. First, it gives physical insight to split them into two parts, one parallel and one orthogonal to u^α:

$$u_\alpha \nabla_\beta T^{\beta\alpha} \;=\; 0\ , \tag{3.3.20}$$

$$h^\gamma_\alpha \nabla_\beta T^\beta_\gamma \;\equiv\; \big(\delta^\gamma_\alpha + u_\alpha u^\gamma\big)\nabla_\beta T^\beta_\gamma = 0\ , \tag{3.3.21}$$

where $h^\gamma_\alpha \equiv \delta^\gamma_\alpha + u_\alpha u^\gamma$ is a projector to the space orthogonal to u^α:

$$u^\alpha h^\gamma_\alpha = u^\gamma + u^\alpha u^\gamma u_\gamma = u^\gamma - u^\gamma = 0\ . \tag{3.3.22}$$

From (3.3.20),

$$\begin{aligned}
0 \;&=\; u_\alpha \nabla_\beta\big(h\rho u^\alpha u^\beta + p g^{\alpha\beta}\big) = \\
&=\; u_\alpha u^\alpha u^\beta \nabla_\beta\big(h\rho\big) + h\rho u^\beta u_\alpha \nabla_\beta u^\alpha + h\rho u_\alpha u^\alpha \nabla_\beta u^\beta + u_\alpha g^{\alpha\beta}\nabla_\beta p = \\
&=\; -u^\beta \nabla_\beta\big(h\rho\big) - h\rho\nabla_\beta u^\beta + u^\beta \nabla_\beta p = \\
&=\; -\rho u^\beta \nabla_\beta h - h\big(u^\beta\nabla_\beta\rho + \rho\nabla_\beta u^\beta\big) + u^\beta\nabla_\beta p = \\
&=\; -\rho u^\beta\nabla_\beta h - h\nabla_\beta\big(\rho u^\beta\big) + u^\beta\nabla_\beta p = u^\beta\nabla_\beta p - \rho u^\beta\nabla_\beta h\ ,
\end{aligned} \tag{3.3.23}$$

where $u_\alpha\nabla_\beta u^\alpha = 0$ and (3.3.15) have been used. From the spatial part of (3.3.21),

$$0 \;=\; h^\alpha_j \nabla_\beta\big(h\rho u^\beta u_\alpha + \delta^\beta_\alpha p\big) = h^\alpha_j h\rho u^\beta \nabla_\beta u_\alpha + h^\alpha_j \delta^\beta_\alpha \nabla_\beta p\ , \tag{3.3.24}$$

since $h^\alpha_j u_\alpha = 0$. The 4-acceleration $a_\alpha = u^\beta\nabla_\beta u_\alpha$ is orthogonal to the 4-velocity, so (3.3.24) becomes

$$\begin{aligned}
0 \;&=\; h\rho h^\alpha_j a_\alpha + h^\alpha_j \partial_\alpha p = h\rho a_j + u^\alpha u_j \partial_\alpha p + \delta^\alpha_j \partial_\alpha p = \\
&=\; h\rho u^\beta \nabla_\beta u_j + u_j u^\alpha \partial_\alpha p + \partial_j p\ .
\end{aligned} \tag{3.3.25}$$

Then, using (3.3.23),

$$\begin{aligned}
0 \;&=\; h\rho u^\beta \nabla_\beta u_j + \rho u_j u^\beta \nabla_\beta h + \partial_j p = \\
&=\; h\rho u^\beta \partial_\beta u_j - h\rho u^\beta \Gamma^\alpha_{\beta j} u_\alpha + \rho u_j u^\beta \partial_\beta h + \partial_j p = \\
&=\; \partial_\beta\big(h\rho u^\beta u_j\big) - h u_j \partial_\beta\big(\rho u^\beta\big) - h\rho u^\beta \Gamma^\alpha_{\beta j} u_\alpha + \partial_j p\ .
\end{aligned} \tag{3.3.26}$$

From the continuity equation (3.3.15), it follows

$$\begin{aligned}
0 \;&=\; \nabla_\beta\big(\rho u^\beta\big) = \frac{1}{\sqrt{-g}}\partial_\beta\big(\rho u^\beta\sqrt{-g}\big) = \\
&=\; \partial_\beta\big(\rho u^\beta\big) + \frac{1}{\sqrt{-g}}\rho u^\beta \partial_\beta\sqrt{-g} = \partial_\beta\big(\rho u^\beta\big) + \rho u^\beta \Gamma^\alpha_{\alpha\beta}\ ,
\end{aligned} \tag{3.3.27}$$

so (3.3.26) becomes

$$\begin{aligned}
0 \;&=\; \partial_\beta\big(h\rho u^\beta u_j\big) + h\rho u_j u^\beta \Gamma^\alpha_{\alpha\beta} - h\rho u^\beta \Gamma^\alpha_{\beta j} u_\alpha + \partial_j p = \\
&=\; \partial_\beta\big(h\rho u^\beta u_j + \delta^\beta_j\big) + h\rho u_j u^\beta \Gamma^\alpha_{\alpha\beta} - h\rho u^\beta \Gamma^\alpha_{\beta j} u_\alpha\ ,
\end{aligned} \tag{3.3.28}$$

which is formally equivalent to

$$0 = \nabla_\beta T^\beta_j = \nabla_\beta (h\rho u_j u^\beta + \delta^\beta_j p) \, . \tag{3.3.29}$$

Now, inside the derivative of (3.3.28) we multiply and divide by $\sqrt{-g}$:

$$0 = \partial_\beta \left[\frac{\sqrt{-g}}{\sqrt{-g}} (h\rho u^\beta u_j + \delta^\beta_j p) \right] + h\rho u_j u^\beta \Gamma^\alpha_{\alpha\beta} - h\rho u^\beta \Gamma^\alpha_{\beta j} u_\alpha \, . \tag{3.3.30}$$

At this point we expand the derivative of the $\sqrt{-g}$ at the denominator to obtain

$$\begin{aligned} 0 \;\; = \;\; & \frac{1}{\sqrt{-g}} \partial_\beta [\sqrt{-g}(h\rho u^\beta u_j + \delta^\beta_j p)] + \sqrt{-g}(h\rho u^\beta u_j + \delta^\beta_j p) \partial_\beta \frac{1}{\sqrt{-g}} + \\ & + h\rho u_j u^\beta \Gamma^\alpha_{\alpha\beta} - h\rho u^\beta \Gamma^\alpha_{\beta j} u_\alpha \, . \end{aligned} \tag{3.3.31}$$

Using now the relation

$$\partial_\beta \frac{1}{\sqrt{-g}} = \frac{1}{g} \partial_\beta \sqrt{-g} = - \frac{1}{\sqrt{-g}} \Gamma^\alpha_{\alpha\beta} \, , \tag{3.3.32}$$

equation (3.3.31) becomes

$$\begin{aligned} 0 \;\; = \;\; & \frac{1}{\sqrt{-g}} \partial_\beta [\sqrt{-g}(h\rho u^\beta u_j + \delta^\beta_j p)] + \\ & - (h\rho u^\beta u_j + \delta^\beta_j p) \Gamma^\alpha_{\alpha\beta} + h\rho u_j u^\beta \Gamma^\alpha_{\alpha\beta} - h\rho u^\beta \Gamma^\alpha_{\beta j} u_\alpha = \\ = \;\; & \frac{1}{\sqrt{-g}} \partial_\beta [\sqrt{-g}(h\rho u^\beta u_j + \delta^\beta_j p)] - p \Gamma^\alpha_{\alpha j} - h\rho u^\beta \Gamma^\alpha_{\beta j} u_\alpha = \\ = \;\; & \frac{1}{\sqrt{-g}} \partial_\beta [\sqrt{-g}(h\rho u^\beta u_j + \delta^\beta_j p)] - p \delta^\beta_\alpha \Gamma^\alpha_{\beta j} - h\rho u^\beta \Gamma^\alpha_{\beta j} u_\alpha = \\ = \;\; & \frac{1}{\sqrt{-g}} \partial_\beta [\sqrt{-g}(h\rho u^\beta u_j + \delta^\beta_j p)] - T^\beta_\alpha \Gamma^\alpha_{\beta j} \, . \end{aligned} \tag{3.3.33}$$

Finally, we split the time and space components to obtain

$$\frac{1}{\sqrt{-g}} \partial_t [\sqrt{-g} h\rho u^0 u_j] + \frac{1}{\sqrt{-g}} \partial_i [\sqrt{-g}(h\rho u^i u_j + \delta^i_j p)] = T^\beta_\alpha \Gamma^\alpha_{\beta j} \tag{3.3.34}$$

and substitute (2.1.6) and (2.1.7) to obtain

$$\frac{1}{\sqrt{-g}} \left\{ \partial_t \left(\frac{\sqrt{-g}}{\alpha} h\rho W^2 v_j \right) + \partial_i \left[\sqrt{-g} \left(h\rho W^2 v_j \left(v^i - \frac{\beta^i}{\alpha} \right) \;\; + \;\; \delta^\beta_j p \right) \right] \right\} = T^\beta_\alpha \Gamma^\alpha_{\beta j} \, . \tag{3.3.35}$$

It is natural now to define the *conserved* variables $S_j = h\rho W^2 v_j$ and write

$$\frac{1}{\sqrt{-g}} \left\{ \partial_t \left(\sqrt{\gamma} S_j \right) + \partial_i \left[\sqrt{-g} \left(S_j \left(v^i - \frac{\beta^i}{\alpha} \right) + \delta^\beta_j p \right) \right] \right\} = T^\beta_\alpha \Gamma^\alpha_{\beta j} \, . \tag{3.3.36}$$

Following the notation of Banyuls *et al.* [36], the source term at the right hand side can also be written as

$$T^\beta_\alpha \Gamma^\alpha_{\beta j} = T^{\alpha\beta} \left(\partial_\beta g_{\alpha j} - \Gamma^\delta_{\alpha\beta} g_{\delta j} \right) \, . \tag{3.3.37}$$

It is possible to get the remaining equation in conservative form analogously. The complete system, in the *conserved* variables

$$\begin{aligned} D &= \rho W \,, \\ S_j &= \rho h W^2 v_j \,, \\ \tau &= \rho h W^2 - \rho W - p \end{aligned} \tag{3.3.38}$$

reads

$$\frac{1}{\sqrt{-g}}\left\{ \partial_t \left[\sqrt{\gamma}\mathbf{F}^0(\mathbf{U})\right] + \partial_i \left[\sqrt{\gamma}\mathbf{F}^i(\mathbf{U})\right] \right\} = \mathbf{s}(\mathbf{U}) \,, \tag{3.3.39}$$

where

$$\begin{aligned} \mathbf{F}^0(\mathbf{U}) &= (D, S_j, \tau)^T \,, \\ \mathbf{F}^i(\mathbf{U}) &= [D(\alpha v^i - \beta^i), S_j(\alpha v^i - \beta^i) + p\delta^i_j, \tau(\alpha v^i - \beta^i) + p v^i]^T \end{aligned} \tag{3.3.40}$$

and the sources are

$$\mathbf{s}(\mathbf{U}) = \Big[0, T^{\mu\nu}\big(\partial_\mu g_{\nu j} + \Gamma^\delta_{\mu\nu} g_{\delta j}\big), \alpha\big(T^{\mu 0}\partial_\mu \ln\alpha - T^{\mu\nu}\Gamma^0_{\nu\mu}\big) \Big] \,. \tag{3.3.41}$$

Note that the source terms do not contain differential operators acting on the stress-energy tensor and that this is important for the numerical preservation of the hyperbolicity character of the system. Also note that in a curved spacetime the equations are not in a strictly-homogeneous conservative form, which is recovered only in flat spacetime. This conservative form of the relativistic Euler equations was first derived by the group at the Universidad de Valencia [36] and therefore was named the *Valencia formulation*.

An important feature of the Valencia formulation is that it allows to extend to relativistic hydrodynamics the powerful numerical methods developed in classical hydrodynamics, in particular the HRSC methods. As explained above, such schemes are essential for a correct representation of shocks, whose presence is expected in several astrophysical scenarios.

3.3.2 Eigenstructure of the relativistic Euler equations

As it will be shown in Section 3.5, all the approximate Riemann solvers implemented in `Whisky` need some knowledge of the eigenstructure of the system to be solved, so we give here the relevant formulas. Three (one per spatial direction) 5×5 Jacobian matrices

$$\mathbf{A}^{(i)} = \frac{\partial(\sqrt{\gamma}\mathbf{F}^i)}{\partial(\sqrt{\gamma}\mathbf{F}^0)} = \frac{\partial \mathbf{F}^i}{\partial \mathbf{F}^0} \tag{3.3.42}$$

are associated with system (3.3.39). The eigenvalues of, say, $\mathbf{A}^{(x)}$ are

$$\lambda_0 = \alpha v^x - \beta^x \quad (\text{triple eigenvalue}) \,, \tag{3.3.43}$$

$$\lambda_\pm = \frac{\alpha}{1 - v^2 c_s^2}\left\{ v^x(1-c_s^2) \pm c_s \sqrt{(1-v^2)[\gamma^{xx}(1-v^2c_s^2) - v^x v^x (1-c_s^2)]} \right\} - \beta^x$$

and a complete set of its right eigenvectors is

$$\mathbf{R}^{(01)} = \begin{bmatrix} \dfrac{\mathcal{K}}{hW} \\ v_x \\ v_y \\ v_z \\ 1-\dfrac{\mathcal{K}}{hW} \end{bmatrix}, \qquad \mathbf{R}^{(02)} = \begin{bmatrix} Wv_y \\ h(\gamma_{xy}+2W^2v_xv_y) \\ h(\gamma_{yy}+2W^2v_yv_y) \\ h(\gamma_{zy}+2W^2v_zv_y) \\ Wv_y(2hW-1) \end{bmatrix}$$

$$\mathbf{R}^{(03)} = \begin{bmatrix} Wv_z \\ h(\gamma_{xz}+2W^2v_xv_z) \\ h(\gamma_{yz}+2W^2v_yv_z) \\ h(\gamma_{zz}+2W^2v_zv_z) \\ Wv_z(2hW-1) \end{bmatrix}, \quad \mathbf{R}^{(\pm)} = \begin{bmatrix} 1 \\ hW(v_x-\mathcal{V}^x_\pm) \\ hWv_y \\ hWv_z \\ hW\mathcal{A}^x_\pm - 1 \end{bmatrix}, \tag{3.3.44}$$

where c_s is the local sound speed (which can be obtained from $hc_s = \chi + \kappa p/\rho^2$ with $\chi \equiv \partial p/\partial\rho$ and $\kappa \equiv \partial p/\partial\epsilon$), $\mathcal{K} \equiv \tilde{\kappa}/(\tilde{\kappa}-c_s^2)$, $\tilde{\kappa} \equiv \kappa/\rho$ and

$$\mathcal{V}^x_\pm \equiv \frac{v^x-\Lambda^x_\pm}{\gamma^{xx}-v^x\Lambda^x_\pm}, \qquad \mathcal{A}^x_\pm \equiv \frac{\gamma^{xx}-v^xv^x}{\gamma^{xx}-v^x\Lambda^x_\pm}, \qquad \Lambda^i_\pm \equiv \frac{\lambda_\pm+\beta^i}{\alpha}. \tag{3.3.45}$$

Similarly, the eigenvalues of $\mathbf{A}^{(y)}$ and $\mathbf{A}^{(z)}$ are the same as in expressions (3.3.43) with y, z in place of x and the corresponding right eigenvectors are the same as in (3.3.44) with the second row exchanged with the third or fourth respectively and with the interchange $x \leftrightarrow y$ or $x \leftrightarrow z$ respectively. Since the left eigenvectors are effectively used in the code (*cf.* Section 4.3.1) in the Roe and Marquina solvers in order to compute the characteristic variables, we give the explicit expressions for them too [121]:

$$\mathbf{L}^{(01)} = \frac{W}{\mathcal{K}-1}\begin{bmatrix} h-W \\ Wv^x \\ Wv^y \\ Wv^z \\ -W \end{bmatrix}, \qquad \mathbf{L}^{(02)} = \frac{1}{h\xi}\begin{bmatrix} -\gamma_{zz}y_y+\gamma_{yz}v_z \\ v^x(\gamma_{zz}y_y-\gamma_{yz}v_z) \\ \gamma_{zz}(1-v_xv^x)+\gamma_{xz}v_zv^x \\ \gamma_{yz}(1-v_xv^x)+\gamma_{xz}v_yv^x \\ -\gamma_{zz}y_y+\gamma_{yz}v_z \end{bmatrix}$$

$$\mathbf{L}^{(03)} = \frac{1}{h\xi}\begin{bmatrix} -\gamma_{yy}v_z+\gamma_{zy}v_y \\ v^x(\gamma_{yy}v_z-\gamma_{zy}v_y) \\ -\gamma_{zy}(1-v_xv^x)+\gamma_{xy}v_zv^x \\ \gamma_{yy}(1-v_xv^x)+\gamma_{xy}v_yv^x \\ -\gamma_{yy}v_z+\gamma_{zy}v_y \end{bmatrix},$$

$$\mathbf{L}^{(\mp)} = \pm\frac{h^2v^x}{\Delta}\begin{bmatrix} hW\mathcal{V}^x_\pm\xi + l^{(5)}_\mp \\ \Gamma_{xx}(1-\mathcal{K}A^x_\pm)+(2\mathcal{K}-1)\mathcal{V}^x_\pm(W^2v^x\xi-\Gamma_{xx}v^x) \\ \Gamma_{xy}(1-\mathcal{K}A^x_\pm)+(2\mathcal{K}-1)\mathcal{V}^x_\pm(W^2v^y\xi-\Gamma_{xy}v^x) \\ \Gamma_{xz}(1-\mathcal{K}A^x_\pm)+(2\mathcal{K}-1)\mathcal{V}^x_\pm(W^2v^z\xi-\Gamma_{xz}v^x) \\ (\mathcal{K}-1)[-\gamma v^x+\mathcal{V}^x_\pm(W^2\xi-\Gamma_{xx})]-\mathcal{K}W\mathcal{V}^x_\pm\xi \end{bmatrix}, \tag{3.3.46}$$

where $\Gamma_{xx} \equiv \gamma_{yy}\gamma_{zz}-\gamma_{yz}^2$, $\xi \equiv \Gamma_{xx}-\gamma v^xv^x$ and $\Delta \equiv h^3W(\mathcal{K}-1)\xi(\mathcal{A}^x_+-\mathcal{A}^x_-)$.

3.4 Godunov type methods

Any finite difference method for solving PDEs for initial-value problems will involve the discretization of the physically continuous initial data to be evolved with the differential equations; the numerical initial data and solution are thus discontinuous and piecewise constant. In addition to this, the non-linear properties of the hydrodynamical equations can generally produce (see *e.g.* the Burger equation [114]) in a finite time non-linear waves with discontinuities even from smooth initial data [242, 143].

High-Resolution Shock-Capturing methods - based on a simple and brilliant idea by Godunov [108] - not only can treat accurately discontinuities, but indeed they exploit them. In fact, Godunov methods consist in setting and solving at every cell interface of the numerical grid a local Riemann problem, for whose solution there exist several accurate and efficient methods, both exact and approximate.

The basic structure of a HRSC scheme consists in the following stages [2]:

- converting the primitive variables to conserved variables;
- finding the values of these variables at cell interfaces, *i.e.* at the intermediate locations $x_{\ p+1/2}$ between all pairs of grid points x_p and x_{p+1}, except for the grid points near the boundaries, which are treated separately; there are two such *extended* or *reconstructed* values (*cf.* Section 3.6) at each cell interface (one being computed from the left stencil, the other from the right stencil) and they are used as initial data for a local Riemann problem;
- solving the local Riemann problem (*cf.* Section 3.5) at each cell interface; this gives the fluxes used for the time integration;
- computing the source terms and adding them to the fluxes from the Riemann solver;
- integrating one step in time;
- applying boundary conditions;
- converting back from the evolved conserved variables to obtain the primitive variables at the updated time.

It is computationally convenient to apply the above procedure as a sequence of three 1-dimensional operations, *i.e.* using what is referred to as *dimensional splitting* and which is constructed using Taylor series expansions of the 3-dimensional function [143]. The solution of the 3-dimensional equation

$$\begin{aligned} &\partial_t \mathbf{U} + \nabla \cdot \mathbf{F}(\mathbf{U}) = 0 \\ &\mathbf{U}(\vec{x}, t^n) = \mathbf{U}^n \ , \end{aligned} \tag{3.4.47}$$

can be approximated by the solution of a sequence of 1-dimensional equations as follows

$$\begin{aligned} &\partial_t \mathbf{U}^* + \partial_{x^1} \mathbf{F}(\mathbf{U}^*) = 0 \ , \\ &\mathbf{U}^*(\vec{x}, 0) = \mathbf{U}^n \ , \end{aligned} \tag{3.4.48}$$

$$\begin{aligned} &\partial_t \mathbf{U}^{**} + \partial_{x^2} \mathbf{F}(\mathbf{U}^{**}) = 0 \ , \\ &\mathbf{U}^{**}(\vec{x}, 0) = \mathbf{U}^*(\vec{x}, 0) \ , \end{aligned} \tag{3.4.49}$$

[2] For additional material on HRSC methods the reader is also referred to [136, 242, 144].

and

$$\begin{aligned} &\partial_t \mathbf{U} + \partial_{x^3} \mathbf{F}(\mathbf{U}) = 0 \,, \\ &\mathbf{U}(\vec{x}, 0) = \mathbf{U}^{**}(\vec{x}, 0) \,. \end{aligned} \tag{3.4.50}$$

If $\mathcal{L}_{x^i}(\Delta t)$ denotes the solution operator for the x^i direction in time increment of Δt, then a first-order approximation in time of $\mathbf{U}(\vec{x}, t^{n+1})$ is

$$\mathbf{U}(\vec{x}, t^{n+1}) = \mathcal{L}_{x^3}\{\mathcal{L}_{x^2}[\mathcal{L}_{x^1}(\Delta t)\mathbf{U}(\vec{x}, t^n)]\} \tag{3.4.51}$$

The order of the operations does not affect the accuracy of the schemes.

3.4.1 Mathematical description of a Riemann problem

Mathematically, a Riemann problem for a general hyperbolic system like (3.2.2) is an initial-value problem with initial conditions given by

$$\mathbf{U}(x, 0) = \begin{cases} \mathbf{U}_{\rm L} & \text{if} \quad x < 0 \,, \\ \mathbf{U}_{\rm R} & \text{if} \quad x > 0 \,, \end{cases} \tag{3.4.52}$$

where $\mathbf{U}_{\rm L}$ and $\mathbf{U}_{\rm R}$ are two constant vectors representing the left (L) and right (R) state respectively. Depending on the particular set of hyperbolic equations considered, different wave structures emerge in the solution. In general, the discontinuity that separates the two states $\mathbf{U}_{\rm R}$ and $\mathbf{U}_{\rm L}$ is classified as a shock wave if all the hydrodynamical variables (ρ, p, v) experience a discontinuous change and as a contact wave if pressure and velocity are continuous while density is not. If, instead, the right and left states are connected through a smooth transition, the connecting region is called a rarefaction wave.

The schematic evolution of a general Riemann problem for a system of equations in three independent variables, as in the case of the 1-dimensional hydrodynamics equations, consists in four states and can be represented as[3] [152]

$$\mathbf{U}_{\rm L} \mathcal{W}_{\leftarrow} \mathbf{U}^*_{\rm L} \mathcal{C} \mathbf{U}^*_{\rm R} \mathcal{W}_{\rightarrow} \mathbf{U}_{\rm R} \,, \tag{3.4.53}$$

where $\mathcal{W}$ denotes a shock or a rarefaction wave that propagates toward the left $(\leftarrow)$ or the right $(\rightarrow)$ with respect to the initial discontinuity and $\mathbf{U}^*_{\rm L}$ and $\mathbf{U}^*_{\rm R}$ are the new hydrodynamical states that form behind the two waves propagating in opposite directions. It can be demonstrated that the wave separating $\mathbf{U}^*_{\rm L}$ and $\mathbf{U}^*_{\rm R}$ is always a contact discontinuity [242], which we call $\mathcal{C}$, and that therefore in the two states pressure and velocity have the same values, while density differs.

A first-order Godunov method for finding the solution[4] $\mathbf{U}(x, t_{n+1})$ at time t_{n+1} consists in solving the Riemann problems set by the piecewise-constant solution at time t_n at each cell boundary. Note that more sophisticated methods have been derived for setting the initial data for these Riemann problems. These procedures are generally referred to as *reconstruction procedures* and lead to methods that are of higher order in space. We will discuss them more in detail in Section 3.6.

[3] Actually, the possible types of waves present in the solution of the Riemann problem depend crucially on the closure conditions (*i.e.* on the EoS) [242]. For the EoSs usually considered in astrophysical evolutions, though, only shocks, contacts and rarefactions appear, so we will restrict our treatment these cases only.

[4] A note on the notation here used: $\mathbf{U} \equiv \mathbf{U}(x, t)$ represents the non-discretized solution at the point (x, t) in the spacetime continuum; $\mathbf{U}^n \equiv \mathbf{U}(x, t_n)$ represents the solution discretized in time, but non-discretized in space, at the time level t_n and the point x in the space continuum; $\mathbf{U}_j \equiv \mathbf{U}(x_j, t)$ represents the solution discretized in space, but non-discretized in time, at the grid point x_j and at the time t in the continuum; $\mathbf{U}^n_j \equiv \mathbf{U}(x_j, t_n)$ represents the solution discretized both in space and in time, at the grid point x_j and at time level t_n.

Since, as we will explain at the end of this section, the time step is chosen in such a way that the waves coming from neighbouring Riemann problems do not interact, the solution $\mathbf{U}(x,t)$ at time $t_n < t < t_{n+1}$ can be found exactly (even if, as we will see, in practice we use approximate Riemann solvers, which are computationally much less expensive while sufficiently accurate) from $\mathbf{U}(x,t_n)$ by simply piecing together the Riemann solution found at each cell boundary. The approximate solution $\mathbf{U}^{n+1}$ at time t_{n+1} is obtained by averaging in space the exact solution at time t_{n+1}:

$$\mathbf{U}_j^{n+1} = \frac{1}{\Delta x}\int_{x_{j-1/2}}^{x_{j+1/2}} \mathbf{U}(x,t_{n+1})\mathrm{d}x\ . \tag{3.4.54}$$

This algorithm is considerably more transparent when using the integral form of the conservation law (3.2.4)

$$\begin{aligned}\int_{x_{j-1/2}}^{x_{j+1/2}} \mathbf{U}(x,t_{n+1})\mathrm{d}x &= \int_{x_{j-1/2}}^{x_{j+1/2}} \mathbf{U}(x,t_n)\mathrm{d}x + \int_{t_n}^{t_{n+1}} F(\mathbf{U}(x_{j-1/2},t))\mathrm{d}t + \\ &\quad - \int_{t_n}^{t_{n+1}} F(\mathbf{U}(x_{j+1/2},t))\mathrm{d}t\ ,\end{aligned}$$

which becomes

$$\mathbf{U}_j^{n+1} = \mathbf{U}_j^n - \frac{\Delta t}{\Delta x}[F(\mathbf{U}_j^n,\mathbf{U}_{j+1}^n) - F(\mathbf{U}_{j-1}^n,\mathbf{U}_j^n)]\ , \tag{3.4.55}$$

where

$$F(\mathbf{U}_j^n,\mathbf{U}_{j+1}^n) \equiv \frac{1}{\Delta t}\int_{t_n}^{t_n+1} F(\mathbf{U}(x_{j+1/2},t))\mathrm{d}t\ . \tag{3.4.56}$$

As mentioned above, a condition must be satisfied for the Godunov method to be applicable: that waves coming from a cell boundary do not influence the Riemann solution on adjacent cell boundaries between time t_n and t_{n+1}. The condition that provides this constraint is

$$\left|\frac{\Delta t}{\Delta x}\lambda_p(\mathbf{U}_j^n)\right| \leq 1 \tag{3.4.57}$$

for all eigenvalues λ_p at each $\mathbf{U}_j^n$. The largest of the λ_p is also referred to as CFL factor, since (3.4.57) coincides with the CFL condition in evolution schemes that do not make use of Godunov methods.

When condition (3.4.57) is satisfied, the time average in (3.4.56) becomes trivial, since the solution $\mathbf{U}(x_{j+1/2},t)$ of the Riemann problem is constant at the cell interface $x = x_{j+1/2}$ over the time interval $t_n < t < t_{n+1}$, because no wave passes through the interface in such a time interval.

3.5 Riemann solvers

In what follows, we discuss how Riemann solvers can be used to solve accurately the hydrodynamics equations. For simplicity we consider equations of the type (3.4.55) in one spatial dimension only. The Riemann problem is said to be solved when the velocity, pressure and density in the new states $\mathbf{U}_{\mathrm{L}}^*$ and $\mathbf{U}_{\mathrm{R}}^*$ have been computed, as well as the positions of the waves separating the four states. The solution of the 1-dimensional Riemann problem in relativistic hydrodynamics was discussed in the general case by Martí and Müller [152] and the reader is referred to their work for further details (see also [185], for the extension to multidimensions).

The knowledge on the wave structure (3.4.53) is exploited in the procedure to find the exact solution of the Riemann problem: since pressure and velocity are continuous on the contact discontinuity $\mathcal{C}$, the pressure in the $\mathbf{U}^*_{\mathrm{L,R}}$states can be calculated by imposing the continuity of the fluid velocity across $\mathcal{C}$

$$v^*_{\mathrm{L}}(p^*) = v^*_{\mathrm{R}}(p^*) \ . \tag{3.5.58}$$

In general, (3.5.58) is a non-linear algebraic equation in the unknown pressure p^* and requires a numerical solution even for simple EoSs [242]. Depending on the different wave patterns forming after the decay of the discontinuity, a different non-linear equation will need to be solved [5]. This initial "ambiguity" in the wave pattern produced corresponds to the fact that the interval in pressure bracketing the solution p^* is not known a priori. In practice this lack of information is compensated by the use of efficient numerical algorithms which, via a process of trial and error, determine the correct wave pattern and then proceed to the solution of the corresponding non-linear equation [153].

Recently, Rezzolla and Zanotti [190] have shown that the relativistic expression for the relative velocity between the two initial states is a function of the unknown pressure p^* and so a new procedure for numerically solving the exact Riemann problem can be proposed in which the pressure p^* is no longer obtained by the solution of equation (3.5.58). Rather, p^* is calculated by equating the relativistic invariant expression for the relative velocity between the two initial states with the value given by the initial conditions.

When compared to equivalent approaches, this exact Riemann solver has some advantages. Firstly, it can remove the ambiguity mentioned above and determine the generated flow pattern by simply comparing the relative velocity between the two initial states with reference values built from the initial conditions of the Riemann problem. Doing so provides immediate information about which of the non-linear equations (one for every wave pattern) needs to be solved. Secondly, by knowing the wave pattern the proposed approach can produce an immediate bracketing of the solution. Doing so gives improved efficiency in the numerical root finding procedure. Finally, for one of the wave patterns (*i.e.* for two rarefaction waves moving in opposite directions) this method provides the solution of the relativistic Riemann problem in a closed analytic form.

When compared with other exact Riemann solvers the method of Rezzolla and Zanotti has also proved to be computationally more efficient. In particular, when solving a generic hydrodynamical problem (in which one solves for very simple Riemann problems) the approach proposed here brackets the solution very closely and this produces substantial reduction of computational time, up to 30%.

3.5.1 Approximate solvers

Since the solution of the Riemann problem is needed at each cell interface, it is too costly to use exact Riemann solvers, even when recast in an efficient form [190, 191]; so we resort to approximate Riemann solvers. Several approximate Riemann solvers of different types have been developed along the years; we will here summarize the ones actually implemented in `Whisky`: the Harten Lax van Leer Einfeldt (HLLE) [116, 90], the Roe [193] and the Marquina [84, 83] solvers. Since they consist in providing approximate formulae for the fluxes, they are often simply called *flux formulae*, instead of Riemann solvers.

[5] This approach is usually referred to as an "exact" Riemann solver to distinguish it from the family of so called "approximate" Riemann solvers, where the system of equations to be solved or the wave pattern is simplified to allow different non-iterative procedures for the solution. We will describe the approximate Riemann solvers implemented in our code in the next section.

The Harten Lax van Leer Einfeldt solver

In the Riemann solver proposed by Harten, Lax, van Leer [116] and later improved by Einfeldt [90], the central region delimited by the fastest wave moving toward the left and by the fastest wave moving toward the right [with speed $\lambda_{\rm L}$ and $\lambda_{\rm R}$ respectively; *cf.* (3.3.43)] is approximated by a single state

$$U_{\rm HLLE} = \frac{\lambda_{\rm R} U_{\rm R} - \lambda_{\rm L} U_{\rm L} + F_{\rm L} - F_{\rm R}}{\lambda_{\rm R} - \lambda_{\rm L}} \,, \tag{3.5.59}$$

thus disregarding the central contact wave. The resulting numerical flux to be used in the Godunov scheme is

$$F_{\rm HLLE} = \frac{\lambda_{\rm R} F(U_{\rm L}) - \lambda_{\rm L} F(U_{\rm R}) + \lambda_{\rm L}\lambda_{\rm R}(U_{\rm R} - U_{\rm L})}{\lambda_{\rm R} - \lambda_{\rm L}} \,. \tag{3.5.60}$$

The HLLE solver is the simplest Riemann solver implemented in `Whisky`. It performs well at rarefactions waves, but, as one should expect, it produces considerable diffusion at contact discontinuities.

The Roe solver

The Roe Riemann solver consists in approximating the non-linear system with a linearized one and then in solving the latter exactly, as shown in Section 3.2. In this case linearized Jacobian matrix $\tilde{\mathbf{A}}(\mathbf{U}_{\rm L}, \mathbf{U}_{\rm R})$ has to satisfy the following conditions:

- hyperbolicity of the system: $\tilde{\mathbf{A}}$ must have real eigenvalues $\tilde{\lambda}_a(\mathbf{U}_{\rm L}, \mathbf{U}_{\rm R})$ and a complete set of linearly independent right eigenvectors $\widetilde{\mathbf{R}}^{(a)}$;
- consistency with the exact Jacobian:

$$\tilde{\mathbf{A}}(\mathbf{U}_{\rm L}, \mathbf{U}_{\rm R}) = \mathbf{A}(\mathbf{U}) \,;$$

- conservation across discontinuities and exact recognition of isolated discontinuities:

$$\tilde{\mathbf{A}}(\mathbf{U}_{\rm L}, \mathbf{U}_{\rm R}) \cdot (\mathbf{U}_{\rm R} - \mathbf{U}_{\rm L}) = \mathbf{F}(\mathbf{U}_{\rm R}) - \mathbf{F}(\mathbf{U}_{\rm L}) \,.$$

These requirements determine the intermediate state $\mathbf{U}_{\rm Roe} = \mathbf{U}_{\rm Roe}(\mathbf{U}_{\rm L}, \mathbf{U}_{\rm R})$ about which to linearize the original Jacobian matrix $\mathbf{A}$. Although it is possible [91] to find such a state, it is more convenient to simply approximate it as

$$\mathbf{U}_{\rm Roe} = \frac{1}{2}(\mathbf{U}_{\rm L} + \mathbf{U}_{\rm R}) \,. \tag{3.5.61}$$

The eigenvalues $\tilde{\lambda}_a$ and eigenvectors $\widetilde{\mathbf{R}}^{(a)}$ computed for $\tilde{\mathbf{A}}(\mathbf{U}_{\rm Roe})$ are then used in the formula [*cf.* (3.2.14)] for the flux across each cell interface:

$$\mathbf{F}_{\rm Roe}^{\text{cell interface}} = \frac{1}{2}\Big\{\mathbf{F}(\mathbf{U}_{\rm L}) + \mathbf{F}(\mathbf{U}_{\rm R}) - \sum_{a=1}^{5} |\tilde{\lambda}_a| [w_{\rm L}^a - w_{\rm R}^a] \tilde{\mathbf{R}}^{(a)} \Big\} \,, \tag{3.5.62}$$

where here $a = 1, \ldots, 5$ since we now specialize the treatment to the specific case of the hydrodynamics equations, which have five variables. We also recall that $w^{\,a}_{\rm L,R} = \widetilde{\mathbf{L}}^{(a)}(\mathbf{U}_{\rm L,R}) \cdot \mathbf{U}_{\rm L,R}$ are the characteristic variables and that $\widetilde{\mathbf{L}}^{(a)}$ are the left eigenvectors of the Jacobian, being the columns of the matrix $\widetilde{\mathbf{K}}^{\,-1}$ [*cf.* (3.2.9) and (3.2.11)]. The Roe solver gives a very good approximation to the Riemann solution, except at rarefactions waves, since linear systems do not admit such waves as solution.

The Marquina solver

The Marquina flux formula can be regarded as an improvement to the Roe solver, since it gives its same results everywhere, except at sonic points (*i.e.* where the fluid velocity equals the speed of sound), where it removes the entropy violation at rarefactions of the Roe solver. We actually use the modified method of [14] instead of the original method. The procedure consists in computing at each cell interface the characteristic variables $w^{\,a}_{\mathrm{L,R}}$ and the numerical fluxes $\phi^a_{\mathrm{L,R}} = \mathbf{L}^{(a)}(\mathbf{U}_{\mathrm{L,R}}) \cdot \mathbf{F}(\mathbf{U}_{\mathrm{L,R}})$ for both the left and right states. Then the flux formula is given by

$$\mathbf{F}^{\mathrm{Marquina}}_{i+1/2} = \sum_{a=1}^{5} \left[\phi^a_+ \mathbf{R}^{(a)}_{\mathrm{L}} + \phi^a_- \mathbf{R}^{(a)}_{\mathrm{R}} \right] , \tag{3.5.63}$$

where the $\phi^a_{+,-}$ are chosen according to the sign of the eigenvalues:

- $\phi^a_+ = \phi^a_{\mathrm{L}}$ and $\phi^a_- = 0$ if both eigenvectors are positive (*i.e.* both waves move to the right and so the flux has to be computed from the left state);
- $\phi^a_- = \phi^a_{\mathrm{R}}$ and $\phi^a_+ = 0$ if both eigenvectors are negative;
- while if the eigenvalues have opposite sign

$$\begin{aligned} \phi^a_+ &= \frac{1}{2}\big(\phi^a_{\mathrm{L}} + \max(|\lambda^a(\mathbf{U}_{\mathrm{L}})|, |\lambda^a(\mathbf{U}_{\mathrm{R}})|) w^a_{\mathrm{L}}\big) , \\ \phi^a_- &= \frac{1}{2}\big(\phi^a_{\mathrm{R}} + \max(|\lambda^a(\mathbf{U}_{\mathrm{L}})|, |\lambda^a(\mathbf{U}_{\mathrm{R}})|) w^a_{\mathrm{R}}\big) . \end{aligned} \tag{3.5.64}$$

In our experience, the Marquina solver has proven to be the best choice.

3.6 Reconstruction methods

The original Godunov method, as presented so far, is only first-order accurate in space. Indeed, it was shown by Godunov in a theorem [108] that it is not possible to build monotone (*i.e.* that do not produce spurious oscillations in the solution in the vicinity of large gradients) linear schemes of second or higher order of accuracy. As a result, one has to turn to non-linear schemes. HRSC methods represent the combination of Godunov type methods, which take advantage of the conservation form of the equations, and of numerical techniques aimed at obtaining second-order (or higher-order) accuracy in the smooth parts of the solution, without producing oscillations.

A way of measuring the amount of oscillations in the solution is to monitor the *total variation* of the solution, defined, for a discretized function $u^{\,n}$ at time level $t^{\,n}$, as

$$\mathrm{TV}(u^n) \equiv \sum_{p=-\infty}^{\infty} |u^n_p - u^n_{p-1}| . \tag{3.6.65}$$

The requirement of non-oscillation of a scheme may then be stated as the requirement that

$$\mathrm{TV}(u^{n+1}) \leq \mathrm{TV}(u^n) \tag{3.6.66}$$

for all the variables $\mathbf{U}$ of the system. A numerical method satisfying this condition is called a *total-variation-diminishing* (TVD) method, since the total variation is bounded by its initial value. As shown by Toro [242], TVD methods cannot generally be extended to accuracies higher than second order. In

order to construct higher-order methods one has to renounce to the strict TVD condition and allow for an increase of the total variation proportional to some power of the typical step size:

$$\mathrm{TV}(u^{n+1}) \leq \mathrm{TV}(u^n) + \mathcal{O}\big[(\Delta x)^k\big] \,. \tag{3.6.67}$$

This leads to higher-order accuracy also near large-gradient regions, by allowing oscillations (that should be small and bounded) near extrema. The resulting methods are called *Essentially-Non-Oscillatory* (ENO) methods [115].

3.6.1 Total-variation-diminishing methods

In the original Godunov method, the initial data for the local Riemann problems at each time step are assumed to be piecewise constant on each cell

$$u(x) \equiv u_p, \qquad x_{p-1/2} < x < x_{p+1/2} \qquad \forall p \,. \tag{3.6.68}$$

A natural way of increasing the order of accuracy is giving a better approximation of the state at the cell interface. The simplest reconstruction is a piecewise-linear approximation

$$u(x) \equiv u_p + S_p(x - x_p), \qquad x_{p-1/2} < x < x_{p+1/2} \qquad \forall p \,, \tag{3.6.69}$$

where S_p is a slope, expressed as either

$$S_p^{\mathrm{upwind}} = \frac{u_{p+1} - u_p}{x_{p+1} - x_p}, \quad \text{or} \quad S_p^{\mathrm{downwind}} \frac{u_p - u_{p-1}}{x_p - x_{p-1}} \tag{3.6.70}$$

or linear combinations of them. The upper superscripts "upwind" and "downwind" refer to the stencil used for computing the slope. For grids with uniform spacing, the cell average, computed between $x_{p-1/2}$ and $x_{p+1/2}$, is equal to the value on the grid point u_p for any choice of the slope. All the possible choices of the slope give second-order accurate schemes, but none of them can avoid introducing oscillations in large-variation regions. This problem motivates the technique of *slope limiting*, consisting in choosing a reconstructing slope which is second order in slowly varying regions of the solution and only first order (*i.e.* piecewise constant) in the vicinity of large-variation regions, in order to avoid numerical oscillations. In practice, the large variation regions are defined as those where S_p^{upwind} and S_p^{downwind} have opposite signs (extrema of the function). The numerous proposed TVD slope limiters differ in the prescription for computing the slope in slowly varying regions. After defining $r \equiv S_p^{\mathrm{upwind}} S_p^{\mathrm{downwind}}$, the possible slopes can be expressed as a function of r:

$$S = \Phi(r) \frac{S_p^{\mathrm{upwind}} + S_p^{\mathrm{downwind}}}{2} \,. \tag{3.6.71}$$

In `Whisky` we implemented some of the most commonly used slope limiters, which we list here.

- The *minmod* slope limiter is

$$\Phi(r) = \min\Big(1, \frac{4}{1+r}\Big) \,. \tag{3.6.72}$$

  Stated differently, minmod consists in choosing the slope with the minimum modulus, when $r > 0$. It is the most diffusive slope limiter.

- The van Leer [246, 247] monotonized centered slope limiter is

$$\Phi(r) = \min\Big(\frac{2r}{1+r}, \frac{2}{1+3}\Big) \,. \tag{3.6.73}$$

  It consists in limiting the value of the slope in a cell following three rules: *i*) it must not take values beyond the average of the neighbouring slopes; *ii*) it is set to zero if the average of the upwind and downwind slopes relative to the cell is an extremum with respect to the one of the neighbouring cells; *iii*) it is set to zero if the average slope and the finite-difference slope have opposite sign, that is if sign(S_p) = sign(S_{p+1}) $\neq$ sign($S_{p+1/2}$), for any computation of the S_p [*cf.* (3.6.70)].

- One more implemented example is the Superbee slope limiter [242]

$$\Phi(r) = \begin{cases} \min\big(2, r, 2/(1+r)\big) & \text{if } r \geq 1 \\ 1 & \text{if } 1/2 \leq r < 1 \\ 2r & \text{if } 0 < r < 1/2 \end{cases} \tag{3.6.74}$$

For a comparison of the numerical accuracy of the TVD methods implemented in `Whisky`, see Fig. 4.3, in the next chapter, which shows why our typical choice for TVD reconstruction is the Van Leer monotized centred method. TVD reconstruction is simple and computationally the least expensive, but – we recall – it is at most second-order accurate and drops to first-order at local extrema.

3.6.2 Essentially-non-oscillatory methods

The ENO methods have a large number of variants; in `Whisky`, the simplest ENO reconstruction method of arbitrary accuracy order k is implemented, following the outline in [220]. The idea at the base of the method is to choose a stencil including $s + t < k + 1$ cells (s cells to the left of the point x_p where we want to reconstruct and t cells to its right), so that the smoothest reconstruction is achieved. A measure of the smoothness of the function inside the stencil is made in terms of the Newton divided differences, which for a stencil of one about point x_p are defined as

$$\begin{aligned} u[x_{p-1}, x_p] &\equiv \frac{u_p - u_{p-1}}{x_p - x_{p-1}} \,, \\ u[x_p, x_{p+1}] &\equiv \frac{u_{p+1} - u_p}{x_{p+1} - x_p} \,. \end{aligned} \tag{3.6.75}$$

For any arbitrary stencil which considers s points to the left of x_p and t points to its right, the Newton divided differences are obtained through recursive relation and are

$$u[x_{p-s}, x_{p+t}] \equiv \frac{u[x_{p-s+1}, x_{p+t}] - u[x_{p-s}, x_{p+t-1}]}{x_{p+t} - x_{p-s}} \,. \tag{3.6.76}$$

The property of the divided differences to be a measurement of the smoothness of the function can be appreciated from the following relation:

$$u[x_{p-s}, x_{p+t}] = \frac{u^{(t+s)}(\xi)}{(t+s)!} \,, \tag{3.6.77}$$

where $u^{(t+s)}(\xi)$ is the $(t+s)$-th derivative of u in some point ξ falling in the interval $[x_{p-s}, x_{p+t}]$. This property is valid only if the function u is smooth in this stencil.

Once the stencil is determined as the one giving the minimum Newton divided differences, a k-polynomial interpolation gives the reconstructed value on the p-th cell interface:

$$u_{p+1/2} = \sum_{q=0}^{k-1} c_{rq} u_{p-r+q} \, , \qquad u_{p-1/2} = \sum_{q=0}^{k-1} c_{r-1q} u_{p-r+q} \, , \tag{3.6.78}$$

where the coefficients

$$c_{rq} = \sum_{m=q+1}^{k} \frac{\prod_{l=0;l\neq m}^{k} \prod_{n=0;n\neq m,l}^{k} (r-n+1)}{\prod_{l=0;l\neq m}^{k} (m-l)} \tag{3.6.79}$$

are determined with the above procedure in terms of the stencil and the known data [219].

ENO methods have no tunable parameters besides the order of accuracy, which is arbitrary. In the next chapter, we will compare this method to the other reconstruction procedures (see Fig. 4.3). We will also see in that section that increasing the order of accuracy beyond $k = 4$ does not improve significantly the reconstruction, while requiring larger computational resources, because of the increase in the stencil width used.

3.6.3 The piecewise parabolic method

The piecewise parabolic method (PPM) of Colella and Woodward is a composite reconstruction method that ensures third-order accuracy [6] [70]. We will show here only a simplified treatment of the method and give only the details of the parts implemented in `Whisky`. Hereafter, we specialize to the case of an evenly-spaced grid: $\Delta x = x_{p+1} - x_p = x_{p+1/2} - x_{p-1/2} \quad \forall \, p$. The basic idea is to construct an interpolating parabola $a(x)$ in each cell $x_{p+1/2} < x < x_{p-1/2}$, such that its integral average coincides with the known solution u_p^n at the point p and at time n

$$\frac{1}{\Delta x} \int_{x_{p-1/2}}^{x_{p+1/2}} a(x) \mathrm{d}x = u_p^n \tag{3.6.80}$$

and such that no new extrema appear in the interpolated function. The method determines the three coefficients of the interpolating parabola by imposing (3.6.80) and that the parabola passes through the points $(x_{p-1/2}, a_p^{\mathrm{L}})$ and $(x_{p+1/2}, a_p^{\mathrm{R}})$, where the values $a_p^{\mathrm{L,R}}$ are found by imposing: *i*) that they do not fall outside the range of values given by u_p and u_{p+1}; *ii*) that in smooth parts away of extrema $a_{p+1}^{\mathrm{L}} = a_p^{\mathrm{R}} \equiv u_{p+1/2}$ (*i.e.* that the interpolating function is continuous); *iii*) that $a(x)$ is a monotone function in each cell. The $a_p^{\mathrm{L,R}}$ are the reconstructed values on cell boundaries, which will be employed as initial data for the local Riemann problems.

The procedure to find $a_p^{\mathrm{L,R}}$ consists in discretizing the indefinite integral $I(x, t^{\,n}) = \int u(\xi, t_n) \mathrm{d}\xi$ and in computing it at the point $x_{p+1/2}$

$$I(x_{p+1/2}, t^n) = \sum_{r \leq p} u_r^n \Delta x \, . \tag{3.6.81}$$

A quartic polynomial is then interpolated through the points $(x_{p+q+1/2}, I(x_{p+q+1/2}))$, $q = 0, \pm 1, \pm 2$ and the reconstructed value follows, after some algebra, from its differentiation:

$$u_{p+1/2}^n = \left. \frac{\mathrm{d}I}{\mathrm{d}x} \right|_{x_{p+1/2}} = \frac{1}{2}(u_p^n + u_{p+1}^n) + \frac{1}{6}(\delta u_p - \delta u_{p+1}) \, , \tag{3.6.82}$$

[6] We try in this description to correct the several typos present in the original article.

where $\delta u_p \equiv \frac{1}{2}(u^n_{p+1} - u^n_{p-1})$. The substitution of the above δu_p with

$$\delta_m u_p \equiv \begin{cases} \min(|\delta u_p|, 2|u^n_p - u^n_{p-1}|, 2|u^n_{p+1} - u^n_p|)\mathrm{sign}(\delta u_p) & \text{if } (u^n_{p+1} - u^n_p)(u^n_p - u^n_{p-1}) > 0 \\ 0 & \text{otherwise} \end{cases} \tag{3.6.83}$$

guarantees that $u^n_{p+1/2}$ is not outside the interval determined by u^n_p and u^n_{p+1} and also leads to a steeper representation of discontinuities. After determining $a^{\mathrm{L,R}}_p$, it is possible to express the interpolating parabola coefficients in terms of them and of the original solution:

$$a(x) = a^{\mathrm{L}}_p + x\left\{(a^{\mathrm{R}}_p - a^{\mathrm{L}}_p) + 6\left[u^n_p - \frac{1}{2}(a^{\mathrm{R}}_p + a^{\mathrm{L}}_p)\right](1-x)\right\} . \tag{3.6.84}$$

This reconstruction may still be oscillatory near large gradients. To take care of these, Colella and Woodward suggested to reset one or both of $a^{\mathrm{L,R}}_p$, according to the following possible cases. If (case I) u^n_p is a local extremum, then the interpolating function is set to be constant. If u^n_p falls between a^{L}_p and a^{R}_p, but is close to one of them so that the interpolated parabola takes on a value that is outside this range, namely, from (3.6.84), when (case II)

$$(a^{\mathrm{R}}_p - a^{\mathrm{L}}_p)\left[u^n_p - \frac{1}{2}(u^{\mathrm{R}}_p + u^{\mathrm{L}}_p)\right] > \frac{(a^{\mathrm{R}}_p - a^{\mathrm{L}}_p)^2}{6} \tag{3.6.85}$$

or (case III)

$$-\frac{(a^{\mathrm{R}}_p - a^{\mathrm{L}}_p)^2}{6} > (a^{\mathrm{R}}_p - a^{\mathrm{L}}_p)\left[u^n_p - \frac{1}{2}(u^{\mathrm{R}}_p + u^{\mathrm{L}}_p)\right] , \tag{3.6.86}$$

then either a^{L}_p or a^{R}_p is reset, so that the interpolation parabola is monotone and so that its derivative at the opposite edge of the zone from the one where the value is being reset is zero. The expressions for a^{L}_p and a^{R}_p in the three cases are as follows:

$$\begin{aligned} &\text{case I} && a^{\mathrm{L}}_p = a^{\mathrm{R}}_p = u^n_p , \\ &\text{case II} && a^{\mathrm{L}}_p = 3u^n_p - 2a^{\mathrm{R}}_p , \\ &\text{case III} && a^{\mathrm{R}}_p = 3u^n_p - 2a^{\mathrm{L}}_p . \end{aligned}$$

The steps discussed so far are those identifying the basic PPM method. However, additional steps were suggested in the original article to improve the reconstruction and we have implemented two of them in `Whisky`. Both have to be performed before the monotonicity preservation enforcement (3.6.87). The first modification helps in obtaining sharper profiles at contact discontinuities. First of all one has to give rules for determining whether the cell is considered to be inside a global discontinuity. In this case then, instead of using the previous $a^{\mathrm{L,R}}_p$, the piecewise-linear distribution given by $\delta_m u_{p\pm1}$ is used:

$$a^{\mathrm{L}}_p \to u_{p-1} + \frac{1}{2}\delta_m u_{p-1}, \quad a^{\mathrm{R}}_p \to u_{p+1} + \frac{1}{2}\delta_m u_{p+1} . \tag{3.6.87}$$

A cell is considered to be inside a discontinuity if *i*) a finite-difference approximation to the third derivative of the solution is sufficiently large, *ii*) a finite-difference approximation to the second derivative changes sign across the cell, *iii*) the finite-difference approximation to the first and third derivative have opposite sign (this ensures that small plateaux within a general increase or decrease are not taken as

discontinuities) and *iv*) the jump is not too small. The final procedure, as conceived by Colella and Woodward, for applying this steepening is

$$\begin{aligned} a_p^{\mathrm{L}} &\to a_p^{\mathrm{L}}(1-\eta_p) + \Big(u_{p-1} + \frac{1}{2}\delta_m u_{p-1}\Big)\eta_p \ , \\ a_p^{\mathrm{R}} &\to a_p^{\mathrm{R}}(1-\eta_p) + \Big(u_{p+1} - \frac{1}{2}\delta_m u_{p+1}\Big)\eta_p \ , \end{aligned} \tag{3.6.88}$$

where

$$\eta_p \equiv \max[0, \min(\eta^{(1)}(\tilde{\eta}_p - \eta^{(2)}), 1)] \tag{3.6.89}$$

and

$$\tilde{\eta}_p = \begin{cases} \dfrac{u_{p-2} - u_{p+2} + 4\delta u_p}{12\delta u_p} & \text{if} \quad \begin{cases} \delta^2 u_{p+1}\delta^2 u_{p-1} < 0 \\ |u_{p+1} - u_{p-1}| - \varepsilon \min(|u_{p+1}|, |u_{p-1}|) > 0 \end{cases} \\ 0 & \text{otherwise} \ , \end{cases} \tag{3.6.90}$$

where

$$\delta^2 u_p \equiv \frac{u_{p+1} - 2u_p + u_{p-1}}{(\Delta x)^2} \tag{3.6.91}$$

and ε, $\eta^{(1)}$ and $\eta^{(2)}$ are positive constant parameters. Condition *iv*) is enforced by the second inequality of (3.6.90), so ε is effectively a parameter specifying how big the jump has to be in order to be considered a discontinuity. Note that $\delta^2 u_p$ is the finite-difference approximation to the second derivative in p and results from the finite-difference approximation to the first derivatives centered in $p \pm \frac{1}{2}$. So condition *ii*) is effectively enforced by the first inequality of (3.6.90). The finite-difference approximation to the third derivative is simply given by

$$\frac{\delta^2 u_{p+1} - \delta^2 u_{p-1}}{2\Delta x} \ , \tag{3.6.92}$$

so that condition *i*) as can be written as

$$\frac{\delta^2 u_{p+1} - \delta^2 u_{p-1}}{2\Delta x} > \eta^{(2)} \frac{2(\Delta x)^3}{u_{p+1} - u_{p-1}} \ , \tag{3.6.93}$$

which is enforced by (3.6.89) (in fact, if (3.6.93) were not satisfied, η_p would be zero and the steepening (3.6.88) would not be applied); so $\eta^{(2)}$ is a parameter specifying how big the third derivative must be in order that we consider it a discontinuity. Condition *iii*) is also contained in (3.6.89), which, apart for constant factors and a negative sign, is the product of the above third derivative and the inverse of the centered first derivative; such a product must be negative for $\tilde{\eta}_p$ to be positive and so for η_p to be different from zero. Finally, $\eta^{(1)}$ is a parameter which determines a continuous transition between the schemes (3.6.82) and (3.6.88).

In principle, this correction could be applied also to shocks, but we have followed Colella and Woodward and have applied it only to contacts. Thus only $\rho_p^{\mathrm{L,R}}$ may be affected by this modification and, in addition to the above rules, we modify $\rho_p^{\mathrm{L,R}}$ only if

$$K \frac{|\delta\rho_p|}{\min(\rho_{p+1}, \rho_{p-1})} \geq \frac{|\delta p_p|}{\min(p_{p+1}, p_{p-1})} \tag{3.6.94}$$

(K is another positive parameter), that is when the detected discontinuity is predominantly a contact discontinuity.

The second modification to basic PPM concerns the flattening of interpolation profiles in the neighbourhood of shocks which are sufficiently strong and steep. In the original calculations, in fact, Colella and Woodward noticed low-amplitude post-shock oscillations in the solution. They found that a flattening technique, in practice a local reduction of the order of the method, is successful in eliminating this error. The flattening is applied to the p-th cell when

$$\frac{|p_{p+1} - p_{p-1}|}{\min(p_{p+1}, p_{p-1})} \quad > \quad \omega^{(0)} \,, \tag{3.6.95}$$

where $\omega^{(0)}$ is a positive constant, and

$$v_{p-1} - v_{p+1} \quad > \quad 0 \,, \tag{3.6.96}$$

i.e. when the cell is inside a pressure and a velocity jump consistent with the possibility of there being a shock. Any application of the flattening procedure can be written as a modification of $a_p^{\mathrm{L,R}}$:

$$(a_p^{\mathrm{L,R}})_{\mathrm{flat}} = a_p^n (1 - f_p) + a_p^{\mathrm{L,R}} f_p \,, \tag{3.6.97}$$

where $0 < f_p < 1$ always and $f_p = 1$ far from shocks. Our implementation of the flattening procedure consists in taking f_p according to the pressure jump $(p_{p+1} - p_{p-1})/(p_{p+2} - p_{p-2})$ across the cell, *i.e.*

$$f_p \quad = \quad \max\left(\tilde{f}_p, \tilde{f}_{p+\mathrm{sign}(p_{p-1}-p_{p+1})}\right) , \tag{3.6.98}$$

where

$$\tilde{f}_p \quad \equiv \quad \max\left\{0, 1 - \max\left[0, \omega^{(2)}\left(\frac{p_{p+1} - p_{p-1}}{p_{p+2} - p_{p-2}} - \omega^{(1)}\right)\right]\right\} , \tag{3.6.99}$$

where $\omega^{(1)}$ and $\omega^{(2)}$ are positive constants, determining respectively how big a pressure jump must be for the flattening procedure to be applied and how continuously do we change from scheme (3.6.82) to (3.6.97).

As we have presented above, PPM has seven tunable parameters; the default values of these parameters used in our implementation are the ones suggested by Colella and Woodward, *i.e.*

$$\begin{aligned}
\varepsilon &= 0.01 \\
\eta^{(1)} &= 20 \\
\eta^{(2)} &= 0.05 \\
K &= 0.1\Gamma \qquad (\Gamma = \text{polytropic index}) \\
\omega^{(0)} &= 0.33 \\
\omega^{(1)} &= 0.75 \\
\omega^{(2)} &= 10 \,.
\end{aligned} \tag{3.6.100}$$

All the presented reconstruction methods are stable in the presence of shocks. By default we use PPM as this seems to be the best balance between accuracy and computational efficiency, as shown, for example, in [104]. As said above (see note on page 31), however, there is no standard "correct" formulation of this method, so it is useful to compare results with TVD methods as well. We refer to the next chapter for a numerical comparison of the reconstruction procedures implemented in `Whisky` (see, in particular, Fig. 4.3).

Chapter 4

The `Whisky` code

In an attempt to respond, at least in part, to the scientific needs presented in Chapter 1, we have developed `Whisky`, a 3-dimensional finite-differencing code, solving the general-relativistic hydrodynamics equations in a conservative formulation (*cf.* Section 3.3.1) and in a generic and time-varying curved background. The `Whisky` code is the result of an ongoing and ever-growing collaboration among several European Institutes, *i.e.* the Albert Einstein Institute (Golm, Germany), SISSA (Trieste, Italy), the University of Thessaloniki (Greece), the University of Valencia (Spain). These Institutes were part, in the years 2000–2003, of a European Research and Training Network investigating sources of gravitational waves [1]. Recent collaborations have started with the group at the Louisiana State University (Baton Rouge, USA).

The `Whisky` code solves the general-relativistic hydrodynamics equations on a 3-dimensional spacelike surface (*i.e.* the spatial numerical grid) with Cartesian coordinates. The code has been constructed within the framework of the `Cactus` Computational Toolkit (see [62] for details), originally developed at the Albert Einstein Institute and now also at the Louisiana State University. This public domain code provides high-level facilities such as parallelization, input/output, portability on different platforms and several evolution schemes to solve general systems of PDEs. Clearly, special attention is dedicated to the solution of the Einstein equations, whose matter terms in non-vacuum spacetimes are handled by the `Whisky` code. While the `Whisky` code is entirely new, its initial development has benefitted in part from the release of a public version of the general-relativistic-hydrodynamics code described in [103, 100] and developed mostly by the group at the Washington University (St. Louis, USA).

The `Whisky` code, however, incorporates important recent developments concerning, in particular, new numerical methods for the solution of the hydrodynamics equations. These improvements have also been described in detail in [32, 31]; they include: *i)* the Piecewise Parabolic Method (PPM) (Section 3.6.3) and the Essentially Non-Oscillatory methods (Section 3.6.2) for the cell reconstruction procedure; *ii)* the Harten Lax van Leer Einfeldt approximate Riemann solver (Section 3.5.1), the Marquina flux formula (Section 3.5.1); *iii)* the analytic expression for the left eigenvectors (Section 3.3.2) and the compact flux formulae [15] for the Roe Riemann solver and the Marquina flux formula; *iv)* the use of a "method of lines" (MoL) approach for the implementation of high-order time-evolution schemes (Section 4.3.1); *v)* the possibility to couple the general-relativistic hydrodynamics equations with a conformally decomposed 3-metric; *vi)* the excision from the numerical domain of regions surrounded by an apparent horizon and possibly containing a singularity (Section 4.3.5). The incorporation of these new numerical techniques in the code has led to a much improved ability to simulate relativistic stars, as shown in Section 4.4 which is devoted to code tests.

4.1 Outline of the code

While the Cactus code provides at each time step a solution of the Einstein equations (2.0.1) [10], the Whisky code provides the time evolution of the hydrodynamics equations, expressed through the conservation equations (3.3.39). In Section 3.4 we described the different stages required for the evolution of the hydrodynamics equations with Whisky. Now we summarize them here with reference to their actual implementation in Whisky: *i*) conversion of the primitive variables to the conserved variables (*cf.* Section 3.3.1); *ii*) reconstruction of the variables on the cell interfaces (*cf.* Section 3.6); *iii*) solution of the Riemann problems (*cf.* Section 3.5); *iv*) computation of the source terms (*cf.* Section 4.3.2); *v*) conversion from the evolved conserved variables to recover the primitive variables at the new time level (*cf.* Section 4.3.3). We have already illustrated in detail in the previous chapter the principles behind stages *ii*) and *iii*) and in this chapter we will discuss the practical implementation of stages *iv*) and *v*) in Whisky. Stage *i*) is a trivial implementation of (3.3.38).

Stages *ii*) and *iii*) are performed on each spatial direction independently and in sequence, following the dimensional-splitting approach discussed in Section 3.4. Before stage *v*), a first check is made in order to ascertain whether each grid point is (or is going to be) located in the atmosphere (*cf.* Section 4.3.4) or in an excised region (*cf.* Section 4.3.5); if this is true, then the variables will not be evolved at that point. After this check, the fluxes computed by the Riemann solvers and the source terms are summed up and used by the routine implementing the evolution by the MoL (*cf.* Section 4.3.1). After stage *v*), the hydrodynamical variables at the points that are located in the atmosphere or in an excised region are reset to small constant values. Finally, both physical and symmetry boundary conditions are applied.

In addition to the basic ones, we have written many other routines that perform secondary, but important tasks, as described below. As far as initial data are concerned, we have written simple routines for the generation of shock-tube test problems and for the construction of Tolman Oppenheimer Volkoff (TOV) stars. The TOV initial data generator, in addition to having been extensively used for testing purposes (*cf.* Section 4.4.2), was also employed in the simulations reported in Chapter 6. For other simulations of physical interest we have used initial data produced by external codes; we have written interface routines to transform and import these data into Cactus. In particular, for rotating NS simulations, we use the 2-dimensional numerical code RNS of Stergioulas [234], that computes accurate stationary equilibrium solutions for axisymmetric and rapidly-rotating relativistic stars in polar coordinates; the data are then transformed to Cartesian coordinates using standard coordinate transformations. For binary NS initial data, instead, we use the spectral-method code LORENE by Gourgoulhon *et al.* [111] and then transform the data into a Cartesian grid.

The data produced in this way satisfy the constraint equations (2.1.12)–(2.1.13). In some cases, though, in order to suit our needs for particular initial conditions, we want to modify the hydrodynamics part of these initial data, as, *e.g.*, in rotating NS collapse (*cf.* Chapter 5), where we reduce the initial pressure to shorten the time before collapse starts, or in TOV head-on collisions (*cf.* Chapter 6), where we need two nearby stars on the grid. In these cases, we want to enforce the constraints (2.1.12)–(2.1.13) again after performing the initial modification. For such purpose, we have implemented an initial-value problem (IVP) solver that uses the York procedure [262] to determine initial data consistent (to the desired accuracy) with the Hamiltonian and momentum constraint equations.

Finally, we have implemented several analysis routines to compute various interesting quantities after each time step computation. With these analysis routines we can monitor the velocity in spherical coordinates, the first and the second time derivatives of the trace-free quadrupole moment (following formulae in [96]), the baryon mass (5.3.1) contained within a sphere of a chosen radius, the angular momentum (2.1.15) and the proper distance between the maximum densities of the stars (for binary

evolutions).

At this point, we would like to underline that our role in the writing of `Whisky` has concentrated on the bulk of the code (*i.e.* stages *i–v* above), on the IVP solver, on the analysis routines for the computation of the quadrupole moment and of the baryon mass and on some other short routines written initially only for testing purposes (*cf.* Section 4.4.3); while we have not participated in the writing of the MoL solver, of the boundary conditions routines, of the excision code (*cf.* Section 4.3.5) and, in general, of the part of the `Cactus` code related to the evolution of the spacetime variables.

4.2 Equations of state

In order to close the system of the hydrodynamics equations (3.3.39), an EoS which relates the pressure to the rest-mass density and to the energy density must be specified. The code has been written to use a generic EoS, *i.e.* a generic subroutine returns the values of the pressure at a given grid point whenever needed, once the values of the density and/or of the specific internal energy are provided at that point. All of the simulations that so far have been performed, however, use either an (isentropic) polytropic EoS

$$p = K\rho^{\Gamma}\,, \tag{4.2.1}$$

$$e = \rho + \frac{p}{\Gamma - 1}\,, \tag{4.2.2}$$

or an "ideal-fluid" EoS

$$p = (\Gamma - 1)\rho\,\epsilon\,. \tag{4.2.3}$$

Here, e is the energy density in the rest frame of the fluid, K the polytropic constant (not to be confused with the trace of the extrinsic curvature defined earlier) and Γ the adiabatic exponent. In the case of the polytropic EoS (4.2.1), $\Gamma = 1 + 1/N$, where N is the polytropic index. Note also that in this case the evolution equation for τ in (3.3.39) needs not be solved, since the pressure and the energy density can be derived directly from the rest-mass density. In the case of the ideal-fluid EoS (4.2.3), on the other hand, non-isentropic changes can take place in the fluid and the evolution equation for τ needs to be solved. In addition to the EoSs (4.2.1) and (4.2.3), a "hybrid" EoS (suitable for core-collapse simulations, as described in [266, 267]), has been implemented, as well as the capability of using tabulated EoSs.

4.3 Numerical methods

4.3.1 The method of lines for the time update

The reconstruction methods guarantee that a prescribed order of accuracy is retained in space. However, the need to retain a high-order accuracy also in time can complicate considerably the evolution from one time-level to the following one. As a way to handle this efficiently, we have chosen to follow a MoL approach [136, 242]. The MoL is a procedure to separate the space and time discretization processes. First, the continuum equations are considered to be discretized in space only, while leaving the problem continuous in time. This is equivalent to transforming a set of PDEs such as (3.2.4) into a set of ODEs. Then, the resulting system of ODEs can be solved numerically with any stable solver. This method minimizes the coupling between the spacetime and hydrodynamics solvers and allows for a transparent implementation of different evolution schemes.

In practice, this is achieved by integrating equations

$$\partial_t \mathbf{U} + \partial_i \mathbf{F}^{(i)}(\mathbf{U}) = \mathbf{s}(\mathbf{U}) \tag{4.3.4}$$

over space in every computational cell defined by its position (x_p, y_q, z_r). Taking, as an example, integration in the x direction, the procedure results in the following ODE

$$\begin{aligned}
&\frac{\mathrm{d}(\widetilde{\mathbf{U}})}{\mathrm{d}t} = \mathbf{L}(\widetilde{\mathbf{U}}) = \\
&= \frac{1}{\Delta V}\left[\iiint \mathbf{s}\,\mathrm{d}^3x + \int_{y_{q-1/2}}^{y_{q+1/2}}\int_{z_{r-1/2}}^{z_{r+1/2}} \mathbf{F}^x(\mathbf{U}(x_{p-1/2}, y, z))\mathrm{d}y\,\mathrm{d}z - \int_{y_{q-1/2}}^{y_{q+1/2}}\int_{z_{r-1/2}}^{z_{r+1/2}} \mathbf{F}^x(\mathbf{U}(x_{p+1/2}, y, z))\mathrm{d}y\,\mathrm{d}z \right],
\end{aligned} \tag{4.3.5}$$

where $\Delta V = \Delta x \Delta y \Delta z$ and $\widetilde{\mathbf{U}}$ is, in our specific case, the spatially-integrated vector of conserved variables, *i.e.*

$$\widetilde{\mathbf{U}} \equiv \frac{1}{\Delta V}\int \mathbf{U}\ \mathrm{d}x\,\mathrm{d}y\,\mathrm{d}z\ , \tag{4.3.6}$$

and $\mathbf{F}^x$ is the x component of the flux five-vector $\mathbf{F}$.

MoL itself does not have a precise truncation error but, rather, it acquires the truncation order of the time-integrator employed, provided that the discrete operator $\mathbf{L}$ is of the same order in space and at least first-order accurate in time. Several integrators are available in our implementation of MoL, including the second-order Iterative Crank Nicholson (ICN) solver and Runge Kutta (RK) solvers of first to fourth-order accuracy. The second and third-order RK solvers are known to be TVD whilst the fourth-order one is known to not be TVD [221, 110]. As the coupling between the spacetime and the hydrodynamics is only second-order accurate, we typically use the ICN solver.

In our implementation of MoL, the right hand side operator $\mathbf{L}(\widetilde{\mathbf{U}})$ is simplified by approximating the integrals (4.3.5) with the midpoint rule

$$\int_a^b g(x)\mathrm{d}x = (b-a)g\Big(\frac{a+b}{2}\Big) + \mathcal{O}[(b-a)^2] \tag{4.3.7}$$

to get

$$\mathbf{L}(\widetilde{\mathbf{U}}) \quad = \quad \mathbf{s}_{p,q,r} + \mathbf{F}^{(1)}(\mathbf{U}_{p-1/2,q,r}) - \mathbf{F}^{(1)}(\mathbf{U}_{p+1/2,q,r})\ . \tag{4.3.8}$$

Given this simplification, the calculation of the right-hand side of (4.3.5) splits into the following stages, as already outlined in Section 4.1:

- calculation of the source terms $\mathbf{s}(\mathbf{U}(x_p, y_q, z_r))$ at all the grid points;
- reconstruction of the data $\mathbf{U}$ to both sides of a cell boundary (*cf.* Section 3.6);
- solution at cell boundaries of the Riemann problem having the values $\mathbf{U}_{\mathrm{L,R}}$ as initial data (*cf.* Section 3.5);
- calculation in each coordinate direction of the inter-cell flux $\mathbf{F}^x(\mathbf{U}_{p+1/2,q,r})$, $\mathbf{F}^y(\mathbf{U}_{p,q+1/2,r})$, $\mathbf{F}^z(\mathbf{U}_{p,q,r+1/2})$, that is the flux across the boundary between a cell (*e.g.* the p-th) and its closest neighbour [*e.g.* the $(p+1)$-th];
- check on the location of atmosphere and excised regions.

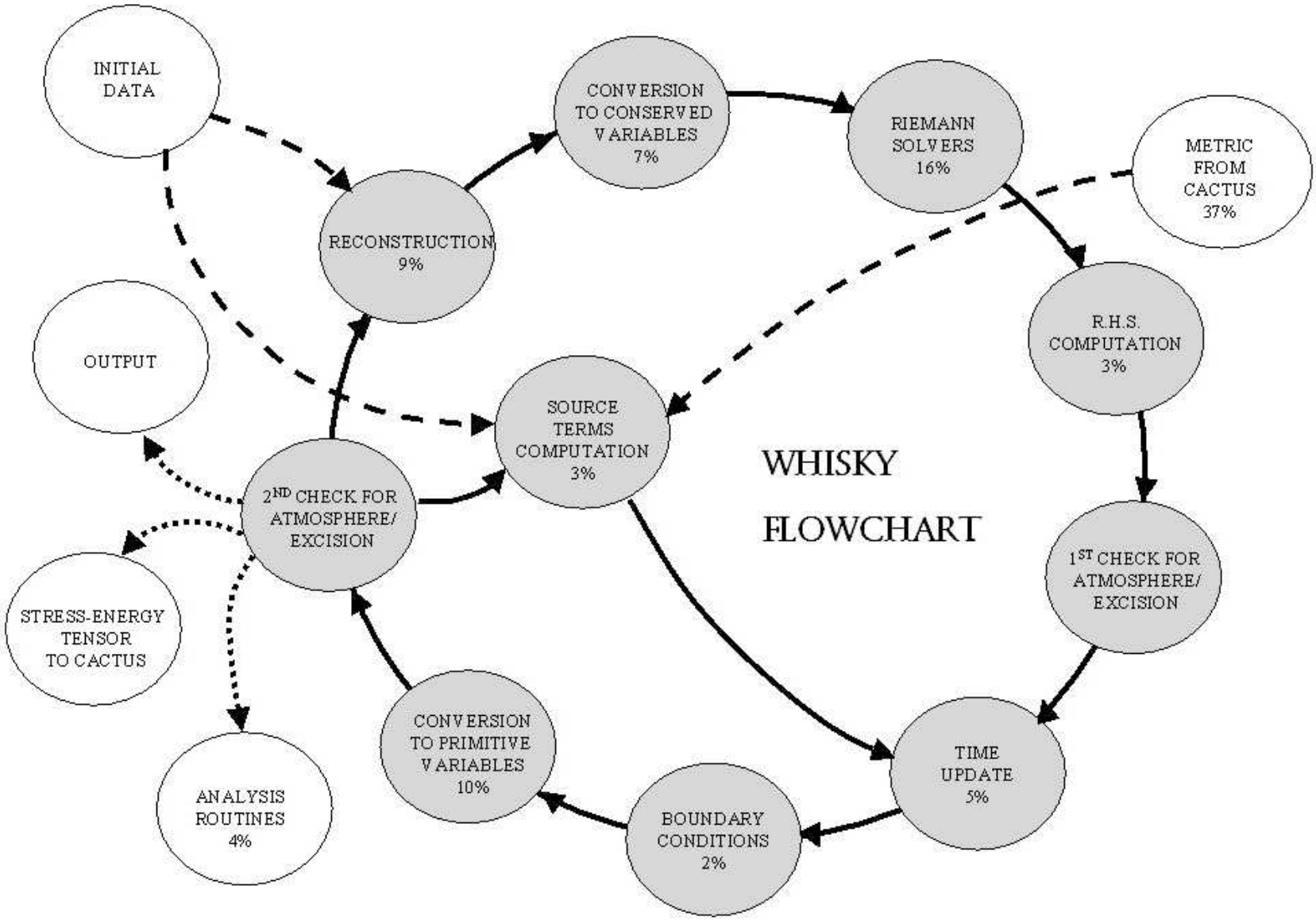

Figure 4.1: A pictorial scheme of the `Whisky` flowchart. The grey ovals represent the different parts of the bulk of the computation of the evolution of the matter terms, while the white ovals represent routines outside the main `Whisky` cycle, which pass data to or receive data from the bulk of `Whisky`. The percentages reported in many of the ovals are the percentages of the typical single-processor running time spent in the routines the oval refers to; the absence of this figure means that it would be less than 1%. The sum of all the percentages does not total 100%, beacuse of these several non-reported little-time-consuming routines. These data refer to a typical evolution with a polytropic EoS; for the more general ideal-fluid EoS the overall running time for the otherwise-equal configuration is increased by 4%, because of the additional equation to solve. The relative percentages of the running time spent in each part vary only slightly.

We underline at this point that the innovation that improved most the speed of our code has been the implementation of the analytic expression for the left eigenvectors (3.3.46), thus avoiding the computationally expensive inversion of the three 5×5 matrices of the right eigenvectors, that was necessary before such analytic expressions were found [121]. We also use a compact version of the flux formula (a variant on the methods described in [15]) to increase speed and accuracy. These implementations have brought a 40% reduction of the computational time spent in the solution of the hydrodynamics equations; however, in evolutions involving also the time integration of the Einstein equations, this is reduced to a 5% decrease in computational cost, because a large part of the running time is spent in the update of the spacetime field variables.

4.3.2 Source terms

For numerical reasons, namely in order to avoid the presence of time derivatives in the source-term computation, the implemented form of the source terms is not (3.3.41) directly, but it has been modified as shown in the following paragraphs.

We need the expression of some of the 4-Christoffel symbols ${}^{(4)}\Gamma^{\rho}_{\mu\nu}$ applied to the 3+1 decomposed variables. In order to remove time derivatives we will frequently make use of the ADM evolution equation (2.1.10) for the 3-metric in the form

$$\partial_t \gamma_{ij} = -2\left(\alpha K_{ij} + \partial_{(i}\beta_{j)} - {}^{(3)}\Gamma^k_{ij}\beta_k\right) . \tag{4.3.9}$$

As it is used in what follows, we also recall that ∇ is the covariant derivative associated with the spatial 3-surface and we note that it is compatible with the 3-metric (*cf.* Section 2.1):

$$\nabla_i \gamma^{jk} = \partial_i \gamma^{jk} + 2\,{}^{(3)}\Gamma^j_{il}\gamma^{lk} = 0 \tag{4.3.10}$$

We start from the ${}^{(4)}\Gamma^0_{00}$ symbol:

$${}^{(4)}\Gamma^0_{00} = \frac{1}{2\alpha^2}\Big[-\partial_t\big(\beta_k\beta^k\big) + 2\alpha\partial_t\alpha + 2\beta^i\partial_t\beta_i - \beta^i\partial_i\big(\beta_k\beta^k\big) + 2\alpha\beta^i\partial_i\alpha\Big] \tag{4.3.11}$$

and we expand the derivatives as

$$\begin{aligned} \partial_t\big(\beta_k\beta^k\big) &= \partial_t\big(\gamma_{jk}\beta^j\beta^k\big) = 2\gamma_{jk}\beta^j\partial_t\beta^k + \beta^j\beta^k\partial_t\gamma_{jk} = \\ &= 2\beta_k\partial_t\beta^k - 2\alpha K_{jk}\beta^j\beta^k - 2\beta^j\beta^k\partial_j\beta_k + 2\,{}^{(3)}\Gamma^i_{kj}\beta_i\beta^j\beta^k \end{aligned} \tag{4.3.12}$$

and

$$\partial_i\big(\beta_k\beta^k\big) = \partial_i\big(\gamma^{jk}\beta_j\beta_k\big) = 2\gamma^{jk}\beta_j\partial_i\beta_k + \beta_j\beta_k\partial_i\gamma^{jk} = 2\beta_k\partial_i\beta_k - 2\,{}^{(3)}\Gamma^j_{ik}\beta_j\beta^k , \tag{4.3.13}$$

where we have used (4.3.9) and (4.3.10), respectively. Inserting (4.3.12) and (4.3.13), equation (4.3.11) becomes

$${}^{(4)}\Gamma^0_{00} = \frac{1}{\alpha}\Big(\partial_t\alpha + \beta^i\partial_i\alpha + K_{jk}\beta^j\beta^k\Big) . \tag{4.3.14}$$

With the same strategy we then compute

$${}^{(4)}\Gamma^0_{i0} = -\frac{1}{2\alpha^2}\Big[\partial_i(\beta^k\beta_k - \alpha^2) - \beta^j(\partial_i\beta_j - \partial_j\beta_i + \partial_t\gamma_{ij})\Big] = -\frac{1}{\alpha}\Big(\partial_i\alpha - \beta^j K_{ij}\Big) \tag{4.3.15}$$

and

$${}^{(4)}\Gamma^0_{ij} = -\frac{1}{2\alpha^2}\Big[\partial_i\beta_j + \partial_j\beta_i - \partial_t\gamma_{ij} - \beta^k(\partial_i\gamma_{kj} + \partial_j\gamma_{ki} - \partial_k\gamma_{ij})\Big] = -\frac{1}{\alpha}K_{ij} . \tag{4.3.16}$$

Other more straightforward calculations give

$$ {}^{(4)}\Gamma_{00j} = {}^{(4)}\Gamma^{\nu}_{0j} g_{\nu 0} = \frac{1}{2}\partial_j \left(\beta_k \beta^k - \alpha^2 \right) , \tag{4.3.17} $$

$$ {}^{(4)}\Gamma_{l0j} = {}^{(4)}\Gamma^{\nu}_{lj} g_{\nu 0} = \alpha K_{lj} + \partial_l \beta_j + \partial_j \beta_l - \beta_k {}^{(3)}\Gamma^{k}_{lj} , \tag{4.3.18} $$

$$ {}^{(4)}\Gamma_{0lj} = {}^{(4)}\Gamma^{\nu}_{0j} g_{\nu l} = -\alpha K_{jl} - \partial_l \beta_j + \beta_k {}^{(3)}\Gamma^{k}_{lj} , \tag{4.3.19} $$

$$ {}^{(4)}\Gamma_{lmj} = {}^{(4)}\Gamma^{\nu}_{lj} g_{\nu m} = {}^{(3)}\Gamma_{lmj} , \tag{4.3.20} $$

where (4.3.9) was used to derive (4.3.18) and (4.3.19). Now we have all the expressions for calculating the source terms. The ones for the variables S_k are [*cf.* (3.3.34)]

$$ \left(\mathcal{S}_{S_k} \right)_j = T^{\mu}_{\nu} \Gamma^{\nu}_{\mu j} = T^{\mu\nu} \Gamma_{\mu\nu j} . \tag{4.3.21} $$

After expanding the derivative in (4.3.17), the coefficient of the T^{00} term in (4.3.21) becomes

$$ {}^{(4)}\Gamma_{00j} = \frac{1}{2}\beta^l \beta^m \partial_j \gamma_{lm} - \alpha \partial_j \alpha + \beta_m \partial_j \beta^m . \tag{4.3.22} $$

The coefficient of the T^{0i} term is

$$ {}^{(4)}\Gamma_{0ij} + {}^{(4)}\Gamma_{i0j} = \partial_j \beta_i = \beta^l \partial_i \gamma_{jl} + \gamma_{il} \partial_j \beta^l . \tag{4.3.23} $$

The coefficient of the T^{lm} term is simply

$$ {}^{(3)}\Gamma_{lmj} = \frac{1}{2}\Big(\partial_j \gamma_{ml} + \partial_m \gamma_{jl} - \partial_l \gamma_{mj} \Big) . \tag{4.3.24} $$

Finally, summing (4.3.22)–(4.3.24) we find

$$ \left(\mathcal{S}_{S_k} \right)_j = T^{00} \left(\frac{1}{2}\beta^l \beta^m \partial_j \gamma_{lm} - \alpha \partial_j \alpha \right) + T^{0i} \beta^l \partial_j \gamma_{il} + T^0_i \partial_j \beta^i + \frac{1}{2} T^{lm} \partial_j \gamma_{lm} , \tag{4.3.25} $$

which is the expression implemented in the code.

The source term for τ is [*cf.* (3.3.41)]

$$ \mathcal{S}_\tau = \alpha \left(T^{\mu 0} \partial_\mu \alpha - \alpha T^{\mu\nu} {}^{(4)}\Gamma^0_{\mu\nu} \right) . \tag{4.3.26} $$

For clarity, again we consider separately the terms containing as a factor the different components of $T^{\mu\nu}$. From (4.3.14) we find the coefficient of T^{00} to be

$$ \alpha \left(\partial_t \alpha - \alpha {}^{(4)}\Gamma^0_{00} \right) = -\alpha \left(\beta^i \partial_i \alpha + \beta^k \beta^l K_{kl} \right) . \tag{4.3.27} $$

The coefficient of the term T^{0i} is given by

$$ \alpha \left(\partial_i \alpha - 2\alpha {}^{(4)}\Gamma^0_{i0} \right) = 2\alpha \beta^j K_{ij} - \alpha \partial_i \alpha \tag{4.3.28} $$

and, finally, the coefficient for T^{ij} is

$$ -\alpha^2 {}^{(4)}\Gamma^0_{ij} = \alpha K_{ij} . \tag{4.3.29} $$

The final expression implemented in the code is thus

$$ \mathcal{S}_\tau = \alpha \left[T^{00} \left(\beta^i \beta^j K_{ij} - \beta^i \partial_i \alpha \right) + T^{0i} \left(-\partial_i \alpha + 2\beta^j K_{ij} \right) + T^{ij} K_{ij} \right] . \tag{4.3.30} $$

These expressions require both the metric and the extrinsic curvature. In order to calculate the Christoffel symbols, the gauge and metric variables must be differenced; in `Whisky` this is currently done through either second-order or fourth-order differencing.

4.3.3 Conversion from conservative to primitive variables

As mentioned repeatedly above, the variables for which we solve the evolution equations are the conserved variables (3.3.38): D, S_i, τ. On the other hand, in order to calculate the fluxes and source terms, the primitive variables ρ, v^i, p are needed and these are also the hydrodynamical variables which we are directly interested in. The conversion from primitive to conservative variables is given analytically by (3.3.38), but converting in the other direction is not possible in a closed form, except in certain special circumstances. A standard procedure to do the conversion is to write the following equation for the pressure

$$p - \bar{p}\big[\rho(\mathbf{U}, p), \epsilon(\mathbf{U}, p)\big] = 0 \,, \tag{4.3.31}$$

where p is the value of the pressure to be found and $\bar{p}[\rho(\mathbf{U}, p), \epsilon(\mathbf{U}, p)]$ is the pressure as obtained through the EoS in terms of the updated conserved variables $\mathbf{U}$ and of p itself. This is done by inverting (3.3.38) to express ρ and ϵ in terms of the conserved variables and of the pressure only:

$$\rho = \frac{D}{\tau + p + D}\sqrt{(\tau + p + D)^2 - S^2} \,, \tag{4.3.32}$$

$$\epsilon = D^{-1}\left(\sqrt{(\tau + p + D)^2 - S^2} - p\frac{\tau + p + D}{\sqrt{(\tau + p + D)^2 - S^2}} - D\right) \,, \tag{4.3.33}$$

where

$$S^2 = \gamma^{ij} S_i S_j \,. \tag{4.3.34}$$

Then (4.3.31) is solved numerically. In Whisky we use a Newton Raphson root finder, for which we need the derivative of the function with respect to the dependent variable, *i.e.* the pressure. This is given by

$$\frac{\mathrm{d}}{\mathrm{d}p}\Big\{p - \bar{p}\big[\rho(\mathbf{U}, p), \epsilon(\mathbf{U}, p)\big]\Big\} = 1 - \frac{\partial\bar{p}(\rho, \epsilon)}{\partial\rho}\frac{\partial\rho}{\partial p} - \frac{\partial\bar{p}(\rho, \epsilon)}{\partial\epsilon}\frac{\partial\epsilon}{\partial p} \,, \tag{4.3.35}$$

where

$$\frac{\partial\rho}{\partial p} = \frac{DS^2}{\sqrt{(\tau + p + D)^2 - S^2}(\tau + p + D)^2}, \tag{4.3.36}$$

$$\frac{\partial\epsilon}{\partial p} = \frac{pS^2}{\bar{\rho}\left((\tau + p + D)^2 - S^2\right)(\tau + p + D)} \tag{4.3.37}$$

and where $\partial\bar{p}/\partial\rho$ and $\partial\bar{p}/\partial\epsilon$ given by the EoS. Once the pressure is found, the other variables follow simply. In the case of a polytropic EoS, instead of (4.3.31), we solve an equation for the rest mass density ρ:

$$\rho\widetilde{W} - D = 0 \,, \tag{4.3.38}$$

where the pressure, the specific internal energy and the enthalpy are computed from the EoS and the Lorentz factor is computed from the first equation in (3.3.38) as

$$\widetilde{W} = \sqrt{1 + \frac{S^2}{(Dh)^2}} \,. \tag{4.3.39}$$

The derivative of (4.3.38) needed for the Newton Raphson solver is given by

$$\frac{\mathrm{d}}{\mathrm{d}\rho}(\rho\widetilde{W} - D) = \widetilde{W} - \frac{\rho S^2 h'}{\widetilde{W} D^2 h^3} \,, \tag{4.3.40}$$

where

$$
\begin{aligned}
h' &= \frac{\partial h}{\partial \rho} = \frac{\partial}{\partial \rho}\left(1+\epsilon+\frac{p}{\rho}\right) = \frac{\partial}{\partial \rho}\left[1+\frac{p}{(\Gamma-1)\rho}+\frac{p}{\rho}\right] = \frac{\partial}{\partial \rho}\left[1+\frac{\Gamma p}{(\Gamma-1)\rho}\right] = \\
&= \frac{\partial}{\partial \rho}\left[1+\frac{\Gamma K \rho^{\Gamma}}{(\Gamma-1)\rho}\right] = \frac{\Gamma K \rho^{\Gamma}}{\rho^2} = \frac{\Gamma p}{\rho^2} = \frac{1}{\rho}\frac{\partial p}{\partial \rho}\,. \qquad (4.3.41)
\end{aligned}
$$

The last expression is the one used in the code.

4.3.4 The atmosphere

Numerical methods for the solution of the hydrodynamics equations in Lagrangian formulation evolve portions of the fluid only, *i.e.* all grid points refer to values of ρ, p and v which are non zero. In Eulerian formulation, instead, this is clearly impossible, even for the study of static configurations. As a consequence, part of the domain will be covered by vacuum regions. This is made more serious in general relativity, where one has to accommodate at the same time the need to resolve well objects that are intrinsically compact and the need to place the outer boundaries at very large distances from the compact object. As a results, over much of the domain that we evolve, the hydrodynamical variables ρ and p are, at least mathematically, supposed to be zero. However, in the vacuum limit the hydrodynamics equations break down, the speed of sound tends to the speed of light and HRSC schemes, that – we recall – use the characteristic structure of the equations, fail. So this region must be treated specifically.

To avoid this problem we introduce a tenuous *atmosphere*, *i.e.* a low-density and low-pressure region surrounding the compact objects. We treat the atmosphere as a perfect fluid having a zero coordinate velocity. This approach, was implemented also in [100, 218]. The atmosphere is first specified by the initial data routines. Typically, the atmosphere values are set to be more than seven orders of magnitude smaller than the evolved values. Before computing the fluxes, `Whisky` checks whether the conserved variables D or τ are below some minimum value or whether an evolution step might push them below such a value. If this is the case, the relevant cell is not evolved and the hydrodynamical variables at that point are set to *atmosphere values*. The other stage where `Whisky` checks about the location of the atmosphere is in the routine that converts from conserved variables to primitive variables. This is where the majority of the atmosphere points are usually reset. For all points, an attempt is made to convert conserved to primitive variables. If the EoS is polytropic and if the iterative algorithm returns a negative value of ρ, then ρ is reset to the atmosphere value, the velocities are set to zero and p, ϵ, S^i and τ are reset to be consistent with ρ. If, on the other hand, the EoS is the more general type (such as an ideal-fluid one), then we check whether the specific internal energy ϵ is less than a specified minimum. If this is the case then we assume we are in the atmosphere and we apply the procedure that changes from the conserved to the primitive variables for the polytropic EoS, instead.

Note that even though the polytropic EoS gives sufficient information to calculate a consistent value of D, this is not done. The reason for this is that, if the variables are set precisely to the values of the atmosphere, then very small errors would start to move certain cells above the atmosphere values. This would lead to waves of matter falling onto the compact object which, despite the extremely low density (typically only an order of magnitude higher than the floor), will influence the evolution; for example, in the case of isolated NS, this produces visible secondary overtones in the oscillations of, *e.g.*, the central density. Note that the atmosphere values used for the calculation of the initial data and the ones used during the simulations need not be the same. Indeed, we typically set the initial atmosphere values to be two orders of magnitude smaller than the evolved ones to minimize initial truncation error problems leading to spurious low-density-matter waves across the atmosphere.

With appropriate choices of the parameters regulating the atmosphere implementation, the evolution of the compact objects in our simulations is not affected by the atmosphere. As an example, we anticipate here a quantitative measure of the influence of the atmosphere during the collapse of rotating NS (*cf.* Section 5.3.2); once the apparent horizon has been found and all of the stellar material has fallen inside, the atmosphere continues to fall in. However, at the measured accretion rate, it would take an evolution time of $\sim 10^4 M$ to produce a net increase of $\sim 1\%$ in the black hole mass. Clearly, these systematic errors are well below the truncation errors even at our present highest resolutions.

4.3.5 Hydrodynamical excision

Excision boundaries are usually based on the principle that a region of spacetime that is causally disconnected can be ignored without this affecting the solution in the remaining portion of the spacetime. Although this is true for signals and perturbations travelling at physical speeds, numerical calculations may violate this assumption and disturbances, such as gauge waves, may travel at larger speeds thus leaving the physically disconnected regions.

A first naive implementation of an excision algorithm within a HRSC method could ensure that the data used to construct the flux at the excision boundary is extrapolated from data outside the excision region. This may appear to be a good idea since HRSC methods naturally change the stencils depending on the data locally. In general, however, this approach is not guaranteed to reduce the total variation of the solution (indeed, in practice, we have observed that this is not the case).

An effective solution, however, is not much more complicated and can be obtained by applying at the excision boundary the simplest outflow boundary condition (here, by outflow we mean flow into the excision region). In practice, we apply a zeroth-order extrapolation to all variables at the boundary, *i.e.* a simple copy of the hydrodynamical variables across the excision boundary. Note that setting the hydrodynamical fields inside the excised region to zero (this is what is done, for instance, in codes using artificial viscosity methods [89]) would still yield an outflow boundary condition, but leads to incorrect outflow speeds. If the reconstruction method requires more cells inside the excision region, we force the stencil to only consider the data in the exterior and the first interior cell. Although the actual implementation of this excision technique may depend on the reconstruction method used, the working principle is always the same.

We have not directly participated to the implementation and testing of the excision algorithm in `Whisky`; we report here the work done by our collaborators Hawke, Löffler and Nerozzi [117]. The location of the excision boundary itself is based on the determination of the apparent horizon which, within the `Cactus` code, is obtained using the fast apparent-horizon finder of Thornburg [240]. We note that for the cubical region that is excised on a Cartesian grid to be a true trapped surface it may have to be placed well within the horizon, as pointed out by [63]. So our excision boundary is placed a few grid points (typically four) within a surface which is typically 0.6 times the size of the apparent horizon. This may still not be a suitable outflow boundary on a Cartesian grid, as pointed out by [126, 63]. However, similar or larger excision regions show no problems in vacuum evolutions and since the sound-cones are always contained within the light-cones, we expect no additional problems to arise from the hydrodynamics.

As a summary of what we have mentioned above, we schematically report the outline of our method for solving the hydrodynamics equations on numerical grids containing excised regions:

i) any point for which all possible reconstruction stencils are not contained within the excision region are evolved in the normal fashion;

ii) all points within the excision region are not evolved;

iii) for all other points (*i.e.* those that are not in the excised region, but that have stencils containing at least one excised point), the stencil is modified in such a way that it does not contain excised points, even if this operation forces us to use a *non-standard* stencils for the selected reconstruction method.

The solution for the points on the excision boundary are not computed using Riemann solvers. We know, in fact, that all the information required to compute the solution at a point of type *iii*) must come from the exterior of the excised region. Therefore at the internal cell interfaces of these points we simply calculate the fluxes from the exterior reconstruction only.

To conclude the discussion on the excision of the hydrodynamical variables, in addition to what mentioned above, we report below how the stencil is altered when different reconstruction methods are used.

- *Slope-limited TVD reconstruction.* In this case, only the reconstructions at $x_{B\pm 1/2}$ (the subscript $_B$ indicates the point on the excision boundary) are affected by the excision region. Thus setting $S_B = 0$ [*cf.* (3.6.70)] ensures that only data outside the excision region are used, which is consistent with the TVD reconstruction.

- *ENO reconstruction.* As described in Section 3.6.2, the ENO methods use a stencil of width k, where k is the order of accuracy. Hence the reconstruction in the cells centred between x_B and x_{B-k+2} are affected by the excision region. However, it is easy to ensure that the stencil chosen by the ENO reconstruction does not include points from inside the excision region. In practice, if after checking the Newton divided differences the stencil giving the smoothest solution is one containing an excised point, this is discarded and the next smoothest stencil not containing excised points is instead selected.

- *PPM reconstruction.* We have not attempted to find a consistent third-order reconstruction for these points. Instead, we use the same reconstruction as in the TVD case. Since this provides a second-order stable reconstruction at an outflow boundary, it does not affect the order of accuracy in the rest of the domain.

4.4 Numerical Tests

This section is devoted to the tests and thus to the validation of `Whisky`. Indeed, validation represents an important aspect of the development of any code. The reasons for this are rather simple and are related to: *i)* the lack of precise knowledge of the space of solutions of the coupled system of the Einstein and general relativistic hydrodynamics equations; *ii)* the likely chance that coding errors are made in the implementation of the thousands of terms involved in the solution of such a complicated set of coupled PDEs; *iii)* the complexity of the computational infrastructure needed for the use of the code in a massively parallel environment which increases the risk of computational errors.

In addition to comparing the numerically computed solutions to available analytical solutions and to assessing its convergence in model problems, it is also fundamental to validate the convergence properties for each physical problem under study and to confirm that they hold up to the time when the desired physical information is extracted. We will do so in each of the following chapters, devoted to the application of `Whisky` to specific physical problems.

The tests presented here[1] will show both the accuracy and the convergence of our implementation of the conservative formulation of the general-relativistic hydrodynamics equations, which are coupled to a conformal transverse traceless formulation of the Einstein equations (*cf.* Chapters 2 and 3). They will also show the ability of the code to follow stably the linear and non-linear dynamics of isolated relativistic stars. More specifically, we will first present results of shock-tube tests and then of the linear pulsations of spherical and rapidly rotating stars. The computed frequencies of radial and quasi-radial oscillations will be compared with the corresponding frequencies obtained with lower-dimensional numerical codes or with alternative techniques such as the *Cowling approximation* (in which the spacetime is held fixed and only the general relativistic hydrodynamics equations are evolved) or with relativistic perturbative methods.

We will also investigate the non-linear dynamics of stellar models that are unstable to the fundamental radial mode of pulsation. We will show that, upon the addition of a small perturbation, the unstable models will either collapse to a black hole or migrate to a configuration in the stable branch of equilibrium configurations.

4.4.1 Shock-tube test

First of all, we consider a standard shock-tube test, setting as initial data a global Riemann problem. In order to test the 3-dimensional capabilities of our code, we have set the initial discontinuity for the Riemann problem to be orthogonal to the main diagonal of the cubic grid. More precisely the initial data consist of a left and right state with values

$$\begin{aligned} \rho_{\rm R} &= 1; \quad p_{\rm R} = 1.666 \times 10^{-6}; \quad v_{\rm R} = 0 \\ \rho_{\rm L} &= 10; \quad p_{\rm L} = 13.333; \qquad\quad v_{\rm L} = 0 \end{aligned} \tag{4.4.42}$$

An ideal-fluid EoS with $\Gamma = 3/2$ was used for the evolution. In Fig. 4.2 we show the solution at a given time together with the exact solution. The agreement of the two sets of curves is remarkable, especially if one bears in mind that the initial discontinuity does not propagate along a coordinate direction.

Since the shock-tube test is the most fundamental test and easiest to interpret, we also use it to assess the accuracy of the different numerical methods we have implemented. In particular, in Fig. 4.3, we show the comparison of the solution for the density obtained with different TVD reconstruction methods for

[1] Some of the most representative of these tests and results have also been reported in [32, 31].

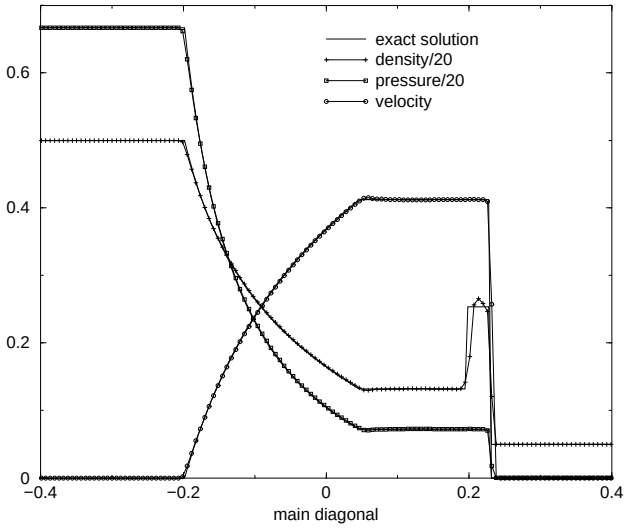

Figure 4.2: Solution of a Riemann problem set on the main diagonal of a cubic grid. The fi gure shows the comparison of the hydrodynamical variables evolved by `Whisky`, indicated with symbols, with the exact solution. The numerical simulation was obtained with the van Leer reconstruction method and the Roe solver, on a grid with 140^3 points.

the same problem as in Fig. 4.2. We use the density in order to make such a comparison because in the shock-tube test with the initial data (4.4.42) the evolution of the density is the most difficult to reproduce accurately, since with the typical resolution of 3-dimensional calculations the region included between the shock and the contact discontinuity is covered only by a small number of points. From the upper panels of the figure, it is possible to note that the minmod slope limiter is the one which produces the most diffusive evolution, both near the contact discontinuity and in the top part of the rarefaction wave. The van Leer reconstruction, instead, produces accurate results even at this medium resolution. The central panels of Fig. 4.3 show a comparison among different orders of accuracy for the ENO method; we note that using an ENO order of accuracy higher than four produces only small improvements in the reconstruction, while increasing considerably the computational resources required, because of the wider stencil. The lower panels show a comparison among our best TVD method (*i.e.* the van Leer one), the ENO method of fourth order and the PPM method with default values of the parameters. We note that, while ENO and PPM give similar results, they are clearly better than TVD reconstruction. As already mentioned in Section 3.6, we typically choose the PPM reconstruction, because it is the best compromise between accuracy and computational efficiency.

4.4.2 Tolman Oppenheimer Volkoff stars and rotating stars

Next, we consider the evolution of stable relativistic polytropic spherical stars. Since these represent static solutions, no evolution is expected, at least in the absence of any truncation error. Yet, as shown in Fig. 4.4 which refers to a stable TOV star with rest mass $M_0 = 1.4\,M_\odot$ and polytropic exponent $\Gamma = 2$, both a small periodic oscillation and a small secular increase of the stellar central density are detected during the numerical evolution of the equations. Both effects have, however, a single explanation and at least one of them faithfully reproduces physical process. Since the initial data contains also a small truncation error, this is responsible for triggering quasi-radial oscillations which appear as periodic variations in the central density. As the resolution is increased, the truncation error is reduced and so is the amplitude of the oscillation. The secular growth, on the other hand, is a purely numerical problem, which also shows up as a growing violation of the constraint equations. As for the oscillations, also the secular

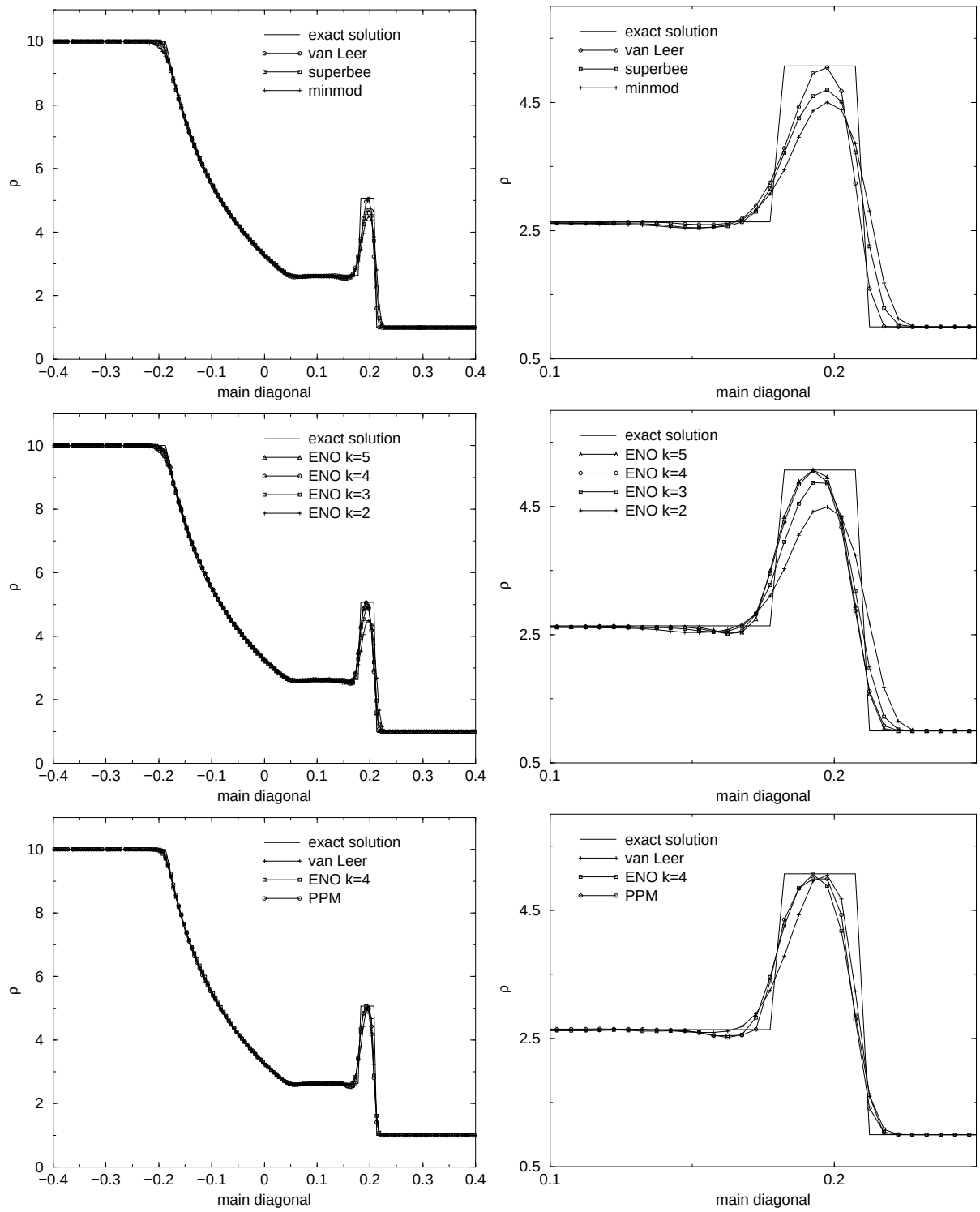

Figure 4.3: Solution of the same Riemann problem as in Fig 4.2, but for the rest-mass density only. The figure shows the comparison of the exact solution for the density with the solution evolved by `Whisky` with different reconstruction methods, indicated with symbols. The right panels are magnifications of the corresponding left panels. The upper panels show a comparison among the TVD methods; the central panels show a comparison among the ENO method with different orders of accuracy; the lower panels show a comparison among our best TVD method (*i.e.* the van Leer one), the ENO method of fourth order and the PPM. All these numerical simulations were obtained with the Roe solver, on a grid with 100^3 points.

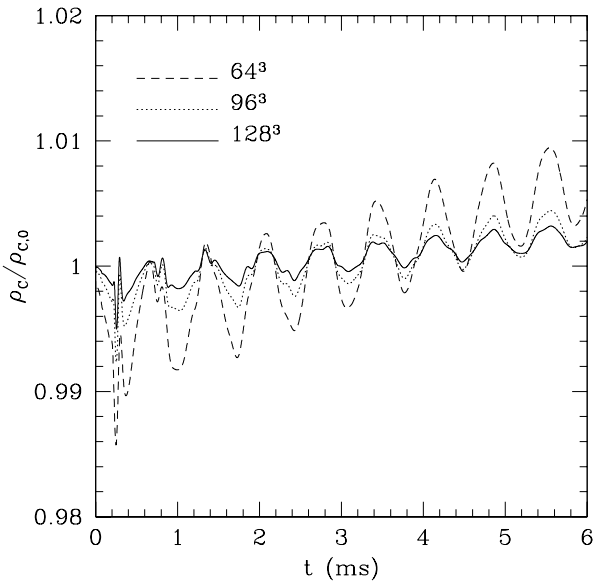

Figure 4.4: Central rest-mass density, normalized to the initial value, in a stable TOV star with rest mass $M_0 = 1.4\ M_\odot$ and polytropic exponent $\Gamma = 2$. Different lines refer to different resolutions and all were obtained with a PPM reconstruction and the Marquina flux formula.

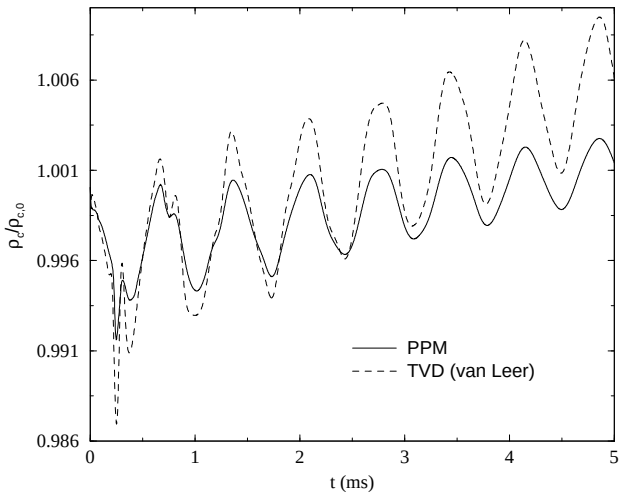

Figure 4.5: Central rest-mass density, normalized to the initial value, in a stable TOV star with rest mass $M_0 = 1.4\ M_\odot$ and polytropic exponent $\Gamma = 2$, evolved with the Marquina flux formula on a grid with 64^3 points. The figure shows the comparison between the PPM and the van Leer reconstruction methods.

growth converges to zero with increasing resolution.

Using the initial data described above, we have compared the evolutions obtained with a PPM and a TVD reconstruction. Fig. 4.5 shows the central density oscillations obtained with the PPM reconstruction and those obtained with the best of the TVD methods (*i.e.* the van Leer slope limiter) and highlights how the PPM reconstruction scheme has proved to be more accurate than the TVD one. Note that the PPM reconstruction is more effective in reducing both the initial truncation error (as shown by the smaller amplitudes in the oscillations) and the secular error (as shown by the smaller growth rate).

The convergence properties of the code are also shown in the growth of the Hamiltonian constraint violation. Fig. 4.6 shows that almost second-order convergence is achieved. Note that the convergence

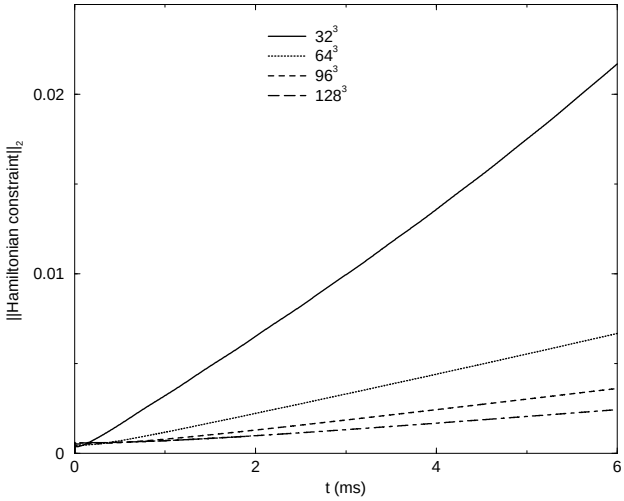

Figure 4.6: The L_2 norm of the Hamiltonian constraint violation for the same evolutions as in Fig. 4.4.

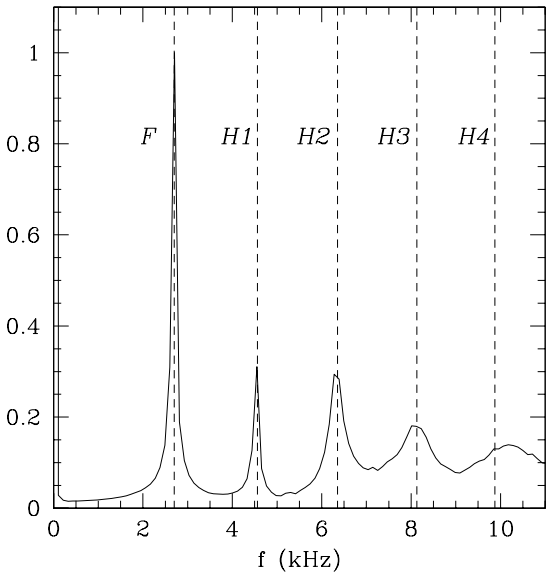

Figure 4.7: Power-spectrum density of the central mass-density evolution of an $M_0 = 1.4\,M_\odot$, $\Gamma = 2$ stable TOV star performed on a grid with 128^3 points. The units of the vertical axis are arbitrary.

rate is not exactly second order but slightly smaller, because the reconstruction schemes are only first-order accurate at local extrema (*i.e.* the centre and the surface of the star) thus increasing the overall truncation error [7].

In order to further investigate the accuracy of our implementation of the hydrodynamics equations, we have suppressed the spacetime evolution and solved only the hydrodynamics equations in the fixed spacetime of the initial TOV solution. This approximation is referred to as the *Cowling approximation* and is widely used in perturbative studies of oscillating stars, in which the perturbation in the background metric (or in the gravitational potential for Newtonian studies) are neglected. In this case, in addition to the convergence rate, we have also compared the frequency spectrum of the numerically induced oscillation with the results obtained by an independent 2-dimensional code [104] and with perturbative analyses.

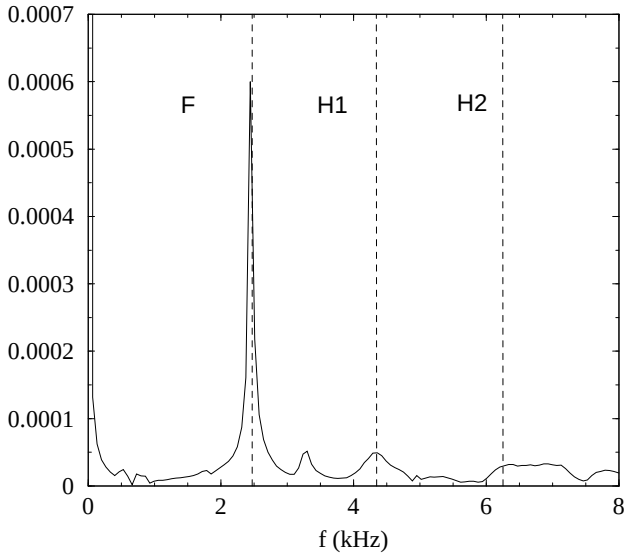

Figure 4.8: Power-spectrum density of the central mass-density evolution of an $M = 1.4\,M_{\odot}$, $\Gamma = 2$ stable uniformly-rotating star with axes ratio equal to 0.65, *i.e.* near the mass-shedding limit. The simulation was performed on a grid with 128^3 points. The units of the vertical axis are arbitrary.

In Fig. 4.7 we show a comparison between the two codes reporting the power-spectrum density of the central density oscillations computed with the `Whisky` code and the corresponding frequencies as obtained with perturbative techniques and with the 2-dimensional code. Clearly the agreement is very good with an error below 1% in the fundamental frequency. The fact that the frequencies computed with the code coincide with the physical eigenfrequencies calculated through perturbative analysis is a convincing evidence of consistency. Stated differently, it shows that `Whisky` is not simply providing a second-order solution of a set of PDEs, but it is actually providing a consistent solution of the Einstein field equations in a non-vacuum spacetime. Furthermore, it also shows that we can use our code to study the physical properties of normal modes of oscillation of relativistic stars; as we will discuss below, this is of great importance in the case of rapidly rotating stars.

The last test performed in the linear regime consists in the evolution of stationary solutions of rapidly uniformly-rotating stars, with angular velocity up to 95% of the allowed mass-shedding limit for uniformly rotating stars. The initial data used for these stars are the same as those used in our studies of collapse of rotating stars, which we will discuss in Chapter 5. A number of small improvements on the boundary and gauge conditions have allowed us to extend considerably the timescale of our evolutions of stable rapidly rotating stars, which can now be evolved for about 10 ms, a timescale which is three times larger than the one reported in [100]. As in previous tests, the Hamiltonian constraint shows a convergence rate of nearly second order everywhere, except at the surface and the center of the star.

In analogy with the non-rotating case, the truncation error triggers quasi-radial oscillations in the star. Such pulsations converge to zero with increasing resolution. Determining the frequency spectrum of fully-relativistic and rapidly-rotating stars is an important achievement, allowing the investigation of a parameter space which is astrophysically relevant but too difficult to treat with current perturbative techniques [232]. As we show in Fig. 4.8, the fundamental frequency of the oscillations is well determined also in this case, while its overtones are not well resolved at this resolution. Furthermore, we notice a small but distinguishable peak between the fundamental frequency and its first overtone, which has not been firmly interpreted and could be associated to p-mode oscillations.

Finally, we have considered tests of the non-linear dynamics of isolated spherical relativistic stars

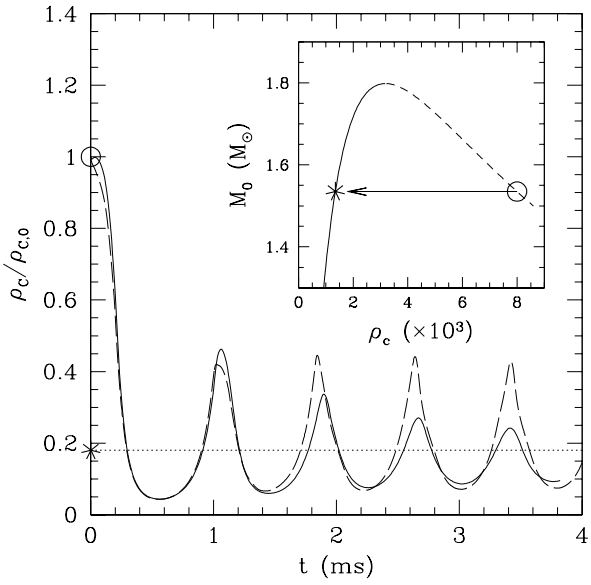

Figure 4.9: Normalized central mass-density evolution of an $M_0 = 1.4\ M_\odot$, $\Gamma = 2$ unstable TOV star performed on a grid with 96^3 points.

(analogous tests could be carried out for rotating stars). To this purpose we have constructed TOV solutions that are placed on the unstable branch of the equilibrium configurations (see inset of Fig. 4.9). The truncation error in the initial data for a TOV solution is sufficient to move the model to a different configuration and in `Whisky` this leads to a rapid migration toward a stable configuration of equal rest mass but smaller central density. Such a violent expansion produces large amplitude oscillations (that are essentially radial) in the star that are either at constant amplitude, if the polytropic EoS (4.2.1) is used, or are damped through shock heating, if the ideal-fluid EoS (4.2.3) is used and the equation for τ is evolved in time. A summary of this dynamics is presented in Fig. 4.9, which shows the time series of the normalized central density for a TOV solution. Note that the asymptotic central density tends to a value corresponding to a rest mass slightly smaller than the initial one (straight dotted line). This is the energy loss due to the internal dissipation.

Note that the migration to the stable branch is only one of the two possible evolutions of the unstable configurations. The other is, of course, that leading to a black-hole formation, in which the star moves to increasingly larger density configurations. This requires the addition of a small perturbation in the pressure and will be discussed in detail in the following chapter.

4.4.3 Other tests

Several other tests on specific parts of the code were performed in the initial stages of its development in order to check the possible presence of implementation errors. It would be uninteresting even to report their list.

Instead, another important test has recently been performed to check the excision algorithm. It consists in comparing the exact and numerically evolved Michel solution [159], *i.e.* a steady-state spherically-symmetric solution for accretion onto a compact object, a Schwarzschild black hole in this case. This solution has been used to validate axisymmetric hydrodynamical excision also by other groups [182, 101]. We do not report the results of these tests here, because we were not directly involved with them, although they were obtained by using the code we have developed. We just point out that also

these tests were very successful [117]. We also wish to underline that, instead, we directly performed all the other tests, both those here reported and those not reported.

4.5 Further code development

Several people are constantly working on further development and improvement of `Whisky`. New analysis tools are frequently added and the existing ones are refined. In addition to these, far-reaching development is also under way; this involves the extension of the code to incorporate the evolution of magnetic fields (magneto-hydrodynamics) and of non-ideal fluids, with the inclusion of physically-realistic processes such as radiation transport and viscosity. The possibility to use tabulated EoSs has been recently implemented, even though it is not yet computationally efficient.

Chapter 5

Collapse of uniformly-rotating neutron stars

After outlining the structure of the implementation of our code and after illustrating the physical and numerical theory upon which it is based, we now come to the first extended application of `Whisky` in the study of a physical problem. In the present chapter we report the application of `Whisky` to the study of gravitational collapse of rotating NS models.

5.1 Description of the problem and previous work

The numerical investigation of gravitational collapse of rotating stellar configurations leading to black-hole formation is a long standing problem in numerical relativity. However, it is through numerical simulations in general relativity that one can hope to improve our knowledge of fundamental aspects of Einstein's theory such as the cosmic-censorship hypothesis and black-hole no-hair theorems, along with that of current open issues in relativistic-astrophysics research, such as the mechanism responsible for γ-ray bursts. Furthermore, numerical simulations of stellar gravitational collapse to black holes provide a unique mean of computing the gravitational waveforms emitted in such events, believed to be among the most important sources of detectable gravitational radiation.

However, the modelling of black-hole spacetimes with collapsing matter sources in multidimensions is one of the most formidable efforts of numerical relativity. This is due, on one hand, to the inherent difficulties and complexities of the system of equations which is to be integrated, the Einstein field equations coupled to the general-relativistic hydrodynamics equations, and, on the other hand, to the immense computational resources needed to integrate the equations in the case of 3-dimensional evolutions. In addition to the practical difficulties encountered in the accurate treatment of the hydrodynamics involved in the gravitational collapse of a rotating NS to a black hole, the precise numerical computation of the gravitational radiation emitted in the process is particularly challenging as the energy released in gravitational waves is much smaller than the total rest-mass energy of the system.

The presence of rotation in the collapsing stellar models requires multidimensional investigations, either in axisymmetry or in full 3 dimensions. The numerical investigations of black-hole formation (beyond spherical symmetry) started in the early 1980's with the pioneering work of Nakamura [174]. He adopted the (2+1)+1 formulation of the Einstein equations in cylindrical coordinates and introduced regularity conditions to avoid divergences at coordinate singularities. Nakamura used a "hypergeometric" slicing condition which prevents the grid points from reaching the singularity when a black hole forms. The simulations could track the evolution of the collapse of a $10M_{\odot}$ "core" of a massive star with dif-

ferent amounts of rotational energy, up to the formation of a rotating black hole. However, the numerical scheme employed was not accurate enough to compute the emitted gravitational radiation. In subsequent works, Nakamura [171] (see also [173]) considered a configuration consisting of a NS with an accreting envelope, which was thought to mimic mass fall-back in a supernova explosion. Rotation and infall velocity were added to such a configuration, simulating an evolution dependent on the prescribed rotation rates and rotation laws.

Later on, in a series of articles [38, 229, 230, 231], Bardeen, Stark and Piran studied the collapse of rotating relativistic polytropes to black holes, succeeding in computing the associated gravitational radiation. The gravitational-field and hydrodynamics equations were formulated using the $3+1$ formalism in two spatial dimensions, using the radial gauge and a mixture of singularity-avoiding polar and maximal slicings. The initial model was a spherically-symmetric relativistic polytrope of mass M in equilibrium. The gravitational collapse was induced by lowering the pressure in the initial model by a prescribed (and very large: 60-99%) fraction and by simultaneously adding an angular-momentum distribution approximating rigid-body rotation. Their simulations showed that Kerr black-hole formation occurs only for angular momenta less than a critical value. Furthermore, the energy ΔE carried away through gravitational waves from the collapse to a Kerr black hole was found to be $\Delta E/Mc^2 < 7 \times 10^{-4}$, the shape of the waveforms being nearly independent of the details of the collapse (*cf.* Fig. 5.18).

The axisymmetric codes employed in the aforementioned works adopted curvilinear coordinate systems which may lead to long-term numerical instabilities at coordinate singularities. These coordinate problems are not actually serious in 2-dimensional simulations, but they have deterred researchers from building 3-dimensional codes in spherical coordinates. Recently, a general-purpose method (called "cartoon"), has been proposed to enforce axisymmetry in numerical codes based on Cartesian coordinates and which does not suffer from stability problems at coordinate singularities [7]. It should be noted, however, that the stability properties of the cartoon method are not fully understood yet, as discussed by [105]. Using this method, Shibata [211] investigated the effects of rotation on the criterion for prompt adiabatic collapse of rigidly and differentially-rotating polytropes to a black hole, finding that the criterion for black-hole formation depends strongly on the amount of angular momentum, but only weakly on its (initial) distribution. The effects of shock heating when using a non-isentropic EoS are important in preventing prompt collapse to black holes in the case of large rotation rates.

More recently, Shibata [212, 213] has performed axisymmetric simulations of the collapse of rotating supramassive NSs to black holes for a wide range of polytropic EoSs and with an improved implementation of the hydrodynamics solver (based on approximate Riemann solvers) with respect to the original implementation used in [211]. Parameterizing the "stiffness" of the EoS through the polytropic index N, the final state of the collapse is a Kerr black hole without any noticeable disc formation, when the polytropic index N is in the range $2/3 \leq N \leq 2$. Based on the specific angular-momentum distribution in the initial star, Shibata has estimated an upper limit to the mass of a possible disc as being less than 10^{-3} of the initial stellar mass [213]. Unfortunately, such small masses cannot currently be confirmed with the presently-available resolutions in 3-dimensional simulations on uniform grids.

3-dimensional, fully-relativistic simulations of the collapse of supramassive uniformly-rotating NSs to rotating black holes were presented in [214]. The simulations focused on $N = 1$ polytropes and showed no evidence of massive disc formation or outflows. These results are in agreement with those obtained in axisymmetry [212, 213] and with the new simulations reported by [89] (both in axisymmetry and in 3 dimensions) which show that for a rapidly-rotating polytrope with $J/M^2 < 0.9$ (J being the angular momentum) all the mass falls promptly into the black hole, with no disc being formed. Hence, all existing simulations agree that massive disc formation from the collapse of NSs, if at all possible,

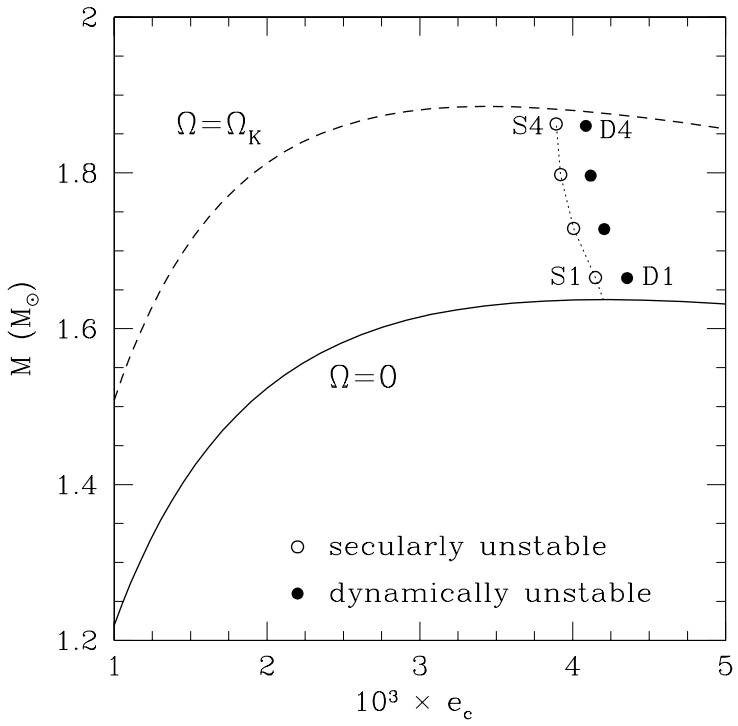

Figure 5.1: Gravitational mass shown as a function of the central energy density for equilibrium models constructed with the polytropic EoS, for $\Gamma = 2$ and polytropic constant $K_{\rm ID} = 100$. The solid, dashed and dotted lines correspond to the sequence of non-rotating models, the sequence of models rotating at the mass-shedding limit and the sequence of models that are at the onset of the secular instability to axisymmetric perturbations. Also shown are the secularly (open circles) and dynamically-unstable (filled circles) initial models used in the collapse simulations.

requires differential rotation, at least for a polytropic EoS with $1 \leq N \leq 2$.

Here, we present the results of new, fully-3-dimensional simulations of gravitational collapse of uniformly-rotating NSs, both secularly and dynamically unstable, which we model as relativistic polytropes. The angular velocities of our sample of initial models range from slow rotation to the mass-shedding limit. For the first time in such 3-dimensional simulations, we have detected the *event* horizon of the forming black hole and showed that it can be used to achieve a more accurate determination of the black-hole mass and spin than it would be otherwise possible using the area of the *apparent* horizon. We have also considered several other approaches to measure the properties of the newly-formed Kerr black hole, including the recently proposed *isolated* and *dynamical horizon* frameworks. A comparison among the different methods has indicated that the dynamical horizon approach is simple to implement and yields estimates which are accurate and more robust than those of the equivalent methods. Also for the first time in 3-dimensional simulations, we have reliably computed the gravitational waveforms produced during the collapse and we have found a remarkable agreement both with the waveforms calculated by Stark and Piran [229] in axisymmetry and with the frequencies calculated in perturbation theory for NS and black-hole oscillations.

5.2 Initial stellar models

Given equilibrium models of gravitational mass M and central energy density e_c along a sequence of fixed angular momentum or fixed rest mass, the Friedman, Ipser and Sorkin criterion $\partial M/\partial e_c = 0$

[106] can be used to locate the exact onset of the secular instability to axisymmetric collapse. The onset of the dynamical instability to collapse is located near that of the secular instability, but at somewhat larger central energy densities. Unfortunately, no simple criterion exists to determine this location, but the expectation mentioned above has been confirmed by the simulations performed here and by those discussed in [214]. Note that in the absence of viscosity or strong magnetic fields, the star is not constrained to rotate uniformly after the onset of the secular instability and could develop differential rotation. In a realistic NS, however, viscosity or intense magnetic fields are likely to enforce a uniform rotation and cause the star to collapse soon after it passes the secular-instability limit.

The initial data for our simulations are constructed using the 2-dimensional numerical code of Stergioulas [234], that computes accurate stationary equilibrium solutions for axisymmetric and rapidly-rotating relativistic stars in polar coordinates. The data are then transformed to Cartesian coordinates using standard coordinate transformations. The same initial data routines have been used in previous 3-dimensional simulations [10, 100, 233] and details on the accuracy of the code can be found in [232]. Our calculations are starting from initially-axisymmetric stellar models but are performed in full 3 dimensions to allow for departures from the initial axial symmetry.

For simplicity, we have focused on initial models constructed with the polytropic EoS (4.2.1), choosing $\Gamma = 2$ and polytropic constant $K_{\rm ID} = 100$ to produce stellar models that are, at least qualitatively, representative of what is expected from observations of NSs. More specifically, we have selected four models located on the line defining the onset of the secular instability and having polar-to-equatorial axes ratio of roughly 0.95, 0.85, 0.75 and 0.65 (these models are indicated as S1–S4, respectively, in Fig.5.1). Four additional models were defined by increasing the central energy density of the secularly unstable models by 5%, keeping the same axis ratio. These models (indicated as D1–D4 in Fig.5.1) were expected and have been found to be dynamically unstable.

Fig. 5.1 shows the gravitational mass as a function of the central energy density for equilibrium models constructed with the chosen polytropic EoS. The solid, dashed and dotted lines correspond respectively to the sequence of non-rotating models, the sequence of models rotating at the mass-shedding limit and the sequence of models that are at the onset of the secular instability to axisymmetric perturbations. Furthermore, the secularly and dynamically-unstable initial models used in the collapse simulations are shown as open and filled circles, respectively.

Table 5.1 summarizes the main equilibrium properties of the initial models. The circumferential equatorial radius is denoted as R_e, while Ω is the angular velocity with respect to an inertial observer at infinity, and r_p/r_e is the ratio of the polar to equatorial coordinate radii. The height of the corotating innermost stable circular orbit (ISCO) is defined as $h_+ = R_+ - R_e$, where R_+ is the circumferential radius for a corotating ISCO observer. Note that in those models for which a value of h_+ is not reported, all circular geodesic orbits outside the stellar surface are stable. Other quantities shown are the central rest-mass density ρ_c, the angular momentum J and the ratio of rotational kinetic energy to gravitational binding energy $T/|W|$.

5.3 Dynamics of the matter

All the simulations reported in this and the next section have been computed using a uniformly-spaced computational grid for which symmetry conditions are imposed across the equatorial plane. Several different spatial resolutions have been used to check convergence and improve the accuracy of the results, with the finest resolution having been obtained using $288^2 \times 144$ cells. While the precise numbers depend on the resolution used and on the model simulated, as a general rule we have used $\sim 50\%$

Table 5.1: Equilibrium properties of the initial stellar models. The different columns refer respectively to: the central rest-mass density ρ_c, the ratio of the polar to equatorial coordinate radii r_p/r_e, the gravitational mass M, the circumferential equatorial radius R_e, the angular velocity Ω, the ratio J/M^2 where J is the angular momentum, the ratio of rotational kinetic energy to gravitational binding energy $T/|W|$ and the "height" of the corotating ISCO h_+. All models have been computed with a polytropic EoS with $K_{\rm ID} = 100$ and $\Gamma = 2$.

Model	$\rho_c^{\dagger}$	r_p/r_e	M	R_e	$\Omega^{\ddagger}$	J/M^2	$T/\|W\|^{\ddagger}$	h_+
S1	3.154	0.95	1.666	7.82	1.69	0.207	1.16	1.18
S2	3.066	0.85	1.729	8.30	2.83	0.363	3.53	0.51
S3	3.013	0.75	1.798	8.90	3.49	0.470	5.82	0.04
S4	2.995	0.65	1.863	9.76	3.88	0.545	7.72	–
D1	3.280	0.95	1.665	7.74	1.73	0.206	1.16	1.26
D2	3.189	0.85	1.728	8.21	2.88	0.362	3.52	0.58
D3	3.134	0.75	1.797	8.80	3.55	0.468	5.79	0.10
D4	3.116	0.65	1.861	9.65	3.95	0.543	7.67	–

† $\times 10^{-3}$
‡ $\times 10^{-2}$

of the grid points in the x direction to cover the star in the case D1 and $\sim 66\%$ of the grid points in the x direction to cover the star in D4. As a result, the outer boundary is set at ~ 2.0 times the stellar equatorial radius for D1 and at ~ 1.4 times the stellar equatorial radius for D4.

The hydrodynamics equations have been solved employing the Marquina flux formula and the PPM reconstruction. The "1+log" slicing condition and the "Gamma-driver" shift conditions [11] have been used. The time update of all the equations has been performed using the ICN evolution scheme. Finally, both polytropic and ideal-fluid EoSs have been used, although no significant difference has been found in the dynamics between the two cases. This is most probably related to the small J/M^2 of the uniformly-rotating initial models considered here. This implies a relatively rapid collapse and as a result we do not see any shocks form (see below for a more complete discussion). Hereafter, we will restrict our attention to a polytropic EoS only.

Given an initial stellar model which is dynamically unstable, simple round-off errors would be sufficient to produce an evolution leading either to the gravitational collapse to a black hole or to the migration to the stable branch of the equilibrium configurations [100] (*cf.* Section 4.4.2). In general, however, leaving the onset of the dynamical instability to the cumulative effect of the numerical truncation error is not a good idea, since this produces instability-growth times that are dependent on the grid-resolution used.

For this reason, we induce the collapse by slightly reducing the pressure in the initial configuration. This is done uniformly throughout the star by using a polytropic constant for the evolution K that is smaller than the one used to calculate the initial data $K_{\rm ID}$. The accuracy of the code is such that only very small perturbations are sufficient to produce the collapse and we have usually adopted $(K_{\rm ID} - K)/K_{\rm ID} \lesssim 2\%$.

After imposing the pressure reduction, the Hamiltonian and momentum constraints are solved with the York procedure [262] to enforce that the constraint violation is at the truncation-error level. We name this procedure as the solution of the initial-value problem (IVP), which ensures that second-order convergence holds from the start of the simulations, as shown in Fig. 5.2 for the L_2 norm of the Hamiltonian constraint. Note that a strict second-order convergence is lost when the excision is introduced: although the code remains convergent at a lower rate, while the norm of the Hamiltonian constraint starts to grow

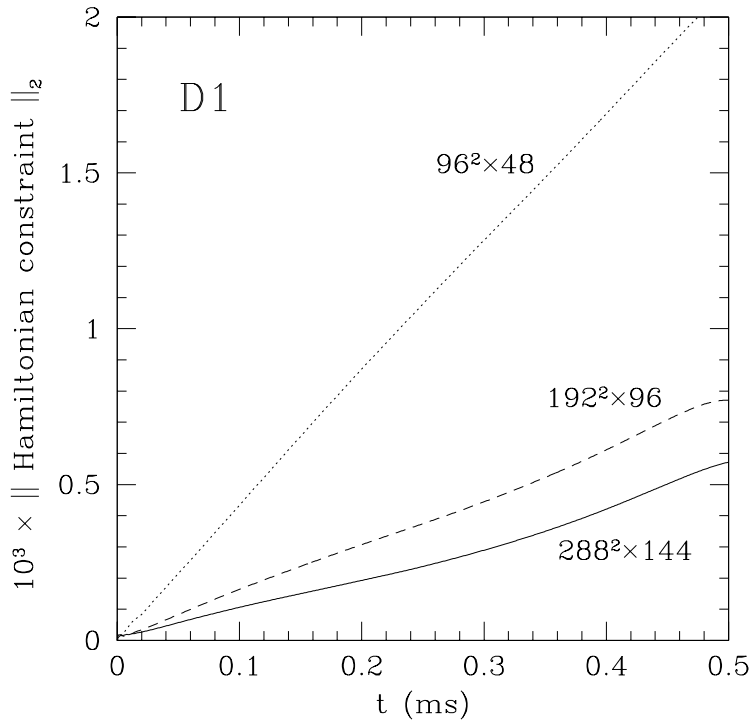

Figure 5.2: L_2 norm of the Hamiltonian constraint violation for the initial model D1 shown as a function of time. The different lines refer to different grid resolutions, but in all cases the IVP was solved after the pressure was uniformly decreased to trigger the collapse.

exponentially (this is not shown in Fig. 5.2). We are presently investigating the origin of the deterioration of the convergence rate at the time of excision, although this is somewhat unavoidable when excising a spherical region in a Cartesian rectangular grid in the course of the evolution.

If, on the other hand, the IVP is not solved after the pressure change, the constraints violation increases twice as fast and converges to second order only after an initial period of about $20\ M \sim 0.17$ ms. To assess the validity of our procedure to trigger the collapse, we also perform the pressure change after the evolution has started and without solving the IVP. In this case, and after the system has recovered from the perturbation, the violation of the constraints is only a few percent different from the case in which the IVP is solved. Furthermore, other dynamical features of the collapse, such as the instant at which the apparent horizon is first formed (see Section 5.4 for a detailed discussion), do not vary by more than 1%.

The dynamics resulting from the collapse of models S1–S4 and D1–D4 are extremely similar and no qualitative differences have been detected. However, as one would expect, models D1–D4 collapse more rapidly to a black hole (the formation of the apparent horizon appears about 5% earlier in coordinate time), are computationally less expensive and therefore better suited for a detailed investigation. As a result, in what follows we will restrict our discussion to the collapse of the dynamically-unstable models and distinguish the dynamics of case D1, in Section 5.3.1, from that of model D4, in Section 5.3.2.

5.3.1 Slowly-rotating stellar models

We start by discussing the dynamics of the matter by looking at the evolution of the initial stellar model D1 which is slowly-rotating (thus almost spherical, with $r_p/r_e = 0.95$) and has the largest central

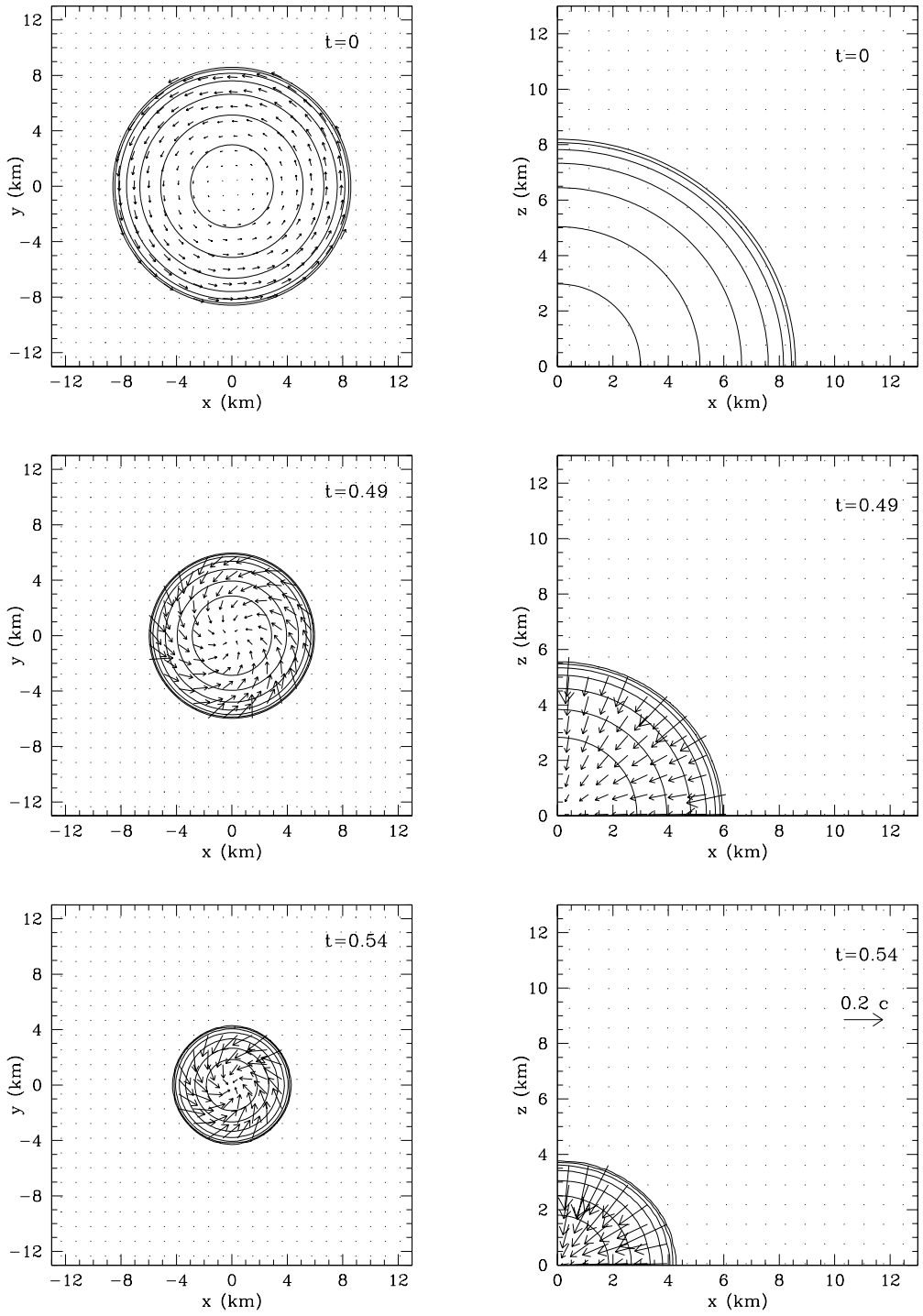

Figure 5.3: Collapse sequence for the slowly-rotating model D1. Different panels refer to different snapshots during the collapse and show the isocontours of the rest-mass density and the velocity field in the (x, y) plane (left column) and in the (x, z) plane (right column), respectively. The isobaric surfaces are logarithmically spaced and a reference length for the vector field is shown in the lower right panel for a velocity of $0.2\ c$.

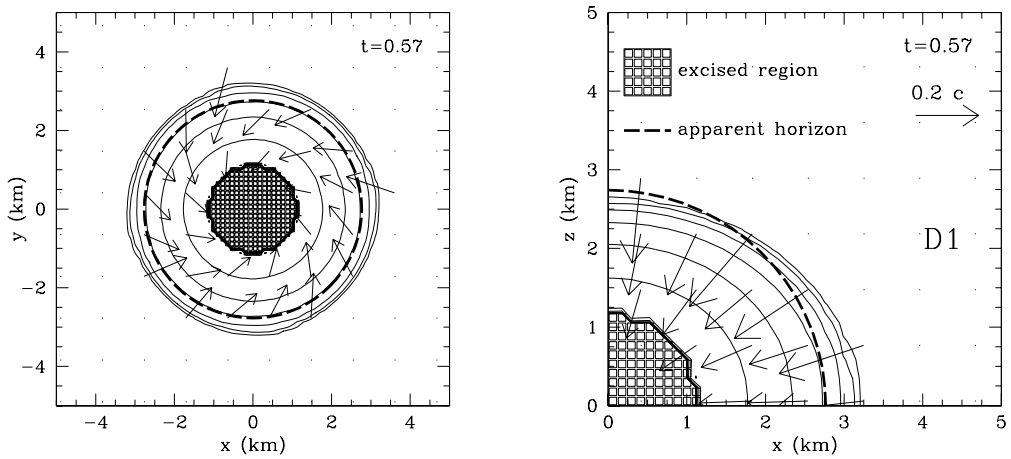

Figure 5.4: Magnified view of the final stages of the collapse of models D1. The representative spherical region where the singularity has formed is excised from the computational domain and is shown as a shaded area. Also shown with a thick dashed line is the coordinate location of the apparent horizon. Note that because of rotation this surface is not a 2-sphere, although the departures are not significant and cannot be appreciated from the Figure (*cf.* Fig. 5.17 for a clearer view).

density (*cf.* Fig. 5.1 and Table 5.1). We show in Figs. 5.3–5.4 some representative snapshots of the evolution of this initial model. The different panels of Fig. 5.3, in particular, refer to the initial and intermediate stages of the collapse and show the isocontours of the rest-mass density and the velocity field in the (x, y) plane (left column) and in the (x, z) plane (right column), respectively. The isobaric surfaces are logarithmically spaced starting from $\rho = 2.0 \times 10^{-5}$ and going up to $\rho = 2.0 \times 10^{-3}$ at the stellar interior. The velocity vector field is expressed in units of c and the length for a velocity of $0.2\ c$ is shown in the lower right panel. The units on both axes refer to coordinate lengths. This sequence has been obtained with a grid of $288^{\ 2} \times 144$ zones but the data for the velocity field has been down-sampled to produce clearer figures and restricted to a single octant in the (x, z) plane to provide a magnified view.

During the collapse of model D1 spherical symmetry is almost preserved; as the star increases its compactness and the matter is compressed to larger pressures, the velocity field acquires a radial component (which was zero initially) that grows to relativistic values. This is clearly shown in the panels at $t = 0.49$ ms and $t = 0.54$ ms, which indicate that the star roughly preserves the ratio of its polar r_p and equatorial r_e radii (see also Fig. 5.7), while radial velocities in excess of $\sim 0.28\ c$ can be easily reached. The behaviour of the angular velocity during this collapse will be analysed in more detail in Section 5.3.3, but we can here anticipate that it does not show appreciable departures from a profile which is uniform inside the star.

Soon after $t = 0.54$ ms, (*i.e.* at $t = 0.546\ \text{ms} = 110.85\ M$ in the high-resolution run), an apparent horizon is found and when this has grown to a sufficiently large area, the portion of the computational domain containing the singularity is excised. The use of an excised region and the removal of the singularity from the computational domain has proven essential for extending the calculations significantly past this point in time. Fig. 5.4 shows a magnified view of the final stages of the collapse of model D1. Indicated as a shaded area is the excised region of the computational domain, which is an approximation of a sphere on the uniform Cartesian grid, *i.e.* a *legosphere*.

Also shown with a thick dashed line is the coordinate location of the apparent horizon and it should be remarked that, because of rotation, this surface is not a coordinate 2-sphere, although the departures are not significant and cannot be appreciated in Fig. 5.4 (see Sect. 5.4 and Table 5.2 for details). Interestingly, at $t = 0.57$ ms, the time which Fig. 5.4 refers to, most of the matter has already fallen within the apparent

horizon and the oblate shape that the stellar matter has assumed at this stage is a first effect of the centrifugal corrections which will become more evident when discussing the collapse of rapidly-rotating models in Section 5.3.2.

The numerical calculations were carried out up to $t \simeq 0.73$ ms $\sim 150\ M$, thus using an excised region in a dynamical spacetime for more than 26% of the total computing time. By this point, all the stellar matter has collapsed well within the event horizon and the Hamiltonian constraint violation has become very large.

Overall, confirming what was already discussed by several authors in the past, the gravitational collapse of the slowly-rotating stellar model D1 takes place in an almost spherical manner and we have found no evidence of shock formation which could prevent the prompt collapse to a black hole, nor appreciable deviations from axisymmetry (*cf.* left panel of Fig. 5.4). It is possible, although not likely, that these qualitative features may be altered when a realistic EoS is used, since in this case shocks may appear, whose heating could stall or prevent the prompt collapse to a black hole. However, more dramatic changes are expected to appear if the initial configurations are chosen to have larger initial angular momenta and in particular when $J/M^2 \gtrsim 1$ [212, 89]. A first anticipation of the important corrections that centrifugal effects could produce is presented in the following Section, where we examine the dynamics of a rapidly-rotating stellar model.

5.3.2 Rapidly-rotating stellar models

We next consider the dynamics of the matter during the collapse of model D4 which, being rapidly rotating, is already rather flattened initially (*i.e.* $r_p/r_e = 0.65$) and has the largest J/M^2 among the dynamically-unstable models (*cf.* Fig. 5.1 and Table 5.1).

As for the slowly-rotating star D1, we show in Figs. 5.5– 5.6 some representative snapshots of the evolution of this rapidly-rotating model. The data has been computed using the same resolution of $288^2 \times 144$ zones and the isocontour levels shown for the rest-mass density are the same used in Fig. 5.3–5.4. It is apparent from the panels of Fig. 5.5 referring to $t = 0$, that model D4 is considerably more oblate than D1, as one would expect for a star rotating at almost the mass-shedding limit.

Note, in particular, how the dynamics is very similar to the one discussed for model D1 up to a time $t \sim 0.49$ ms. However, as the collapse proceeds, significant differences between the two models start to emerge and in the case of model D4 the large angular velocity of the progenitor stellar model produces significant deviations from a spherical infall. Indeed, the parts of the star around the rotation axis that are experiencing smaller centrifugal forces collapse more promptly and, as a result, the configuration increases its oblateness.

This is illustrated in Fig. 5.7, which shows the time evolution of the ratio of the polar and equatorial proper radii for all models in Table 5.1 (note that these ratios should not be confused with those in Table 5.1 that refer, instead, to coordinate radii). Each curve in Fig. 5.7 extends until all the matter along the z-axis has fallen inside the apparent horizon of the newly-formed black hole. Clearly, in all cases the oblateness increases as the collapse proceeds and this is much more evident for those stellar models that are rapidly rotating initially. In particular, for the most rapidly-rotating models D4 and S4, the ratio between polar and equatorial proper radii becomes as small as 0.45 at the time when the matter on the rotation axis gets below the apparent horizon.

At about $t = 0.64$ ms (*i.e.* at $t = 0.649$ ms $= 131.76\ M$ in the high-resolution run), the collapse of model D4 produces an apparent horizon. Soon after this, the central regions of the computational domain are excised, preventing the code from crashing and thus allowing for an extended time evolution. The dynamics of the matter at this stage is shown in the lower panels of Fig. 5.5, which refer to $t = 0.67$

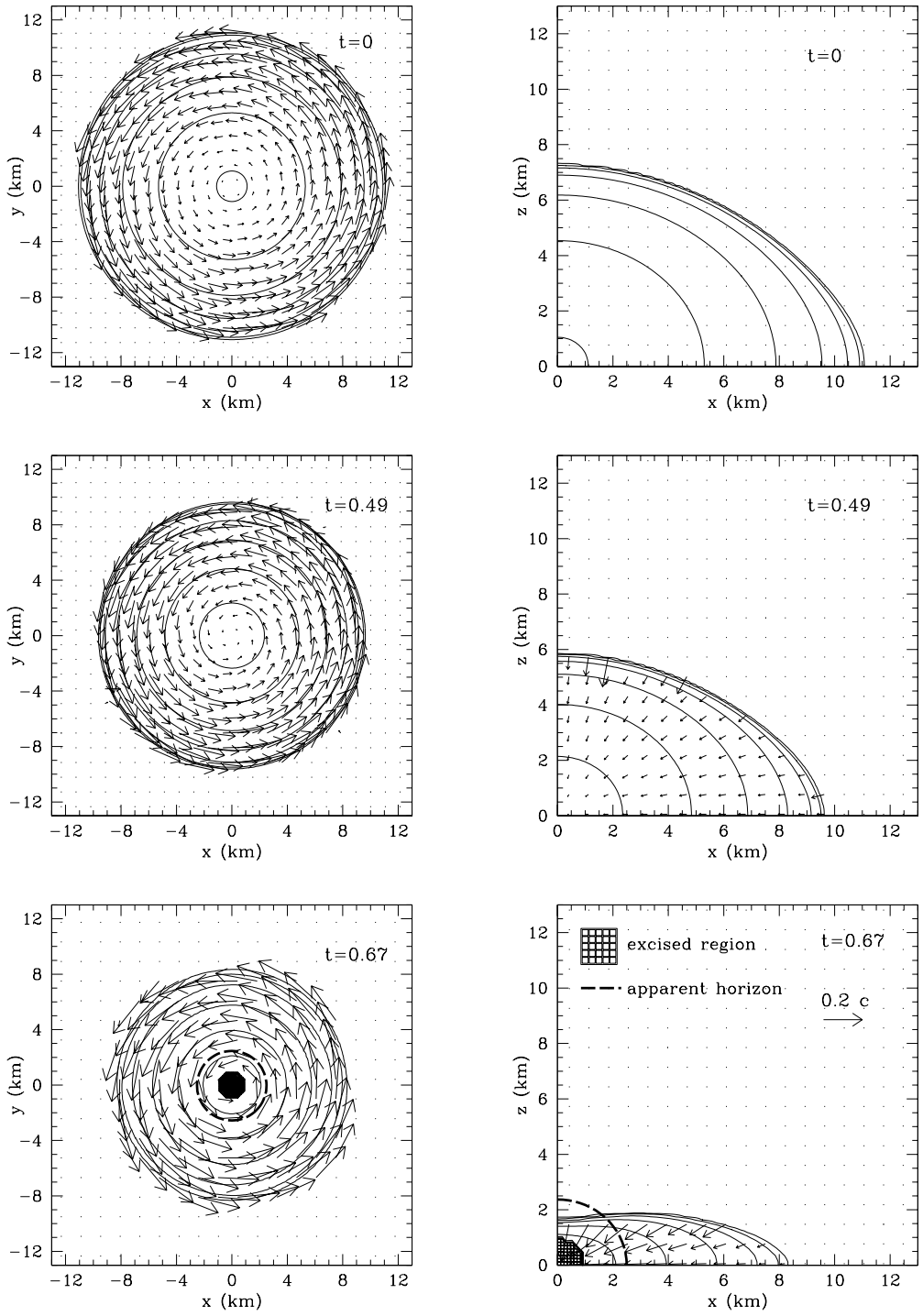

Figure 5.5: Collapse sequence for the rapidly-rotating model D4. The conventions used in these panels are the same as in Fig. 5.3, which can be used for a comparison with the collapse of a slowly-rotating model. Note that the representative spherical region where the singularity has formed is excised from the computational domain and is indicated as a shaded area. Also shown with a thick dashed line is the coordinate location of the apparent horizon.

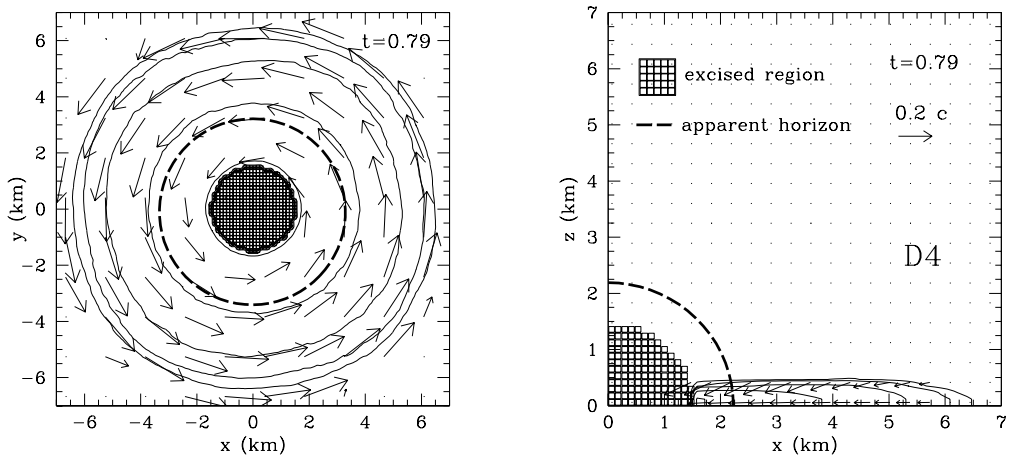

Figure 5.6: Magnified view of the final stages of the collapse of models D4. Note that the representative spherical region where the singularity has formed is excised from the computational domain and this is indicated as a shaded area. Also shown with a thick dashed line is the coordinate location of the apparent horizon. Note that because of the rapid rotation, this surface has significant departures from a 2-sphere (*cf.* Fig. 5.17 for a clearer view).

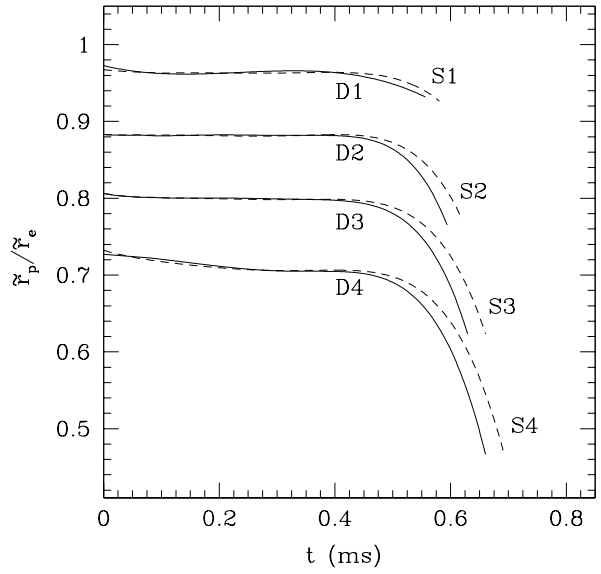

Figure 5.7: Ratio of the proper polar radius to the proper equatorial radius for all the initial models. Each curve ends at the time when, for each simulation, all the matter along the z-axis has fallen below the apparent horizon.

ms and where both the location of the apparent horizon (thick dashed line) and of the effective excised region (shaded area) are shown. By this time the star has flattened considerably, all the matter near the rotation axis has fallen inside the apparent horizon, but a disc of low-density matter has formed near the equatorial plane and is orbiting at very high velocities $\gtrsim 0.2\,c$. This behaviour is the consequence of the large initial angular momentum of the collapsing matter and the appearance of an effective centrifugal barrier preventing a purely radial infall of matter far from the rotational axis. Note, in fact, that the radial velocity at the equator does not increase significantly at the stellar surface between $t \simeq 0.49$ and $t \simeq 0.67$ ms, but that it actually slightly decreases (*cf.* the (x, z) planes in the middle and lower panels of Fig. 5.5). This is the opposite of what happens for the radial velocity of the fluid elements in the stellar interior on

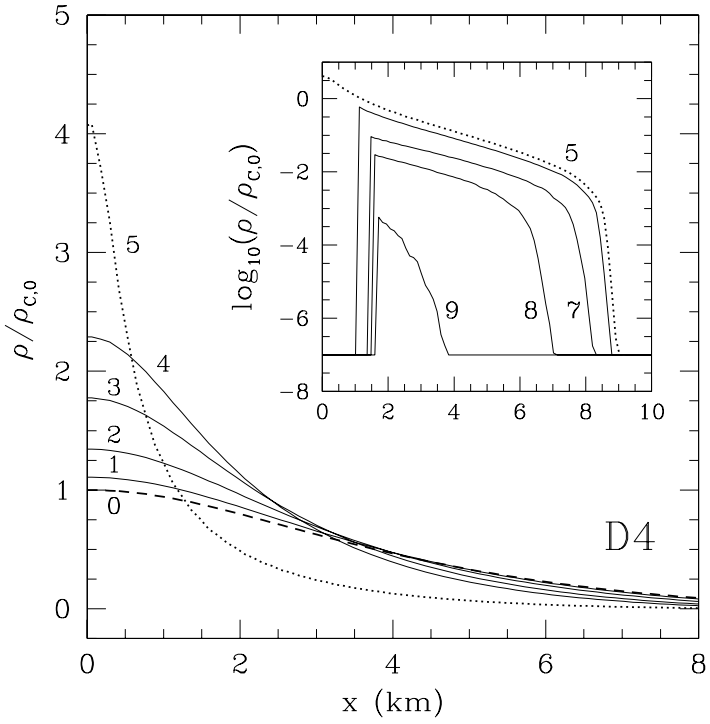

Figure 5.8: Rest-mass density of model D4 normalized to the initial value at the stellar centre. The profiles are measured along the x-axis on the equatorial plane and refer to different times (see main text for details). Line 5, shown as dotted, corresponds to the time when the apparent horizon is first found. The inset shows a magnified view of the final stages of the evolution using a logarithmic scale and also the location of the excised region as it grows in time.

the equatorial plane: it grows also in this time interval. A more detailed discussion of this behaviour will be made in Sect. 5.4.4.

Note that the disc formed outside the apparent horizon is *not* dynamically stable and, in fact, it rapidly accretes onto the newly-formed black hole. This is shown in Fig. 5.6, which offers a magnified view at a later time $t = 0.79$ ms. At this stage the disc is considerably flattened but also has large radial inward velocities which induce it to accrete rapidly onto the black hole. Note that as the area of the apparent horizon increases, so does the excised region, which is allowed to grow accordingly. This can be appreciated by comparing the shaded areas in the lower panels of Fig. 5.5 (referring to $t = 0.67$ ms) with the corresponding ones in Fig. 5.6 (referring to $t = 0.79$ ms).

By a time $t = 0.85$ ms, essentially all (*i.e.* more than 99.9%) of the residual stellar matter has fallen within the trapped surface of the apparent horizon and the black hole thus formed approaches the Kerr solution (see Section 5.4). Note that a simple kinematic explanation can be given for the instability of the disc formed during this oblate collapse and comes from relating the position of the outer edge of the disc when it first forms, with the location of the ISCO of the newly-formed Kerr black hole. Measuring accurately the mass and spin of the black hole reveals, in fact, that the ISCO is located at $x = 11.08$ km, which is always larger than the outer edge of the disc (*cf.* lower panels of Fig. 5.5). Such behaviour is not surprising since we are here dealing with initial models with a moderate J/M^2, that collapse essentially in a dynamical timescale. As a result, simple point-like particle motion in stationary spacetimes is a sufficient approximation to the dynamics.

A more quantitative description of the rest-mass density evolution is presented in Fig. 5.8, where different lines show the profiles of the rest-mass density along the x-axis on the equatorial plane. The

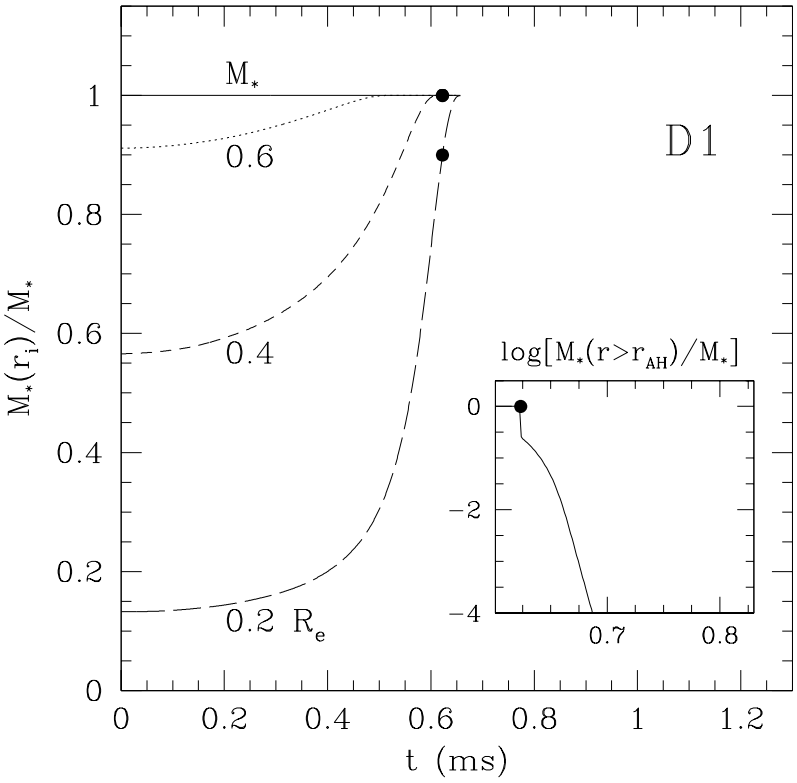

Figure 5.9: Evolution of the mass fraction versus time during the collapse of model D1. The rest mass is measured within 2-spheres of coordinate radii $r_i = 0.2, 0.4$ and 0.6 times the initial stellar equatorial circumferential radius R_e (*cf.* Table 5.1). Marked with filled dots on the different lines are the times at which the apparent horizon is first found (the data refers to a simulation with $96^2 \times 48$ grid zones). The inset shows, on a logarithmic scale, the evolution of the normalized rest mass outside the apparent horizon.

values are normalized to the initial value at the stellar centre, with different labels referring to different times and in particular to $t = 0.0$ (dashed line), $0.25, 0.40, 0.49, 0.54, 0.65, 0.67, 0.74, 0.79$ and 0.89 ms, respectively. Line 5, furthermore, is shown as dotted and refers to the time when the apparent horizon is first formed. After this time, the excised region is cut from the computational domain as shown in the inset of Fig. 5.8, which illustrates the final stages of the evolution. Note that as the matter falls into the black hole, the apparent horizon increases its radius and thus the location of the excised region moves outside. This is clearly shown in the inset. Note also that the rest-mass density does not drop to zero outside the stellar matter but is levelled off to the uniform value of the atmosphere, whose rest-mass density is seven orders of magnitude smaller than the initial central density. It should be remarked that such a tenuous atmosphere has no dynamical impact and does not produce any increase of the mass of the black hole that can be appreciated in our simulations. With such rest-mass densities, in fact, it would take a time $\sim 10^4 M$ to produce a net increase of $\sim 1\%$ in the black-hole mass. Clearly, these systematic errors are well below the truncation errors, even at the highest resolutions.

The simulation ends at $t = 0.91$ ms $\sim 190\ M$, when the rest-mass density is everywhere at the atmosphere level and the violations of the Hamiltonian constraint are large. By this time the evolution has been carried for more than 28% of the total time using a singularity excising region. Also in this case, we do not find evidence of shock formation nor of significant deviations from axisymmetry.

As mentioned in Section 5.1, all simulations to-date agree that no massive and stable discs form for

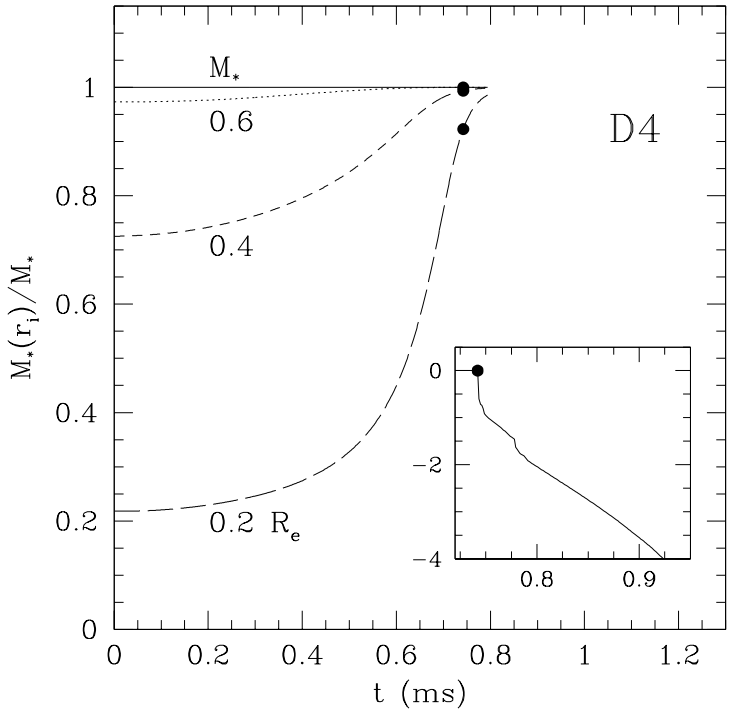

Figure 5.10: Evolution of the mass fraction versus time during the collapse of model D4. The rest mass is measured within 2-spheres of coordinate radii $r_i = 0.2, 0.4$ and 0.6 times the initial stellar equatorial circumferential radius R_e (*cf.* Table 5.1). Marked with filled dots on the different lines are the times at which the apparent horizon is first found (the data refers to a simulation with $96^2 \times 48$ grid zones). The inset shows, on a logarithmic scale, the evolution of the normalized rest mass outside the apparent horizon. Note that this is appreciably non-zero for a rather long time for this model D4.

initial models of NSs that are uniformly rotating and when a polytropic EoS with $1 \leq N \leq 2$ is used. Our results corroborate this view and in turn imply that the collapse of a rapidly-rotating old and cold NS cannot lead to the formation of the central engine believed to operate in a γ-ray burst, namely a rotating black hole surrounded by a centrifugally-supported, self-gravitating torus. Relativistic simulations with more appropriate initial data, accounting in particular for the extended envelope of the massive progenitor star which is essential in the so-called collapsar model of γ-ray bursts [258], will be necessary to shed light on the mechanism responsible for such events.

Convincing evidence has recently emerged [89] that a massive disc can be produced if the stellar models are initially rotating differentially and with initial total angular momenta $J/M^{\,2} \gtrsim 1$, as it may happen for young and hot NSs. In this case, the massive disc could emit intense gravitational radiation either through its oscillations [263] or as a result of the fragmentation produced by non-axisymmetric instabilities [89]. We are presently investigating this possibility and the results of our investigation will be reported in a forthcoming paper.

5.3.3 Disc formation and differential rotation

We now discuss in more detail two interesting properties of the matter dynamics in both slowly and rapidly-rotating models: the evolution of the rest mass outside the apparent horizon and the development of differential rotation during the collapse. In order to monitor the changes of the rest-mass distribution during the collapse we define the rest mass within a 2-sphere of coordinate radius $r_i < R_e$ as (see, for

instance, [209])

$$M_*(r_i) = \int_{r'<r_i} \rho\alpha u^0 \sqrt{\gamma}\, \mathrm{d}^3\mathbf{x}' \,, \tag{5.3.1}$$

where $\mathrm{d}^3\mathbf{x}'$ is the 3-dimensional coordinate volume element. Shown in Fig. 5.9 and 5.10 is the evolution of the rest masses measured within several representative 2-spheres for models D1 and D4, respectively. Different lines refer to different coordinate radii for the 2-spheres (*i.e.* $r_i = 0.2, 0.4$ and $0.6\ R_e$, where R_e is the initial equatorial circumferential radius) and are normalized to the total rest mass within the computational domain M_*, shown as a solid line. Marked instead with filled dots are the values of $M_*(r_i)$ at the times when the apparent horizon is first found; for simplicity, the data shown in Figs. 5.9 and 5.10 refer to a simulation with $96^2 \times 48$ grid zones, but for this quantities higher resolutions have just the effect of shifting the time at which the apparent horizon is first found.

As mentioned before, the excised region is not introduced immediately after the apparent horizon has been found, but only when this has grown to a sufficiently large size to allow for the excision technique to be implemented. When this happens, the inner part of the computational domain is removed and the integrals (5.3.1) are no longer meaningful. As a result, all the curves in Figs. 5.9 and 5.10 are truncated at the time when the excision region is first introduced, which occurs at $t = 0.72$ ms and $t = 0.79$ ms for models D1 and D4, respectively.

A rapid comparison between Fig. 5.9 and 5.10 is sufficient to identify the differences in the rest-mass evolution in slowly and rapidly-rotating models. Firstly, the rest-mass distribution is very different already initially, being more uniform in D1 and more centrally concentrated in D4, as can be appreciated by comparing M_* at $r_i = 0.4R_e$ and $0.6R_e$. Secondly, the rest-mass infall is much faster for the slowly-rotating model D1, while it is more progressive for model D4, as shown by the change in the fractional mass ratio at $r_i = 0.4R_e$. Finally, the amount of matter outside $r_i = 0.4R_e$ at the time when the apparent horizon is found, and which is very close to the amount of matter outside the apparent horizon, is different in the two cases, being essentially zero for model D1 and a few percent for model D4. A clearer view of this is presented in the two insets of Figs. 5.9 and 5.10, which show, on a logarithmic scale, the evolution of the normalized rest masses outside the apparent horizons, *i.e.* $M_*(r > r_{\rm AH})/M_*$, since these first form and as they grow in time. It is interesting to note the different behaviour in this case with a rapid decrease when the rotation rate is small and a much slower one in the case of a rapidly-rotating progenitor (note that the two insets cover the same timescale although they refer to a different time interval).

Two additional comments are worth making. The first one is that M_* effectively includes also the rest mass in the atmosphere but this is always $\lesssim 10^{-4}$ of the total rest mass. The second one is that M_* in Figs. 5.9 and 5.10 does not simply refer to the initial value of the total rest mass but is effectively computed at each step and appears constant in time because of the ability of the code to preserve rest mass. A closer look at the solid curve in Figs. 5.9 and 5.10 reveals, in fact, that M_* varies over time to less than one part in 10^4.

An interesting question to ask at this stage is whether these uniformly-rotating models will develop any degree of differential rotation as the collapse proceeds. Part of the interest in this comes from the fact that NSs are thought to rotate differentially, at least during the initial stages of their life. This is expected to hold both when the NS is produced through a stellar core collapse, in which case the differential rotation may be present already in the stellar progenitor and is then amplified during collapse [82], and when the NS is the end-result of a binary merger of NSs [218]. However, as the NS cools and grows older, dissipative viscous effects or the coupling with non-turbulent magnetic fields are expected to bring the star into uniform rotation (see [208, 73, 147] for a detailed description of this process). It is therefore interesting to investigate whether a degree of differential rotation will be produced also during the final

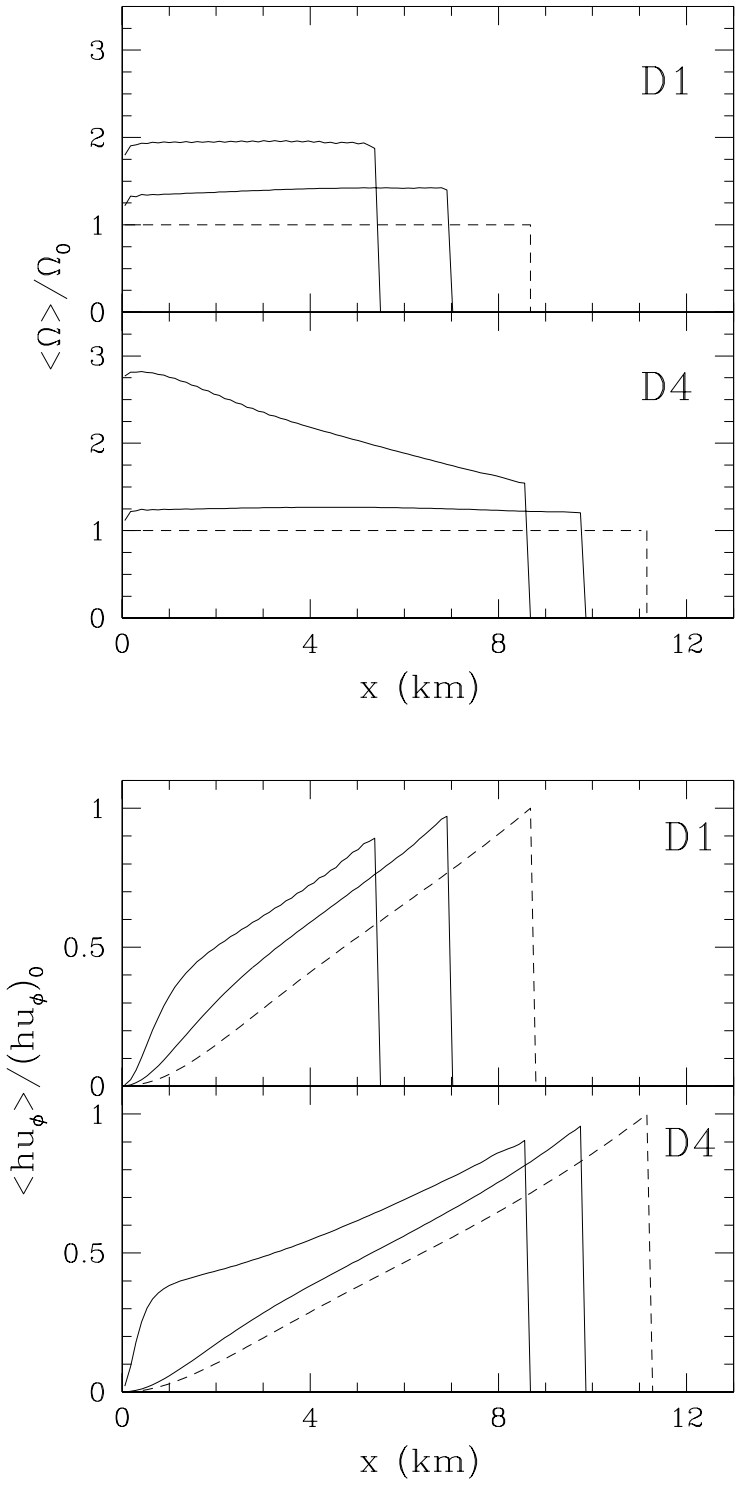

Figure 5.11: Evolution of the averaged angular velocity $\langle\Omega\rangle$ (upper panel) and of the averaged angular momentum per unit mass $\langle hu_\phi\rangle$ (lower panel). Both quantities are measured at the stellar equator, are normalized to the initial value at the stellar surface and refer to both models D1 (upper parts) and D4 (lower parts).

collapse of a uniformly-rotating star to a Kerr black hole. To answer this question we have monitored both the averaged angular velocity $\langle\Omega\rangle$, defined as

$$\langle\Omega\rangle \equiv \frac{1}{2}\left(\left.\frac{u^\phi}{u^t}\right|_{x-\mathrm{axis}} + \left.\frac{u^\phi}{u^t}\right|_{y-\mathrm{axis}}\right) , \tag{5.3.2}$$

and the corresponding averaged angular momentum per unit mass $\langle hu_{\ \phi}\rangle$, which is a conserved quantity along the path lines of fluid elements in an axisymmetric (but not necessarily stationary) spacetime [37]. Note that $u^\phi/u^t = \alpha v^\phi - \beta^\phi$ and the average over the two different directions is here used to compensate the small errors that are produced in the evaluation of these quantities near the axes.

We note that our measure of the differential rotation will depend on the specific slicing chosen. However, for the simulations reported here, the lengthscale of variation of the lapse function at any given time is always larger than the stellar radius at that time, ensuring that the events on the same time slice are also close in proper time. A useful measure of the differential rotation that develops during collapse is the departure from unity of the ratio of the values of Ω at the centre and at the surface of the star on the equatorial plane and it is instructive to compare how this varies in the dynamics of the two models D1 and D4, which have been evolved using the same slicing.

The time evolution of $\langle\Omega\rangle$ and $\langle hu_\phi\rangle$ is presented in the two panels of Fig. 5.11, whose lower parts refer to model D4 and the upper ones to model D1. Both quantities are shown normalized to their initial value at the stellar surface. Let us concentrate on the slowly-rotating model first. The different lines refer to three representative times which are $t = 0.0$ (shown as dashed), $t = 0.45$ and 0.52 ms, respectively. Initially, the angular velocity is, by construction, uniform throughout the star (upper panel) and the corresponding specific angular momentum grows linearly with the distance from the stellar centre (lower panel). As the collapse proceeds and the stellar size decreases, the angular velocity is expected to increase while the angular momentum per unit mass remains constant. This is indeed what happens for model D1, whose specific angular momentum is conserved with an overall error at the stellar surface which is always less than 10% and which decreases with resolution. A similar behaviour is observed also much later in the simulation, when the apparent horizon has been found and the singularity has been excised. Overall, the angular velocity in the collapsing model D1 grows like $\Omega(t) \propto r_e^{-n}$, where $n \simeq 1.5$ and therefore less than it would do in the case of the collapse of a Newtonian, uniform density star (*i.e.* $n = 2$); which is a result of relativistic and rotational effects (see [74]).

A comparison of the lower parts of the two panels in Fig. 5.11 is sufficient to realize that the evolution of the angular velocity is rather different for a rapidly-rotating stellar model. The different lines in this case refer to $t = 0.0, 0.48$ and 0.65 ms, respectively, and it is apparent that a non-negligible degree of differential rotation develops as the collapse proceeds, with a difference of a factor ~ 2 between the angular velocity of the inner and outer parts of the collapsing matter as the apparent horizon first appears. Clearly, this differential rotation is produced very rapidly and will persist only for a very short time before the star is enclosed in a trapped surface.

It is difficult to establish, at this stage, whether the differential rotation generated in this way could produce a phenomenology observable in some astrophysical context and more detailed investigations, in particular of the coupling of this differential rotation with magnetic fields [189, 226], are necessary. Finally, it is worth remarking that while differential rotation develops for model D4 but not for D1, the specific angular momentum is conserved to the same accuracy in both models.

5.4 Dynamics of the horizons

In order to investigate the formation of a black hole in our simulations, we have used horizon finders available through the `Cactus` framework, which compute both the *apparent* horizon and the *event* horizon. The apparent horizon, which is defined as the outermost closed surface on which all outgoing photons normal to the surface have zero expansion, is calculated at every time step and its location is used to set up the excised region inside the horizon. In contrast, the event horizon, which is an expanding null surface composed of photons which will eventually find themselves trapped, is computed *a posteriori*, once the simulation is finished, by reconstructing the full spacetime from the 3-dimensional data each simulation produces. In stationary black-hole systems, where no mass-energy falls into the black hole, the apparent and event horizons coincide, but generally (in dynamical spacetimes) the apparent horizon lies inside the event horizon. We have here used the fast solver of Thornburg [240] to locate the apparent horizon at every time step and the level-set finder of Diener [81] to locate the event horizon after the simulation has been completed and the data produced is post-processed.

In all the considered cases, we have found that the event horizon rapidly grows to its asymptotic value after formation. With a temporal gap of $\sim 10M$ after the formation of the event horizon, the apparent horizon appears and then it rapidly approaches the event horizon, always remaining within it. With the exception of the initial gap, the horizon proper areas as extracted from the apparent and event horizon are very close (see *e.g.*, Fig. 5.17).

5.4.1 Measuring the event-horizon mass

We measure the mass of the newly-formed black hole to estimate the amount of energy that is emitted as gravitational radiation during the collapse. In particular, we do a simple energy accounting, comparing the mass of the black hole with the ADM mass of the spacetime computed by the initial data solver on a compactified grid extending to spatial infinity [234]. This value is slightly different (1% in the worst case) from the one which is instead computed on the finite domain of our computational grid at the initial time and after the constraints are solved. The difference between the two values can be used to define an "error bar" for our measure of the black-hole mass and hence of the energy in gravitational waves (*cf.* Fig. 5.16). Two notes are worth making about this error before we go on to discuss how the black hole is actually measured. Firstly, the difference between the two masses represents the truncation error produced by the finite size of the computational domain and is conceptually distinct from the truncation error introduced by the finite differencing. While the first is assumed to be constant in time, the second in general grows with time (especially after the excision is made) and is monitored through the calculation of the constraint equations. Secondly, this error bar sets a global lower limit on the accuracy of our measure of asymptotic quantities and therefore on the energy lost to gravitational waves during the collapse. No reliable measure of this lost energy can be made below the error bar even if the constraint equations are solved to a larger precision (this will be discussed in more detail in Sect. 5.4.3).

The first and simplest method of approximating the black-hole mass is to note that, for a Kerr (or Schwarzschild) black hole, the mass can be found directly in terms of the event-horizon geometry as

$$M = \frac{C_{\rm eq}}{4\pi}\,, \tag{5.4.3}$$

where $C_{\rm eq} \equiv \int_0^{2\pi} \sqrt{g_{\phi\phi}} d\phi$ is the proper equatorial circumference. Provided there is a natural choice of equatorial plane, it is expected that, as the black hole settles down to Kerr, $C_{\rm eq}$ will tend to the correct value. However, as numerical errors build up at late times it may be impossible to reach this asymptotic regime with sufficient accuracy.

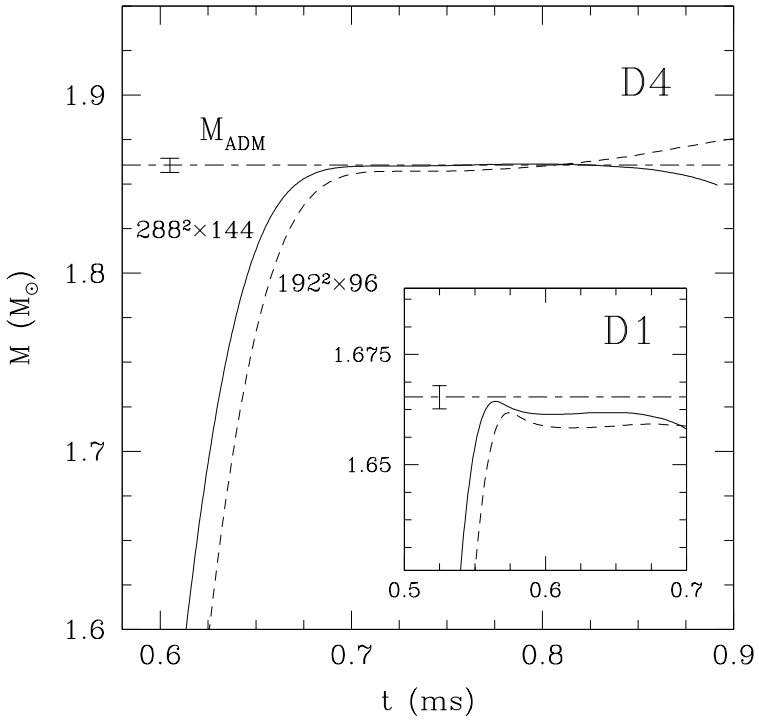

Figure 5.12: Convergence of the measure of the black-hole mass as the resolution is increased. The curves refer to estimates using the event-horizon equatorial circumference [*i.e.* equation (5.4.3)] and have been obtained using $288^2 \times 144$ and $192^2 \times 96$ zones, respectively. Shown in the small inset are the results for model D1, while those for model D4 are in the main panel.

The estimate of M coming from the use of (5.4.3) is presented in Fig. 5.12, which shows the time evolution of the event-horizon equatorial circumference. The two lines refer to two different resolutions ($288^2 \times 144$ and $192^2 \times 96$ zones, respectively) and should be compared with the value of the ADM mass $M_{\rm ADM}$ (indicated with a short-long dashed line) and with the error bars as deduced from the initial data. Shown in the small inset are the results for model D1, while those for model D4 are in the main panel.

Note that if a measure of the event horizon is not available, equation (5.4.3) could be computed using the equatorial circumference of the apparent horizon (this is what was done, for instance, in [89]). Doing so would yield results that are similar to those shown in Fig. 5.12, although with a slightly larger deviation from $M_{\rm ADM}$. This is because we have found the apparent horizon to systematically underestimate the equatorial circumference. In particular, in the high-resolution run for model D4, the differences between the apparent and event-horizon equatorial circumferences are $\lesssim 2$ %.

Clearly, as the equatorial circumference grows, the agreement with the expected ADM mass improves as it does with the use of higher spatial resolution. However, equally evident is that the errors grow as the collapse proceeds and this is due, in part, to the loss of strict second-order convergence at later times, but also to the way the event horizon is found. The level-set approach of [81], in fact, needs initial guesses for the null surface, which converge exponentially to the correct event-horizon surface for decreasing times, hence introduces a systematic error in the calculation of the event horizon at late times. This is shown in Fig. 5.13, which presents the evolution of the event-horizon mass $M = C_{eq}/4\pi$ for models D1 and D4. Different lines refer to the different initial guesses and are numbered "0", "1" and "2", respectively (note that for the curves shown in Fig. 5.12 the initial guesses "0" and "1" were used for cases D4 and D1, respectively).

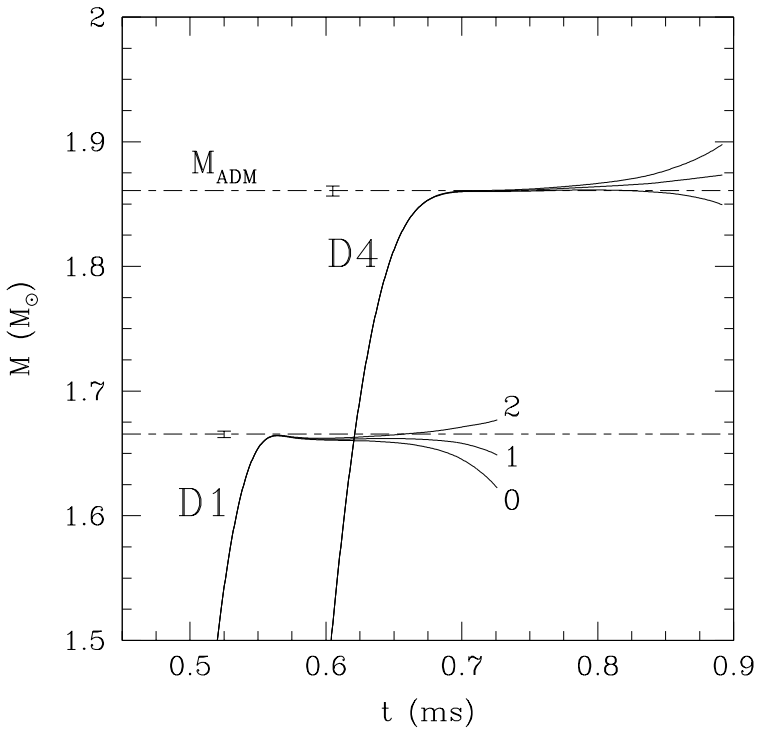

Figure 5.13: Evolution of the event-horizon mass $M = C_{eq}/4\pi$ for models D1 and D4. Different lines refer to the different initial guesses for the null surface and are numbered 0, 1 and 2. Note that they converge exponentially to the correct event-horizon surface for decreasing times.

5.4.2 Measuring the angular momentum of the black hole

A major difficulty in an accurate measurement of M lies in the calculation of its non-irreducible part, *i.e.* in the part that is proportional to the black-hole angular momentum J. We now discuss a number of different ways to calculate J from the present simulations; these measurements will then be used to obtain alternative estimates of M in Section 5.4.3.

Measuring J from the horizon distortion

In a series of papers studying the dynamics of distorted black-hole spacetimes, it was shown that the horizon geometry provides a useful measure of the black-hole properties both in vacuum [17, 19, 18, 59] and when the black holes are accreting matter axisymmetrically [57]. In particular, the idea is to look at the distortion of the horizon using the ratio of polar and equatorial proper circumferences, $C_r \equiv C_{\rm pol}/C_{\rm eq}$. For a perturbed Kerr black hole this is expected to oscillate around the asymptotic Kerr value with the form of a quasi-normal mode (QNM). By fitting to this mode we extract an estimate of the angular-momentum parameter a/M_{hor} from the relation [58]

$$\frac{a}{M_{hor}} = \sqrt{1-\left(-1.55+2.55C_r\right)^2}\,, \tag{5.4.4}$$

where we have indicated with M_{hor} the black-hole mass as measured from expression (5.4.4), which coincides with M only if the spacetime has become axisymmetric and stationary. The fit through expression (5.4.4) is expected to be accurate to $\sim 2.5\%$ [58].

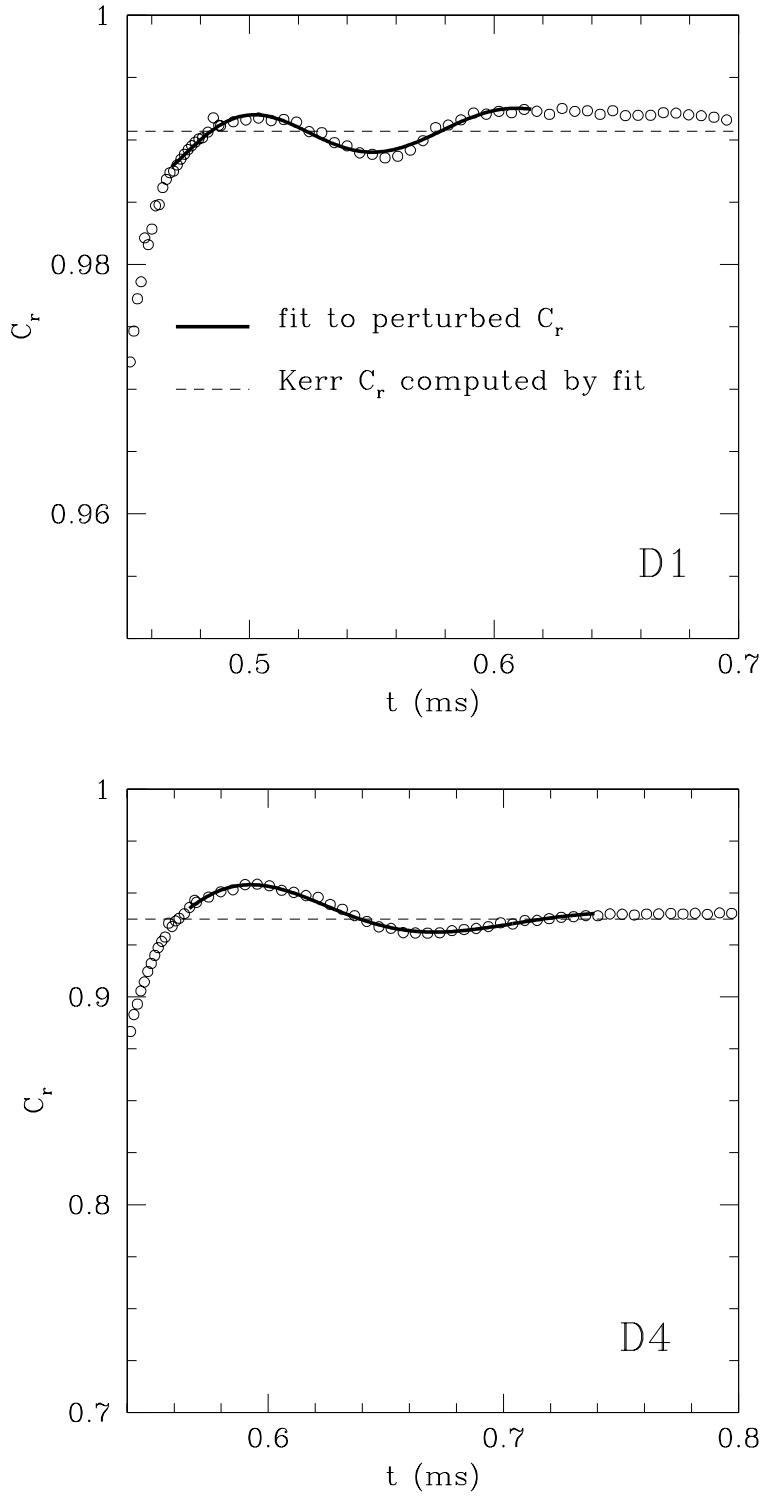

Figure 5.14: Fitting the oblateness of the event horizon to QNMs of a Kerr black hole. The fit is shown with the solid line, while the open circles represent the computed values of C_r. The estimate for C_r of a Kerr black hole having the fitted value of a/M_{hor} is shown with a dashed line.

The fit itself depends on an initial guess for a/M_{hor} and we start from a Schwarzschild black hole and iterate till the desired convergence is reached. This measure is not gauge invariant, although equation (5.4.4) is independent of the spatial coordinates up to the definition of the circumferential planes, but works adequately with the gauges used here. The fit is best performed shortly after black-hole formation as the oscillations are rapidly damped. This minimizes numerical errors but in those cases where matter continues to be accreted, it may lead to inaccurate estimates of the angular momentum.

Examples of the fitting procedure are shown in Fig. 5.14, in which the fit is shown as a solid line, while the open circles represent the computed values of C_r; these are slightly noisy as a result of the interpolation needed by the level-set approach to find points on the horizon 2-surface [81]. The estimate for C_r of a Kerr black hole having the fitted value of a/M_{hor} is shown as a dashed line. Note that the values of $a/M_{hor} = 0.21$ and $a/M_{hor} = 0.54$ are very close to the total J/M^2 of the initial stellar models, *i.e.* 0.2064 and 0.5433 (Table 5.2). This demonstrates that, to within numerical accuracy, the complete angular momentum of the spacetime ends up in the black hole.

Table 5.2: Estimates of the black-hole angular momentum through the oblateness of the event horizon J/M^2. The oscillations in the oblateness of the event horizon, in fact, can be fitted to the normal modes of a Kerr black hole. Note that for each model the measured angular momentum is remarkably close to that of the initial spacetime $(J/M^2)_{\rm ADM}$. Also reported are the initial ADM mass, the value of the equatorial circumference as obtained through the fit $(C_r)_{\rm EH}$, and the corresponding value obtained through the estimated spin parameter $(C_r)_{\rm Kerr}$.

Model	$M_{\rm ADM}$	$(J/M)^2_{\rm ADM}$	$(J/M^2)_{\rm EH}$	$(C_r)_{\rm EH}$	$(C_r)_{\rm Kerr}$
D1	1.6653	0.2064	0.21	0.99	0.9916
D2	1.7281	0.3625	0.36	0.97	0.9734
D3	1.7966	0.4685	0.47	0.95	0.9544
D4	1.8606	0.5433	0.54	0.94	0.9372

Using expression (5.4.4) to estimate the angular momentum J introduces an error, if the black hole has not yet settled to a Kerr solution. Having this in mind, however, it is possible to estimate the angular momentum as

$$J = \left(\frac{a}{M_{hor}}\right) M_{hor} M \simeq \left(\frac{a}{M_{hor}}\right) M^2 \,. \tag{5.4.5}$$

Measuring J with the dynamical-horizon framework

A second method of approximating J and hence measuring M is to use the *isolated* and *dynamical*-horizon frameworks of Ashtekar and collaborators [25, 24, 26, 27, 85]. This assumes the existence of an axisymmetric Killing vector field intrinsic to a marginally-trapped surface such as an apparent horizon. In the case where the marginally trapped surface evolves smoothly so that, for instance, there is a smooth worldtube of apparent horizons, this gives an unambiguous definition of the spin of the black hole and hence of its total mass. If there is an energy flux across the horizon, the isolated-horizon framework needs to be extended to the dynamical-horizon formalism [27, 28].

In practice, our approach to the dynamical horizon framework has been through the use of a code by Schnetter which implements the algorithm of [85] to calculate the horizon quantities. The advantage of the dynamical horizon framework is that it gives a measure of mass and angular momentum which is accurately computed locally, without a global reconstruction of the spacetime. One possible disadvantage is that the horizon itself is required to be (close to) axisymmetric; so in case it deviates largely from axial symmetry, no information can be found. However, because arbitrarily-large distortions are allowed as

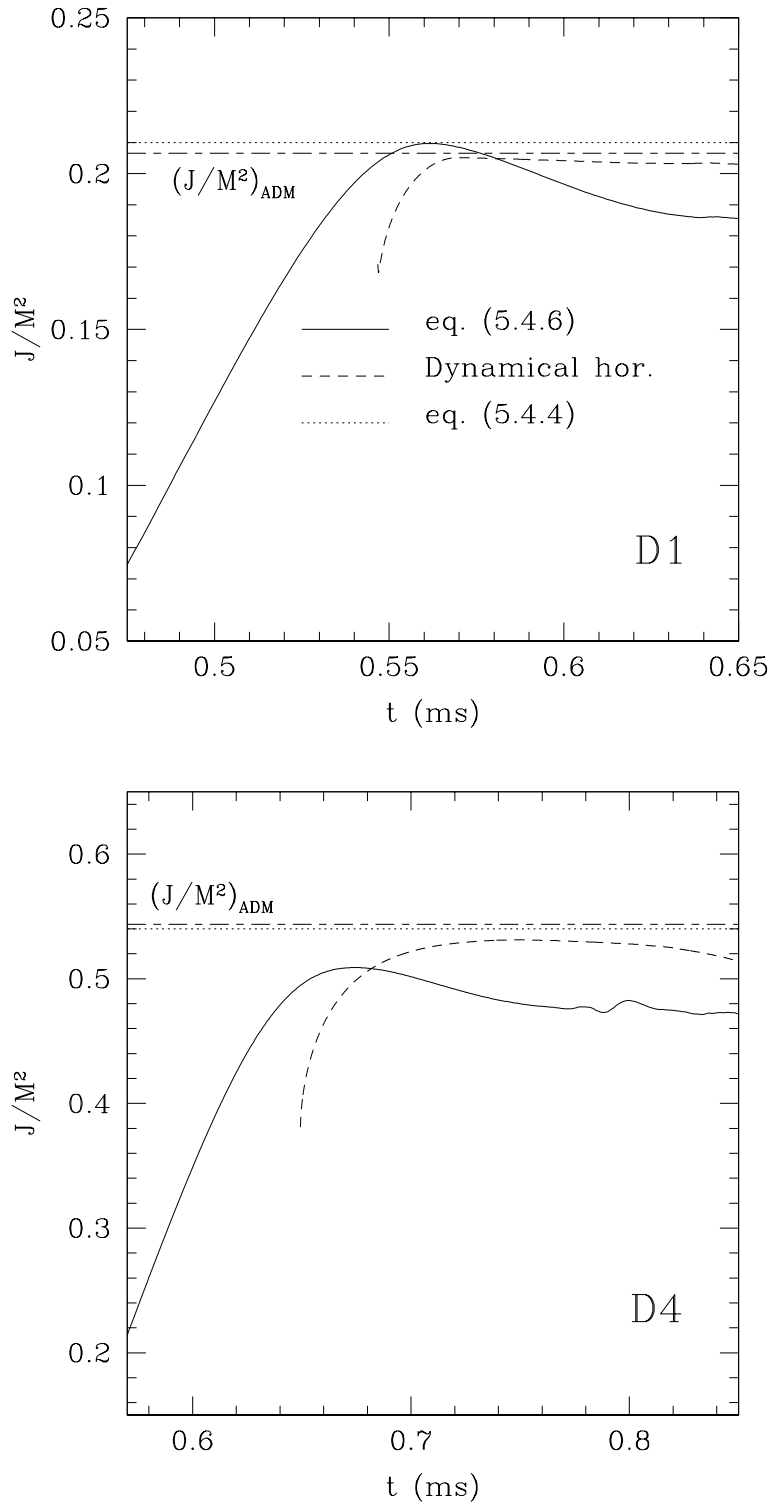

Figure 5.15: Comparison of the different measures of the angular momentum for the cases D1 (upper panel) and D4 (lower panel). The estimate using the fi t to the circumference ratio (see upper panel of Fig. 5.14) is also shown. The dynamical horizon spin measurement is considerably more accurate at late times as the event-horizon surfaces will diverge exponentially at this point. Shown with the horizontal short-long dashed lines are the values of $(J/M^2)_{\rm ADM}$ in the two cases as measured from the initial data (see main text for details).

long as they are axisymmetric, we have not encountered problems in applying the dynamical-horizon framework to the horizons found in our simulations.

Measuring J from the angular velocity of the event horizon

A third method for computing J only applies if an event horizon is found and if its angular velocity has been measured. In a Kerr background, in fact, the generators of the event horizon rotate with a constant angular velocity $\omega \equiv -g_{t\phi}/g_{\phi\phi} = \sqrt{g_{tt}/g_{\phi\phi}}$. In this case the generator velocity can be directly related to the angular-momentum parameter as

$$\frac{a}{M} = \frac{J}{M^2} = \left[\frac{A\omega^2}{\pi}\left(1 - \frac{A\omega^2}{4\pi}\right)\right]^{1/2} . \tag{5.4.6}$$

As with the previous approximations, expression (5.4.6) is strictly valid only for a Kerr black hole and will therefore contain a systematic error which, however, decays rapidly as the black-hole perturbations are damped. On the other hand, the event-horizon generator velocities have the considerable advantage that everything is measured instantaneously and the values of ω are valid whether or not the background is an isolated Kerr black hole. The disadvantage, though, is that, as mentioned above, the numerical event-horizon surfaces become systematically less accurate at late times (*cf.* Fig. 5.13).

Comparison of angular-momentum measurements

A detailed comparison of the three different methods for measuring the angular momentum of the black hole is shown in Fig. 5.15. The measurement of angular momentum using the angular velocity of the generators is shown as solid lines. Both for slowly (upper panel) and rapidly (lower panel) rotating stellar models, the event horizon has zero area (and thus zero angular momentum) when it is first formed. However, as the rotating matter collapses, the event-horizon area and angular momentum grow, the black hole is spun up and, to numerical accuracy, the total angular momentum of the spacetime is contained within the black hole (*cf.* Fig. 5.14). At late times, the estimate using the generator velocities of the event horizon drifts away, probably due to a combination of gauge effects and the systematic errors in the trial guesses for the null surfaces.

In the case of the slowly-rotating model D1, in particular, the estimate from the dynamical horizon finder is perfectly stable (*cf.* dashed line in the upper panel of Fig. 5.15), indicating that an approximately stationary Kerr black hole has been formed by the time the simulation is terminated. In the case of the rapidly-rotating model D4, however, this is no longer the case as matter continues to accrete also at later times, when the errors have also increased considerably. As a result, the measure of the spin through the dynamical horizon finder is less accurate and does not seem to have stabilized by the time the simulation ends (*cf.* dashed line in the lower panel of Fig. 5.15). This may indicate that the final black hole has not settled down to a Kerr black hole on the timescales considered here.

5.4.3 Black-hole mass from the Christodoulou formula

It was shown by Christodoulou that, in the axisymmetric and stationary spacetime of a Kerr black hole, the square of the black hole mass M is given by [69]

$$M^2 = M_{\rm irr}^2 + \frac{4\pi J^2}{A} = \frac{A}{16\pi} + \frac{4\pi J^2}{A} , \tag{5.4.7}$$

where $M_{\rm irr}$ is the irreducible mass, A is the event-horizon proper area, and J is the black-hole angular momentum. As the black hole approaches a stationary state at late times, the apparent and event horizons

will tend to coincide and in that case the mass of the black hole is very well approximated by the above formula.

We have applied the above formula, using the various methods for measuring the angular momentum J. In particular, using the method for obtaining J from the distortion of the event horizon, through equation (5.4.5), the black-hole mass is given by

$$M^2 = \frac{A}{8\pi}\left(\frac{M_{hor}}{a}\right)^2\left[1-\sqrt{1-\left(\frac{a}{M_{hor}}\right)^2}\right] \,. \tag{5.4.8}$$

If, on the other hand, J is found from the angular velocity ω of the event horizon, then it is possible to use (5.4.6) in (5.4.7) and obtain

$$M^2 = \frac{A}{16\pi - 4A\omega^2} \,. \tag{5.4.9}$$

In the framework of dynamical horizons, expression (5.4.7) holds for *any* axisymmetric isolated or dynamical horizon, independently of whether it is stationary.

Fig. 5.16 collects the four different ways of measuring the black-hole mass for the collapse of models D1 and D4. The different lines refer to the different approaches we have outlined above. In addition, we display the irreducible mass $M_{\rm irr}$. The upper panel of Fig. 5.16, in particular, shows the results of the different measures for the slowly-rotating model D1. Because in this case all the matter rapidly collapses into the black hole, the different estimates of the total mass agree very well. However, already in this slowly-rotating case the irreducible mass of the apparent horizon is noticeably lower. The upper panel also shows that while the different methods provide comparable estimates, only the one corresponding to equation (5.4.3) (*i.e.* the solid line) falls for some time within the error bar provided by the initial estimate of $M_{\rm ADM}$ (this is particularly evident in the inset). Because when this happens the norms of the Hamiltonian constraint have not yet started to grow exponentially and the largest value of the constraint violation is about an order of magnitude smaller (*i.e.* the L_1 norm of the Hamiltonian constraint is $\sim 4.9\times10^{-4}$ at $t = 0.56$ ms) we can use the error bar in $M_{\rm ADM}$ to place an upper bound of 0.5% $M_{\rm ADM}$ to the energy lost through the emission of gravitational radiation in this case. This method of ours for estimating the energy loss in gravitational waves is rough, but it was the only one available for 3-dimensional simulations until recently. Actually, it has been the first method ever used to produce such estimates. As we will show in Section 5.5, the true bound we can now compute through better-suited techniques is considerably lower, even lower than the value found by Stark and Piran [229] in 2-dimensional simulations.

The lower panel of Fig. 5.16, on the other hand, shows the results of the different mass measures for the rapidly-rotating model D4. In this case, the contribution from the spin energy is considerably larger and noticeable differences appear among the different approaches. Since all seem to have systematic errors, this makes it less trivial to establish which method is to prefer. On one hand, those methods using information from the event-horizon equatorial circumference or that fit the perturbations of the event horizon [*i.e.* equations (5.4.3) and (5.4.8)] seem to provide accurate estimates at earlier times but suffer of the overall inaccuracy at later stages, when the initial guesses for the null surface are distinct. It is indeed at these early times that these measurements are within the error bar provided by the initial estimate of $M_{\rm ADM}$. On the other hand, those methods that measure the angular velocity of the null generators [*i.e.* equation (5.4.9)] or that use the dynamical horizon framework, produce reasonably accurate estimates, that converge with resolution, that monotonically grow in time and that are within the error bar of the initial estimate of $M_{\rm ADM}$. Furthermore, in the case of the dynamical horizon framework, this is not only physically expected, given that a small but non-zero fraction of the matter continues to accrete nearly until the end of the simulation, but it is also guaranteed analytically.

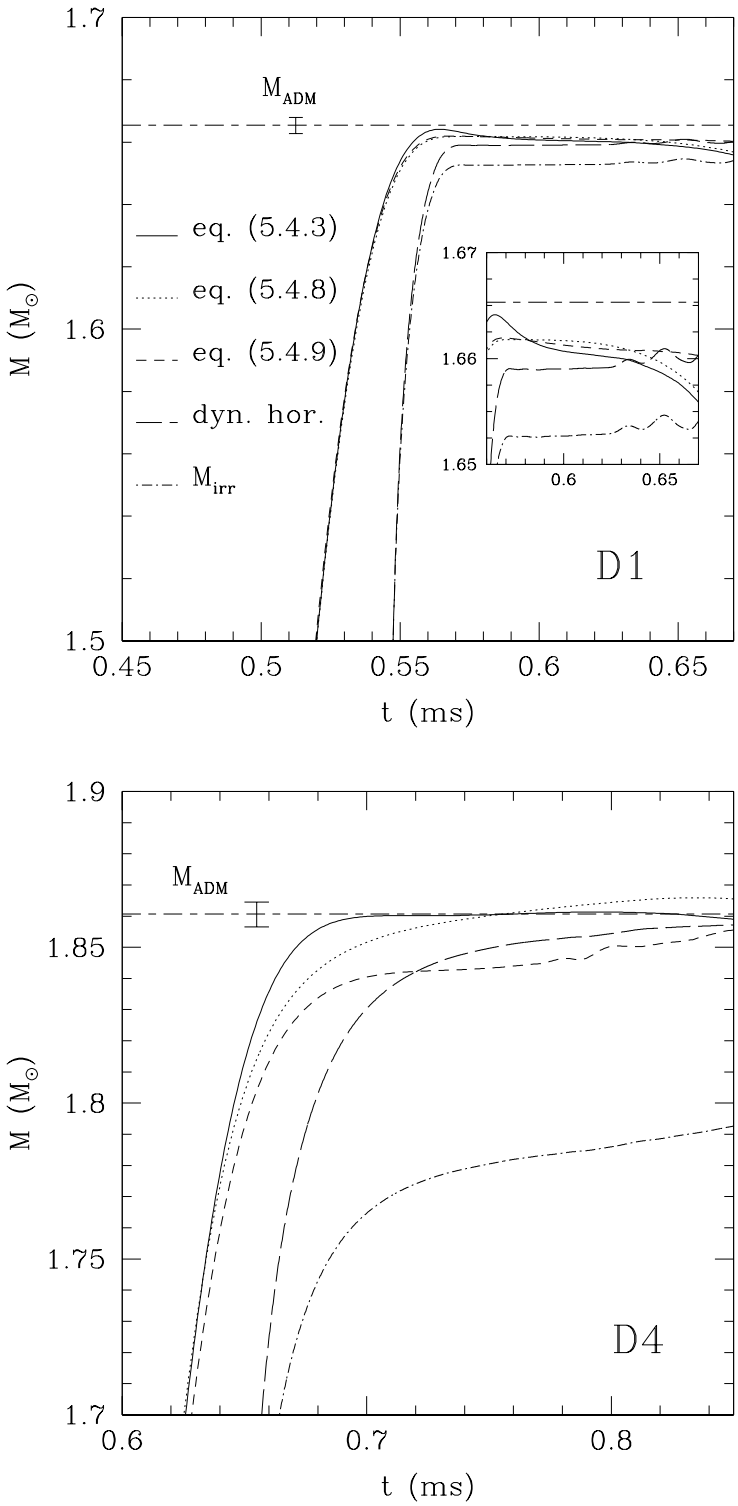

Figure 5.16: Comparison of the five different approaches used in the measure of the total black-hole mass for the collapse of models D1 and D4. Different lines refer to the different methods discussed in the main text. The upper panel (model D1), shows that the different methods are overall comparable when the rotation is slow, but that differences are already present (this is as shown in the inset). The lower panel (model D4) shows that the different measures can be considerably different when the rotation is large.

Because of these differences in the measures of M and because the black hole does not have time to settle down to a constant total mass, the upper bound on the energy emission is more conservative than in the D1 case. In particular, taking again as a reference the time when the estimate relative to equation (5.4.3) is within the error bar (*i.e.* at $t = 0.70$ ms) and the largest value of the constraint violation is about an order of magnitude smaller (*i.e.* the L_1 norm of the Hamiltonian constraint is $\sim 1.2 \times 10^{-3}$) and is not yet growing exponentially, we place an upper bound of 1% $M_{\rm ADM}$ on the energy lost through gravitational radiation. Once again, the comments on the goodness of this result we have made above for the D1 case apply.

One obvious and expected result is that the irreducible mass in the collapse of model D4 (the dot-dashed line in the lower panel of Fig. 5.16) deviates by a large amount from the actual black-hole mass, since it does not include the rotational energy of the black hole.

Finally, we will make a comment on the different methods used for measuring the mass and spin of a black hole in a numerical simulation. Although the direct comparison of many different methods employed here have provided valuable information on the dynamics of the system, we have found the dynamical horizon framework to be simple to implement, accurate and not particularly affected by the errors from which equivalent approaches seem to suffer, as shown in our Figs. 5.16 and 5.15. As a result, we recommend its use as a standard tool in numerical relativity simulations.

5.4.4 Reconstructing the global spacetime

All the results presented and discussed in the previous sections of this chapter describe only a small portion of the spacetime which has been solved during the collapse. In addition to this, it is interesting and instructive to collect all these pieces of information into a *global* description of the spacetime and look for those features which mark the difference between the collapse of slowly and rapidly-rotating stellar models. As we discuss below, these features emerge in a very transparent way within a global view of the spacetime.

To construct this view, we use the worldlines of the most representative surfaces during the collapse, namely those of the equatorial stellar surface, of the apparent horizon and of the event horizon. For all of them we need to use properly defined quantities and, in particular, circumferential radii. The results of this spacetime reconstruction are shown in Fig. 5.17, whose upper and lower panels refer to the collapse of models D1 and D4, respectively. The different lines indicate the worldlines of the circumferential radius of the stellar surface (dotted line), as well as of the apparent horizon (dashed line) and of the event horizon (solid line). Note that for the horizons we show both the equatorial and the polar circumferential radii, with the latter being always smaller than the former. For the stellar surface, on the other hand, we show the equatorial circumferential radius only. This is because the calculation of the stellar polar circumferential radius requires a line integral along the stellar surface on a given polar slice. Along this contour one must use a line element which is suitably fitted to the stellar surface and diagonalized (see [59] for a detailed discussion). In the case of model D4, however, this is difficult to compute at late times, when the disc is formed and the line integral becomes inaccurate.

Note that in both panels of Fig. 5.17 the event horizon grows from an essentially zero size to its asymptotic value. In contrast, the apparent horizon grows from an initially non-zero size and, as it should, is always contained within the event horizon. At late times, the worldlines merge to the precision at which we can compute them. A rapid look at the two panels of Fig. 5.17 is sufficient to appreciate the different properties in the dynamics of the collapse of slowly and rapidly-rotating models.

Firstly, in the case of model D1, the differences between the equatorial and polar circumferential radii of the two trapped surfaces are very small and emerge only in the inset that offers a magnified view

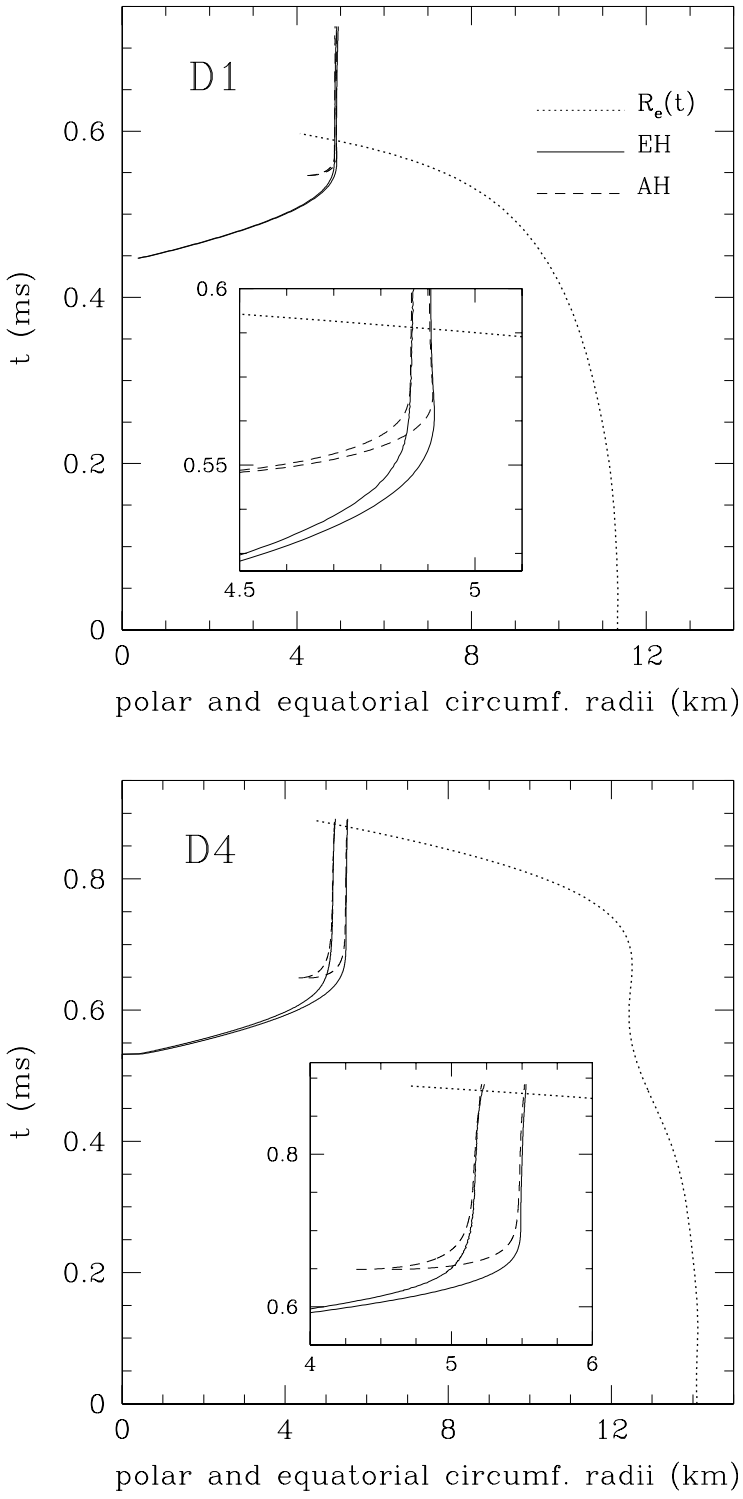

Figure 5.17: Evolution of the most relevant surfaces during the collapse for the D1 and D4 cases. Solid, dashed and dotted lines represent the worldlines of the circumferential radii of the event horizon, of the apparent horizon and of the stellar surface, respectively. Note that for the horizons we plot both the equatorial and the polar circumferential radii, while only the equatorial circumferential radius is shown for the stellar surface. Shown in the insets are the magnified views of the worldlines during the final stages of the collapse.

of the worldlines during the final stages of the collapse. This is not the case for model D4, for which the differences are much more evident and can be appreciated also in the main panel. Of course, this is what one expects given that the ratio of these two quantities depends on a/M and is ~ 1 for a slowly-rotating black hole (*cf.* Table 5.2).

Secondly, the worldlines of the stellar equatorial circumferential radius are very different in the two cases. In the slowly-rotating model D1, in particular, the star collapses smoothly and the worldline always has negative slope, thus reaching progressively smaller radii as the evolution proceeds (*cf.* upper panel of Fig. 5.17). By time $t \simeq 0.59$ ms, the stellar equatorial circumferential radius has shrunk below the corresponding value of the event horizon. In the case of the rapidly-rotating model D4, on the other hand, this is no longer true and after an initial phase which is similar to the one described for D1, the worldline does not reach smaller radii. Rather, the stellar surface slows its inward motion and, at around $t \sim 0.6$ ms, the stellar equatorial circumferential radius does not vary appreciably. Indeed, the lower panel of Fig. 5.17 shows that at this stage the stellar surface moves to slightly larger radii. This behaviour marks the phase in which a flattened configuration has been produced and the material at the outer edge of the disc experiences a pressure hang-up (*cf.* the middle and lower panels of Fig. 5.5). This is due to fact that the more rapid infall of matter along the polar axis produces a bounce and an expansion on the equatorial plane at this time. As the collapse proceeds, however, also this material will not be able to sustain its orbital motion and, after $t \sim 0.7$ ms, the worldline moves to smaller radii again. By a time $t \simeq 0.9$ ms, the stellar equatorial circumferential radius has shrunk below the corresponding value of the event horizon.

5.5 Gravitational waveforms

5.5.1 Previous work

The fact that on this specific topic, *i.e.* the extraction of gravitational waveforms from collapsing rotating stars, only one work is available in the literature and that it dates back to 20 years ago is indicative of the difficulty of the problem. Stark and Piran [229] in 1985 used their axisymmetric fully-general-relativistic code to evolve rotating axisymmetric configurations and to compute directly the gravitational-radiation emission produced by their collapse to a black hole. As already mentioned in Section 5.1, they presented results for the collapse of an initial configuration consisting of spherically-symmetric polytropic (with exponent $\Gamma = 2$) stars which underwent collapse after the pressure was reduced of a factor ranging from 0.01 to 0.4. The stars were also given an angular-momentum distribution approximating rigid-body rotation, with different configurations having different initial total angular momentum J, which was measured in terms of the parameter $a = J/M^2$. They found that, while the nature of the collapse depended on the parameter a, the form of the wave instead remained the same over the entire range of the values of a, even if the amplitude of the wave increased with a. A figure from reference [229] reporting the waveforms extracted at a distance of $50M$ from the origin for different values of a from an evolution with a pressure depletion of 99% is reproduced in Fig. 5.18. In the next section, we will compare this figure with the one produced by `Whisky`.

As mentioned in Section 5.1, there have been studies of the collapse of rotating NS to Kerr black holes in 3 dimensions after the seminal work of Stark and Piran (*e.g* [214, 212, 213, 89]). Despite the great improvements on the evolution of the hydrodynamics and of the spacetime achieved in these numerical computations, none of these, however, has addressed the problem of waveform extraction. The reason for this is at least twofold: firstly, the gravitational signal is intrinsically small (we recall that, following Stark and Piran and also our upper limits discussed in Section 5.4.3, the energy carried away

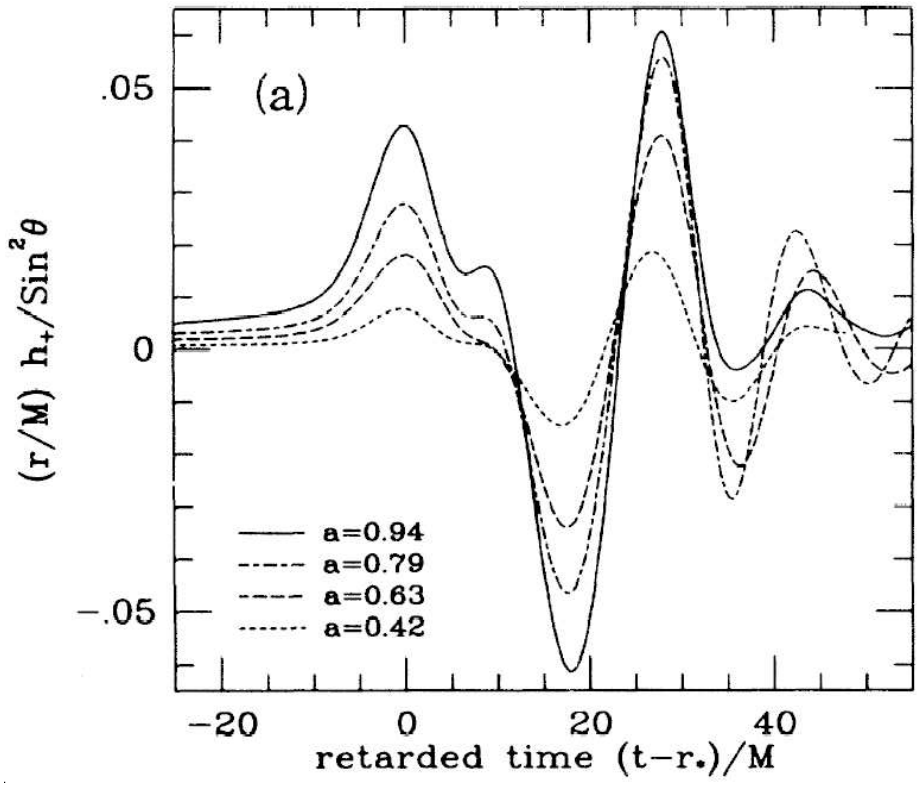

Figure 5.18: Gravitational waveforms for a collapse to a black hole of stars of various angular momenta a evolved after an initial pressure depletion of 99% with the axisymmetric code of Stark and Piran. This figure is taken from [229].

by the gravitational waves is $\Delta M/M \lesssim 0.001$); secondly, the necessity of performing wave extraction at large distances from the collapsing object would require, for uniform grids, computational resources exceeding the current available ones. As we will illustrate in the next section, we have succeeded in solving both these problems by evolving on grids with several levels of refinement.

5.5.2 Our results

The use of numerical grids with uniform spacing and the present computational resources have initially forced us to place the outer boundary of our computational domain in the *near zone, i.e.* in regions of the spacetime where the gravitational waves have not yet reached their asymptotic form, which instead happens in what is usually referred to as the *wave zone*. Under these constraints, the information on the gravitational waveforms that we extract through perturbative techniques [197, 188] does not provide interesting information besides the obvious change in the quadrupole moment of the background spacetime.

Several different methods are possible for the extraction of the gravitational-radiation content in numerical spacetimes: we have adopted a gauge-invariant approach in which the spacetime is matched with the non-spherical perturbations of a Schwarzschild black hole (see refs. [13, 197, 64] for applications to Cartesian coordinates grids). In practice, a set of "observers" is placed on 2-spheres of fixed coordinate radius, where they extract the gauge-invariant, even $\Psi^{(\mathrm{e})}_{\ell m}$ and odd-parity $Q^{(\mathrm{o})}_{\ell m}$ metric perturbations [165]. Here ℓ, m are the indices of the angular decomposition and we usually compute modes up to $\ell = 5$ with $m = 0$; modes with $m \neq 0$ are essentially zero because of the high degree of axisymmetry in the collapse. Validations of this approach in vacuum spacetimes can be found in refs. [64, 188, 34], while its use with matter sources has been reported in [100].

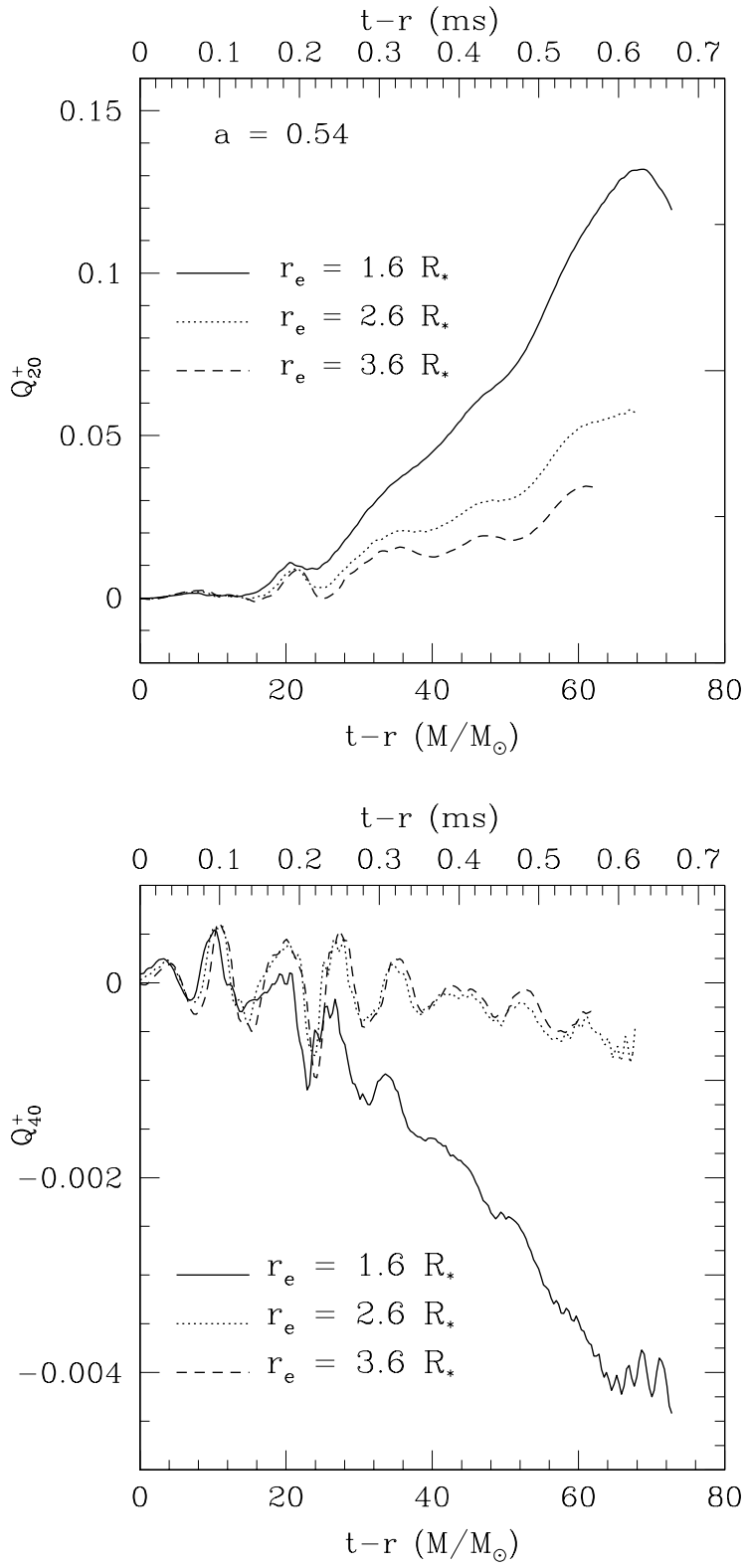

Figure 5.19: Gravitational wave extraction at short distances: waveforms of the even-parity metric perturbation as functions of retarded time (shown both in ms and solar-mass units) for model D4 evolved on a uniform grid. Different lines refer to different extraction distances.

Using the even and odd-parity perturbations $Q^{+}_{\ell m}$ and $Q^{\times}_{\ell m}$

$$Q^{+}_{\ell m} \equiv \sqrt{\frac{2(\ell+2)!}{(\ell-2)!}}\, \Psi^{(\mathrm{e})}_{\ell m}\,, \quad Q^{\times}_{\ell m} \equiv \sqrt{\frac{2(\ell+2)!}{(\ell-2)!}}\, Q^{(\mathrm{o})}_{\ell m}\,, \tag{5.5.10}$$

we report in Fig. 5.19 the extracted signal at coordinate radii 1.6, 2.6 and 3.6 times the initial coordinate stellar equatorial radius R_*, or, equivalently, at distances $8.1M$, $13.4M$, $18.8M$. This are clearly not far out enough to be in the wave zone. Indeed, we see (upper panel) that the waveforms for the $\ell = 2$ mode compared at the same retarded time do not overlap, as they should if they were computed in the wave zone, since the invariance under a retarded-time scaling is a property of the solutions of a wave equation. The overlapping for the $\ell = 4$ mode waves (lower panel) seems better. The higher frequency waves, in fact, are easier to compute, because they have a wavelength which is smaller than the typical linear dimension of the computational domain (for the $\ell = 2$ mode the wavelength is comparable to the linear dimension of the computational domain), so that they are less influenced by the secular changes of the metric. However, also in this case there clearly are secular variations of the waveforms that are probably related to the dynamics of the gravitational field in the near zone. We also note that the amplitude of the $\ell = 4$ mode is much smaller (one or two orders of magnitude) than that of the $\ell = 2$ mode, so one has to look primarily at the latter mode to ascertain whether wave extraction has been performed successfully.

Recent progress has been made in the use of progressive fixed mesh refinement techniques [203] to move the outer boundary far from the source. This has two important advantages: firstly it reduces the influence of inaccurate boundary conditions at the outer boundaries of the domain; secondly it allows for the wave zone to be included in the computational domain and thus for the extraction of important information about the gravitational wave emission produced during the collapse. Interesting preliminary results on these recent investigations have become available while writing this thesis. In particular, we have performed simulations of the above model D4 on a grid initially composed by four levels of refinement (see Fig. 5.20), which becomes further refined in the course of the evolution; at the end of the simulation seven refined levels are present on the grid (see Fig. 5.21, where the lower panel shows a magnification of the innermost levels of the upper panel). The innermost and highest resolution level always covers the whole star (or the whole horizon), so that the evolution of matter is as accurate as the one obtained in the preceding sections. The outermost levels, on the other hand, allow to extend the computational outer boundary to distances as large as $160M$. Note, however, that we do not extract waves at such large distances, but, rather, at about $50M$ from the origin (this is similar to what Stark and Piran did in [229]). There are two different reasons for this; the first one is rather trivial and is due to the fact that only very little of the gravitational waves has reached the outer boundary by the time the simulation is terminated, The second reason is that the amplitude of the wave is progressively reduced as it propagates toward the outer boundary, making the extraction increasingly more difficult.

The upper panel of Fig. 5.22 shows the waveform for the $\ell = 2$ mode (with the offset produced by the stellar quadrupole removed) computed on the multilevel grid at different and larger distances with respect to Fig. 5.19, that is at $7.3R_*$, $8.3R_*$, $9.3R_*$ and $10.4R_*$, or $37.1M$, $43.0M$, $48.4M$ and $53.8M$, respectively. It is now evident that the wave extraction has been performed in the wave zone, since the waveforms compared at retarded times overlap very well. A similar overlapping is observed (but not shown here) among the $\ell = 4$ mode waves. The lower panel of Fig. 5.22 shows the $\ell = 4$ mode waveform extracted at a distance $8.3R_*$ and the inset offers a comparison at this distance between the $\ell = 2$ and $\ell = 4$ mode waveforms; it is again clear that the quadrupolar is the dominant mode of the gravitational radiation. It is now interesting to compare Fig. 5.22 with Fig. 5.18, where we should select a line between the dashed and the dotted ones, since the parameter a in our model D4 has the value

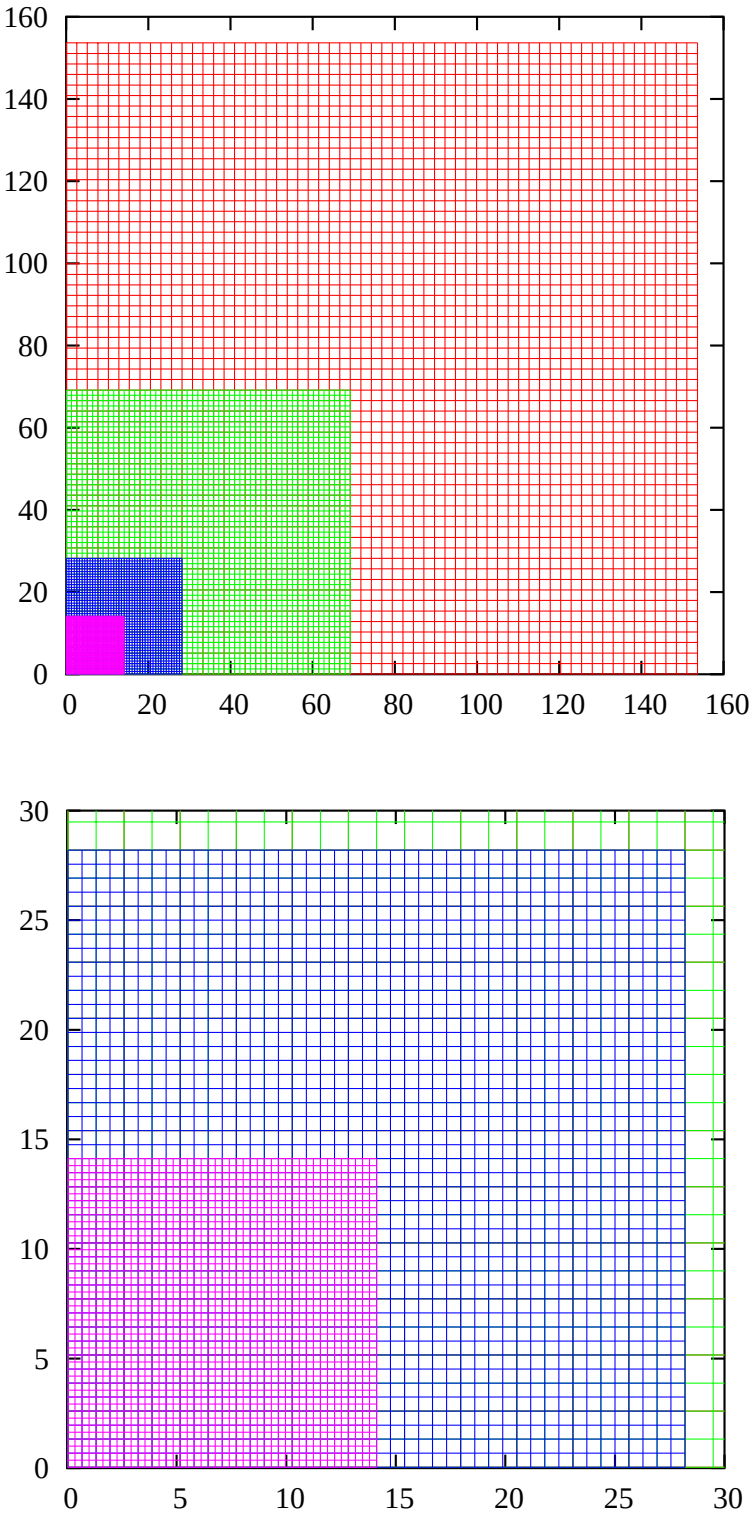

Figure 5.20: Refined grids at the initial time: 2-dimensional slices orthogonal to one of the axes of the initial refined grid used for the evolutions described in the text. Four levels are present and the finest one contains the entire star. The lower panel shows a magnification of the upper panel.

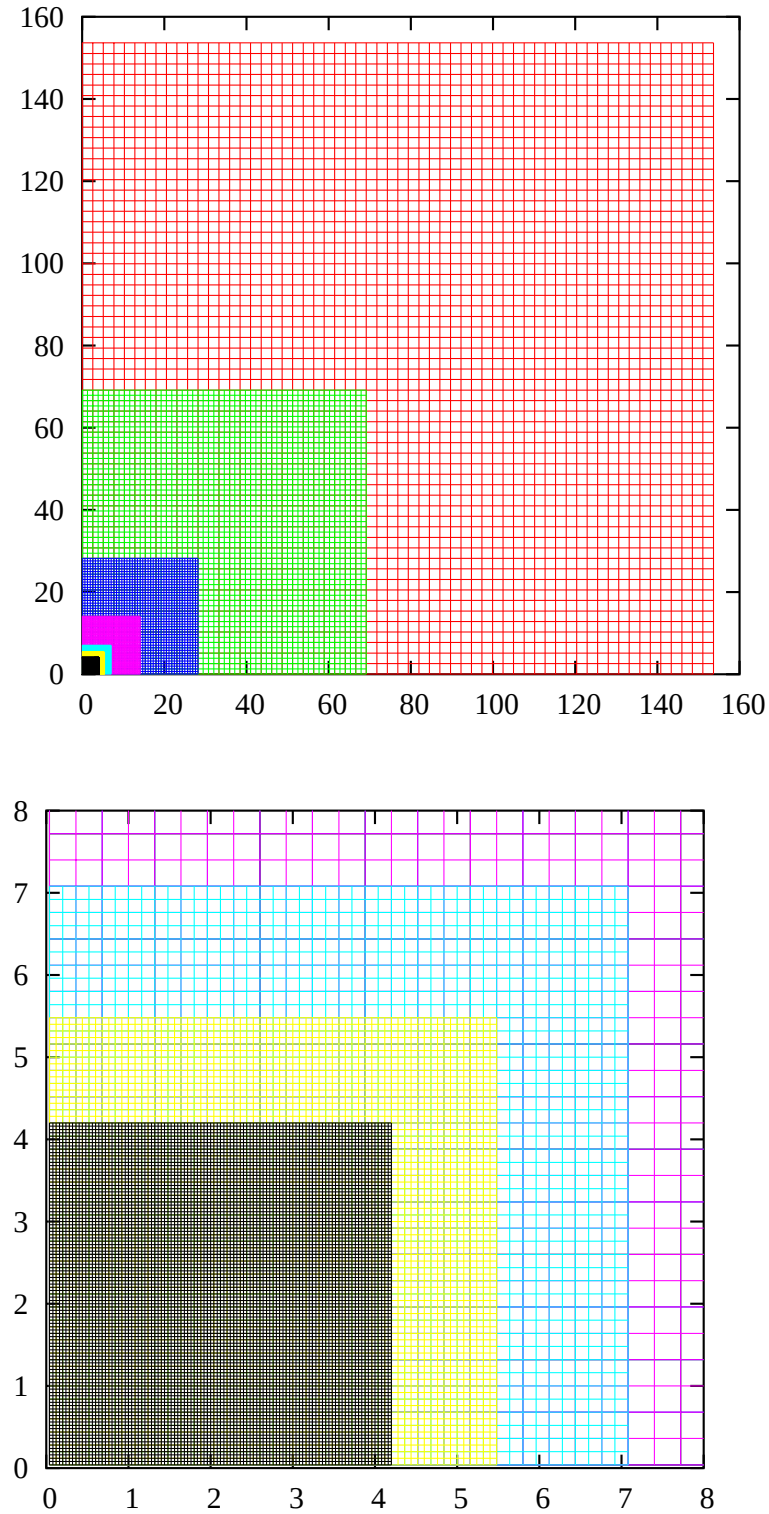

Figure 5.21: Refined grids at the final time: 2-dimensional slices orthogonal to one of the axes of the final refined grid used for the evolutions described in the text. Seven levels are present and the finest one contains the entire apparent horizon (no matter is left outside the horizon at this time). The lower panel shows a magnification of the upper panel.

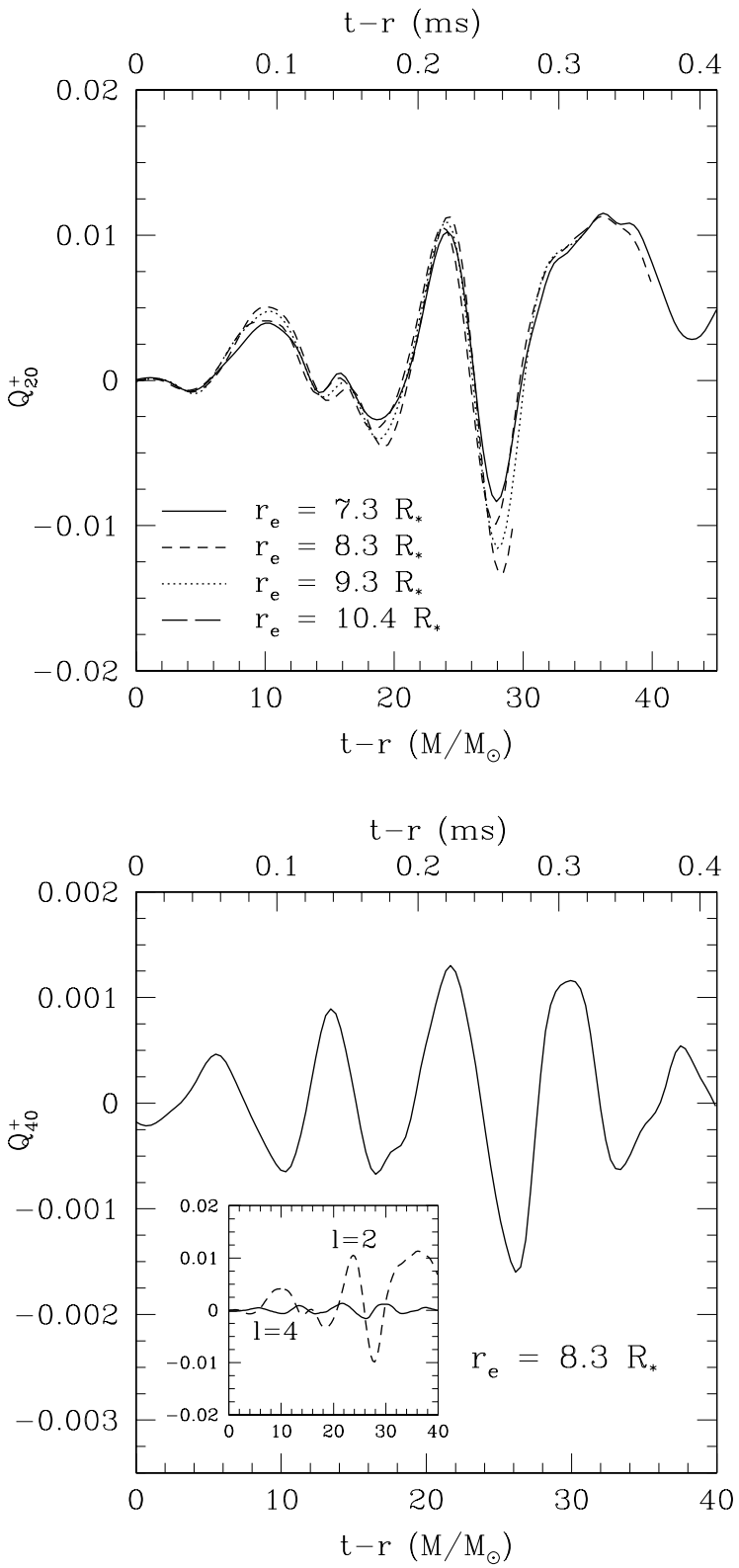

Figure 5.22: Gravitational wave extraction in the *wave zone*: gravitational waveforms as functions of retarded time (shown both in ms and solar mass units) for model D4 evolved on a multilevel grid, as specified in the text. Different lines refer to different extraction distances. The inset of the lower panel displays a comparison between the $\ell = 2$ and $\ell = 4$ modes.

$a = 0.54$. The comparison shows clearly that the forms of the two waves and their periods are very similar.

Another indication that the waveforms in Fig. 5.22 are an accurate description of the gravitational radiation produced by the collapse comes by analysing their power-spectrum densities. The collapse, in fact, can be viewed as the rapid transition between the spacetime of the initial equilibrium star and the spacetime of the produced rotating black hole. It is natural to expect, therefore, that the waveforms produced in this process will reflect the basic properties of both spacetimes and in particular the fundamental frequencies of oscillation. As a result, we expect the frequencies of the extracted waveforms to be similar both to the w-mode oscillation frequencies of typical NSs [129] and to those of the QNMs of black holes. The w-modes are pure spacetime oscillations (*i.e.* they do not involve fluid perturbations at first order) and have the highest frequencies and the shortest damping times among all NS oscillation modes. For polytropic stars with a given index, their frequencies vary only of a few percent with the compactness of the star. They are the most similar to black-hole QNMs and are thought to be an important source of gravitational radiation during the central phase of NS collapse [130].

A comparison of the typical frequencies associated to the waveforms in Fig. 5.22 and the expected ones is presented in Fig. 5.23 and shows that the largest peak of the power-spectrum densities indeed falls in the small region included between the known frequencies of the corresponding QNM of a Schwarzschild black hole of the same mass[1] (marked by a dashed vertical line in the figure) and the known frequencies of w-modes of a typical NS (dotted line) with the same mass and same polytropic EoS. In the upper panel of Fig. 5.23, we compare with the frequency of the family of w-modes named w_{II}-modes [130] and we notice that the peak is located nearer to the frequency of the w_{II}-mode than to the frequency of the QNM of the black hole. In the lower panel, instead, the power-spectrum density for the $\ell = 4$ mode is shown. Here, instead, we compare with the frequency of another family of w-modes named w_1-modes [142] and we notice that in this case the interval between the QNM frequency and the w-mode frequency is much smaller and that the peak frequency is nearer to the former frequency. The very good agreement shown in this figure is a convincing evidence that the waveforms presented in Fig. 5.22 do represent the gravitational waves produced in the collapse of a rotating NS to a Kerr black hole.

Using the extracted gauge-invariant quantities it is also possible to calculate the transverse traceless gravitational wave amplitudes in the two polarizations h_+ and $h_\times$ as

$$h_+ - \mathrm{i}h_\times = \frac{1}{2r}\sum_{\ell,m}\left(Q^+_{\ell m} - \mathrm{i}\int_{-\infty}^{t} Q^\times_{\ell m}(t')dt'\right) {}_{-2}Y^{\ell m}, \tag{5.5.11}$$

where ${}_{-2}Y^{\ell m}$ is the -2 spin-weighted spherical harmonic. Because of the small amplitude of higher-order modes, the transverse traceless wave amplitudes can be simply expressed as $h_+ \simeq h_+(Q^+_{20}, Q^+_{40})$ and $h_\times \simeq h_\times(Q^\times_{30}, Q^\times_{50})$, where $Q^\times_{30} \gg Q^\times_{50}$. Their waveforms are shown in Fig. 5.24 for the detector placed at distance $7.3R_*$ and for two different inclination angles. Note that the amplitudes in the cross polarization are about one order of magnitude smaller than those in the plus polarization, with the maximum amplitudes in a ratio $|rh_\times|_{\max}/|rh_+|_{\max} \simeq 0.06$. This is because the odd-parity perturbations, which are zero in a nonrotating axisymmetric spacetime, appear here only as a result of the coupling, induced by the rotation, with the even-parity perturbations.

A precise comparison of the amplitudes in Fig. 5.24 with the corresponding ones calculated in [229] is made difficult by the differences in the choice of initial data and, in particular, by the impossibility

[1]The frequencies of the QNMs of Kerr black holes for angular-momentum parameters a not near unity (*i.e.* as in our case) differ only of a few percent from the frequencies relative to a Schwarzschild black hole of the same mass. In Fig. 5.23, anyway, we show the frequency of the Kerr QNM [139].

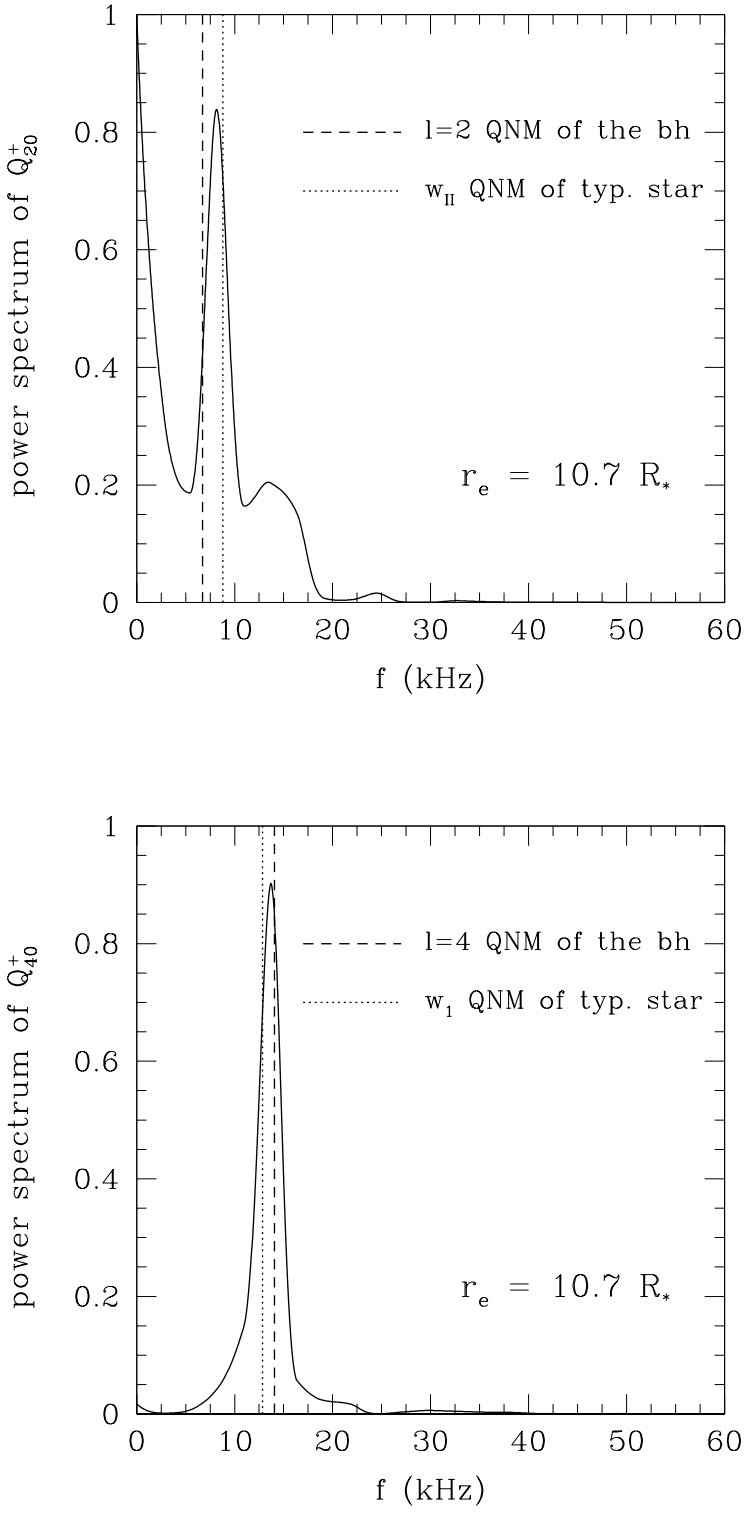

Figure 5.23: Power-spectrum density of the waveforms reported in Fig. 5.22. The units on the y-axis are arbitrary. The dashed vertical lines indicate the frequency of the QNM of a black hole with the same mass, while the dotted vertical line indicates those of the w-modes of a NS.

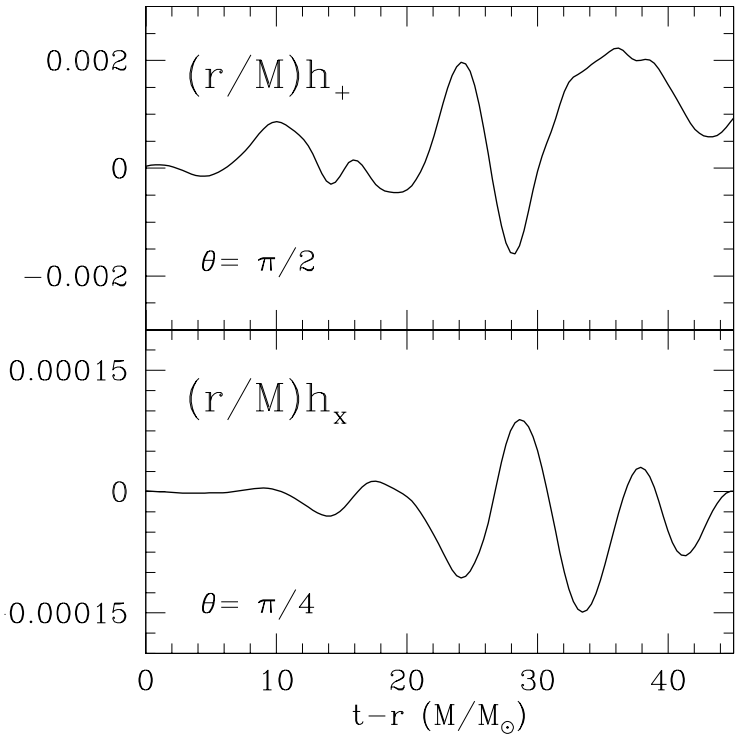

Figure 5.24: Transverse traceless gravitational-wave amplitudes extracted by the detector located at $37.1\,M$ and for two different inclination angles.

of reaching $a \gtrsim 0.54$ when modelling consistently stationary polytropes in uniform rotation. However, when interpolating the results in [229] for the relevant values of a, we find a very good agreement in the form of the waves, but also that our estimates are about one order of magnitude smaller, with $|rh_+|_{\max} \simeq 0.00225$.

Considering the sensitivity of VIRGO and only the burst signal, we can set an upper limit for the characteristic amplitude produced in the collapse of a rapidly and uniformly-rotating polytropic star at 10 kpc that is $h_c = 5.77 \times 10^{-22}(M/M_\odot)$ at a characteristic frequency $f_c = 931$ Hz. In the case of LIGO I, instead, we obtain $h_c = 5.46 \times 10^{-22}(M/M_\odot)$ at $f_c = 531$ Hz. In both cases, the signal-to-noise ratio is $S/N \sim 0.25$, but this can grow to be ~ 4 in the case of LIGO II. These ratios could be increased considerably if the black hole ringing following the initial burst could be detected. Computing the emitted power as

$$\frac{dE}{dt} = \frac{1}{32\pi} \sum_{\ell,m} \left(\left| \frac{dQ^+_{\ell m}}{dt} \right|^2 + \left| Q^\times_{\ell m} \right|^2 \right) , \tag{5.5.12}$$

the total energy lost to gravitational radiation is $\Delta E \equiv \int [dE/dt](t')dt' = 1.45 \times 10^{-6}(M/M_\odot)$. This is about two orders of magnitude smaller than the estimate made in [229] for a star with $a = 0.54$, but closer to the very small energy losses computed recently in the collapse of rotating stellar cores [166]. The origin of the quantitative difference with the results in [229] could be due to the different specification of the initial data.

5.6 Conclusion

As a first astrophysical problem for our novel code, we have here focused on the collapse of rapidly-rotating relativistic stars to Kerr black holes. The stars are assumed to be in uniform rotation and dynamically unstable to axisymmetric perturbations. Overall, our results show that the dynamics of the

collapsing matter is strongly influenced by the initial amount of angular momentum in the progenitor NS, which, when sufficiently high, leads to the formation of an unstable flattened object. While the collapse of slowly-rotating initial models proceeds with the matter remaining nearly uniformly-rotating, the dynamics is shown to be very different in the case of initial models rotating near the mass-shedding limit. Strong differential rotation develops, in fact, during the collapse, which is delayed due to a pressure hang-up. Although the stars become highly flattened during collapse, attaining a disc-like shape, the collapse cannot be halted because the specific angular momentum is not sufficient for a stable disc to form. Instead, the matter in the disc spirals toward the black hole and angular momentum is transferred inward to produce a spinning black hole.

All the simulations performed for realistic initial data and a polytropic or ideal-fluid EoS show no evidence of shock formation preventing a prompt collapse to a black hole. It should be remarked, however, that both these conclusions (absence of shocks and of matter on stable orbits outside the black hole) may change if other non-isentropic EoSs are used or if the initial stellar models are rotating differentially.

Several different approaches have been employed to compute the mass and angular momentum of the newly-formed Kerr black hole. Besides more traditional methods involving the measure of the geometrical properties of the apparent and event horizons, we have fitted the oscillations of the perturbed Kerr black hole to specific QNMs obtained by linear perturbation theory. In addition, we have also considered the recently proposed *isolated* and *dynamical*-horizon frameworks, finding it to be simple to implement and yielding estimates which are accurate and more robust than those of the equivalent methods. This variety of approaches has allowed for the determination of both the mass and angular momentum of the black hole with an accuracy unprecedented for a 3-dimensional simulation. These measures, in turn, have allowed us to set upper limits on the energy and angular momentum that could be lost during the collapse in the form of gravitational radiation.

Our recent simulations on multilevel grids are giving the first reliable results about gravitational wave extraction in 3 dimensions, 20 years after the milestone work of [229] in axisymmetry. We have been able to place the outer boundaries of the grid far enough so that the computation of the wave signals performed at different distances gives consistent results. We have found that the dominant radiation mode is the $\ell = 2$ mode, the amplitude of the $\ell = 4$ mode being at least one order of magnitude smaller. From the analysis of the power-spectrum density of the signal, we assessed that our computed gravitational waves have a frequency lying in the interval delimited by the frequencies of the QNMs of the black hole and by those of the w-modes of the NS with mass equal to the one used in our simulation. All these results are in agreement with [229], while the our computation of the energy emitted in gravitational waves gives values that are two orders of magnitude smaller than those of [229]. This is probably due to the different specification of the initial data.

Finally, all the techniques discussed here are now being applied to the study of the collapse of differentially-rotating stars, governed by more realistic and non-isentropic EoSs. Preliminary results in the simulations of the collapse of differentially-rotating stars indicate, as expected, that, if the initial configuration has $J/M^2 \gtrsim 1$, its collapse leads to the formation of strong shocks and long-lasting torii. In particular, we have found that double, essentially axisymmetric shocks appear around the central object and that they produce two torii which do not collapse on a dynamical timescale, because of the excess of angular momentum. The formation of single massive discs orbiting around a central object was also found by [212, 213, 89], who, however, did not report the formation of the second disc nor the occurrence of the strong shocks. Both these new results (about gravitational waveforms from the collapse of uniformly-rotating initial models and about the collapse of differentially-rotating initial models) will be soon separately submitted for publication.

Chapter 6

Head-on collisions of neutron stars

6.1 Description of the problem and previous work

As a further intermediate step before studying the merger of binary NS systems, but yet investigating an important physical scenario, we have simulated head-on and near-head-on collisions of two identical, non-spinning, cold NSs which fall toward the centre of mass of the system from rest at infinity or with other initial velocities. In our simulations we have modelled the stars either with a polytropic or with an ideal-fluid EoS. We have used stars that may or may not have a combined rest mass exceeding the hydrostatical-equilibrium mass limit for an isolated, non-rotating, spherical star governed by the same cold EoS.

From the purely numerical point of view, these simulations are another severe test for the shock-capturing capability of our code, since, as expected, these configurations evolve with very strong shocks, in which the Lorentz factor becomes also > 50. However, this is more than a numerical test. It has been argued in [124] that head-on and near-head-on collisions of NSs could have a significant event rate and could be a candidate for a sub-class of short γ-ray bursts. The results of prompt collapse reported in [163, 94] (and confirmed here) could have implications on the observation of such processes, since the prompt formation of the horizon may cut the causal connection of the shock-heated matter from outside observers. Furthermore, these results have important implications also for the detection of gravitational-wave signals and will serve to study in more detail the physics related to the final coalescence of NSs in binary systems.

This specific problem received a particular attention in 1998, when Shapiro [207] produced a simplified, but analytical model of the head-on collision of two equal-mass NSs, based on the hypothesis that the process evolves through a sequence of quasi-equilibrium configurations. As a result of his analysis, he concluded that a large fraction of the stellar kinetic energy would be converted into thermal energy because of the strong shocks, thus preventing the prompt collapse of the merged object to a black hole, even if the total mass of the system exceeded the maximum allowed mass for a single equilibrium NS with the same EoS. The collapse could be delayed also by fragmentation, mass shedding or angular-momentum hang-up. The collapse will then eventually happen, only when the thermal pressure has decreased by a substantial amount through neutrino-cooling processes. This equilibrium state will last many dynamical timescales (of the order of milliseconds), because the thermal neutrinos, which eventually carry off the thermal energy, leak out slowly (the neutrino-diffusion timescale is ~ 10 sec). Shapiro pointed out that off-axis collisions are also of interest, since, while shock heating will be less important in this case, the angular momentum acquired by the remnant may supplement the reduced thermal pressure to prevent sudden collapse.

The above conclusions are usually referred to as the *Shapiro conjecture*. A numerical approach in full general relativity is required even for deciding between these qualitatively different outcomes, as also Shapiro [207] states. Miller *et al.* [163] were the first to investigate this conjecture systematically. Firstly, they criticized the validity of the major assumption of the conjecture, namely that the collision process of heavier NSs can be approximated by a quasi-equilibrium process. It could happen in fact that the coalesced object collapses before it can thermalize (thus involving a non-constant *effective polytropic constant*, for which the conjecture hypothesis does not allow) or that the collision process is so dynamic that, even though a stable equilibrium state exists, it is not attained in the collapse. However, they also pointed out that whether the collapse is delayed or prompt in head-on collision can depend on the initial NS configuration and that fully-relativistic simulations are necessary to demonstrate either process.

In their investigations, Miller *et al.* carried out simulations of two TOV stars with rest mass $M_0 = 1.4M_\odot$ and a polytropic EoS with exponent $\Gamma = 2$ and constant $K = 1.16 \times 10^5 \mathrm{cm}^5\mathrm{g}^{-1}\mathrm{s}^2$. We recall that the maximum allowed stable rest mass for these values of K and Γ is $1.46M_\odot$. At the initial time the stars are placed at a proper distance $d_0 = 44$ km (they do not say exactly what this distance refers to; we assume here that it is the distance between the maximum densities of the two stars) and are given an initial uniform velocity $v_0 = \sqrt{M_0/d_0}$ (*i.e.* the Newtonian infall velocity from infinity) along the axis on which the stars lie. They then use the York procedure [262] for determining a solution of the initial data satisfying the constraints and evolve it using as a slicing condition either "maximal" or "1+log" (and finding similar results). Their results show that an apparent horizon forms promptly, confining the whole shock into a region causally disconnected from the exterior. Less than 5% of the mass is left outside the apparent horizon at the time when the apparent horizon first meets the shock front. They repeated the simulation increasing the initial velocity by 10%, which generates more shock heating, and confirmed that their results are insensitive to such a difference in the initial velocity. Finally, they evolved a similar configuration, but with stars of $0.1M_\odot$ and showed that in this case the apparent horizon does not form within the time of the simulation, instead there is a bounce in the central density of the merged object.

In a subsequent article [94], the authors studied how these results are affected by using a more realistic EoS and considered configurations whose total rest mass was lower than the critical mass for a cold NS with the same EoS. Using the Lattimer-Swesty EoS [137], they constructed two initial NSs with rest mass $M_0 = 1.6M_\odot$. For this EoS, the critical mass is $3.67M_\odot > 2M_0$. Also in this case, they found prompt collapse to a black hole on a dynamical timescale, both for head-on and near-head-on (impact parameter equal to half of the NS coordinate radius) collisions with Newtonian initial velocities or with such velocities increased by 10%. As a result of their investigations, the authors proposed a *prompt-collapse conjecture*: for head-on and near-head-on collisions of NSs described by a generic EoS and infalling from rest at infinity, there exists a threshold in the rest mass of the merged object below the critical single-star rest mass, where prompt collapse to a black hole can occur, independently from small (10%) perturbations of the initial velocities.

6.2 Simulations of neutron-star head-on collisions with `Whisky`

6.2.1 Initial data

As initial data we also consider two TOV stars with the chosen EoS and rest mass M_0 at a proper distance d_0 (measured using the position of the maximum densities of the stars) aligned with one of the computational axes and give them a uniform velocity v_0 parallel to that axis. Then we use the York procedure [262] to determine initial data consistent with the Hamiltonian and momentum constraint equations (2.1.12) and (2.1.13). In order to determine an initial guess for applying this method, we

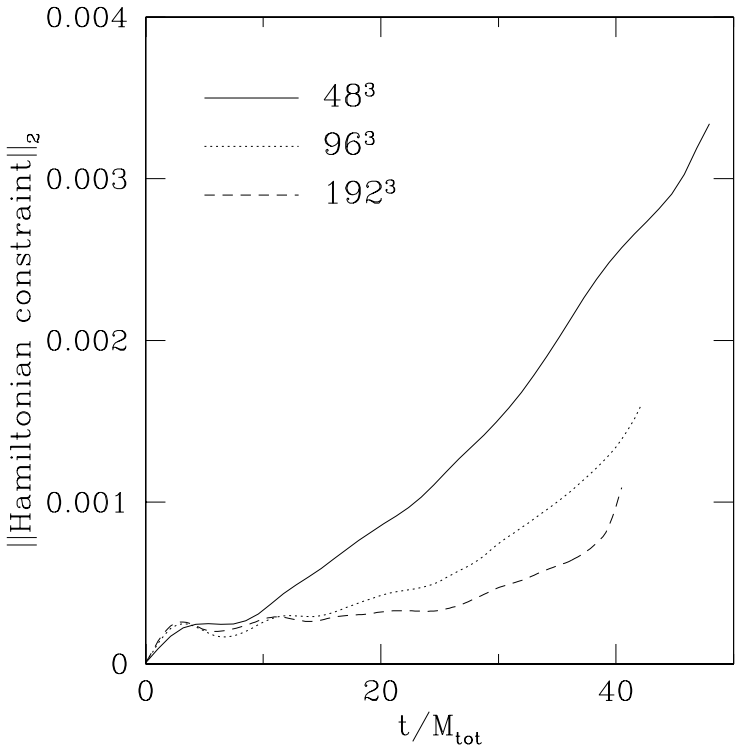

Figure 6.1: Comparison of the Hamiltonian constraint violation at different resolutions for model C1. After an initial transition stage in which we do not observe convergence, convergence is established, even if it is less than second order, as explained in the text. The lines stop soon after the apparent-horizon formation.

choose the global metric $(g_{\mu\nu})^{\rm guess}$ with the following prescription:

$$\begin{aligned}(g_{ij})^{\rm guess} &= (g_{ij})_1 + (g_{ij})_2 \qquad \text{if} \quad i \neq j\,, \\ (g_{ij})^{\rm guess} &= (g_{ij})_1 + (g_{ij})_2 - 1 \qquad \text{if} \quad i = j\,,\end{aligned} \tag{6.2.1}$$

where the subscripts 1 and 2 refer to the different stars, so that at large distances we would recover Minkowski spacetime. We also we multiply the two lapses and choose the shift to be zero:

$$\begin{aligned}(\alpha)^{\rm guess} &= \alpha_1 \alpha_2 \\ (\beta^i)^{\rm guess} &= 0\,.\end{aligned} \tag{6.2.2}$$

Once the IVP is solved the terms in the constraints at the initial time cancel out to an accuracy of 10^{-6}. We have studied configurations both with a $\Gamma = 2$ ideal-fluid EoS (4.2.3) and with a polytropic EoS (4.2.1) with polytropic exponent $\Gamma = 2$ and constant $K = 1.16 \times 10^5 {\rm cm}^5 {\rm g}^{-1} {\rm s}^2$, in order to make comparisons with the previous work [163]. We have also performed simulations with various initial velocities, ranging from $v_0 = 0$, to the Newtonian free-fall velocities, to $v_0 = 0.4c$.

6.2.2 Evolution

The simulations have been carried out on uniform grids with resolutions ranging from $\Delta x = 0.46$ km $\simeq 0.12 M_{\rm tot}$ to $\Delta x = 2.3$ km $\simeq 0.60 M_{\rm tot}$; with outer boundaries at a coordinate distance ranging from 44 km $\simeq 11 M_{\rm tot}$ to 103 km $\simeq 27 M_{\rm tot}$, where $M_{\rm tot}$ is the total rest mass of the system. In practice, with the resolutions used, each star at the initial time was covered by 12 – 50 grid points. The results

reported below do not change with respect to all the above numerical details, except for models which – as we will see – are close to the critical mass. In the latter cases, the results refer to the higher-resolution simulations.

All our evolutions of the above initial data here discussed are performed with the "1+log" slicing condition and with a "Gamma-driver" shift evolution. In order to ensure the reliability of the results, we first focus on the long-term convergence of the code in this specific problem. The IVP is solved with the same precision at all resolutions and this is larger than the truncation error, so we do not expect to see convergence on the initial data. Instead, we expect to see a transient period in which we do not see convergence in, *e.g.*, the violation of the Hamiltonian constraint (see the time interval between $t = 0$ and $t = 20M_{\rm tot}$ in Fig. 6.1). While the simulations proceed, however, the convergence properties of the code show up also in this specific problem. Since, with respect to the evolution of isolated stars, here we have more points near extrema, we expect the convergence to be lower than second order and this can be seen in Fig. 6.1. Another check of the accuracy of the code and of the reliability of its results comes from the computation of the total rest mass $M_{\rm tot}$ [*cf.* equation (5.3.1)] of the system, which is conserved within 0.2% for all the simulations discussed below.

A typical evolution of an ideal-fluid TOV head-on collision which forms promptly an apparent horizon is shown in Fig. 6.2, which refers do model C7, for which we set initial velocities to be very relativistic, namely $v_0 = 0.4c$. We show snapshots of isodensity contours, of isolines of the gradient of the density ($\sqrt{\nabla^i \rho \nabla_i \rho}$) and the location of the apparent horizon. The left and right panels show the (x, y) and the (x, z) plane, respectively (only one quarter of the (x, z) plane is shown, in order to have a magnified view). The upper panels display the initial data. Note that the deviations of each star from spherical symmetry are very small. The total time of the simulation is $46M_{\rm tot}$. The middle panels show snapshots at a time in which strong shocks have formed, after the stellar collision. The matter in the shocks has acquired relativistic velocities also in the y and z directions, orthogonally to the direction of motion of the centre of mass of each star.

Note that the torus of matter which is ejected in the (y, z) plane after the collision then falls back toward the (x, y) plane and will be finally engulfed in the apparent horizon, which forms at about $t = 39M_{\rm tot}$ and, at this time, is significantly non-spherical. A snapshot of this event is shown in the lower panels. In the direction along which the collision takes place, the shock is completely inside the apparent horizon from its very appearance, while it is not so on the plane orthogonal to this direction. Before the end of the simulation, however, all the matter has fallen inside the apparent horizon. Note also that at this time excision has not yet started, but will soon follow.

In Fig. 6.3, instead, we show the evolution sequence for a polytropic TOV near-head-on collision, that also forms promptly an apparent horizon. The different lines refer to the same quantities as in Fig. 6.2, but the right panels here show the whole (x, z) plane. Note that also at $t = 0$ the stellar centres do not lie on the x axis, but at a coordinate distance of 3.5 km from it. The velocities are parallel to the x axis and have the Newtonian infall values. The total time of the simulation is $30M_{\rm tot}$ and the middle panels show snapshots at about half that time. The stars have started to collide and a shock front has formed. They have acquired relativistic velocities in the y direction as well and, in the proximity of the shock front, also in the z direction. In the lower panels, the situation at the time of the formation of the non-spherical apparent horizon is displayed. The shock front has now extended and has taken an *s*-shaped form in the (x, y) plane. Along the collision direction, the shock is completely inside the apparent horizon from its very appearance, while it is not so on the plane orthogonal to this direction. Before the end of the simulation, though, all the matter has crossed the apparent horizon.

We note that in the evolution shown in Fig. 6.3, as in all the other models with initial impact parameter

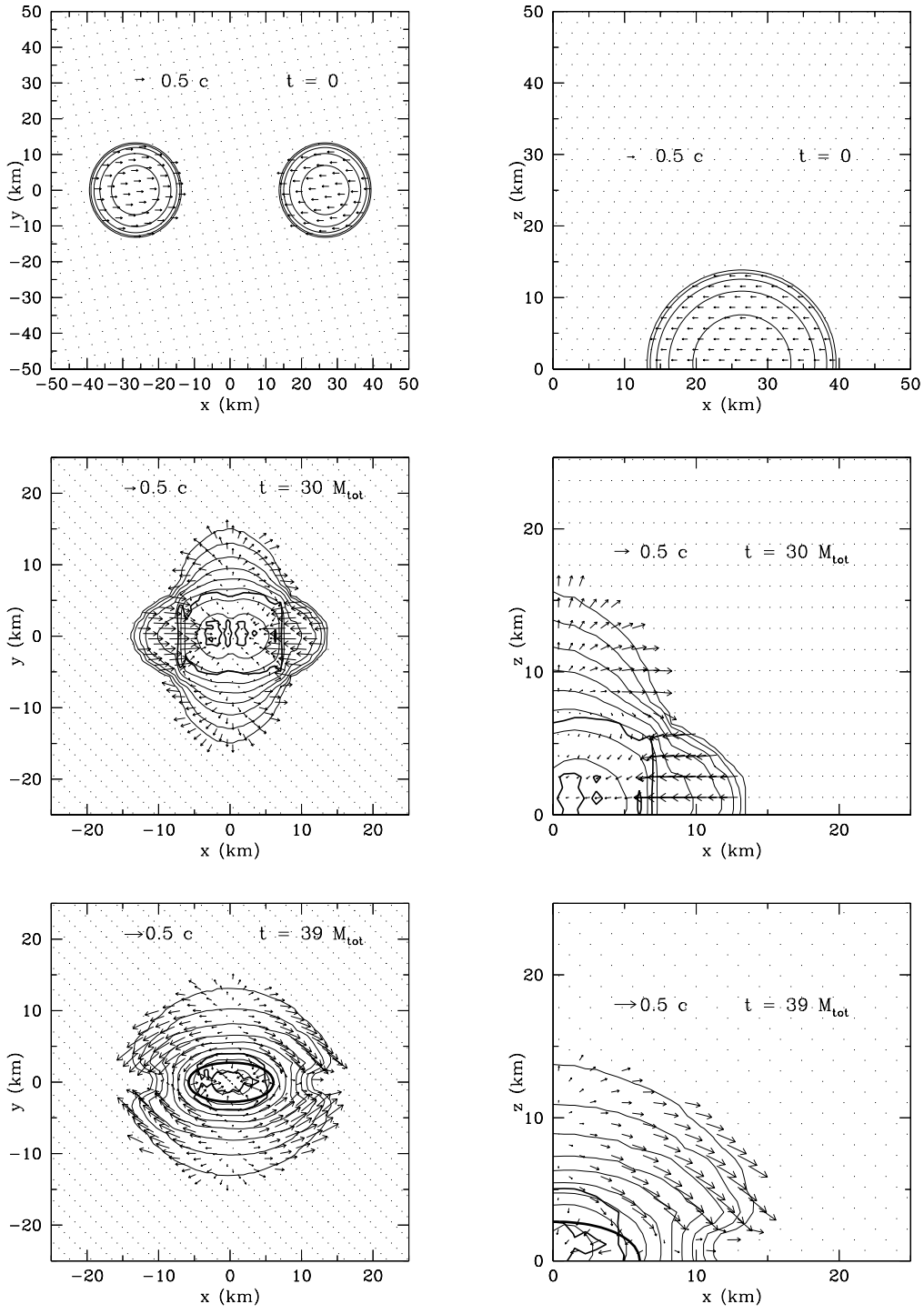

Figure 6.2: Snapshots of the (x, y) plane (left column) and of (x, z) plane (right column) at different times for model C7. The thin solid lines are isocontours of rest-mass density and are logarithmically spaced; the thick solid lines in the lower panels are isocontours of the gradient of rest-mass density and are logarithmically spaced to show the position of the shock; the very thick solid line shows the location of the apparent horizon; the arrows represent the velocity field, which is downsampled to allow for a clearer figure and whose reference length is shown in the legend of each panel for a velocity of $0.5\ c$. The units on both axes refer to coordinate lengths. Differently from Fig. 6.3, here in the left panels we show only a quadrant of the total data, in order to appreciate better the details.

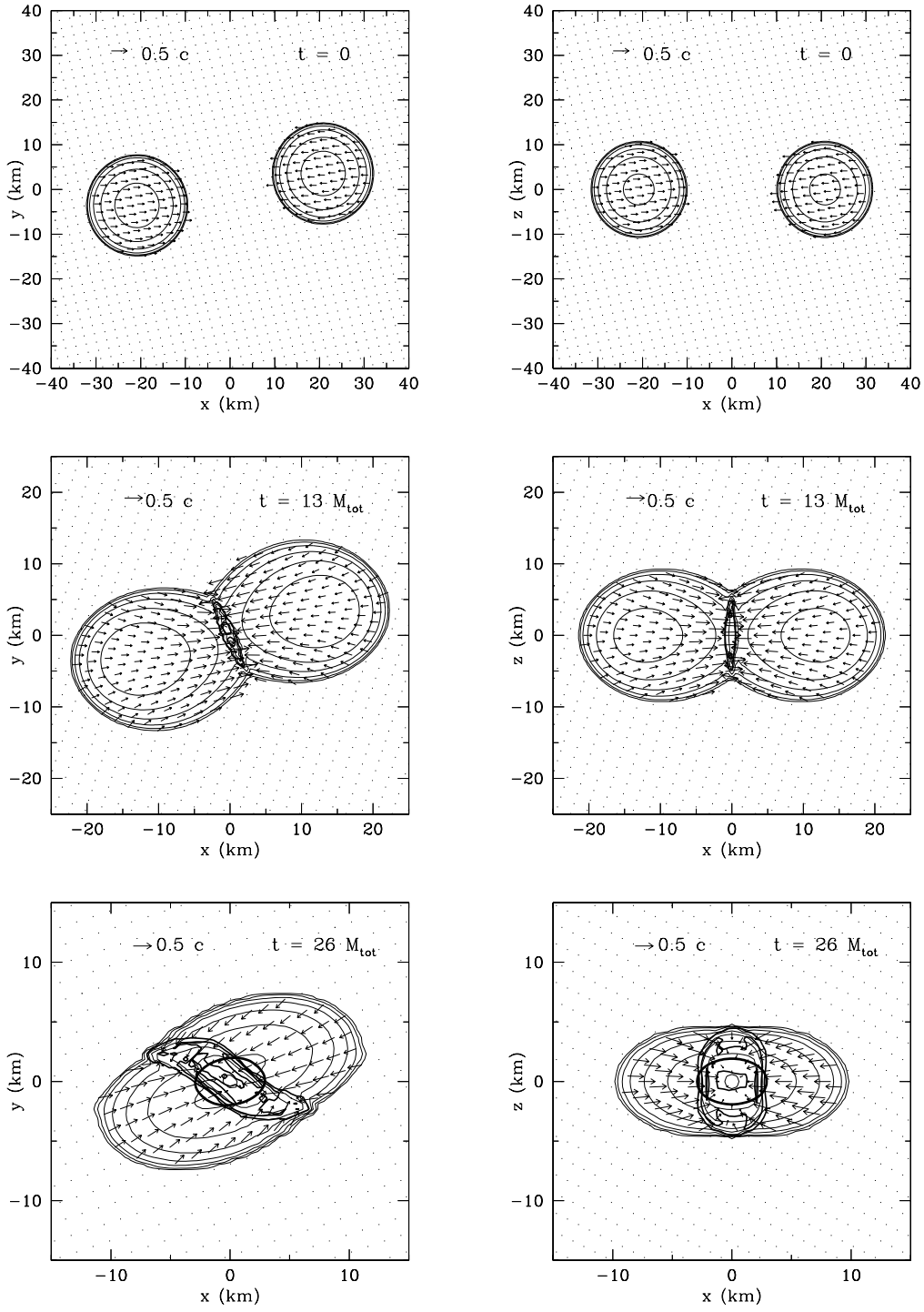

Figure 6.3: Snapshots of the (x, y) plane (left column) and of (x, z) plane (right column) at different times for a near-head-on-collision model not reported in table 6.1 and with the following properties (we refer to table 6.1 for the meaning of the symbols): $M_{\rm tot}/M_{c,0} = 1.79$, $R = 17$ km, polytropic EoS, $v_0 = 0.22c$ (Newtonian infall velocity), $d_0 = 3.2R$, impact parameter $= 0.5R$. The thin solid lines are isocontours of rest-mass density and are logarithmically spaced; the thick solid lines in the lower panels are isocontours of the gradient of rest-mass density and are logarithmically spaced to show the position of the shock; the very thick solid line shows the location of the apparent horizon; the arrows represent the velocity field, which is downsampled to allow for a clearer figure and whose reference length is shown in the legend of each panel for a velocity of $0.5\ c$. The units on both axes refer to coordinate lengths.

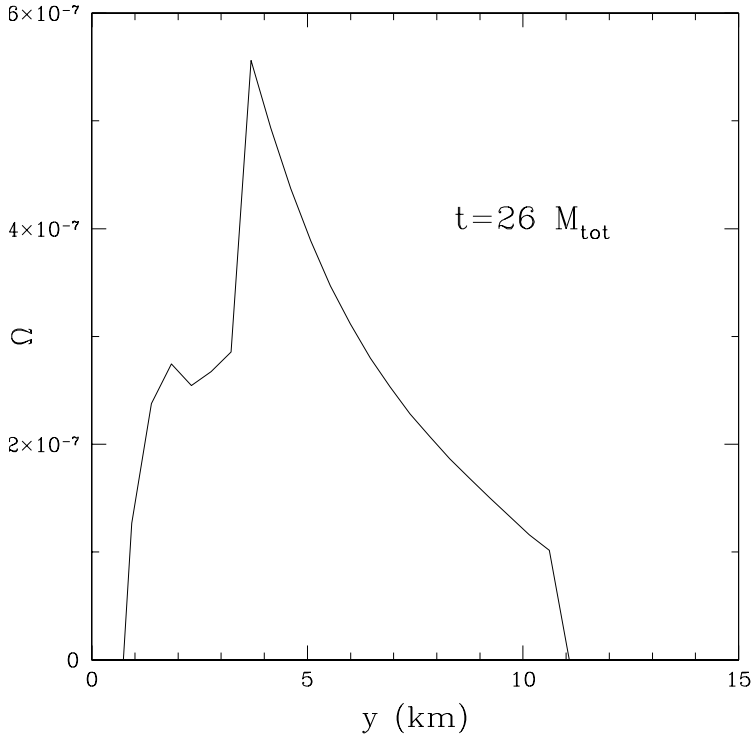

Figure 6.4: Profile of the angular velocity $\Omega = u^\phi/u^t$ at $t = 20M_{\rm tot}$ for the model described in Fig. 6.3.

different from zero (not shown in table 6.1), the object formed after the collision acquires a differential rotation, characterized by angular velocities as high as $5 \times 10^{-7}\mathrm{rad/s}$ at the peak, which is near the shock front on the (x, y) plane in the direction perpendicular to the initial star motion. This is shown in Fig. 6.4, which refers to the model of Fig. 6.3 at the instant preceding the apparent horizon formation. In the specific case shown, even the addition of this small amount of angular momentum is not sufficient to delay the collapse: the apparent horizon engulfs all the matter before the end of the simulation. Other possible outcomes of the evolution of systems with non-zero impact parameter will be briefly described in the next section.

The only differences among the models having a black hole as the final state (*i.e.* models of class A and C, *cf.* table 6.1) are the time interval between the start of the simulation and the beginning of the merger and the apparent horizon formation (see Fig. 6.5, which refers to models of class A) and to the fraction of matter which is inside the apparent horizon at the time when it first appears. This fraction decreases at the increase of the rest mass of the system and lies between 95% and 30%. However, all the matter ends up inside the apparent horizon before the end of the simulation. We also note that no qualitative differences are found between polytropic and ideal-fluid models; this is shown in Fig. 6.6, which offers a comparison between the central rest-mass densities for models A1 and C1, namely between a polytropic and an ideal-fluid EoS with identical initial conditions.

Larger differences can be noted, instead, in the comparison among models with different EoSs and for which the apparent horizon does not appear during the simulation. In this case, our code could follow many oscillations of the merged NS, as shown in Fig. 6.7, where we see the comparison between a polytropic and an ideal-fluid model (models B2 and D5, respectively). In the figure, we note that, despite having a slightly larger mass, the ideal-fluid model has a lower peak density with respect to the one of the polytropic model. The same holds true for the subsequent oscillations, the reason being the larger

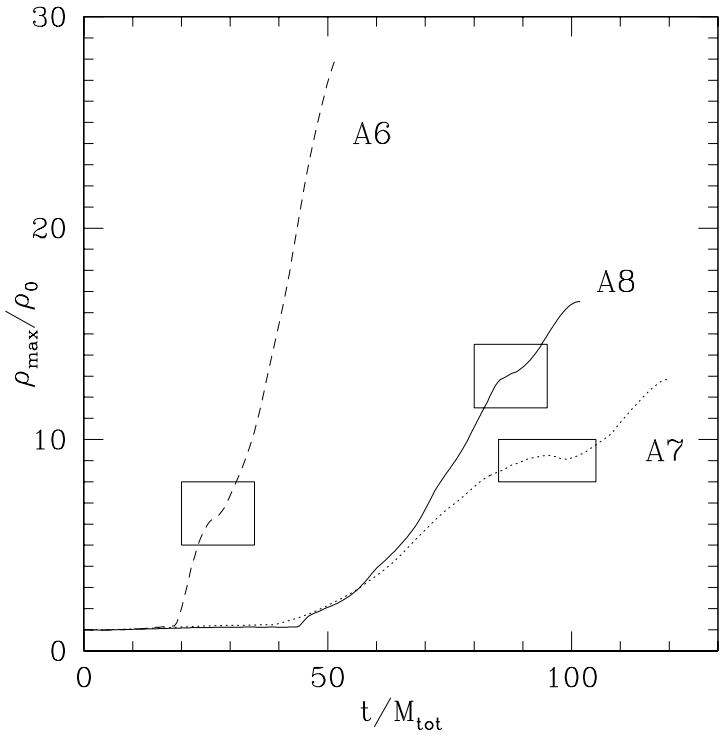

Figure 6.5: Comparison between the central rest-mass densities for models A6 (dashed line), A7 (dotted line) and A8 (solid line), namely between polytropic evolutions with different initial velocities and initial positions of the stars. We note a temporary slowing down in the increase of the central density, which we mark with the boxes. However, this does not significantly delay the collapse. The densities are normalized to the value at $t = 0$. The lines end when the apparent horizon forms and excision starts.

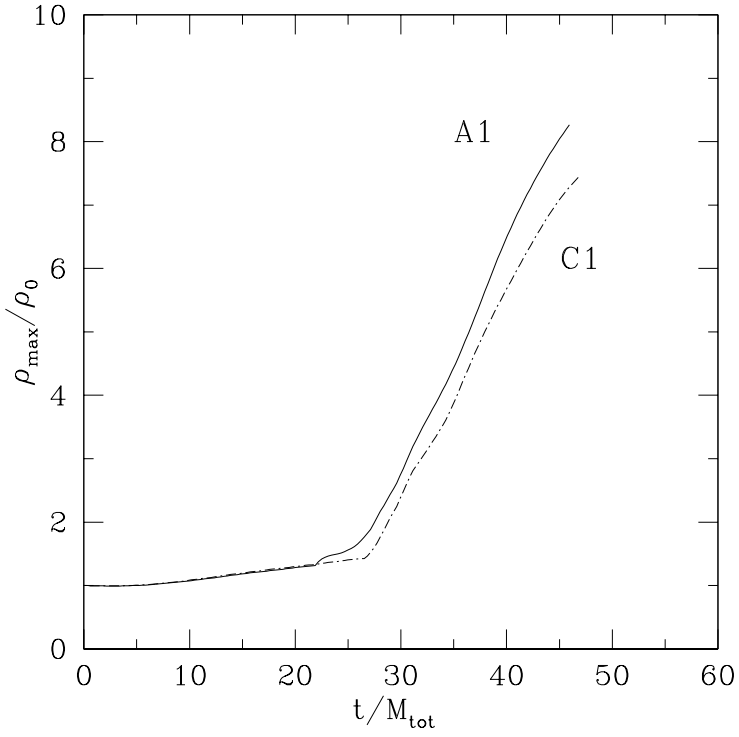

Figure 6.6: Comparison between the central rest-mass densities for models A1 and C1, namely between equivalent models except for the EoS. The densities are normalized to the values at $t = 0$. The lines end when the apparent horizon forms and excision starts.

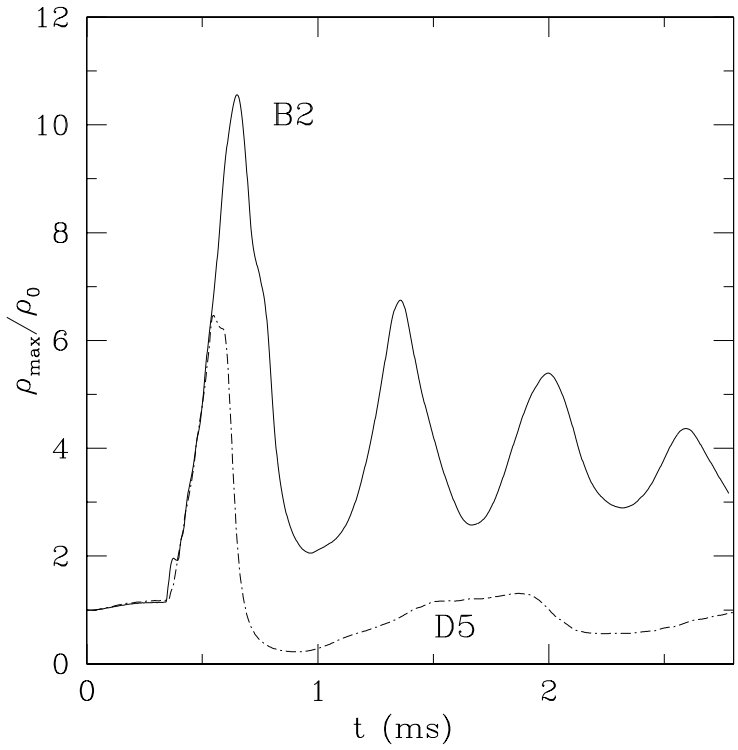

Figure 6.7: Comparison between the central rest-mass densities for models B2 and D5, namely between a polytropic and an ideal-fluid evolution not collapsing promptly, but exhibiting several oscillations of the merged NS. The densities are normalized to the value at $t = 0$. Here the time on the axis is shown in milliseconds, since the two models have (slightly) different mass.

dissipation occurring for the non-isentropic EoS.

6.3 Discussion of the results

From the results reported in table 6.1 (which includes only some of the performed simulations), we can see that the state reached by the merged object during the simulation varies according to the initial rest mass of the system and to the EoS, but it does not depend on the initial distance between the stars nor on their initial velocities, except for systems whose rest mass is very close to the critical mass. We have also performed some simulations with an impact parameter different from zero and thus with a non-vanishing angular momentum, but we have not included them in table 6.1, because our systematic study of these configurations is not yet concluded and we cannot present quantitative results. We have, however, illustrated the qualitative properties of one of these configurations in Fig.6.3 and in this section we will qualitatively compare them to the models with zero impact parameter as well.

In addition to checking the Shapiro conjecture [207] and the results found by Miller *et al.* [163], we have determined the *effective* critical masses which discriminate between the fates of prompt collapse and delayed collapse[1], for both the EoSs employed. In the following, we indicate the critical mass for a spherical star with the EoSs here used with $M_{c,0}$ and we recall that its value in the chosen units is $M_{c,0} = 1.46\,M_\odot$. We further indicate with $M_{c,\rm poly}$ and $M_{c,\rm IF}$ the *effective* critical masses we have found from our simulations in the case of a polytropic and an ideal-fluid EoS, respectively.

[1] Actually in our present simulations we could not cover evolution times long enough to see the delayed collapse, so we have only observed an oscillating NS.

Table 6.1: Summary of the data for the relevant models of TOV head-on collisions. The different columns refer respectively to: ratio of the total rest mass of the system to the critical mass $M_{c,0}$ for a cold star with the same EoS (for our models $M_{c,0} = 1.46 M_\odot$); mean proper radius of one star; type of EoS; modulus of the initial velocity of each star with respect to the centre of mass of the system (*Newt* stands for Newtonian infall velocity); initial proper separation between the centres of the stars; fate of the star at the end of the simulation, that is whether an apparent horizon (AH) forms or not.

Model	$\frac{M_{\rm tot}}{M_{c,0}}$	R (km)	EoS	v_0	d_0	fate	notes
A1	1.79	17	poly	Newt	$3.2R$	AH	
A2	1.29	16	poly	0.4c	$2.2R$	AH	
A3	1.24	16	poly	0	$3.9R$	AH	stars in contact at $t = 0$
A4	1.21	15	poly	Newt+10%	$3.9R$	AH	
A5	1.14	16	poly	Newt	$4.1R$	AH	
A6	1.13	16	poly	0.4c	$3.9R$	AH	
A7	1.08	16	poly	0	$2.0R$	AH	stars in contact at $t = 0$
A8	1.04	16	poly	Newt	$3.9R$	AH	
B1	1.02	16	poly	Newt	$3.9R$	NS	
B2	0.994	16	poly	Newt	$3.9R$	NS	
B3	0.992	16	poly	0	$3.9R$	NS	stars in contact at $t = 0$
B4	0.983	17	poly	0.4c	$3.7R$	NS	
B5	0.966	16	poly	Newt	$3.9R$	NS	
B6	0.100	18	poly	Newt	$2.4R$	NS	
C1	1.79	17	IF	Newt	$3.2R$	AH	
C2	1.75	17	IF	0	$3.2R$	AH	
C3	1.35	16	IF	Newt	$4.1R$	AH	
C4	1.26	16	IF	Newt	$4.0R$	AH	
C5	1.24	16	IF	0	$2.0R$	AH	stars in contact at $t = 0$
C6	1.23	16	IF	Newt	$4.0R$	AH	
C7	1.23	16	IF	0.4c	$2.2R$	AH	
C8	1.20	15	IF	Newt	$4.0R$	AH	
D1	1.16	15	IF	Newt	$4.2R$	NS	
D2	1.13	16	IF	Newt	$4.1R$	NS	
D3	1.13	16	IF	0.4c	$3.9R$	NS	
D4	1.08	16	IF	0	$2.0R$	NS	stars in contact at $t = 0$
D5	1.04	16	IF	Newt	$3.9R$	NS	
D6	0.100	18	IF	Newt	$2.4R$	NS	

In the models with polytropic EoS, since entropy is conserved, we expect that $M_{c,\rm poly} \simeq M_{c,0}$, while in the models with an ideal-fluid EoS, since entropy is not conserved, we expect that indeed some (spatially non-uniform) transfer of kinetic energy to internal energy does increase the *effective* critical mass with respect to the critical mass for a cold star, *i.e.* $M_{c,\rm IF} > M_{c,0}$.

In table 6.1, we divide the models we have evolved into four classes:

- *class A*: the polytropic models that promptly form an apparent horizon;
- *class B*: the polytropic models that do not form an apparent horizon within a dynamical timescale (and within the total time of the simulation);
- *class C*: the ideal-fluid models that promptly form an apparent horizon;

- *class D*: the ideal-fluid models that do not form an apparent horizon within a dynamical timescale (and within the total time of the simulation).

We now summarize the results of the simulations, first concentrating on the polytropic models, since this was the EoS used in the arguments of Shapiro [207] and in the computations of Miller *et al.* [163]. All the models of class A have total rest masses larger than $M_{c,0}$, while they differ in initial velocities, initial separation and initial impact parameter. At this point, we can already state that the Shapiro conjecture does not hold, namely that there exist some systems of head-on collisions with polytropic EoS that do collapse promptly to a black hole. This result is in agreement with the one found by Miller *et al.* [163].

All the models of class B have an initial rest mass smaller than $M_{c,0}$, except for model B1, which is, however, very near to the critical threshold. Our experience with the apparent-horizon finder in `Cactus` and `Whisky` (in particular in NS collapse simulations) indicates that for configurations in which an apparent horizon forms it does not always form at all resolutions; instead, in some cases, at lower resolutions the apparent horizon is not found. Thus, we think that model B1 would indeed form promptly an apparent horizon, if we evolved this configuration at a higher resolution, for which we did not have sufficient computational resources. By comparing the results for class A and B, we note that a $M_{c,\mathrm{poly}} \simeq M_{c,0}$, as expected.

The situation for the models of class C and D is analogous to those of models of class A and B, respectively. However, in the case of an ideal-fluid EoS, even though we expect $M_{c,\mathrm{IF}}$ to be larger than $M_{c,0}$, we have no a-priori indications of its value. Furthermore, we underline that these critical values cannot be computed analytically or through perturbative calculations, but only with fully-dynamical simulations. From our results, we can numerically delimit the value of the critical mass to be $1.16 M_{c,0} \lesssim M_{c,\mathrm{IF}} \lesssim 1.20 M_{c,0}$.

The value of the effective critical mass for a given EoS is also strongly influenced by the impact parameter of the near-head-on collision. In this case, in fact, the system has a non-vanishing angular momentum which shows up in the (differential) rotation of the merged object, as discussed in the previous section, and the rotation contributes to delaying the collapse. So, in general, the effective critical masses in these near-head-on cases are larger than the effective critical masses for the corresponding head-on collisions. Work is now in progress to perform a systematic study of near-head-on collisions. One of the possible outcomes has been shown in Fig. 6.3, where an apparent horizon promptly forms despite the presence of some amount of differential rotation in the merged object right after the collision. For similar models but with higher angular momentum and lower masses with respect to the one of Fig. 6.3, we have found that prompt collapse is avoided. In other models with still larger impact parameter, we have also found that the stars scatter away from the computational grid after a collision in which however a large fraction of the material of the two stars had temporarily merged.

6.4 Conclusion

We have performed numerous simulations of TOV head-on and near-head-on collisions and we summarize here the indications that we have inferred from them. We confirm and extend the results by [163, 94], showing that the Shapiro conjecture does not hold in all cases, but only under some more restrictive conditions. In our experiments, the most important factors that control the promptness or the deferment of the collapse are the EoS and the differential rotation that appears when the impact parameter is non-zero. The initial velocities are instead irrelevant for the qualitative end point of the simulation, at least in the cases of initial systems with masses far from the critical values for the total rest mass.

We have also analysed a more realistic reformulation of the Shapiro conjecture, that can be stated as follows:

> for every EoS and for every impact parameter b, there exists an effective critical mass $M_c(\mathrm{EoS}, \mathrm{b}) \geq M_{c,0}$ such that for every total rest mass of the system $M > M_c(\mathrm{EoS}, \mathrm{b})$ prompt collapse follows the collision, while for every $M < M_c(\mathrm{EoS}, \mathrm{b})$ the collapse is at least delayed, because of the increased pressure support generated by shock-heating and/or because of the centrifugal hang-up due to (differential) rotation.

Needless to say, more work is necessary to achieve a satisfactory knowledge on this scenario. Higher resolution simulations are required in order to improve the constrained region for the critical masses and repeating these simulations with realistic EoSs would give more physical insight in these violent events. These results will be presented in an upcoming article [33]. Finally, these simulations have shown that `Whisky` is capable of evolving very strong shocks in highly curved spacetimes and thus that it is ready for the more difficult problem of binary NS systems, which we will discuss in the next chapter.

Chapter 7

Toward the merger of binary neutron-star systems

In this chapter we describe the problem of binary systems of compact stars in general relativity. After an introduction on the relevance of the problem and a summary of the previous work, we will discuss our setup for binary NS simulations and the first tests performed. These tests have started only very recently (April 2004) and have proven to be satisfactory only in part. Although no definitive results have been obtained in the short time we have investigated this project, we have felt it important enough to be mentioned in this thesis. We are confident that, given the general tests done on `Whisky` (*cf.* Section 4.4) and the physical results discussed in Chapter 5 and Chapter 6, this preliminary phase in the study of the binary problem will be followed by one in which our numerical simulations will be used to study this process in detail. Our goal is primarily the computation of the gravitational radiation emitted by the merger, but we will be also interested in all the other aspects summarized in the following two sections.

7.1 The importance of the problem

Little is required to justify one's efforts in the study of binary systems. The relativistic *binary problem* still poses a fundamental challenge in general relativity and in theoretical and observational astrophysics, as well as in numerical relativity. The two-body problem, in fact, is one of the outstanding unsolved problems in classical general relativity, despite the simplicity of its formulation; furthermore, binary systems of compact objects are considered one of the most important sources for gravitational-wave emission and are thought to be at the origin of some of the most violent events in the Universe; finally, the numerical difficulties involved in the simulations of such highly dynamical systems (both of black holes and of NSs) have not yet been fully overcome by present-day numerical codes. We will summarize some of the most popular motivations (in addition to the sheerly theoretical, academical ones) for which so many researchers are attracted by this problem. Hereafter, we will focus on NS binaries only.

Binary NSs are known to exist and for some of the systems in our own galaxy (like the relativistic binary radio pulsars PSR B1913+16 and PSR B1534+12) general-relativistic effects in the binary orbit have been measured to high precision [249, 227, 131]. The coalescence and merging of two NSs in binary orbit into a single object is the inevitable fate of close-binary evolution. The most relevant dissipation mechanism for this systems is the emission of gravitational radiation.

For relativists, the main interest in the study of coalescing systems of compact objects arises from the richness of general-relativistic effects that accompany these processes, the gravitational-wave emission

in primis[1]. Detection of gravitational waves from NS binaries will provide a wide variety of physical information on the component stars, including their mass, spin, radius and EoS. The produced waveforms, in fact, depend on all these characteristics of the system [3].

NS binary systems are thought to be one of the most promising sources for the detection of the gravitational waves, because sources of this kind which would produce gravitational signals of amplitude large enough to be relevant for Earth-based gravitational-wave detection seem to be numerous. Recent improved estimates[2] of the extrapolation of the estimated galactic coalescence rates of NS binary systems to the local group indicates, that the most probable rates for detectable coalescences are 1 event per 3–10 years and 10–500 events per year, for the first-generation and the advanced gravitational-wave interferometric detectors [3], respectively [123]. These detectors are expected to be sensible to the gravitational signal produced by the last stages of the inspiral of coalescing systems situated up to a distance of hundreds of Mpc.

There are three possible characteristic gravitational-wave frequencies related to the inspiral and merger of binary systems. The first is the frequency of the orbital motion of the stars in the last stages of inspiral before tidal distortions become important. For typical NS binaries, the total inspiral timescale across the detectable frequency band is approximately 15 minutes [76]. During this time the number of cycles of gravitational waves, is approximately $\sim 10^3 - 10^4$. This radiation is characterized by low frequencies (tens of Hz to kHz) and by low amplitudes. The expectation of detecting such gravitational waves lies in the relatively long duration of the signal and in the rather accurate knowledge of its waveform, which can be computed with high-order post-Newtonian calculations [4]. High accuracy is essential during these stages since the templates must cover a large number of orbits and a phase error as small as $\sim 10^{-4}$ could in principle prevent detection [75, 95]. The aim of the post-Newtonian analysis is to compute the terms of the expansion up to the term $\mathcal{O}[(v/c)^{11}]$, in order to ensure that theoretical waveforms are sufficiently free of systematic errors to be reliable as templates against which the interferometric observational data can be compared [77] through matched-filtering techniques.

The other two characteristic frequencies are related to the gravitational waves produced during the merger stage[5] of the binaries. One frequency is associated with the fundamental oscillation modes of the

[1]There are also several cases in which the coalescence process of binary systems which are well approximated as Newtonian systems is of great current interest; these include the formation of blue stragglers in globular clusters from mergers of main-sequence-star binaries and the nuclear explosion or gravitational collapse of white-dwarf binary mergers (for other examples and discussions, see, *e.g.*, [30]).

[2]This estimate was made after the recent discovery of a new galactic NS binary population type [61].

[3]Two main types of gravitational-wave detectors are currently in operation or coming into operation: kilometer-size laser interferometers (LIGO [3] in the USA, VIRGO [54] in Italy, GEO [78] in Germany and TAMA [132] in Japan) and resonant-mass antennas [*Explorer* [29] in Geneva (Switzerland), *Nautilus* [29] in Frascati (Rome, Italy), *Auriga* [66] in Legnaro (Padua, Italy), *Allegro* [155] in Livingstone (Louisiana, USA), *Niobe* [45] in Perth (Australia) and *Mario Schenberg* [4] in São Paulo (Brazil)]. All these detectors can be tuned to have broader or narrower sensitivity regions and consequently lower or higher peak sensitivities, respectively. Interferometric detectors are better suited to measure gravitational signals in the frequency range between 1 Hz and some kHz; detection at lower frequencies is hindered by seismic noise, while at higher frequencies it is hindered by laser shot noise. Resonant-mass detectors are usually sensible to higher frequencies, of the order of kHz.

Furthermore, although much of the current theoretical focus is directed toward terrestrial interferometric experiments, yet another important type of detector will become operational in the future: LISA [79], the space-based five-million-kilometer-arm interferometer that will be placed in heliocentric orbit. The relevant frequency band for LISA is $10^{-4} - 1$ Hz, which is situated in a lower range with respect to terrestrial detectors.

[4]The post-Newtonian formalism consists in a series expansion in the parameter $\epsilon \sim M_{\rm tot}/r \sim v^2$, where $M_{\rm tot}$ is the total rest mass of the binary, r is the orbital separation and v is the orbital velocity. This parameter is small whenever the gravitational field is weak and the velocity is slow. In this analytic formalism the stars are treated as point masses. For further discussion of the post-Newtonian formalism, see [46] and references therein.

[5]By definition, the merger stage starts with the hydrodynamical interaction between the two NSs.

merged massive object formed (also if only transiently) after the onset of a merger (*c.f.* also Section 5.5). The other is that of the QNMs of the black hole, if it is formed in the final stage of the merger. Perturbation studies have revealed that the frequency f_{QNM} of the fundamental quadrupolar QNM of the black hole is $\sim (5-10)(3M_{\odot}/M_{\rm BH})$ kHz, where $M_{\rm BH}$ is the mass of the black hole. Note that f_{QNM} depends strongly on the angular-momentum parameter of the black hole $a = J/M_{\rm BH}^2$, but only when a approaches unity [140]. Numerical simulations in the frameworks of Newtonian [186], post-Newtonian [194], semi-relativistic [177] and fully-general-relativistic gravity [217] have instead indicated that, if a black hole is not produced promptly, the frequency of the fundamental oscillation modes of the merged massive object is between 2 and 3 kHz, depending on the EoS and on the initial compactness $M_{\rm NS}/R_{\rm NS}$ of each NS. Therefore, also these gravitational waves have a frequency that is too high to be detected by first-generation laser-interferometric detectors. However, in contrast with the frequencies of the QNMs of the formed black hole, these frequencies are not extremely high and they may be in the frequency range of advanced laser-interferometric detectors or resonant-mass detectors. Alternatively, for the detection of these high frequency waves, specially-designed narrow-band interferometers or resonant-mass detectors may be built.

As mentioned before, the signal of gravitational waves reaching the detectors has to be analysed using matched-filter techniques to extract the physical information. To apply this technique, theoretical templates of gravitational waveforms are needed. This fact has motivated an even more intense theoretical effort for preparing such templates. However, at present, no unified prescription is available for calculating gravitational waveforms over all the regimes and all the corresponding bands of detectable frequencies from binary NS coalescences. Indeed, an important theoretical goal is the construction of a smooth, self-consistent join between the different solutions for the different phases of the coalescence. Existing theoretical machineries for handling the separate wave frequencies differ considerably.

The study of NS binary systems is also finalized to the understanding of the origin of some type of γ-ray bursts, because the short rise times of the bursts imply that their central sources have to be highly relativistic objects [184]. After the observational confirmation that γ-ray bursts a have cosmological origin, it has been estimated that the central sources powering these bursts must provide a large amount of energy ($\sim 10^{51}$ ergs) in a very short timescale, going from one millisecond to one second (at least for a subclass of them, called *short γ-ray bursts*). It has been suggested that the merger of NS binaries could be a likely candidate for the powerful central source. The typical scenario is based on the assumption that a system composed of a rotating black hole and a surrounding massive disc is formed after the merger. If the disc had a mass $\gtrsim 0.1M_{\odot}$, it could supply the large amount of energy by neutrino processes or by extracting the rotational energy of the black hole.

The understanding of γ-ray bursts is a further motivation to investigate the final fate of binaries after mergers. The total gravitational masses of the known galactic NS binaries systems are in a narrow range $\sim 2.65-2.85M_{\odot}$. The present observational evidence indicates that the masses of the two stars in the known binaries are nearly equal and, if this is the general situation, then NSs in binary systems will not be tidally disrupted before the merger. As a result, the mass loss from the binary systems is expected to be small during the evolution and the mass of the merged object will be approximately equal to the initial mass of the binary system. The maximum allowed gravitational mass for spherical NSs is in the range $\sim 1.5-2.3M_{\odot}$, depending on the EoS. Even if we take into account the effect of rapid rigid rotation, this limit is increased by 20% at most. For uniform rotation, in fact, the angular velocity, and hence the centrifugal force which balances the gravitational force to increase the maximum mass, is limited by the Kepler limit at the equator, above which matter there would no longer be gravitationally bound.

On the basis of these considerations, the compact objects formed just after the merger of these binary

systems seem to be bound to collapse promptly to a black hole. However, this is not necessarily the case if the merged object rotates differentially. With differential rotation, in fact, the core may rotate faster than the outer envelope and may further increase the maximum mass without violating the Kepler limit at the equator. Baumgarte *et al.* [42] have found that differential rotation is very effective in increasing the maximum mass, up to over 60% even for very modest degrees of differential rotation. This suggests that merged objects of $\sim 2.5-3M_{\odot}$ may be dynamically stable against gravitational collapse to a black hole. Such differentially-rotating stars cannot maintain their state of rotation, since viscosity or magnetic fields would bring them to rigid rotation in a sufficiently long time. These processes dissipate or redistribute the angular momentum and so induce the eventual gravitational collapse to a black hole. These facts indicate that, while the end product of a binary merger would almost certainly be a black hole, this state may not be reached immediately. The final product of the merger of NS binaries is an open question depending not only on the nuclear EoS for high density neutron matter but also on the rotational profile of the merged object.

Another piece of information of great interest is the location of the innermost stable [6] circular orbit (ISCO). The evolution of a binary system is expected to occur in three distinct phases: *i*) a slow, adiabatic inspiral phase that is driven by gravitational-wave emission and can be approximated as a sequence of quasi-circular orbits; *ii*) a brief transition phase, where the inward radial motion increases and the orbital motion changes from slow inspiral to rapid plunge; *iii*) a plunge phase, terminating in the merger of the stars. The ISCO resides within the transition phase *ii*). The location of the ISCO is important because the gravitational wave quasi-periodic *chirp* signal of the slow binary inspiral ends at about twice the orbital angular frequency of the ISCO, when it changes its form to a gravitational-wave signal typical of a burst [87]. This determines the maximum frequency for the *chirp* signal, which is an important parameter for building templates for gravitational-wave detectors. The measure of the ISCO frequency can also provide direct information on the NS EoS [187].

Within the framework of Newtonian, post-Newtonian and spatially-conformally-flat approximations, the ISCO has been determined by different methods (see, *e.g.*, [187, 107] and references therein). Much less is known for fully-relativistic binaries. In the approximation of quasi-equilibrium, a turning point on a curve of the binding energy versus separation along a sequence of constant-rest-mass models marks the onset of secular instability. This turning-point theorem [224] was applied by Friedman, Ipser and Sorkin [106] to axisymmetric spacetimes and its applicability was extended to relativistic binary systems by Friedman, Uryu and Shibata [107]. This result applies equally to corotational binaries [7] and to irrotational binaries [8]. No such theorem exists, instead, for the onset of dynamical instability in full general relativity. Locating the ISCO instability therefore requires dynamical evolution simulations of the full set of Einstein equations for the gravitational field, coupled to those of relativistic hydrodynamics. A first attempt at this has been made by Marronetti *et al.* [149].

[6] We refer here to dynamical instabilities.

[7] These are binaries in which the stellar spins are locked with the orbital rotation in such a way that the stars do not spin in a frame rotating with the orbital velocity; for this reason, corotating binaries are also known as *synchronized* or *locked* binaries.

[8] For these binaries the spins of the stars and the orbital motion are not locked; instead, they are defined so as to have vanishing vorticity.

7.1.1 A summary of previous work

Newtonian simulations and analytical computations

For NS binaries, some aspects of coalescence can be understood by solving the Newtonian equations of hydrodynamics while treating the gravitational radiation as a perturbation in the quadrupole approximation. Such an analysis is valid only if $v \ll 1$ and $M/R \ll 1$, where M and R are the NS mass and radius, respectively. Newtonian treatments of the coalescence waveform come in two forms: numerical hydrodynamical simulations and analytic studies based on triaxial ellipsoid models for the interacting stars. The ellipsoidal treatments can handle the influence of tidal distortion and internal fluid motions and spin, but not the final merger and coalescence [148]. Given the absence of any underlying symmetry in the problem, numerical calculations must be done in 3 dimensions. They are also required to treat the complicated hydrodynamical interaction with ejection of mass and shock dissipation, which usually accompany the merger.

The first Newtonian numerical investigations on binary systems focused on the instabilities of the last stage of the inspiral phase, leading to the merger. The final merger of two stars in close-binary systems, in fact, takes place on a timescale comparable to the orbital period. In the case of stars with very different masses, this may happen because mass transfer from one star to the other leads to a rapid shrinking of the binary separation, which in turns accelerates the mass transfer rate, leading to an instability [223]. In addition to mass transfer instabilities, global hydrodynamical instabilities can drive a close-binary system to rapid coalescence once the tidal interaction between the two stars becomes sufficiently strong. The existence of these global instabilities for close-binary equilibrium configurations containing a compressible fluid and their particular importance for NS binary systems was demonstrated by Rasio and Shapiro [186] using numerical hydrodynamical calculations.

Instabilities in close-binary systems were also studied using analytic methods. The classical analytic work of Chandrasekar [67] for close binaries composed by NSs described as incompressible fluids was extended to compressible fluids in the work of Lai *et al.* [135]. This analytic study confirmed the existence of dynamical and secular instabilities for sufficiently close binaries containing polytropes. Although these simplified analytic studies gave some physical insight into problem of global fluid instabilities, fully-numerical calculations remain essential for establishing the stability limits of close binaries accurately and for following the non-linear evolution of unstable systems all the way to complete coalescence.

Several groups have performed Newtonian calculations using different numerical methods and focusing on different aspects of the problem. Nakamura and collaborators (see [172] and references therein) were the first to perform 3-dimensional hydrodynamical calculations of binary NS coalescence, using a traditional Eulerian finite-difference code. Rasio and Shapiro [186], instead, used smoothed particle hydrodynamics (SPH) in Newtonian gravity and focused on determining the stability properties of initial binary models in strict hydrostatical equilibrium and on calculating the emission of gravitational waves from the coalescence of unstable binaries. Many of the results of [186] were later independently confirmed by New and Tohline [175], who used a completely different numerical method, and by Zhuge *et al.* [264, 265], who also used SPH and also explored in detail the dependence of the gravitational wave signals on the initial NS spins. Ruffert *et al.* [196, 194, 195] incorporated a treatment of the nuclear physics (realistc EoSs, allowing for the study of neutrino physics) in their hydrodynamical calculations (done using both SPH and PPM codes), motivated by cosmological models of γ-ray bursts.

The above-mentioned Newtonian hydrodynamical calculations yielded some insight into the coalescence process. These calculations also served as benchmarks in the weak-field, slow-velocity limit of

general relativity for later-developed relativistic codes. However, fully-relativistic calculations are clearly required for quantitatively reliable coalescence waveforms and to determine those qualitative features of the final merger which can only result from strong-field effects.

Quasi-equilibrium simulations

Equilibrium circular orbits do not exist in general relativity because of the emission of gravitational waves. However, outside the ISCO, the timescale for orbital decay by radiation is much longer than the orbital period, so that the binary can be considered to be in quasi-equilibrium. This allows one to neglect both gravitational waves and wave-induced deviations from a circular orbit to a very good approximation outside the ISCO. Accordingly, the stability of quasi-circular orbits can be studied by truncating the radiation-reaction terms in a post-Newtonian expansion of the equations of motion [146, 253]. Alternatively, one can solve a subset of the full non-linear Einstein equations numerically in the 3 + 1 formalism on time slices with a spatial 3-metric chosen to be conformally flat [256]. In the spirit of the York-Lichnerowicz conformal decomposition, which separates radiative variables from non-radiative ones [145, 261], such a choice is believed to effectively minimize the gravitational wave content of the space-time. In addition, one can set the time derivatives of the metric functions equal to zero in the comoving frame, forcing the solution to be approximately time independent in that frame.

Lombardi *et al.* [148] calculated post-Newtonian quasi-equilibrium configurations of NS binaries obeying a polytropic EoS and used the second-order variation of the energy functional to identify the ISCO along their sequences. The first calculations in full general relativity of equal-mass, polytropic corotating NS binaries were performed by Baumgarte *et al.* [40]. They integrated the Einstein equations together with the relativistic equations of hydrostatical equilibrium, obtaining numerical solutions of the initial-value problem and approximate quasi-equilibrium evolution models for these binaries. Their numerical method for the coupled set of non-linear elliptic equations consisted in adaptive multi-grid integrations in 3 dimensions. Baumgarte *et al.* [40] used the resulting models to construct sequences of constant rest mass at different radii, locating turning points along binding-energy equilibrium curves to identify the ISCO and its angular velocity. They found, in agreement with Newtonian treatments, that an ISCO exists only for polytropic indexes $N \geq 1.5$; for softer EoSs, the stars are in contact before the ISCO is reached. Generalizing these calculations for realistic EoSs is straightforward, but has not yet been performed.

Subsequently, Uryu and Eriguchi [243] numerically calculated the first 3-dimensional equilibrium solutions for irrotational equal-mass binaries with polytropic component stars in Newtonian gravity. Constructing irrotational binaries is much more involved than constructing corotational binaries. On the other hand, unlike what happens for binaries consisting of ordinary stars, irrotational NS binary configurations are thought to be the most realistic configurations; it was in fact shown by Bildsten and Cutler [43] with simple dimensional arguments that an implausibly small value of the effective viscous time would be needed in order to reach complete synchronization just before final merging. Fully-relativistic generalizations of the calculations by Uryu and Eriguchi were performed by several groups. Bonazzola *et al.* [50, 52] reported the first relativistic results from calculations of irrotational equilibrium sequences with constant baryon number.

Later, different groups [51, 111, 244, 150, 239, 236, 237, 238] used a multi-domain spectral method to tackle the same problem. Marronetti *et al.* [150] constructed irrotational models of NS binaries in Cartesian coordinates in the approximations that a helicoidal Killing vector exists and that the 3-geometry is conformally flat. Similar results by Uryu *et al.* [244] demonstrated that, as in corotational binaries, the maximum mass increases with decreasing separation. However, they also found that the

increase in maximum mass is smaller for irrotational binaries than for corotational binaries. This result is not surprising, since NSs in corotational binaries are rotating with respect to the rest frame of the binary, which by itself increases their maximum mass (see, *e.g.*, [71]).

While evolutionary sequences of corotational binaries end either at the ISCO or at contact, irrotational sequences typically end with the formation of a cusp before they reach the ISCO [51, 244]. As analysed by Uryu *et al.* [244], this cusp corresponds to an inner Lagrange point, across which the NSs will transfer mass. Uryu *et al.* [244] found that only binaries with very stiff EoS ($\Gamma = 2 - 3$) reach an ISCO before they form a cusp, while binaries with softer EoSs form a cusp first. The cusp and the ISCO occur at very similar frequencies. In general, corotational binaries have more angular momentum, since the individual stars carry a spin angular momentum in addition to the orbital angular momentum of the binary. Similarly, the binding energy of corotational binaries is slightly larger than the one of irrotational binaries, because the ADM mass includes the additional spin kinetic energy of the individual stars.

"Hydro-without-hydro" simulations

As discussed above, in order to produce templates for gravitational-wave detection, it is important to have a continuous theoretical knowledge of the gravitational-wave signal emitted from the last stages of binary NS coalescences. On one side, it is hard to imagine that fully-general-relativistic hydrodynamical numerical calculations will be able to follow the inspiral reliably from outside the ISCO through many orbital periods to the onset of instability at the ISCO, followed by the plunge and the merger. Such calculations would accumulate significant amounts of numerical error and would be computationally prohibitive. On the other side, it is possible that other means of modeling NS binaries, in particular post-Newtonian point-mass techniques, break down somewhere outside of the ISCO, when finite-size and relativistic effects become important.

This leaves a gap between the regimes that post-Newtonian and fully-numerical calculations can model. Filling this gap for the late inspiral, immediately prior to the plunge therefore requires an alternative, approximate approaches. Several different such approaches have been suggested [44, 55, 133, 251, 250, 86, 87, 217]. Here we will focus on the *hydro-without-hydro* approach adopted by Duez *et al.* [86, 87]. This approach approximates the binary orbit outside of the ISCO as circular and treats the orbital decay as a small correction. For each binary separation, the matter distribution can then be determined independently by the quasi-equilibrium methods. The emitted gravitational radiation is then computed by using the binary solution for the matter terms in the Einstein field equations. In particular, the gravitational fields are be evolved in the presence of these predetermined matter sources with a relativistic evolution code using a *hydro-without-hydro* approach. Within this approximation, there is no need to evolve any of the hydrodynamics equations for the source, since it is assumed that the stars move in circular orbits and are little affected by the gravitational waves; instead, it is possible to simply rotate the source terms on the numerical grid by an angle ϕ obtained by the relation $\mathrm{d}\phi/\mathrm{d}t = \Omega_{\rm orb}$, where $\Omega_{\rm orb}$ is the orbital angular velocity. Repeating this calculation for members of an evolutionary sequence at discrete separations r, the gravitational-wave amplitude [9] $A(r,t)$ and the orbit-averaged gravitational-wave luminosity $\mathrm{d}M/\mathrm{d}t(r)$ at these separations are obtained. A fitting function based on least squares can then be used to interpolate A, M and $\mathrm{d}M/\mathrm{d}t$ to any intermediate separation. The inspiral is determined

[9] The wave amplitude is here defined as

$$A(r,t) = \sqrt{\frac{5}{16\pi}(\psi_{22}^2 + \psi_{2-2}^2)}\,, \tag{7.1.1}$$

where ψ_{lm} are even-parity gauge-invariant metric perturbations.

by computing the effective radiation reaction due to the radiation of mass-energy by gravitational waves. The inspiral rate is thus $\mathrm{d}r/\mathrm{d}t = (\mathrm{d}M/\mathrm{d}t)/(\mathrm{d}M/\mathrm{d}r)$. Solving this equation determines r as a function of t, which then allows to express $A(r,t)$ in terms of t only and so gives the complete quasi-equilibrium wavetrain.

Duez *et al.* [86] implemented such a scheme for corotational binaries, based on the quasi-equilibrium models of Baumgarte *et al.* [40]. In Duez *et al.* [87], these results were compared with those for an irrotational sequence, based on the models of Uryu *et al.* [245]. These simulations are only illustrative because the position at which gravitational extraction was performed was not in the wave zone. For a given separation, the gravitational-wave luminosity $\mathrm{d}M/\mathrm{d}t$ is very similar for corotational and irrotational models, as expected, since the gravitational-wave emission is dominated by the matter density, which is fairly similar for the corotational and irrotational binaries, while matter current distributions play a less important role. However, the inspiral of corotational binaries proceeds faster than that of irrotational binaries. Duez *et al.* [87] also pointed out that the entire gravitational wavetrain, from the slow inspiral to the ISCO and the subsequent plunge and merger, can be constructed by matching results from a quasi-adiabatic approximation of the inspiral and a dynamical simulation of the coalescence.

General-relativistic simulations

Several groups have launched efforts to solve the equations of relativistic hydrodynamics together with Einstein equations and to model the coalescence and merger of NS binaries [179, 39, 99, 100]. The first successful simulations of binary NS mergers were those of Shibata and Uryu [210, 216]. They adopted a polytropic EoS with index $N = 1$ and solved the equations of relativistic hydrodynamics with artificial viscosity schemes and the Einstein equations in the original form studied by one of the authors [215] (*cf.* Section 2.2). In a more recent work [218], these authors modified the scheme for solving the hydrodynamics equations and adopted a conservative formalism. As gauge conditions, they used "approximate maximal slicing" to specify the lapse and "approximate minimal distortion" to determine the shift. They also added a radial component to the shift vector to avoid grid stretching in collapse situations. As initial data, Shibata and Uryu [210, 216, 218] prepared equal-mass polytropic models of NS binaries in quasi-equilibrium with both corotational and irrotational velocity profiles. For both velocity profiles they prepared different models with individual stellar masses ranging from about 75% to 100% of the maximum allowed mass of non-rotating stars in isolation. For corotating models, they adopted as initial data models in which the inner surfaces of the stars were in contact; in these configurations the stars were fairly close to the ISCO. Since quasi-equilibrium irrotational sequences with this polytropic index, instead, terminate with the formation of a cusp formation for orbits that are still outside of the ISCO, Shibata and Uryu [210, 216] considered in this case the initial data consisting in binaries possessing a cusp and triggered the merger by artificially reducing the angular momentum by about 2.5% (this last restriction was later removed in [218]).

Overall, Shibata and Uryu [210, 216, 218] found fairly similar results for corotational and irrotational binary models. The most significant difference is that corotational binaries have more angular momentum in the outer parts of the binary, which leads to the formation of spiral arms during the coalescence. The spiral arms contain a few percent of the total mass and may ultimately form a disc around the central object. Initially, in their simulations one of the largest limitation on the accuracy was represented by the location of the outer boundaries, which, because of limited computational resources, had to be imposed well within a wavelength $\lambda_{\rm GW}$ (where $\lambda_{\rm GW} = 1/(2f_{\rm GW})$ and $f_{\rm GW}$ is the initial orbital frequency) of the gravitational radiation from the binary (*i.e.* at about $\lambda_{\rm GW}/3$). This means that the gravitational waves were extracted without being in the wave zone, which necessarily introduces errors. After having gained

access to a more powerful supercomputer, Shibata and Uryu [218] therefore repeated these calculations on computational grids that extended to about a gravitational wavelength. Qualitatively, these improved results are very similar to their earlier ones, although the onset of black-hole formation shifts to slightly larger masses. As expected, the features of this simulations which were the most affected by these improvements were the gravitational waveforms.

It should be noted that the gravitational waveforms produced during the merger depend sensitively on the compactness of the merging NSs. For mergers containing stars which are not very compact, a transient massive NS is formed and survives for a time much longer than the dynamical timescale. Such massive NSs are highly non-axisymmetric, so that quasi-periodic gravitational waves associated with non-axisymmetric deformations are emitted. These quasi-periodic gravitational waves have typical frequencies of $\sim 2-3$ kHz, which fall in the sensitivity region of present gravitational-wave detectors. The ratio of the frequencies of these peaks to the frequencies of the innermost orbits seems to be insensitive to the compactness of the stars, but to depend on the stiffness of their EoS. This indicates that its observation could constrain the stiffness of the EoS. It was also found that the luminosity of quasi-periodic gravitational waves is fairly large, so that a massive transient NS would likely collapse to a black hole eventually, due to the angular momentum dissipation through gravitational radiation.

For mergers of binaries containing stars with slightly larger compactness, on the other hand, a transient massive highly-non-axisymmetric object is also formed and its lifetime is fairly long, so that it is possible to identify clearly the characteristic peaks in the power spectrum of the emitted gravitational waves. Finally, for models with large compactness, the merged object collapses into a black hole on a dynamical timescale and hence quasi-periodic gravitational waves are excited only on a short timescale. Since the amplitude of the peaks in the Fourier spectra of gravitational waves associated with the non-axisymmetric, quasi-periodic oscillations of the merged object depends on the lifetime of the transient massive object, from observations of such amplitudes it may be possible to determine the properties of the object formed after the merger.

While the simulations of Shibata and Uryu [216, 218] are pioneering, it would be desirable to confirm their findings with independent simulations with other fully-general-relativistic codes. Many aspects of the simulations could also be improved in the future. In fact, several other factors, including effects of a realistic EoSs, magnetic fields and neutrino transport, may play an important role in the coalescence of NS binaries. It will probably take still a long time before all these improvements can be incorporated in fully-general-relativistic simulations.

7.2 Simulating binary neutron-star systems with Whisky

7.2.1 Initial data

As initial data for NS binary simulations we use the ones produced by the group working at the Observatoire de Paris-Meudon [111, 239, 236, 237, 238]. These data, which we refer to also as the *Meudon data*, are obtained under the simplifying assumptions of quasi-equilibrium and of conformally-flat spatial metric, which were discussed in Section 7.1.1. These initial configurations are computed using a multi-domain spectral-method code named LORENE, which is a free software under the GNU General Public License; a specific routine then converts from spherical coordinates to a Cartesian grid of the desired dimensions and shape.

It is in general useful to have initial data in a co-rotating coordinate frame (*i.e.* a frame rotating with the initial orbital angular velocity of the system), since this has superior capabilities in conserving angular momentum as compared to inertial frames. Furthermore, in such coordinates the evolved quantities

change on the timescale of inspiral, which is much longer than the orbital timescale and therefore a more regular evolution is obtained [88]. For these reasons and because the Meudon data are not provided in a co-rotating frame[10], we make a transformation from an inertial frame with coordinates $(\bar{t}, \bar{x}, \bar{y}, \bar{z})$ (barred variables will represent quantities in the inertial frame in the remainder of this section) to a co-rotating frame with coordinates (t, x, y, z) and constant angular velocity $\vec{\Omega}$, which is assumed to be aligned with the z axis. To obtain this, we apply the following relations

$$\begin{aligned} \bar{t} &= t \\ \bar{x} &= x\ \cos(\Omega t) - y\ \sin(\Omega t) \\ \bar{y} &= x\ \sin(\Omega t) + y\ \cos(\Omega t) \\ \bar{z} &= z\ . \end{aligned} \tag{7.2.2}$$

It is convenient to compare variables in the two frames at an instant $\bar{t} = t = 0$, at which the two frames are aligned. At this instant, the line element transforms from

$$d\bar{s}^2 = -(\bar{\alpha} - \bar{\beta}^i\bar{\beta}_i)d\bar{t}^2 + 2\bar{\beta}_i d\bar{x}^i d\bar{t} + \bar{\gamma}_{ij} d\bar{x}^i d\bar{x}^j \tag{7.2.3}$$

to

$$\begin{aligned} ds^2 &= -\left(\bar{\alpha} - \bar{\gamma}_{ij}(\bar{\beta}^i + (\vec{\Omega}\times\vec{r})^i)(\bar{\beta}^j + (\vec{\Omega}\times\vec{r})^j)\right) dt^2 \\ &\quad +2\bar{\gamma}_{ij}(\bar{\beta}^i + (\vec{\Omega}\times\vec{r})^i)dx^j dt + \bar{\gamma}_{ij}dx^i dx^j, \end{aligned} \tag{7.2.4}$$

where $\vec{r}$ has components (x, y, z). From this equation, we see that the following transformation rules apply at $\bar{t} = t = 0$:

$$\begin{aligned} \alpha &= \bar{\alpha} \\ \beta^i &= \bar{\beta}^i + (\vec{\Omega}\times\vec{r})^i \\ \gamma_{ij} &= \bar{\gamma}_{ij}\ . \end{aligned} \tag{7.2.5}$$

Equations (7.2.5) provide the transformation rules for the initial metric data; effectively, the only change is the addition of a new rotation term in the shift. Like γ_{ij}, also any other spatial second-rank tensor is not modified, *e.g.* $T_{ij} = \bar{T}_{ij}$ and $K_{ij} = \bar{K}_{ij}$. At later times, vectors and tensors in the two frames will also differ by a rotation. However, we note that at all times there will be some inertial frame, related to $(\bar{t}, \bar{x}, \bar{y}, \bar{z})$ by a rotation matrix, which has axes aligned with the rotating frame and whose metric is related to that of the rotating frame by equation (7.2.5). Using the coordinate transformations (7.2.2) we can derive further relations frames at $\bar{t} = t = 0$, for example

$$\begin{aligned} u^0 &= \bar{u}^0 \\ u^i &= \bar{u}^i - (\vec{\Omega}\times\vec{r})^i\bar{u}^0 \\ u_i &= \bar{u}_i \\ v^i &= \bar{v}^i - (\vec{\Omega}\times\vec{r})^i\ . \end{aligned} \tag{7.2.6}$$

Since the inverse of a tensor is unique, the last equation of (7.2.5) implies $\gamma^{ij} = \bar{\gamma}^{ij}$ and, equivalently, $T^{ij} = \bar{T}^{ij}$ and $K^{ij} = \bar{K}^{ij}$.

In Section 2.2.1, we defined the total mass and angular momentum of an asymptotically flat spacetime by two volume integrals (2.2.29) and (2.2.30). These integrals remain valid also in rotating frames, since

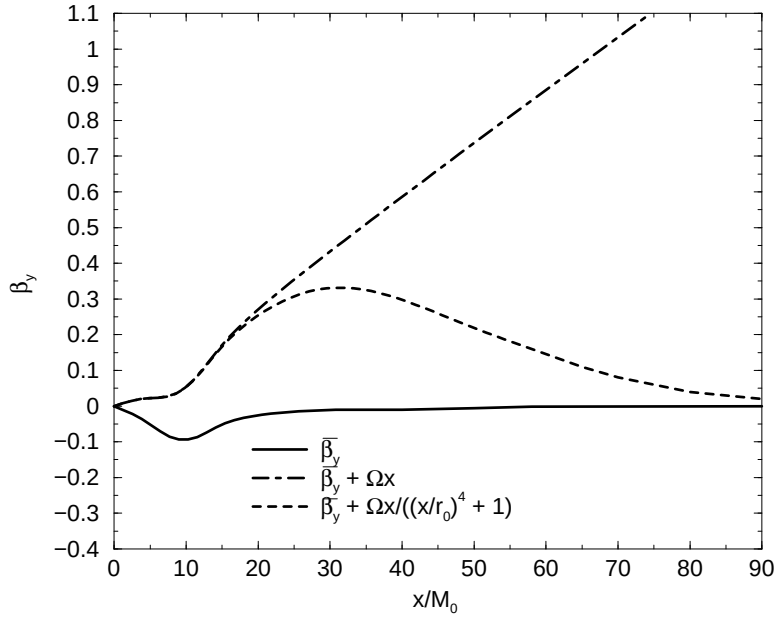

Figure 7.1: Comparison of the profiles of the y component of the shift along the x axis for the typical simulation as reported in the text: the solid line corresponds to the shift as set in the *Meudon data*; the dot-dashed line corresponds to the *Meudon-data* shift plus the co-rotating shift and the dashed line corresponds to the *Meudon-data* shift plus the corrected co-rotating shift. Note that *i*) the stellar center is at about $10M_0$, where M_0 is the rest mass of one of the stars; *ii*) the dot-dashed line extends outside the light cylinder ($|\boldsymbol{\beta}| > 1$); *iii*) the maximum of the corrected shift is shown to be around $30M_0$ only for graphical purposes, In the actual simulations it is usually placed to farther distances (*e.g.* at $60M_0$).

the surface integral formulae (2.1.14) and (2.1.15) from which they are derived can be obtained assuming only that the 3-metric and extrinsic curvature are asymptotically flat [178, 53].

The transformation to the co-rotating frame is not, however, devoid of drawbacks. In fact, the transformation (7.2.5) yields

$$\begin{aligned} \beta^x &= \bar{\beta}^x - \Omega y \,, \\ \beta^y &= \bar{\beta}^y + \Omega x \,, \\ \beta^z &= \bar{\beta}^z \,, \end{aligned} \tag{7.2.7}$$

where we have expanded the components of $\vec{\Omega}$, namely $(0, 0, \Omega)$. Note that, if the outer boundary is moved to the large distances which one would like to reach, this yields potentially large shifts, which could lead to large deformations of the metric and make the code crash. In order to avoid this problem and following what is done in binary black-hole simulations (where this problem shows up even at shortest distances with respect to binary NS simulations, since the angular velocity Ω is higher), we impose a fall-off on the shift at large distances. In particular, instead of (7.2.7) we use

$$\begin{aligned} \beta^x &= \bar{\beta}^x - \Omega \frac{y}{(y/r_0)^4 + 1} \,, \\ \beta^y &= \bar{\beta}^y + \Omega \frac{x}{(x/r_0)^4 + 1} \,, \\ \beta^z &= \bar{\beta}^z \,, \end{aligned} \tag{7.2.8}$$

[10]The shift condition used in producing these data is determined through the Killing equation which is implicit in the quasi-equilibrium assumption for binary systems.

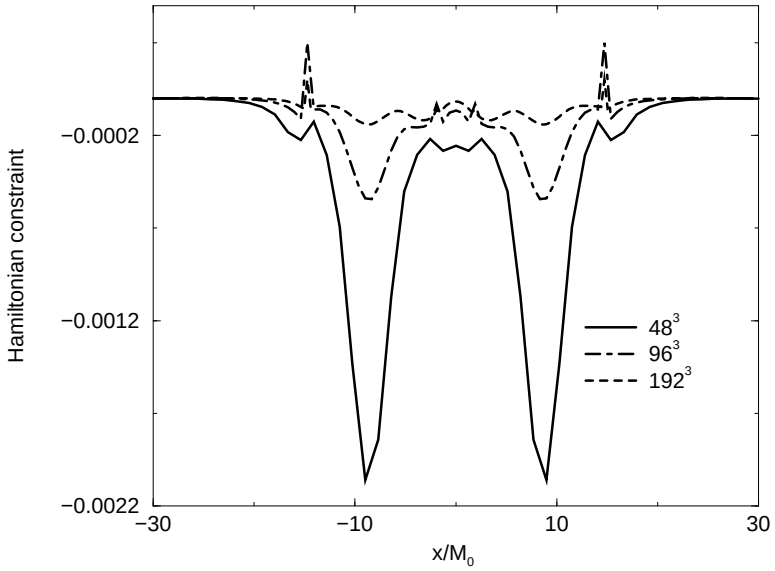

Figure 7.2: Comparison of the Hamiltonian constraint violation as computed along the x axis on the initial data for different resolutions.

which has the same behaviour as (7.2.7) for distances $r \ll r_0/\sqrt[4]{3}$, which is the location of the maximum of the shift (see Fig. 7.1, where we show a comparison of some different possibilities for the initial shift), while it goes asymptotically as $1/r^3$ for $r \gg r_0/\sqrt[4]{3}$, mimicking the asymptotic behaviour of the frame dragging of a rotating star.

7.2.2 Specific convergence tests with uniform grids

The simulations we discuss in this section refer to evolutions of equal-mass irrotational initial data having the following properties:

- orbital period : $T = 3.395$ ms
- rest mass of a star : $M_0 = 1.625 M_\odot$
- gravitational mass of a star : $M = 1.456 M_\odot$
- radius of a star : $R = 13.68$ km
- coordinate distance between stellar centres : $45 \text{ km} = 41 M_0 = 0.19 \lambda_{\rm GW} = 3.4 R$
- compactness of a star : $M/R = 0.14$
- ratio of the polar to the equatorial radius of a star : 0.93
- polytropic exponent : $\Gamma = 2$

Initially, the centers of the stars lie on the x axis. In Fig. 7.2 we show a slice along the x axis of the Hamiltonian constraint violation as computed at the initial time at different resolutions. We recall that the Hamiltonian constraint equation (2.1.12) does not depend on the shift, so our choices of the initial shift do not influence this result. As expected, the convergence factor for these data is nearly two, except near extrema.

The convergence is still globally second order also in the first stages of the evolution, namely for a fraction of a period. This is shown in Fig. 7.3, where upper and lower panels refer to evolutions in the inertial frame and in the co-rotating frame, respectively. While comparing the growth of the Hamiltonian

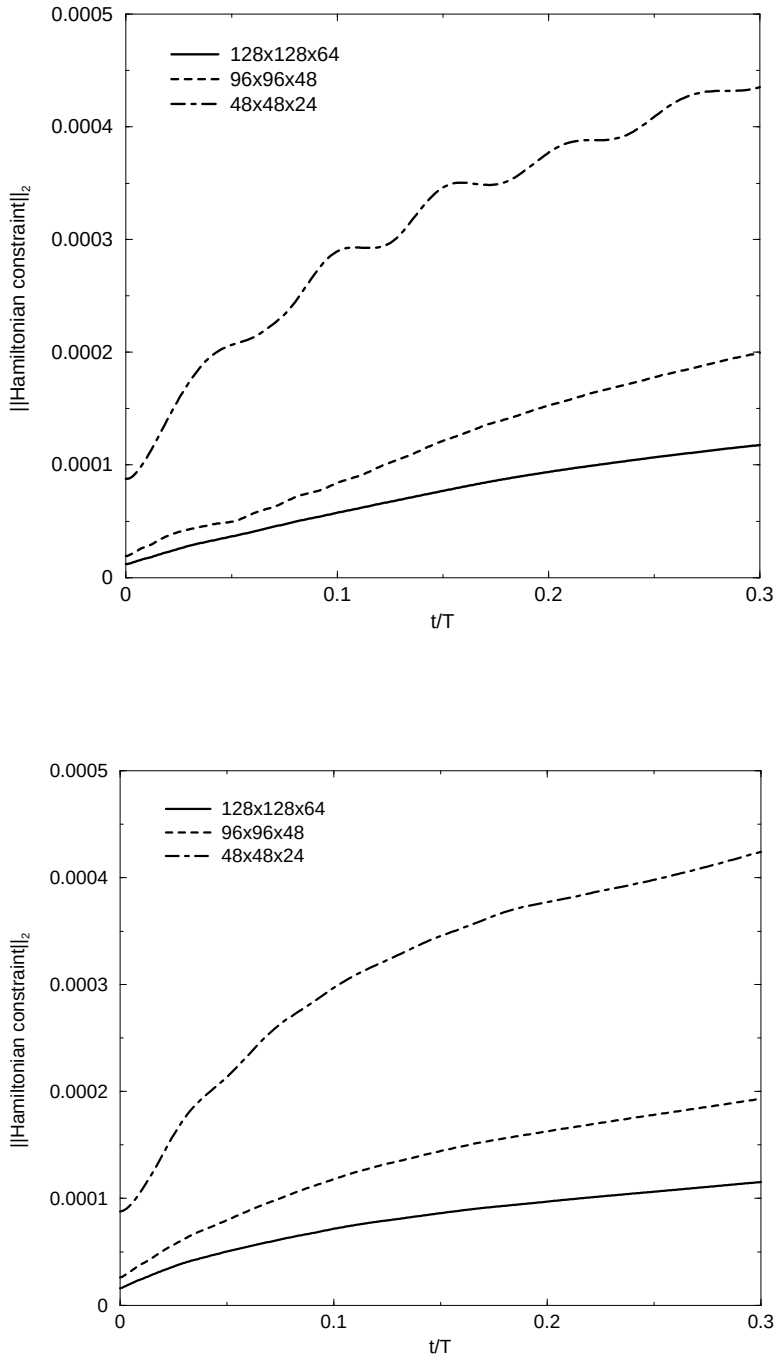

Figure 7.3: Comparison of the time evolution of the L_2 norm of the Hamiltonian constraint violation in the first stages of evolution at different resolutions. The upper panel refers to an evolution in the inertial frame, while the lower panel to an evolution in the co-rotating frame. Time is expressed in terms of the initial orbital period T.

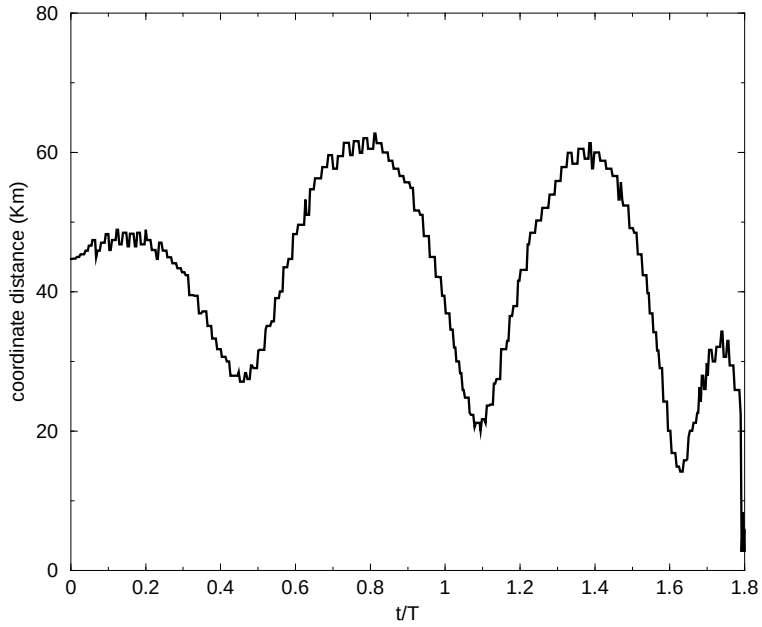

Figure 7.4: Time evolution of the coordinate distance between the maximum-rest-mass-density points of the stars. Time is expressed in terms of the initial orbital period T.

constraint violation in the two cases, we note two main differences: firstly, the evolution in the co-rotating frame is less oscillatory and secondly the absolute values of the violation in the evolution in the co-rotating frame are slightly smaller than those obtained in the inertial frame (*cf.*, for example, at $t/T = 0.3$).

Over longer evolution times, however, the second-order convergence is not preserved and the behaviour of the fields, gauges and matter variables varies sensibly with resolution as well as with the location of the outer boundary. We performed evolutions with resolutions ranging from $0.9M_0$ to $0.3M_0$ and outer boundary distances ranging from $31M_0$ to $124M_0$ or, equivalently, from $0.14\lambda_{\rm GW}$ to $0.56\lambda_{\rm GW}$. Clearly these resolutions are not sufficient for reliable evolutions (*cf.*, for example, [209]). We are presently experiencing the same limitations on the convergence as those reported by Miller *et al.* [162], while it is interesting to note that Marronetti *et al.* [149], with similar resolutions, claimed to have been able to keep convergence for longer times and so to have been able to locate the position of the ISCO.

One positive remark we can make at this point is that in our evolutions for the above-mentioned initial data we can follow the orbit of the stars for more than one period, before the beginning of the plunge, as is shown in Fig. 7.4, which reports the time evolution of the coordinate distance between the maximum-rest-mass-density points of the stars. Comparing evolutions with the same resolution, boundary location and initial data, except for different initial distances of the stars, ranging from 40 to 100 km, we have found similar behaviours. In Fig. 7.5 we report snapshots at different times of a typical evolution obtained from the above initial data.

We expect that the problems discussed above will be strongly suppressed, if not completely removed, by increasing the resolution in the regions occupied by the stars and by moving the outer boundaries further out. As for the collapse calculation, we are going to achieve this by using grids with several levels of refinement.

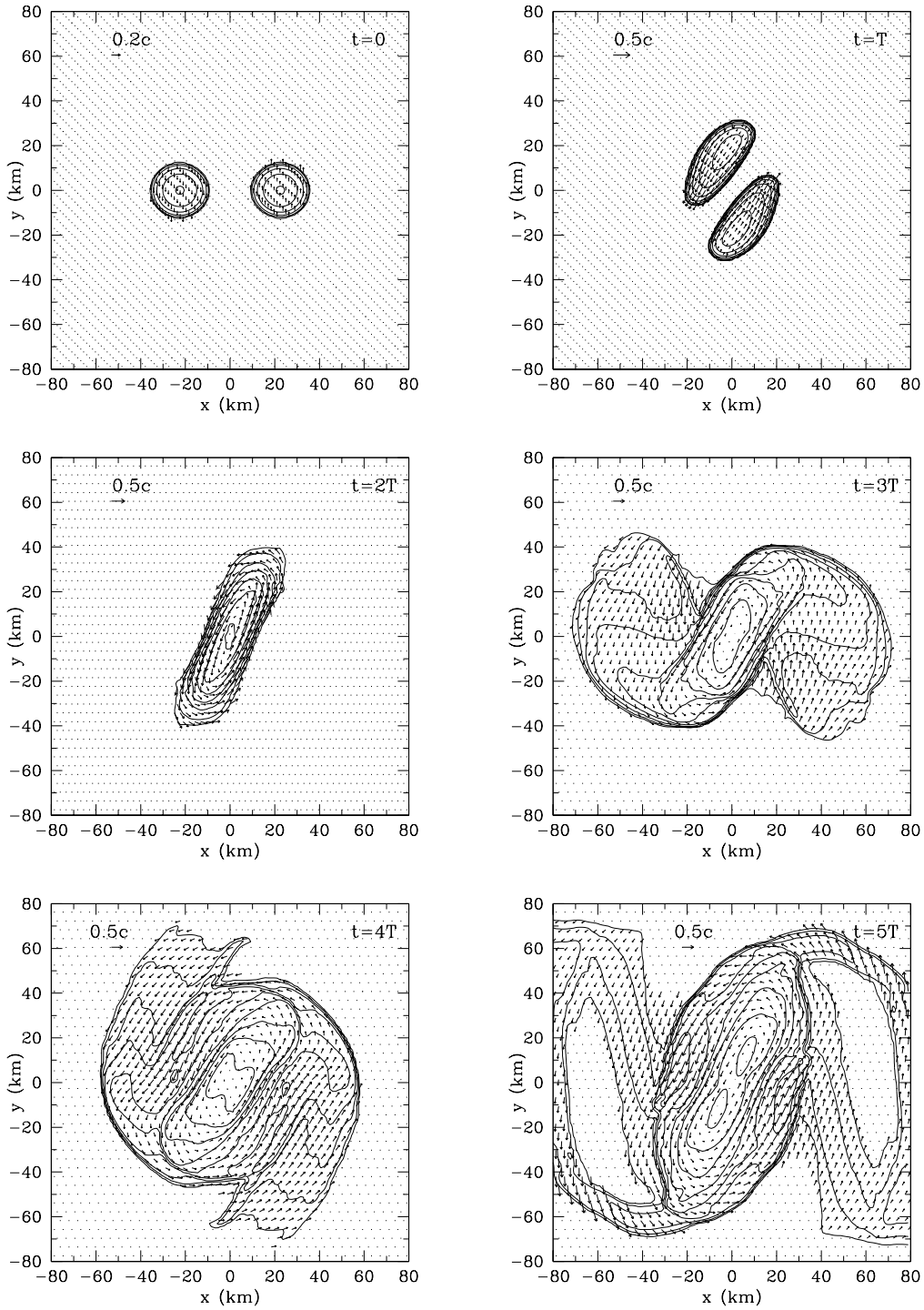

Figure 7.5: Merger sequence for the initial data reported in the text. Different panels refer to different snapshots during the merger and show the isocontours of the rest-mass density and the (downsampled) velocity field in the (x, y). The isobaric surfaces are logarithmically spaced and the length of the vector field is shown in each panel for a reference velocity. The time of the different snapshots appears in the top-right corner of each panel and it is given in multiples of the initial orbital period T, while the units on both axes are expressed in km.

Chapter 8

Conclusions

Although 3-dimensional numerical relativity has been a very active research area for several years now, there are still several technical issues to be addressed and physical problems to be investigated in detail. Separate progress has been made so far in obtaining long-term stable evolutions of vacuum spacetimes and of spacetimes with matter. Both of them have posed significant numerical problems because of the existence of horizons containing physical singularities, in one case, and the development of non-linear hydrodynamical phenomena such as shocks, in the other. In black-hole vacuum spacetimes, these problems have successfully been dealt with by using better suited formulations of the Einstein equations and by employing excision techniques for the regions of the spacetime containing the singularity. In spacetimes containing matter, on the other hand, sophisticated numerical techniques have been employed to accurately track the dynamics of the shocks.

In writing the `Whisky` code, we have combined these two winning approaches: we have implemented HRSC methods to solve the general-relativistic hydrodynamics equations in a curved spacetime, which is evolved with the NOK formulation of the Einstein equations and with "Gamma-driver" shift conditions. In addition to this, we have used excision techniques within an evolving horizon, thus following the dynamics of the matter as it moves around or accretes onto a black hole. We have shown that doing so allows the numerical evolution to proceed uninhibited also from fully-regular initial conditions of matter in equilibrium and devoid of trapped surfaces, up to a vacuum spacetime featuring an event horizon enclosing an excised physical singularity. This new important ability in numerical-relativity evolutions will help in a more detailed investigation of complex astrophysical systems, such as the ones we have begun to study in this thesis.

Now in its third year of life, `Whisky` has reached an advanced development status and is being used by several people, also other than the original groups of developers, to study different sorts of physical problems. `Whisky`, in fact, is a code thought, built and tested to be a general tool, for dealing with general scenarios involving high-density matter and strong-gravitational-field evolutions. Indeed, in addition to the works presented in this thesis, `Whisky` is presently used to perform simulations of stellar core collapse, rotating NS instabilities, collapse of differentially-rotating NS progenitors and efforts are being made to include in it the possibility to use tabulated EoSs and to extend it to magneto-hydrodynamics.

As a first astrophysical problem for this novel setup, we have focused on the collapse of rapidly-rotating relativistic stars to Kerr black holes. The stars are assumed to be in uniform rotation and dynamically unstable to axisymmetric perturbations. While the collapse of slowly-rotating initial models proceeds with the matter remaining nearly uniformly rotating, the dynamics is shown to be very different in the case of initial models rotating near the mass-shedding limit. Strong differential rotation develops, in fact, during the collapse, which is delayed due to centrifugal hang-up of the outer layers of the star. Al-

though the stars become highly flattened during collapse, attaining a disc-like shape, the collapse cannot be halted because the specific angular momentum is not sufficient for a stable disc to form. Instead, the matter in the disc spirals toward the black hole and angular momentum is transferred inwards to produce a spinning black hole.

In addition to the difficulties associated with the appearance of singularities in a numerical simulation, another special difficulty that confronts numerical relativity is the challenge of determining the asymptotic gravitational waveform which is generated during a strong-field interaction. The asymptotic waveform is just a small perturbation to the background metric and it must be determined in the wave zone, far from the strong-field sources. Such a determination presents a problem of dynamic range: one wants to measure the waveform accurately far from the sources, but one must concentrate most of the computational resources in the vicinity of those same sources, where most of the non-linear dynamics occurs. Moreover, to determine the outgoing asymptotic emission, one must wait for the wave train to propagate out into the far zone, but by then, the simulation may be losing accuracy because of the growth of singularities in the strong-field near zone. We could overcome these difficulties only by turning to level-refined grids.

In fact, by using several progressively-added nested levels of increasing resolutions, we were – on one side – able to have in the region occupied by the central object the high resolution needed there for accurately following the collapse, the horizon formation and evolution and the matter accretion, while – on the other side – we could extend the computational domain to include the wave zone. The farther position of the outer boundaries, in addition to ensuring a smaller influence of imprecise outer boundary conditions, have allowed us to reliably extract the gravitational waveforms produced in the collapse. Our confidence in the reliability of these results in threefold. Firstly, we have shown that the extracted waves are consistent, since the extraction performed at different distances from the central object well overlap when compared at the same retarded times. Secondly, inspection of the fundamental frequencies of these waves tells us that they fall in the small interval bracketed by the frequencies of the QNMs of a ringing black hole and those of the w-modes of NSs; which brings convincing physical support to our measurements. Lastly, the frequency and the shape of the waves are very similar to those computed in axisymmetry by Stark and Piran [229]. Taking the risk of being self-celebrative, we stress one final time that this is the first reliable extraction of gravitational waveforms from 3-dimensional fully-general-relativistic spacetime and hydrodynamics computations of rotating NSs collapsing to black holes.

All the techniques recalled above are being applied to the study of other physically-relevant scenarios. Studies of the collapse of differentially-rotating stars, governed by more realistic and non-isentropic EoSs are being performed while this thesis is being written. As far as this thesis is concerned, we have presented preliminary results about head-on collisions of NSs and of binary NS coalescences. Both these catastrophic events are thought to be rather common in the Universe and, especially the binary coalescence, to be one of the strongest sources of gravitational radiation detectable from Earth-based instruments.

In the case of head-on collision, we have made a systematic (but not yet complete) analysis spanning the parameter space defined by the total rest mass of the system, the EoS (polytropic or "ideal fluid") describing the NSs, their initial velocities and the initial impact parameter of the collision, while we have limited ourselves to systems of stars of equal mass. For head-on collisions, *i.e.* those with zero impact parameter, we have found that there is a critical mass for the system, above which an apparent horizon is promptly formed, while below this threshold an (also violently) oscillating NS is formed, which does not collapse to a black hole in a dynamical timescale or even in the time of the simulation (several dynamical timescales). The value of this critical mass depends on the EoS chosen for describing

the stellar material, while it is not very sensitive to the initial velocities of the stars. The value of the critical mass for the polytropic EoS coincides with the maximum mass allowed for a stable spherical NS with the same EoS parameters. In this case, in fact, the transfer of kinetic energy to internal energy which may support the collapse of more massive stars cannot occur because polytropic EoSs cannot describe shock-heating. On the contrary, shock-heating occurs for stars described with an ideal-fluid EoS and we have found that this process increases the maximum mass below which prompt collapse is avoided by about 20%. We have also noticed that, if the impact parameter is set to values different from zero and so the system is given a non-zero angular momentum (*i.e.* in near-head-on collisions), the collapse may also be delayed because of centrifugal hang-up. Only few simulations have been performed with this modification and consequently we could not yet determine the amount of angular momentum necessary to delay the collapse.

In conclusion, our work on head-on collisions implies a revision of the *Shapiro conjecture*, *i.e.* that in head-on collisions shock-heating may – in some cases – prevent prompt collapse, and we have determined which are such more stringent limits for the conjecture. We found no case in which systems with a total rest mass smaller than the critical mass for spherical stars with the same EoS promptly collapse to a black hole because of dynamical compression, as was instead claimed by Evans *et al.* [94], who, however, used an EoS different from ours.

In the case of binary NS mergers, we have discussed results concerning tests of the code for the specific problem. In this problem, in fact, the resolution and the position of the outer boundaries are crucial even for obtaining qualitatively correct results, as also found by Miller *et al.* [162], who experienced the same limitations on uniform grids. Marronetti *et al.* [149], instead, claimed to have reached a convergence, even when using resolutions and outer-boundary locations similar to ours. At present, we have not yet started simulations with level-refined grids for this specific scenario, but we are going to do so in the near future. It has to be said, however, that our code has already shown the capability of simulating the evolution of such systems for more than one orbit.

Writing this thesis has been pleasant and useful to better fix and sometimes reorganize many aspects of the work we have done in these years. We are now thrilled at the huge potential we have built for exploring and investigating complex systems in relativistic astrophysics and we are looking forward to do this in the coming years. The Universe lies still mostly unexplored above our heads. Or, perhaps, inside our heads.

Bibliography

[1] European RTN on Sources of Gravitational Waves, www.eu-network.org.

[2] Abrahams A.M., Rezzolla L., Rupright M.E., Anderson A., Anninos P., Baumgarte T.W., Bishop N.T., Brandt S.R., Browne J.C., Camarda K., Choptuik M.W., Cook G.B., Correll R.R., Evans C.R., Finn L.S., Fox G.C., Gómez R., Haupt T., Huq M.F., Kidder L.E., Klasky S.A., Laguna P., Landry W., Lehner L., Lenaghan J., Marsa R.L., Massó J., Matzner R.A., Mitra S., Papadopoulos P., Parashar M., Saied F., Saylor P.E., Scheel M.A., Seidel E., Shapiro S.L., Shoemaker D., Smarr L., Szilagyi B., Teukolsky S.A., van Putten M.H.P.M., Walker P., Winicour J., J. W. York J. *Phys. Rev. Lett.*, **80**: 1812 (1998).

[3] Abramovici A.A., Althouse W., Drever R.P., Gursel Y., Kawamura S., Raab F., Shoemaker D., Sievers L., Spero R., Thorne K.S., Vogt R., Weiss R., Whitcomb S., Zuker M. *Science*, **256**: 325 (1992).

[4] Aguiar O., *et al. Braz. J. Phys.*, **32**: 866 (2002).

[5] Alcubierre M. *Phys. Rev.*, **D55**: 5981 (1997).

[6] Alcubierre M., Allen G., Br¨ugmann B., Seidel E., Suen W.M. *Phys. Rev.*, **D62**: 124011 (2000).

[7] Alcubierre M., Benger W., Br¨ugmann B., Lanfermann G., Nerger L., Seidel E., Takahashi R. *Phys. Rev. Lett.*, **87**: 271103 (2001).

[8] Alcubierre M., Br¨ugmann B. *Phys. Rev.*, **D63**: 104006 (2001).

[9] Alcubierre M., Br¨ugmann B., Diener P., Koppitz M., Pollney D., Seidel E., Takahashi R. *Phys. Rev.*, **D67**: 084023 (2003).

[10] Alcubierre M., Br¨ugmann B., Dramlitsch T., Font J., Papadopoulos P., Seidel E., Stergioulas N., Takahashi R. *Phys. Rev.*, **D62**: 044034 (2000).

[11] Alcubierre M., Br¨ugmann B., Pollney D., Seidel E., Takahashi R. *Phys. Rev.*, **D64**: 61501 (R) (2001).

[12] Alcubierre M., Massó J. *Phys. Rev.*, **D57(8)**: 4511 (1998).

[13] Allen G., Camarda K., Seidel E. *submitted to Phys. Rev. D* (1998). gr-qc/9806036.

[14] Aloy M.A., Ibánez J.M., MartíJ.M., M¨uller E. *Astroph. J. Supp.*, **122**: 151 (1999).

[15] Aloy M.A., Pons J.A., Ibánez J.M. *Comput. Phys. Commun.*, **120**: 115 (1999).

[16] Anderson M., Matzner R.A. *Submitted to Phys. Rev. D* (2004).

[17] Anninos P., Bernstein D., Brandt S., Hobill, Seidel E., Smarr L. *Phys. Rev.*, **D50**: 3801 (1994).

[18] Anninos P., Bernstein D., Brandt S., Hobill D., Seidel E., Smarr L. *Austral. Journ. Phys.*, **48**: 1027 (1995).

[19] Anninos P., Bernstein D., Brandt S., Libson J., Massó J., Seidel E., Smarr L., Suen W.M., Walker P. *Phys. Rev. Lett.*, **74**: 630 (1995).

[20] Anninos P., Camarda K., Libson J., Seidel J.M.E., Suen W.M. *Phys. Rev.*, **D58**: 24003 (1998).

[21] Anninos P., Camarda K., Massó J., Seidel E., Suen W.M., Towns J. *Phys. Rev.*, **D52(4)**: 2059 (1995).

[22] Anninos P., Daues G., Massó J., Seidel E., Suen W.M. *Phys. Rev.*, **D51(10)**: 5562 (1995).

[23] Arnowitt R., Deser S., Misner C.W. In L. Witten (ed.), *Gravitation: An Introduction to Current Research*, pp. 227–265. John Wiley, New York (1962).

[24] Ashtekar A., Beetle C., Dreyer O., Fairhurst S., Krishnan B., Lewandowski J., Wisniewski J. *Phys. Rev. Lett.*, **85**: 3564 (2000).

[25] Ashtekar A., Beetle C., Fairhurst S. *Class. Quantum Grav.*, **17**: 253 (2000).

[26] Ashtekar A., Beetle C., Lewandowski J. *Phys. Rev.*, **D64**: 044016 (2001).

[27] Ashtekar A., Krishnan B. *Phys. Rev. Lett.*, **89**: 261101 (2002).

[28] Ashtekar A., Krishnan B. *Phys. Rev.*, **D68**: 104030 (2003).

[29] Astone P., *et al. Astroparticle Physics*, **7**: 231 (1997).

[30] Bailyn C.D. *Nature*, **364**: 388 (1993).

[31] Baiotti L., Hawke I., Montero P., Loeffler F., Rezzolla L., Stergioulas N., Font J., Seidel E. *submitted to Phys. Rev. D* (2004). gr-qc/0403029.

[32] Baiotti L., Hawke I., Montero P., Rezzolla L. In R. Capuzzo-Dolcetta (ed.), *Mem. Soc. Astron. It.*, vol. 1, p. 327 (2003).

[33] Baiotti L., Rezzolla L. *in preparation* (2004).

[34] Baker J., Brandt S.R., Campanelli M., Lousto C.O., Seidel E., Takahashi R. *Phys. Rev.*, **D62**: 127701 (2000).

[35] Balakrishna J., Daues G., Seidel E., Suen W.M., Tobias M., Wang E. *Class. Quantum Grav.*, **13**: L135 (1996).

[36] Banyuls F., Font J.A., Ibánez J.M., Martí J.M., Miralles J.A. *Astrophys. J.*, **476**: 221 (1997).

[37] Bardeen J. *Astrophys. J.*, **162**: 171 (1970).

[38] Bardeen J.M., Piran T. *Phys. Reports*, **196**: 205 (1983).

[39] Baumgarte T., Hughes S., Rezzolla L., Shapiro S.L., Shibata M. In C. Burgess, R. Myers (eds.), *General Relativity and Relativistic Astrophysics Eighth Canadian Conference*, vol. 493. AIP Conference Proceedings, Melville, New York.

[40] Baumgarte T.W., Cook G.B., Scheel M.A., Shapiro S.L., Teukolsky S.A. *Physical Review*, **D57(12)**: 7299 (1998).

[41] Baumgarte T.W., Shapiro S.L. *Physical Review*, **D59**: 024007 (1999).

[42] Baumgarte T.W., Shapiro S.L., Shibata M. *Astrophys. J.*, **528**: L29 (2000).

[43] Bildsten L., Cutler C. *Astrophys. J.*, **400**: 175 (1992).

[44] Blackburn J.K., Detweiler S. *Phys. Rev.*, **D46**: 2318 (1992).

[45] Blair D., *et al*. *Phys. Rev. Lett.*, **74**: 1908 (1995).

[46] Blanchet L., Damour T., Iyer B., Will C., Wiseman A. *Phys. Rev. Lett.*, **74**: 3515 (1995).

[47] Bona C., Ledvinka T., Palenzuela C., Zacek M. (2003). gr-qc/0307067.

[48] Bona C., Massó J., Seidel E., Stela J. *Phys. Rev. Lett.*, **75**: 600 (1995).

[49] Bonazzola S., Gourgoulhon E., Grandclément P., Novak J. *submitted to Phys. Rev. D* (2004).]mbox gr-qc/0307082.

[50] Bonazzola S., Gourgoulhon E., Marck J.A. *Phys. Rev.*, **D56**: 7740 (1997).

[51] Bonazzola S., Gourgoulhon E., Marck J.A. *Proceedings of the 19th Texas Symposium* (1998).

[52] Bonazzola S., Gourgoulhon E., Marck J.A. *Phys.Rev.Lett.*, **82**: 892 (1999).

[53] Bowen J., York J.W. *Phys. Rev.*, **D21**: 2047 (1980).

[54] Bradaschia C., *et al. Nucl. Instr. Meth. A.*, **289**: 518 (1990).

[55] Brady P.R., Creighton J.D.E., Thorne K.S. *Phys. Rev.*, **D58**: 061501 (1998).

[56] Brandt S., Correll R., Gómez R., Huq M.F., Laguna P., Lehner L., Marronetti P., Matzner R.A., Neilsen D., Pullin J., Schnetter E., Shoemaker D., Winicour J. *Phys. Rev. Lett.*, **85**: 5496 (2000).

[57] Brandt S., Font J.A., Ibáñez J.M., Massó J., Seidel E. *Comp. Phys. Comm.*, **124**: 169 (2000).

[58] Brandt S., Seidel E. *Phys. Rev.*, **D52(2)**: 856 (1995).

[59] Brandt S., Seidel E. *Phys. Rev.*, **D52(2)**: 870 (1995).

[60] Br¨ugmann B. *Phys. Rev.*, **D54(12)**: 7361 (1996).

[61] Burgay M., D'Amico N., Possenti A., Manchester R., Lyne A., Joshi B., McLaughlin M., Kramer M., Sarkissian J., Camilo F., Kalogera V., C.Kim, Lorimer D. *Nature*, **426**: 531 (2003).

[62] `Cactus Computational Toolkit`. `www.cactuscode.org`.

[63] Calabrese G., Lehner L., Neilsen D., Pullin J., Reula O., Sarbach O., Tiglio M. *Class. Quantum Grav*, **20**: L245 (2003).

[64] Camarda K., Seidel E. *Phys. Rev.*, **D59**: 064019 (1999).

[65] Centrella J., Wilson J. *Astrophys. J. SS*, **54**: 229 (1984).

[66] Cerdonio M., *et al. Class. Quantum Grav.*, **14**: 1491 (1997).

[67] Chandrasekhar S. *Ellipsoidal Figures of Equilibrium*. Yale University Press, New Haven, USA (1969). Revised edition 1987.

[68] Choptuik M.W., Hirschmann E.W., Liebling S.L., Pretorius F. *Phys. Rev.*, **D68**: 044007 (2003).

[69] Christodoulou D. *Phys. Rev. Lett.*, **25(22)**: 1596 (1970).

[70] Collela P., Woodward P.R. *J. Comput. Phys.*, **54**: 174 (1984).

[71] Cook G.B. *Phys. Rev.*, **D50(8)**: 5025 (1994).

[72] Cook G.B., Huq M.F., Klasky S.A., Scheel M.A., Abrahams A.M., Anderson A., Anninos P., Baumgarte T.W., Bishop N., Brandt S.R., Browne J.C., Camarda K., Choptuik M.W., Correll R.R., Evans C.R., Finn L.S., Fox G.C., Gómez R., Haupt T., Kidder L.E., Laguna P., Landry W., Lehner L., Lenaghan J., Marsa R.L., Masso J., Matzner R.A., Mitra S., Papadopoulos P., Parashar M., Rezzolla L., Rupright M.E., Saied F., Saylor P.E., Seidel E., Shapiro S.L., Shoemaker D., Smarr L., Suen W.M., Szilagyi B., Teukolsky S.A., van Putten M.H.P.M., Walker P., Winicour J., York Jr J.W. *Phys. Rev. Lett*, **80**: 2512 (1998).

[73] Cook J.N., Shapiro S.L., Stephens B.C. *Astrophys. J.*, **599**: 1272 (2003).

[74] Cumming A., Morsink S.M., Bildsten L., Friedman J.L., Holz D.E. *Astrophys. J.*, **564**: 343 (2000).

[75] Cutler C., Apostolatos T., Bildsten L., Finn L., Flanagan E., Kennefi ck D., Markovic D., Ori A., Poisson E., Sussman G., Thorne K. *Phys. Rev. Lett.*, **70**: 2984 (1993).

[76] Cutler C., Apostolatos T.A., Bildsten L., Finn L.S., Flanagan E.E., Kennefi ck D., Markovic D.M., Ori A., Poisson E., Sussman G.J., Thorne K.S. *Phys.Rev.Lett.*, **70**.

[77] Cutler C., Flanagan E.E. *Phys. Rev.*, **D49**: 2658 (1994).

[78] Danzmann K. *Lecture Notes in Physics*, **410**: 184 (1992).

[79] Danzmann K., Bender P., Brillet A., Cruise I.C.A., Cutler C., Fidecaro F., Folkner W., Hough J., McNamara P., Peterseim M., Robertson D., Rodrigues M., R¨udiger A., Sandford M., Sch¨afer G., Schilling R., Schutz B., Speake C., Stebbins R., Sumner T., Touboul P., Vinet J.Y., Vitale S., Ward H., Winkler W. *Max-Planck-Inistitut für Qunatenoptik, Report MPQ*, **233** (1998).

[80] Daues G.E. *Numerical Studies of Black Hole Spacetimes*. Ph.D. thesis, Washington University, St. Louis, Missouri (1996).

[81] Diener P. *Class. Quantum Grav.*, **20(22)**: 4901 (2003).

[82] Dimmelmeier H., Font J.A., M¨uller E. *Astron. and Astrophys.*, **393**: 523 (2002).

[83] Donat R., Font J.A., Ibánez J.M., Marquina A. *Journ. Comput. Phys.*, **146**: 58 (1998).

[84] Donat R., Marquina A. *Journ. Comput. Phys.*, **125**: 42 (1996).

[85] Dreyer O., Krishnan B., Shoemaker D., Schnetter E. *Phys. Rev.* (2002).

[86] Duez M.D., Baumgarte T.W., Shapiro S.L. *Phys. Rev.*, **D63**: 084030 (2001).

[87] Duez M.D., Baumgarte T.W., Shapiro S.L., Shibata M., Uryu K. *Phys. Rev.*, **D65**: 024016 (2002).

[88] Duez M.D., Marronetti P., Shapiro S.L., Baumgarte T.W. *Phys. Rev.*, **D67**: 024004 (2003).

[89] Duez M.D., Shapiro S.L., Yo H.J. *Phys.Rev.*, **D69**: 104016 (2004).

[90] Einfeldt B. *Journal of Computational Physics*, **25**: 294 (1988).

[91] Eulderink F., Mellema G. *Astron. Astrophys.*, **284**: 652 (1994).

[92] Eulderink F., Mellema G. *Astron. Astrophys.Suppl.*, **110**: 587 (1995).

[93] Evans C. In J. Centrella (ed.), *Dynamical Spacetimes and Numerical Relativity*, pp. 3–39. Cambridge University Press, Cambridge, England (1986).

[94] Evans E., Gopakumar A., Gressman P., Iyer S., Miller M., Suen W., Zhang H. *Phys. Rev.*, **D67**: 104001 (2003).

[95] Finn L.S., Chernoff D.F. *Phys. Rev.*, **D47**: 2198 (1993).

[96] Finn L.S., Evans C.R. *Ap. J.*, **351**: 588 (1990).

[97] Flanagan E.E., Hughes S. *Phys. Rev.*, **D57**: 4535 (1998).

[98] Flanagan E.E., Hughes S. *Phys. Rev.*, **D57**: 4566 (1998).

[99] Font J.A. *Living Rev. Relativity*, **2000-2** (2000).

[100] Font J.A., Goodale T., Iyer S., Miller M., Rezzolla L., Seidel E., Stergioulas N., Suen W.M., Tobias M. *Phys. Rev.*, **D65**: 084024 (2002).

[101] Font J.A., Ibánez J.M. *Astrophys. J.*, **494**: 297 (1998).

[102] Font J.A., Miller M., Suen W.M., Tobias M. *Phys. Rev.*, **D61**: 044011 (2000).

[103] Font J.A., Miller M., Suen W.M., Tobias M. *Phys. Rev.*, **D61**: 044011 (2000).

[104] Font J.A., Stergioulas N., Kokkotas K.D. *Mon. Not. R. Astron. Soc.*, **313**: 678 (2000).

[105] Frauendiener J. *Phys. Rev.*, **D66**: 104027 (2002).

[106] Friedman J.L., Ipser J.R., Sorkin R.D. *Astrophys. J.*, **325**: 722 (1988).

[107] Friedman J.L., Uryu K., Shibata M. *Phys. Rev.*, **D65**: 064035 (2002).

[108] Godunov S.K. *Mat. Sb.*, **47**: 271 (1959). In Russian.

[109] Gómez R., Lehner L., Marsa R., Winicour J., Abrahams A.M., Anderson A., Anninos P., Baumgarte T.W., Bishop N.T., Brandt S.R., Browne J.C., Camarda K., Choptuik M.W., Cook G.B., Correll R., Evans C.R., Finn L.S., Fox G.C., Haupt T., Huq M.F., Kidder L.E., Klasky S.A., Laguna P., Landry W., Lenaghan J., Masso J., Matzner R.A., Mitra S., Papadopoulos P., Parashar M., Rezzolla L., Rupright M.E., Saied F., Saylor P.E., Scheel M.A., Seidel E., Shapiro S.L., Shoemaker D., Smarr L., Szilagyi B., Teukolsky S.A., van Putten M.H.P.M., Walker P., York Jr J.W. *Phys. Rev. Lett.*, **80**: 3915 (1998).

[110] Gottlieb S., Shu C. *Math. Comp.*, **67**: 73 (1998).

[111] Gourgoulhon E., Grandclement P., Taniguchi K., Marck J., Bonazzola S. *Phys. Rev.*, **D63**: 064029 (2001).

[112] Gundlach C., Walker P. *Class. Quantum Grav.*, **16**: 991 (1999). Gr-qc/9809021.

[113] Gustafsson B., Kreiss H. *J. Comp. Phys.*, **30**: 333 (1979).

[114] Gustafsson B., Kreiss H.O., Oliger J. *Time dependent problems and difference methods*. Wiley, New York (1995).

[115] Harten A., Engquist B., Osher S., Chakrabarty S.R. *J. Comput. Phys.*, **71**: 2311 (1987).

[116] Harten A., Lax P.D., van Leer B. *SIAM Rev.*, **25**: 35 (1983).

[117] Hawke I., L¨offler F., Nerozzi A. (2004). *in preparation*.

[118] Hawley J., Smarr L., Wilson J. *Astrophys. J.*, **277**: 296 (1984).

[119] Hou T.Y., LeFloch P.G. *Math. of Comp.*, **62**: 497 (1994).

[120] Hulse R., Taylor J. *Astrophys. J.*, **195**: L51 (1975).

[121] Ibánez J., Aloy M., Font J., Martí J., Miralles J., Pons J. In E. Toro (ed.), *Godunov methods: theory and applications*. Kluwer Academic/Plenum Publishers (2001).

[122] Isaacson R., Welling J., Winicour J. *J. Math. Phys.*, **24**: 1824 (1983).

[123] Kalogera V., Kim C., Lorimer D.R., Burgay M., D'Amico N., Possenti A., Manchester R.N., Lyne A.G., Joshi B.C., McLaughlin M.A., Kramer M., Sarkissian J.M., Camilo F. *Astrophys. J.*, **601**: L179 (2004).

[124] Katz J.I., Canel L.M. *Astrophys. J.*, **471**: 915 (1996).

[125] Kawamura M., Oohara K. *Prog. Theor. Phys.*, **111**: 589 (2004).

[126] Kidder L., Scheel M., Teukolsky S., Cook G. In *Miniprogram on Colliding Black Holes: Mathematical Issues in Numerical Relativity* (2000).

[127] Kidder L.E., Scheel M.A., Teukolsky S.A. *Phys. Rev.*, **D64**: 064017 (2001).

[128] Kidder L.E., Scheel M.A., Teukolsky S.A., Carlson E.D., Cook G.B. *Phys. Rev.*, **D62**: 084032 (2000).

[129] Kokkotas K.D., F.Schutz B. *Mon. Not. R. astr. Soc.*, **255**: 118 (1992).

[130] Kokkotas K.D., Schmidt B.G. *Living Rev. Relativity*, **2**: 1999 (1999).

[131] Kramer M., Lyne A., Burgay M., Possenti A., Manchester R., Camilo F., McLaughlin M., Lorimer D., D'Amico N., Joshi B., Reynolds J., Freire P. In R.. Stairs (ed.), *Binary Pulsars*. PSAP (2004).

[132] Kuroda K., *et al*. In I.C..F. Fidecard (ed.), *Proceedings of the international conference on gravitational waves: Sources and Detectors*, p. 100.

[133] Laguna P. *Phys. Rev.*, **D60**: 084012 (1999).

[134] Laguna P., Shoemaker D. *Class. Quantum Grav.*, **19**: 3679 (2002).

[135] Lai D., Rasio F.A., Shapiro S.L. *Astrophys. J., Suppl. Ser.*, **88**: 205 (1993).

[136] Laney C.B. *Computational Gasdynamics*. Cambridge University Press (1998).

[137] Lattimer J.M., Swesty F.D. *Nucl. PHys. A*, **535**: 331 (1991).

[138] Lax P.D., Wendroff B. *Comm. Pure Appl. Math.*, **13**: 217 (1960).

[139] Leaver E. *Proc. R. Soc.London*, **A402**: 285 (1985).

[140] Leaver E.W. *Phys. Rev.*, **D41** (1990).

[141] Lehner L. *Class. Quantum Grav.*, **18**: R25 (2001).

[142] Leins M., Nollert H.P., Soffel M.H. *Phys. Rev.*, **D 48**: 3467 (1993).

[143] Leveque R.J. *Numerical Methods for Conservation Laws*. Birkhauser Verlag, Basel (1992).

[144] Leveque R.J. In E. Steiner O. & Gautschy A. (ed.), *Computational Methods for Astrophysical Fluid Flow*. Springer-Verlag (1998).

[145] Lichnerowicz A. *J. Math Pures et Appl.*, **23**: 37 (1944).

[146] Lincoln C.W., Will C.M. *Phys. Rev.*, **D42**: 1123 (1990).

[147] Liu Y.T., Shapiro S.L. *Phys. Rev.*, **D69**: 044009 (2004).

[148] Lombardi J.C., Rasio F.A., Shapiro S.L. *Phys. Rev.*, **D56**: 3416 (1997).

[149] Marronetti P., Duez M.D., Shapiro S.L., Baumgarte T.W. *Phys. Rev. Lett.*, **92**: 141101 (2004).

[150] Marronetti P., Mathews G.J., Wilson J.R. *Phys. Rev.*, **D60**: 087301 (1999).

[151] Marsa R., Choptuik M.W. *Phys. Rev.*, **D54**: 4929 (1996).

[152] Martí J.M., M¨uller E. *J. Fluid Mech.*, **258**: 317 (1994).

[153] Martí J.M., M¨uller E. *Living Rev. Relativity* (1999).

[154] Mathews G., Wilson J. *Phys. Rev.*, **D61**: 127304 (2000).

[155] Mauceli E., *et al. Phys. Rev.*, **D54**: 1264 (1996).

[156] May M.M., White R.H. *Phys. Rev.*, **141**: 1232 (1966).

[157] May M.M., White R.H. In B. Alder (ed.), *Methods in Computational Physics*, vol. 7, p. 129 (1967).

[158] McAbee T., J.R. W. *Nucl. Phys. A*, **576**: 626 (1994).

[159] Michel F.C. *Astrophys. Spa. Sci.*, **15**: 153 (1972).

[160] Miller J.C., Motta S. *Class. Quantum Grav.*, **6**: 185 (1989).

[161] Miller J.C., Sciama D.W. In H. A. (ed.), *General relativity and gravitation, II*, pp. 359–391. Plenum Press, New York, U.S.A. (1980).

[162] Miller M., Gressman P., Suen W.M. *Phys.Rev.*, **D69**: 64026 (2004).

[163] Miller M., Suen W.M., Tobias M. *Phys. Rev. Rapid Comm.*, **D63**: 121501(R) (2001).

[164] Misner C.W., Sharp D.H. *Physical Review*, **b136(2)**: 571 (1964).

[165] Moncrief V. *Annals of Physics*, **88**: 323 (1974).

[166] M¨uller E., Rampp M., Buras R., Janka H.T., Shoemaker D.H. *Astrophys. J.*, **603**: 221 (2004).

[167] Nad¨ezhin D., Novikov I., Polnarev A. *Sov. Astron.*, **22(2)**: 129 (1978).

[168] Nagy G., Ortiz O.E., Reula O.A. *Phys. Rev.*, **D70**: 044012 (2004).

[169] Nakamura T. *Prog. Theor. Phys.*, **65**: 1876 (1980).

[170] Nakamura T. *Prog. Theor. Phys.*, **66**: 2038 (1981).

[171] Nakamura T. *Prog. Theor. Phys.*, **70**: 1144 (1983).

[172] Nakamura T., Oohara K. In *Numerical Astrophysics 1998 (NAP98) - Proceedings* (1998).

[173] Nakamura T., Oohara K., Kojima Y. *Prog. Theor. Phys. Suppl.*, **90**: 1 (1987).

[174] Nakamura T., Sasaki M. *Phys. Lett.*, **106 B**: 69 (1981).

[175] New K.C.B., Tohline J.E. *Astrophys. J*, **(490)**: 311 (1997).

[176] Norman M.L., Winkler K.H.A. In M.L. Norman, K.H.A. Winkler (eds.), *Astrophysical Radiation Hydrodynamics*. Reidel (1986).

[177] Oechslin R., Rosswog S., Thielemann F. *Phys.Rev.*, **D65**: 103005 (2002).

[178] O'Murchadha N., York J. *Phys. Rev.*, **D10(8)**: 2345 (1974).

[179] Oohara K.I., Nakamura T. *Prog. Theor. Phys. Suppl.*, **128**: 183 (1997).

[180] Papadapoulos P., Font J.A. *Physical Review*, **D59**: 044014 (1999).

[181] Papadapoulos P., Font J.A. *Physical Review*, **D63**: 044016 (2001).

[182] Papadopoulos P., Font J.A. *Physical Review*, **D58**: 24005 (1998).

[183] Petrich L.I., Shapiro S.L., Stark R.F., Teukolsky S.A. *Astrophys. J.*, **336**: 313 (1989).

[184] Piran T. *Phys.Rept.*, **314**: 575 (1999).

[185] Pons J.A., Martí J.M., M¨uller E. *Journ. Fluid Mech.*, **422**: 125 (2000).

[186] Rasio F.A., Shapiro S.L. *Astrophys. J.*, **401**: 226 (1992).

[187] Rasio F.A., Shapiro S.L. *Class. Quantum Grav.*, **16**: R1 (1999).

[188] Rezzolla L., Abrahams A.M., Matzner R.A., Rupright M., Shapiro S.L. *Phys. Rev.*, **D59**: 064001 (1999).

[189] Rezzolla L., Lamb F.K., Shapiro S.L. *Astrophys. J.*, **531**: L141 (2000).

[190] Rezzolla L., Zanotti O. *Journ. Fluid. Mech.*, **449**: 395 (2001).

[191] Rezzolla L., Zanotti O., Pons J.A. *Journ. Fluid. Mech.*, **479**: 199 (2003).

[192] Richtmyer R.D., Morton K. *Difference Methods for Initial Value Problems*. Interscience Publishers, New York (1967).

[193] Roe P.L. *J. Comput. Phy.*, **43**: 357 (1981).

[194] Ruffert M., Janka H.T., Sch¨afer G. *Astron. Astrophys.*, **311**: 532 (1996).

[195] Ruffert M., Janka H.T., Takahashi K., Schaefer G. *Astron. Astrophys.*, **319**: 122 (1997).

[196] Ruffert M., Rampp M., Janka H.T. *Astron. Astrophys.*, **321**: 991 (1997).

[197] Rupright M.E., Abrahams A.M., Rezzolla L. *Phys. Rev.*, **D58**: 044005 (1998).

[198] Sarbach O., Calabrese G., Pullin J., Tiglio M. *Phys. Rev.*, **D66**: 064002 (2002).

[199] Scheel M., Baumgarte T.W., Cook G., Shapiro S.L., Teukolsky S. *Phys. Rev.*, **D56**: 6320 (1997).

[200] Scheel M.A., Baumgarte T.W., Cook G.B., Shapiro S.L., Teukolsky S.A. *Phys. Rev.*, **D58**: 044020 (1998).

[201] Scheel M.A., Shapiro S.L., Teukolsky S.A. *Phys. Rev.*, **D51(8)**: 4208 (1995).

[202] Schnetter E. *Gauge fixing for the simulation of black hole spacetimes*. Ph.D. thesis, Universit¨at T¨ubingen, T¨ubingen, Germany (2003).

[203] Schnetter E., Hawley S.H., Hawke I. *Class. Quantum Grav.*, **21**: 1465 (2004).

[204] Seidel E., Moore T. *Phys. Rev.*, **D35**: 2287 (1987).

[205] Seidel E., Myra E., Moore T. *Phys. Rev.*, **D38**: 2349 (1988).

[206] Seidel E., Suen W.M. *Phys. Rev. Lett.*, **69(13)**: 1845 (1992).

[207] Shapiro S.L. *Phys. Rev.*, **D58** (1998).

[208] Shapiro S.L. *Astrophys. J.*, **544**: 397 (2000).

[209] Shibata M. *Phys. Rev.*, **D60**: 104052 (1999). Gr-qc/9908027.

[210] Shibata M. *Prog. Theor. Phys.*, **101**: 1199 (1999). Gr-qc/9905058.

[211] Shibata M. *Prog. Theor. Phys.*, **104**: 325 (2000).

[212] Shibata M. *Phys. Rev.*, **D67**: 024033 (2003).

[213] Shibata M. *Astrophys. J.*, **595**: 992 (2003).

[214] Shibata M., Baumgarte T.W., Shapiro S.L. *Phys. Rev.*, **D61**: 044012 (2000).

[215] Shibata M., Nakamura T. *Phys. Rev.*, **D52**: 5428 (1995).

[216] Shibata M., Uryu K. *Phys. Rev.*, **D61**: 064001 (2000). Gr-qc/9911058.

[217] Shibata M., Uryu K. *Phys. Rev.*, **D64**: 104017 (2001).

[218] Shibata M., Uryu K. *Prog. Theor. Phys.*, **107**: 265 (2002).

[219] Shu C.W. Essentially non-oscillatory and weighted essentially non-oscillatory schemes for hyperbolic conservation laws. *Lecture notes ICASE Report 97-65; NASA CR-97-206253*, NASA Langley Research Center (1997). `http://techreports.larc.nasa.gov/icase/1997/icase-1997-65.pdf`.

[220] Shu C.W. In T.J. Barth, H. Deconinck (eds.), *High-Order Methods for Computational Physics*. Springer (1999).

[221] Shu C.W., Osher S.J. *Journ. Comput. Phys.*, **77**: 439 (1988).

[222] Smarr L., York J. *Phys. Rev.*, **D17**: 2529 (1978).

[223] Soberman G., Phinney E., van den Heuvel E. *Astronomy and Astrophysics*, **327**: 620 (1997).

[224] Sorkin R.D. *Astrophys. J.*, **257**: 847 (1982).

[225] Sperhake U., Smith K.L., Kelly B., Laguna P., Shoemaker D. *Phys.Rev.*, **D69**: 024012 (2003).

[226] Spruit H.C. *Astron. and Astrophys.*, **341**: L1 (1999).

[227] Stairs I., Arzoumanian Z., Camilo F., Lyne A., Nice D., Taylor J., Thorsett S., Wolszczan A. *Ap. J.*, **505**: 352 (1998).

[228] Stairs I., Thorsett S., Taylor J., Wolszczan A. *Ap. J.*, **581**: 501 (2001).

[229] Stark R.F., Piran T. *Phys. Rev. Lett.*, **55**: 891 (1985).

[230] Stark R.F., Piran T. In R. Ruffi ni (ed.), *Proceedings of the Fourth Marcell Grossman Meeting on General Relativity*, p. 327. Elsevier Science Publisher (1986).

[231] Stark R.F., Piran T. *Comp. Phys. Rep.*, **5**: 221 (1987).

[232] Stergioulas N. *Living Rev. Relativity*, **6**: 3 (2003).

[233] Stergioulas N., Font J. *Phys. Rev. Lett.*, **86**: 1148 (2001).

[234] Stergioulas N., Friedman J.L. *Astrophys. J.*, **444**: 306 (1995).

[235] Swesty F.D., Lattimer J.M., Myra E.S. *Astrophys. J.*, **425**: 195 (1994).

[236] Taniguchi K., Gourgoulhon E. *Phys. Rev.*, **D65**: 44027 (2002).

[237] Taniguchi K., Gourgoulhon E. *Phys. Rev.*, **D66**: 104019 (2002).

[238] Taniguchi K., Gourgoulhon E. *Phys. Rev.*, **D68**: 124025 (2003).

[239] Taniguchi K., Gourgoulhon E., Bonazzola S. *Phys. Rev.*, **D64**: 64012 (2001).

[240] Thornburg J. *Classical and Quantum Gravity*, **21(2)**: 743 (2004).

[241] Thorne K.S. In H. S.W., I. W. (eds.), *300 hundred years of gravitation*. Cambridge University Press.

[242] Toro E.F. *Riemann Solvers and Numerical Methods for Fluid Dynamics*. Springer-Verlag (1999).

[243] Uryu K., Eriguchi Y. *Mon. Not. R. Astron. Soc.*, **296**: L1 (1998).

[244] Uryu K., Eriguchi Y. *Phys. Rev.*, **D61**: 124023 (2000).

[245] Uryu K., Shibata M., Eriguchi Y. *Phys. Rev.*, **D62**: 104015 (2000).

[246] van Leer B.J. *Journ. Comput. Phys.*, **23**: 276 (1977).

[247] van Leer B.J. *Journ. Comput. Phys.*, **32**: 101 (1979).

[248] Walker P. *Horizons, Hyperbolic Systems, and Inner Boundary Conditions in Numerical Relativity*. Ph.D. thesis, University of Illinois at Urbana-Champaign, Urbana, Illinois (1998).

[249] Weisberg J.M., Romani R.W., Taylor, H. J. *Astrophysical Journal*, **347**: 1030 (1989).

[250] Whelan J.T., Krivan W., Price R.H. *Class. Quantum Grav.*, **17**: 4895 (2000).

[251] Whelan J.T., Romano J.D. *Phys. Rev.*, **D60**: 084009 (1999).

[252] Will C.M. *Theory and Experiment in Gravitational Physics*. Cambridge University Press, Cambrodge, Massachusetts (1992).

[253] Will C.M. *Phys. Rev.*, **D50**: 6058 (1994).

[254] Wilson J.R. *Astrophys. J.*, **173**: 431 (1972).

[255] Wilson J.R. In L. Smarr (ed.), *Sources of Gravitational Radiation*, p. 275. Cambridge University Press, Cambridge, England (1979).

[256] Wilson J.R., Mathews G.J. *Phys. Rev. Lett.*, **75**: 4161 (1995).

[257] Wilson J.R., Mathews G.J., Marronetti P. *Phys. Rev.*, **D54**: 1317 (1996).

[258] Woosley S.E. In F.F. E. Costa, J. Hjorth (eds.), *Proceedings of the International Workshop held in Rome, CNR headquarters, October, 2000*, p. 257. Springer, Berlin Heidelberg (2000).

[259] Yo H.J., Baumgarte T., Shapiro S.L. *Phys. Rev.*, **D66**: 084026 (2002).

[260] Yoneda G., Shinkai H. *Phys. Rev.*, **D66**: 124003 (2002).

[261] York J.W. *Phys. Rev. Lett.*, **26**: 1656 (1971).

[262] York Jr. J.W. In L.L. Smarr (ed.), *Sources of Gravitational Radiation*, p. 83. Cambridge University Press, Cambridge, UK (1979).

[263] Zanotti O., Rezzolla L., Font J.A. *MNRAS*, **341**: 832 (2003).

[264] Zhuge X., Centrella J.M., McMillan S.L. *Phys. Rev.*, **D50**: 6247 (1994).

[265] Zhuge X., Centrella J.M., McMillan S.L. *Phys. Rev.*, **D54**: 7261 (1996).

[266] Zwerger T. Ph.D. thesis, Technische Universit¨at M¨unchen, M¨unchen, Germany (1995).

[267] Zwerger T., M¨uller E. *Astron. Astrophys.*, **320**: 209 (1997).